

Development and Validation of Empirical and Analytical Reaction Wheel Disturbance Models

by

Rebecca A. Masterson

S.B. Mechanical Engineering (1997)
Massachusetts Institute of Technology

Submitted to the Department of Mechanical Engineering
in partial fulfillment of the requirements for the degree of

Master of Science in Mechanical Engineering

at the

MASSACHUSETTS INSTITUTE OF TECHNOLOGY

June 1999

© Massachusetts Institute of Technology 1999. All rights reserved.

Author . . . ✓

.....
Department of Mechanical Engineering
May 24, 1999

Certified by
i j n

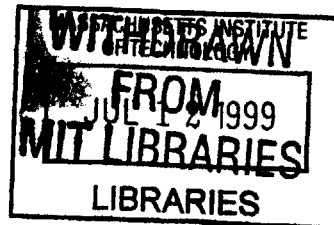
.....
David W. Miller
Associate Professor
Thesis Supervisor

Certified by

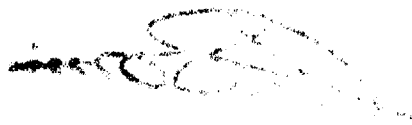
.....
Warren P. Seering
Professor/Director
Departmental Reader

Accepted by

.....
Ain A. Sonin
Chairman, Department Committee on Graduate Students



ENG



Development and Validation of Empirical and Analytical Reaction Wheel Disturbance Models

by

Rebecca A. Masterson

Submitted to the Department of Mechanical Engineering
on May 24, 1999, in partial fulfillment of the
requirements for the degree of
Master of Science in Mechanical Engineering

Abstract

Accurate disturbance models are necessary to predict the effects of vibrations on the performance of precision space-based telescopes, such as the Space Interferometry Mission (SIM) and the Next-Generation Space Telescope (NGST). There are many possible disturbance sources on such a spacecraft, but the reaction wheel assembly (RWA) is anticipated to be the largest. This thesis presents three types of reaction wheel disturbance models. The first is a steady-state empirical model that was originally created based on RWA vibration data from the Hubble Space Telescope (HST) wheels. The model assumes that the disturbances consist of discrete harmonics of the wheel speed with amplitudes proportional to the wheel speed squared. The empirical model is extended for application to any wheel through the development of a MATLAB toolbox that extracts the model parameters from steady-state RWA data. Experimental data obtained from wheels manufactured by Ithaco Space Systems are used to illustrate the empirical modeling process and provide model validation. The model captures the harmonic disturbances of the wheel quite well, but does not include interactions between the harmonics and the structural modes of the wheel which result in large disturbance amplifications at some wheel speeds. Therefore the second model, an analytical model, is created using principles from rotor dynamics to model the structural wheel modes. The model is developed with energy methods and captures the internal flexibilities and fundamental harmonic of an imbalanced wheel. A parameter fitting methodology is developed to extract the analytical model parameters from steady-state RWA vibration data. Data from an Ithaco E type wheel are used to illustrate the parameter matching process and validate the analytical model. It is shown that this model provides a much closer prediction to the true nature of RWA disturbances than the empirical model. Finally, an extended model, which combines features of both the empirical and analytical models, is introduced. This model captures all the wheel harmonics as well as the disturbance amplifications that occur due to excitation of the structural wheel modes by the harmonics. In addition, preliminary analyses that explore the dynamic coupling between RWA and spacecraft are presented and a plan for laboratory testing to gain insight into the effects of coupling and provide disturbance model validation is outlined.

Thesis Supervisor: David W. Miller

Title: Associate Professor

Acknowledgments

The author was supported in part by a fellowship from TRW Space and Electronics Group. This work was performed for the Jet Propulsion Laboratory under JPL Contract #961123 (Modeling and Optimization of Dynamics and Control for the NASA Space Interferometry Mission and the Mirco-Precision Interferometer Testbed) with Dr. Robert Laskin as Technical/Scientific Officer, Dr. Sanjay Joshi as Contract Monitor and Ms. SharonLeah Brown as MIT Fiscal Officer.

Many people have contributed to the this work. My advisor, Prof. Dave Miller, was a great source of knowledge and support. He provided valuable insights throughout the research process and spent long hours helping me through technical issues and searching for that “sign error.” It was a pleasure working for him. I also worked closely with Bob Grogan (JPL) throughout the development of these models. He provided the Ithaco B Wheel data and was always available for questions and advice. He also wrote some great MATLAB files for data processing.

I’d like to thank everyone in the Space Systems and the Active Materials and Structures Laboratories for making my two years in graduate school a fun experience. The following people, in particular, deserve special mention: Homero Gutierrez for being my mentor when I first arrived in the lab and teaching me everything I know about PSDs and RMS. He’s also a wealth of MATLAB and \LaTeX knowledge. This thesis could not possible look this good without him! Greg Mallory, for teaching me how to design my tachometer control loop, guiding me in the lab and on the analytical model, and singing 80’s songs in the “Sun Room”. Sean Kenny provide me with some valuable Lagrangian methods Maple code that made my life *much* happier. Special thanks to him for accepting a 20+ page fax and checking it meticulously for a sign error that didn’t exist, keeping me company while spinning wheels in the lab, and for being a wealth of knowledge and support. My office mate, Alice Liu, was very supportive and listened to me babble about Euler angles and patiently watched me draw that wheel diagram on the board over and over again....Her modeling insights were quite valuable throughout the analytical modeling process. Olivier deWeck aided in the final stages of the development of the RWA DADM toolbox and helped solve the mystery of the units on amplitude spectra. My UROP, Sarah Carlson, was very helpful in the lab. She designed and machined all our interfaces and spent hours taking data. She also bakes

wonderful chocolate things and laughs at all my jokes. Alvar Saenz Otero answered my million and one lab questions, made sure I didn't blow anything up and was invaluable in closing my control loop. Laila Elias spent hours running models with me over and over again and did a great job proofreading some chapters for me. Tim Glenn, the graphics guru, guided me through the scary world of .eps, .gif, .jpeg and Adobe Photoshop.

Special thanks goes to those people whose support carried me through the whole research/thesis writing process. I owe any sanity I have left to Patrick Trapa and Malinda Lutz. Trapa, thanks for all the games of Cruisin' World, lunches and dinners at Chicago Pizza and Bertuccis, taking me to McD's and making sure I got my weekly quota of french fries, solving every little trauma that occurred and *always* being able to make me smile. Malinda, thanks for eating countless lunches and dinners with me, going for numerous chocolate breaks, being my Marathon training partner, listening to me babble about reaction wheels and any other topic I could come up with and being a great source of Xfig and L^AT_EX wisdom. I'd like to recognize the Marathon D League Team - Mindy, Wicked, Stopper and Warlock. Nothing beats stress like a rocket launcher! I'd also like to thank my roommates Corinne Ilvedson and Lindsay Dolph for their support and for putting up with my mood swings! Thank you to SharonLeah Brown for always being there and to Justin Panchley being a great friend and a great source of encouragement. And, of course, A big thanks to my parents. Mom, thanks for calling to make sure I was alive, keeping me in your thoughts, believing in me and understanding when I didn't always call you back. Dad, thanks for encouraging me to be an engineer in the first place and for proofreading this *whole* thing!

Contents

1	Introduction	17
1.1	Motivation	17
1.2	Reaction Wheel Assembly	18
1.3	Disturbance Modeling	21
1.4	Thesis Overview	22
2	RWA Vibration Testing	27
2.1	Spectral Analysis	28
2.1.1	Root Mean Square	29
2.1.2	Example	31
2.2	Ithaco RWA Disturbance Data	32
2.2.1	B Wheel	33
2.2.2	E Wheel	37
2.3	Structural Wheel Modes	38
2.4	Summary	41
3	Empirical Model	43
3.1	RWA Data Analysis and Disturbance Modeling Toolbox	44
3.1.1	Overview	45
3.1.2	Identifying Harmonic Numbers	49
3.1.3	Calculating Amplitude Coefficients	54
3.1.4	Model Validation: Comparing to Data	61
3.2	Examples	65
3.2.1	Ithaco B Wheel Empirical Model	66
3.2.2	Ithaco E Wheel Empirical Model	73
3.2.3	Observations	89
3.3	Summary	92
4	Analytical Model	93
4.1	Model Development	94
4.1.1	Balanced Wheel: Rocking and Radial Modes	94
4.1.2	Static Imbalance	100
4.1.3	Dynamic Imbalance	102
4.1.4	Extended Model: Additional Harmonics	106
4.2	Model Simulation	108
4.2.1	Analytical Solutions of EOM	108
4.2.2	Preliminary Simulation Results	118

4.3	Choosing Model Parameters	120
4.3.1	Stiffness Parameters	123
4.3.2	Static and Dynamic Imbalance Parameters	126
4.3.3	Damping Parameters	128
4.3.4	Preliminary Results: Ithaco E Wheel	130
4.4	Summary	132
5	Model Coupling	135
5.1	Motivating Example	136
5.2	Component Modeling	139
5.2.1	Example	141
5.3	RWA Coupling Analyses	146
5.3.1	Case #1: No Compliance in RWA or Test Fixture	147
5.3.2	Case #2: Internal Compliance in RWA Only	151
5.3.3	Capturing the Coupled Dynamics	156
5.4	Coupling Experiments	159
5.4.1	Test Setup	159
5.5	Summary	161
6	Conclusions and Recommendations	165
6.1	Thesis Summary	165
6.2	Recommendations for Future Work	169
A	Coefficient Curve Fit Plots	173
A.1	Ithaco B Wheel	173
A.1.1	Radial Force	173
A.1.2	Radial Torque	176
A.1.3	Axial Force	179
A.2	Ithaco E Wheel	180
A.2.1	Radial Force	180
A.2.2	Radial Torque	182
A.2.3	Axial Force	184
B	Derivation of Empirical Model Autocorrelation	187
C	Tachometer Controller Design	191

List of Figures

1-1	Ithaco Type B Reaction Wheel	19
1-2	Ithaco Type E Reaction Wheel	20
1-3	Performance Assessment and Enhancement Framework	22
1-4	RWA Disturbance Models	25
2-1	Time and Frequency Domain Representations of Stochastic Process, $X(t)$.	32
2-2	Comparison of Noise and Disturbance Data (at 500 rpm) for Ithaco B Wheel (FUSE Flight Unit)	34
2-3	Waterfall Plot of Ithaco B Wheel F_x Disturbance Data	35
2-4	RWA Disturbance Data - Ithaco B Wheel	36
2-5	Wheel Speeds Corresponding to Quasi-Steady State Time Slices	38
2-6	RWA Disturbance Data - Ithaco E Wheel	39
2-7	Structural Wheel Modes	40
2-8	Disturbance Amplification from Structural Wheel Modes	41
3-1	RWA Data Analysis Process for Axial Force Disturbance	47
3-2	RWA Data Analysis Process for Radial Force Disturbance	48
3-3	RWA DADM Toolbox Function <code>iden_harm.m</code> and Sub-functions	50
3-4	Frequency Normalization of Ithaco B Wheel F_x Data (3400 rpm)	51
3-5	Disturbance Peak Identification in Ithaco B Wheel F_x Data (3400 rpm) . .	52
3-6	RWA DADM Toolbox Function <code>find_coeff.m</code>	55
3-7	Amplitude Coefficient Curve Fits for Ithaco B Wheel Radial Force Data . .	58
3-8	Amplitude Coefficient Curve Fit Showing Low Confidence Fit: $h_i = 12.38$ (Ithaco B Wheel Radial Force)	59
3-9	Effects of Internal Wheel Modes on Amplitude Coefficient Curve Fit: $h_2 =$ 1.99 (Ithaco B Wheel Radial Torque)	60
3-10	RWA DADM Toolbox Function <code>remove_mode.m</code>	60
3-11	RWA DADM Toolbox Function <code>comp_model.m</code>	61
3-12	Waterfall Plot Comparison of Radial Force Model to F_x Data (Ithaco B Wheel)	64
3-13	PSD Comparison of Radial Force Model to F_x Data (Ithaco B Wheel) with Cumulative RMS at 3000 rpm	65
3-14	Waterfall Comparison of Radial Force Model and Ithaco B Wheel F_y Data .	67
3-15	RMS Comparison of Empirical Model and Ithaco B Wheel Data: Radial Force (with and without noise floor)	68
3-16	Elimination of Rocking Mode Disturbance Amplification from Calculation of C_3 ($h_3 = 3.16$)	69
3-17	Waterfall Comparisons of Radial Torque Model and Ithaco B Wheel Data .	70

3-18	RMS Comparison of Empirical Model and Ithaco B Wheel Data: Radial Torque (with and without noise floor)	71
3-19	Elimination of Axial Mode Disturbance Amplification from Amplitude Coefficient Calculations: Ithaco B Wheel Axial Force	72
3-20	Waterfall Comparison of Axial force Model and Ithaco B Wheel F_z Data . .	73
3-21	RMS Comparison of Empirical Model and Ithaco B Wheel Data: Axial Force (with and without noise floor)	74
3-22	Amplitude Coefficient Curve Fit for Radial Force Harmonic, $h_1 = 1.0$	76
3-23	Waterfall Comparison of Radial Force Model and Ithaco E Wheel F_x Data Showing Modal Excitation	78
3-24	Elimination of Disturbance Amplification from Amplitude Coefficient Calculations: Ithaco E Wheel Radial Force (1)	79
3-25	Elimination of Disturbance Amplification from Amplitude Coefficient Calculations: Ithaco E Wheel Radial Force (2)	80
3-26	Waterfall Comparison of Radial Force Model and Ithaco E Wheel Data . .	81
3-27	RMS Comparison of Empirical Model and Ithaco E Wheel Data: Radial Force	81
3-28	Waterfall Comparison of Radial Torque Model and Ithaco E Wheel T_x Data Showing Modal Excitation	83
3-29	Elimination of Disturbance Amplification from Amplitude Coefficient Calculations: Ithaco E Wheel Radial Torque	84
3-30	Waterfall Comparison of Radial Torque Model and Ithaco E Wheel Data . .	85
3-31	RMS Comparison of Empirical Model and Ithaco E Wheel Data: Radial Torque	85
3-32	Waterfall Comparison of Axial Force Model and Ithaco E Wheel F_z Data Showing Modal Excitation	87
3-33	Elimination of Disturbance Amplification from Amplitude Coefficient Calculations: Ithaco E Wheel Axial Force	88
3-34	Waterfall Comparison of Axial force Model and Ithaco E Wheel F_z Data . .	89
3-35	RMS Comparison of Empirical Model and Ithaco E Wheel Data: Axial Force	90
3-36	Model/Data Comparison Plots with Cumulative RMS Curves	91
4-1	Model of Balanced Flywheel on Flexible Supports	95
4-2	Euler Angle Rotations and Coordinate Frame Transformations for Balanced Wheel	96
4-3	Model of Static Wheel Imbalance	100
4-4	Model Dynamic Wheel Imbalance	103
4-5	Analytical RWA Model	105
4-6	Incorporation of Harmonic Disturbances into Analytical Model	107
4-7	Extended Analytical Model Simulation	120
4-8	Frequency of Rocking Mode Whirls and Fundamental Harmonic as Function of Wheel Speed, $\omega_r=70$ Hz	122
4-9	Setting Analytical Model Parameter, k , Using Ithaco E Wheel Radial Force Data	125
4-10	Setting Analytical Model Parameter, d_k , Using Ithaco E Wheel Radial Torque Data	127
4-11	Setting Imbalance Parameters for Analytical Model Using Ithaco E Wheel Data for Fundamental Harmonic	128
4-12	Setting Damping Parameters for Analytical Model Using Ithaco E Wheel Radial Torque Data for Fundamental Harmonic	129

4-13	RMS Comparison of Ithaco E Wheel Radial Torque Data and RWA disturbance Models, frequency bandwidth: $[0, 1.3\Omega]$	131
5-1	Spring Mass Models	136
5-2	Coupled spacecraft and RWA system	137
5-3	Connection of two components through feedback	139
5-4	Example system containing two subsystems	141
5-5	Isolated components in free-free form	141
5-6	Coupled system for Case #1	148
5-7	Component Models for Case #2	152
5-8	System Model for Case #2	152
5-9	Comparison of Exact Solution and Current Methods Using Varying Model Parameters.	156
5-10	Representative Reaction Wheel Hard-mounted to Load Cell	160
5-11	Block Diagram Representation Data Acquisition Configuration for Wheel	160
5-12	Full View of Flexible Truss Testbed	161
5-13	Representative Reaction Wheel Mounted to Flexible Testbed	163
A-1	Coefficient Curve Fits - Ithaco B Wheel Radial Force (1)	173
A-2	Coefficient Curve Fits - Ithaco B Wheel Radial Force (2)	174
A-3	Coefficient Curve Fits - Ithaco B Wheel Radial Force (3)	175
A-4	Coefficient Curve Fits - Ithaco B Wheel Radial Torque (1)	176
A-5	Coefficient Curve Fits - Ithaco B Wheel Radial Torque (2)	177
A-6	Coefficient Curve Fits - Ithaco B Wheel Radial Torque (3)	178
A-7	Coefficient Curve Fits - Ithaco B Wheel Axial Force	179
A-8	Coefficient Curve Fits - Ithaco E Wheel Radial Force (1)	180
A-9	Coefficient Curve Fits - Ithaco E Wheel Radial Force (2)	181
A-10	Coefficient Curve Fits - Ithaco E Wheel Radial Torque (1)	182
A-11	Coefficient Curve Fits - Ithaco E Wheel Radial Torque (2)	183
A-12	Coefficient Curve Fits - Ithaco E Wheel Axial Force (1)	184
A-13	Coefficient Curve Fits - Ithaco E Wheel Axial Force (2)	185
C-1	Schematic Diagram of Representative Reaction Wheel Showing Flywheel and Motor	191
C-2	Fitting Plant Transfer Function for Open Loop System	193
C-3	Block Diagram of Tachometer Control Loop	193
C-4	Circuit Diagram of Tachometer Controller	194

List of Tables

2.1	Frequencies and Amplitudes of X(t)	31
2.2	Ithaco TORQWHEEL Design Specifications	33
2.3	Frequencies of Ithaco Structural Wheel Modes	40
3.1	Ithaco B Wheel F_x Data Set	49
3.2	Bin Statistics for Ithaco B Wheel Radial Harmonics($f_{Lim} = 200$ Hz)	54
3.3	Empirical Model Parameters for Ithaco B Wheel	66
3.4	Empirical Model Parameters for Ithaco E Wheel	74
3.5	Inputs for Ithaco E Wheel Radial Force Modeling	75
3.6	Disturbance Amplification in Radial Force Harmonics	77
3.7	Disturbance Amplification in Radial Torque Harmonics	83
3.8	Inputs for Ithaco E Wheel Axial Force Modeling	86
3.9	Disturbance Amplification in Axial Force Harmonics	87
4.1	Model Parameters and Fitting Methodologies	121
4.2	Parameters for Analytical Model of Ithaco E Wheel	130
5.1	Plant Models	146
5.2	Compliance conditions for RWA Disturbance Models	146
5.3	RWA/Spacecraft Coupling Analysis	147
5.4	Summary of Results	162

Nomenclature

Abbreviations

DADM	Data Analysis and Disturbance Modeling
EOM	equations of motion
FEM	finite element model
FFT	fast Fourier transform
GSFC	Goddard Space Flight Center
HST	Hubble Space Telescope
JPL	Jet Propulsion Laboratory
NGST	Next Generation Space Telescope
PSD	power spectral density
RMS	root mean square
RWA	reaction wheel assembly
SIM	Space Interferometry Mission

Symbols

A	amplitude spectrum
$\tilde{A}, \tilde{B}, \tilde{C}, \tilde{D}$	constants
C	amplitude coefficient
\tilde{C}	amplitude coefficient (with modal effects)
\mathcal{D}	data set
E	expected value
F	force
$\mathbf{F}_{peak}, \mathbf{F}_{bin}, \mathbf{F}_{stat}$	harmonic number identification matrices
\mathcal{F}	Fourier transform operator
H	transfer function
I	inertia
\mathcal{L}	Lagrangian
M, m	mass
R, r	radius
$R_X(\tau)$	autocorrelation
S	power spectral density
T	torque, kinetic energy
U	position in inertial frame
u_s	static imbalance
u_d	dynamic imbalance
V	potential energy, voltage
W	work

$X(t)$	stochastic process
XYZ	ground-fixed reference frame
a	acceleration
d	distance
c	damping coefficient
c_θ	torsional damping coefficient
f	frequency variable (Hz)
h	harmonic number
i	harmonic index, $\sqrt{-1}$
j	wheel speed index
k	stiffness
k_θ	torsional stiffness
n	number of harmonics in model
s	Laplace variable
t, τ	time variables
u	position in body-fixed frame
v	translational velocity
x, y	translational displacement
xyz	body-fixed reference frame
Φ	transformation matrix
Ω	wheel speed
α	phase angle
δ	variation
ζ	damping ratio
θ, ϕ, ψ	Euler angles for analytical model
μ	mean
ξ	generalized coordinate
σ^2	variance
σ	root mean square
ω	frequency variable (rad/s), natural frequency, angular velocity
$\bar{\omega}$	RWA disturbance frequency

Subscripts and Superscripts

$\hat{(\cdot)}$	unit vector
$(\cdot)^*$	normalized quantity
$(\cdot)^H$	Hermitian (complex-conjugate transpose)
$(\cdot)^T$	transpose
$(\cdot)_{axi}$	indicates axial force disturbance
$(\cdot)_h$	homogeneous solution
$(\cdot)_{ij}$	(i,j) entry of a matrix
$(\cdot)_p$	particular solution
$(\cdot)_{rad}$	indicates radial force disturbance
$(\cdot)_{tor}$	indicates radial torque disturbance

matrices and vectors are denoted with bold type, i.e **f** and Φ

Chapter 1

Introduction

1.1 Motivation

NASA's Origins program is a series of missions planned for launch in the early part of the 21st century that is designed to search for Earth-like planets capable of sustaining life and to answer questions regarding the origin of the universe. The first generation missions include the Space Interferometry Mission (SIM), which is a space-based interferometer with astrometry and imaging capabilities [1], and the Next-Generation Space Telescope (NGST), a near-infrared telescope ¹. These telescopes will employ new technologies to achieve large improvements in angular resolution and image quality and to meet the goals of high resolution and high sensitivity imaging and astrometry [2]. The ability of the missions to accomplish their objectives will depend heavily on their structural dynamic behavior.

SIM and NGST pose challenging problems in the areas of structural dynamics and control since both instruments are large flexible, deployed structures with tight pointing stability requirements. The optical elements on SIM must meet positional tolerances on the order of 1 nanometer across the entire 10 meter baseline of the structure to meet astrometry requirements [3], and those on NGST must be aligned within a fraction of a wavelength to meet optimal observation requirements [4]. Disturbances from both the orbital environment (atmospheric drag, gravity gradient, thermal "snap" [5], solar pressure), and on-board mechanical systems and sensors (reaction wheels, optical delay lines, cryo-coolers, mirror drive motors, tape recorders) are expected to impinge on the structure

¹see Origins website: <http://origins.jpl.nasa.gov>

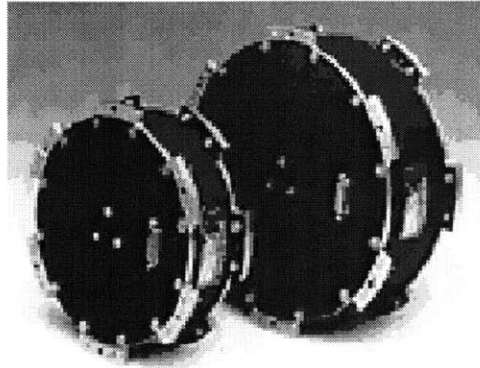
causing vibrations which can introduce jitter in the optical train exceeding the performance requirements. It is expected that the largest disturbances will be generated on-board and will be dominated by vibrations from the reaction wheel assembly (RWA) [3].

1.2 Reaction Wheel Assembly

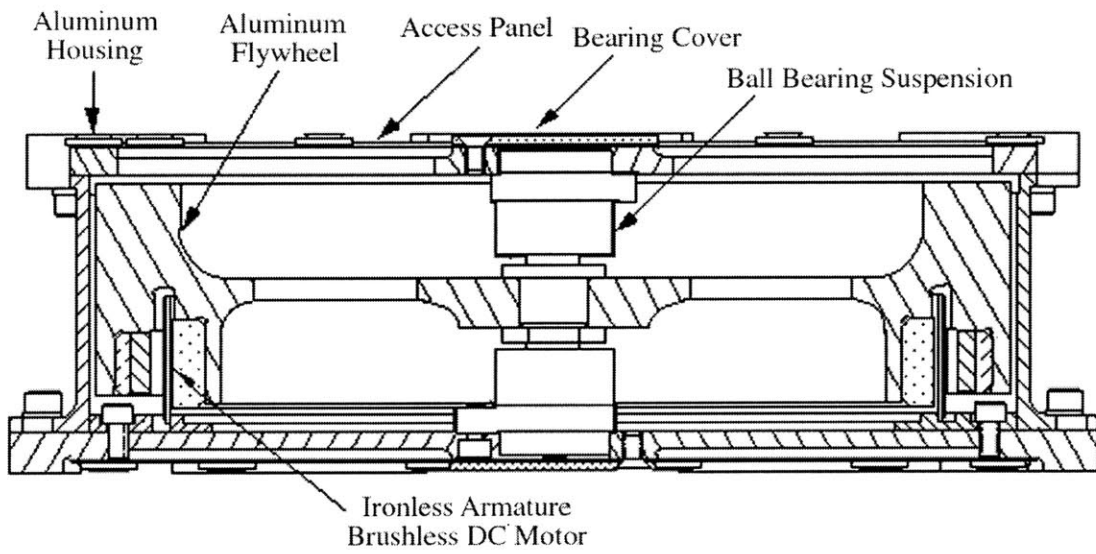
When maneuvering on orbit, spacecraft generally require an external force, or torque, which is sometimes provided by thrusters. As an alternative, RWA can counteract zero-mean torques on the spacecraft without the consumption of precious fuel and can store momentum induced by very low frequency or DC torques. [6]. They are often used for both spacecraft attitude control [7] and performing large angle slewing maneuvers [8]. Other applications include vibration compensation and orientation control of solar arrays [9]. A typical RWA consists of a rotating flywheel suspended on ball bearings encased in a housing and driven by an internal brushless DC motor. Ithaco type B and E Wheels are shown in Figures 1-1 and 1-2². The Ithaco B Wheel is the larger of the two wheels pictured in Figure 1-1(a). The smaller wheel is the Ithaco type A wheel and is not discussed in this thesis. The cross-sectional views show that the flywheel is designed such that its mass is concentrated on the outer edges to provide maximum inertia for minimum mass. Alternative RWA designs include the use of magnetic bearings to replace traditional ball bearings [10, 11].

During the manufacturing process, RWAs are balanced to minimize the vibrations that occur during operation. However, it has been found that the vibration forces and torques emitted by the RWA can still degrade the performance of precision instruments in space [8, 12, 13, 14, 15]. These vibrations generally result from four main sources: flywheel imbalance, bearing disturbances, motor disturbances and motor driver errors [16]. Flywheel imbalance is generally the largest disturbance source in the RWA and causes a disturbance force and torque at the wheel's spin rate, that is referred to as the fundamental harmonic. There are two types of flywheel imbalances, static and dynamic. Static imbalance results from the offset of the center of mass of the wheel from its spin axis, and dynamic imbalance is caused by the misalignment of the wheel's principle axis and the rotation axis. Bearing disturbances, which are caused by irregularities in the balls, races, and/or cage [17], produce disturbances at both sub- and super-harmonics of the wheel's spin rate. Low frequency

²obtained from Ithaco web site: www.ithaco.com

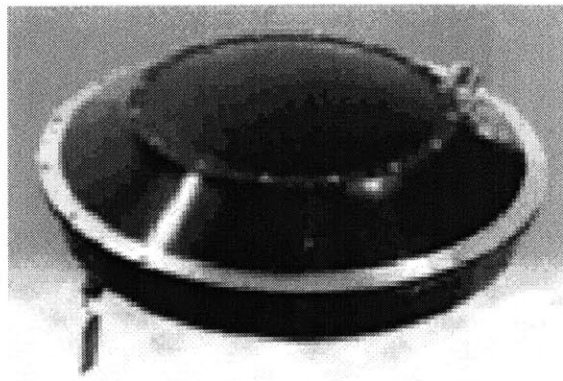


(a) External View

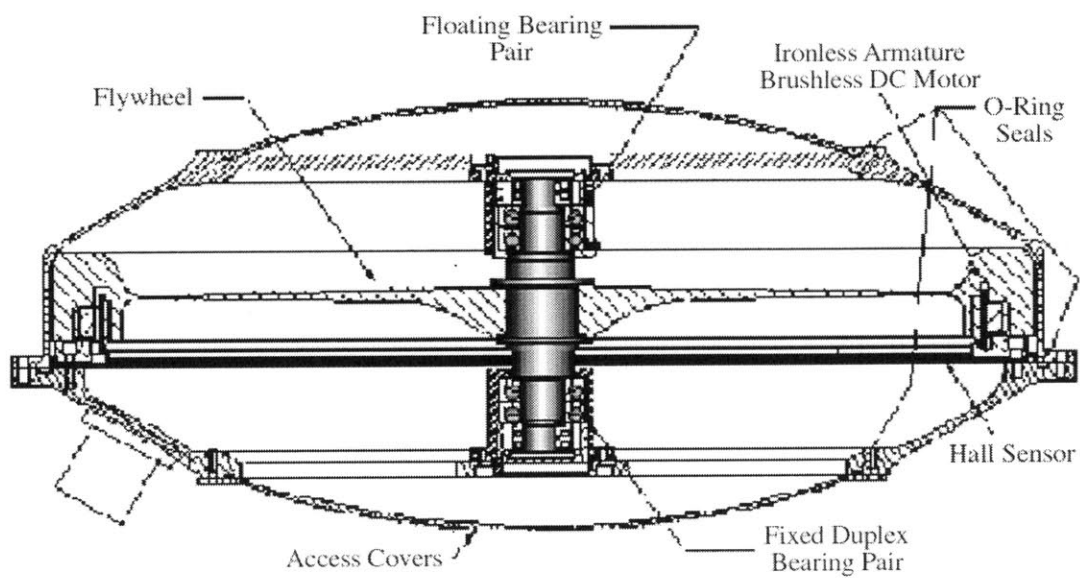


(b) Cross-Section

Figure 1-1: Ithaco Type B Reaction Wheel



(a) External View



(b) Cross-Section

Figure 1-2: Ithaco Type E Reaction Wheel

disturbances are generally a result of lubricant dynamics, while high frequency disturbances are caused by the bearing irregularities. The torque motor in a RWA is another possible disturbance source. Brushless DC motors exhibit both torque ripple and cogging which generate very high frequency disturbances [16].

1.3 Disturbance Modeling

In general, isolation systems are used to reduce the effects of RWA disturbances on the spacecraft [8, 12, 14, 18]. Models of the disturbances are created for use in disturbance analysis to predict the effects of the vibrations on the spacecraft and allow the development of suitable control and isolation techniques. The most commonly used RWA disturbance model was created to predict the effects of RWA induced vibrations on the Hubble Space Telescope (HST) [15]. The model is based on induced vibration testing performed on the HST flight wheels and assumes that the disturbances are a series of harmonics at discrete frequencies with amplitudes proportional to the wheel speed squared. The model is fit to the vibration data and provides a prediction of the disturbances at a given wheel speed. However, during operation it is often necessary to run the RWAs at a range of speeds. Therefore the discrete frequency model was used to create a stochastic broad-band model that predicts the power spectral density (PSD) of RWA disturbances over a given range of wheel speeds [18]. The model assumes that the wheel speed is a random variable with a given probability density function. Both the discrete frequency and stochastic models capture the disturbances of a single RWA. However, in application, multiple RWAs are used to provide multi-axis torques to the spacecraft and for redundancy. Therefore a model was developed which predicts the disturbance PSDs of multiple RWAs in a specified orientation based on a frequency domain disturbance model of a single wheel [4, 19]. The multiple wheel model transforms the RWA disturbances from a frame attached to the RWA to the general spacecraft frame allowing a disturbance analysis.

A performance assessment and enhancement methodology was developed to incorporate disturbance, sensitivity and uncertainty analyses into a common framework [19]. The approach is presented in block diagram form in Figure 1-3. A disturbance model, generally created from experimental data, d , is used to drive a model of the spacecraft, or plant. Then performance outputs, z , are compared against the requirements, z_{req} , to assess the

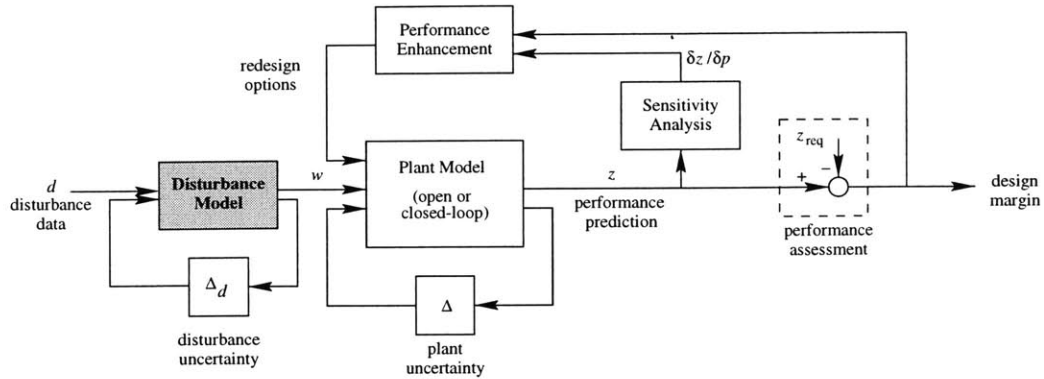


Figure 1-3: Performance Assessment and Enhancement Framework

spacecraft/controller design. The accuracy of the results obtained from this methodology depends heavily on the quality of the disturbance model. If the disturbances are modeled incorrectly the performance output, z , will not correctly predict the performance of the spacecraft when exposed to the disturbance environment. Therefore, in order to meet the stringent performance requirements on next generation telescopes, such as SIM and NGST, accurate disturbance models are necessary. Thus, the focus of this thesis is the development of RWA disturbance models for incorporation into the overall performance assessment and enhancement framework and is represented by the shaded block in Figure 1-3.

1.4 Thesis Overview

Figure 1-4 provides a detailed view of the disturbance model block in Figure 1-3. The input, d , represents RWA vibration data that is used to develop a model, w , for a given wheel. The five blocks within the dashed line represent the RWA disturbance models that can be used for disturbance analysis. The first block, labeled “Empirical”, is based on the discrete frequency HST model. The empirical model extends the HST model for application to any RWA through the development of a MATLAB toolbox that extracts the model parameters from steady-state RWA disturbance data. The empirical model can be represented in either the time or the frequency domain, and can be directly input to the multi-wheel model to predict the disturbances of multiple wheels or can be combined with other models as shown in Figure 1-4. The empirical model alone only captures the disturbances at discrete wheel speeds. In order to predict the broadband behavior of the wheels over a range of speeds

the empirical model parameters are input to the stochastic model (block (e)) to produce a disturbance PSD that can be input to the multi-wheel model. The form of the broadband model also allows easy transformation from PSDs (frequency domain) to state space models [19].

A second drawback of the empirical model is that it does not capture the internal flexibility of the RWA. Therefore, it can be combined with an analytical model (block (d)) to produce a more complete extended model (block (f)). The analytical model is the second model discussed in this thesis and captures the physical behavior of an unbalanced rotating flywheel. The model is developed using principles from rotor dynamics and accounts for the structural modes of the RWA which cause disturbance amplification in the vibration data that are not captured by the empirical model.

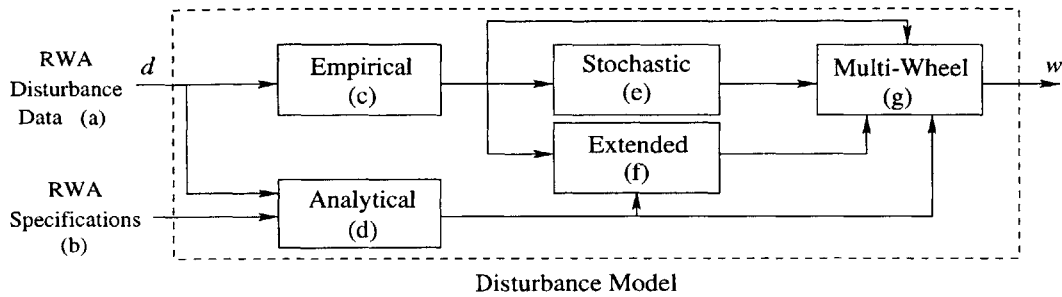
Although the analytical model captures the internal flexibility of the wheel it is not a complete disturbance model because only the fundamental harmonic is included. Therefore, the analytical and empirical model are combined to create the third model, the extended model. Both the analytical and extended model can be represented in either time or frequency domain. Although the models are nonlinear, they can be linearized to obtain time-variant state-space models at discrete wheel speeds. When left in their nonlinear form, the models can be used to explore the transient disturbance behavior of the RWA as it sweeps through wheel speeds.

Both models can be input to the multi-wheel model to produce a disturbance model that can be used in a disturbance analysis. The extended model is the most complete RWA model available, but it is also the most costly to create. Parameter extraction from disturbance data must be performed to obtain both the empirical and analytical model parameters. Therefore, during early stages of design, the use of either the empirical or analytical model may provide a good approximation to the disturbance behavior of the RWA.

The flexibilities of the spacecraft and RWA result in dynamic coupling between the two systems that is not captured in the models discussed above. Therefore it may be necessary to include a final coupling block in Figure 1-4 before the multi-wheel model or between the multi-wheel model and the disturbance, w . This additional block would incorporate the effects of dynamic coupling between the RWA and the spacecraft increasing the accuracy of the disturbance models.

The organization of the thesis is included in Figure 1-4. RWA vibration testing is the

subject of Chapter 2. Methods of processing the time domain data are discussed and the details of vibration tests performed on wheels manufactured by Ithaco Space Systems are presented. The empirical model is presented in Chapter 3. The toolbox functions that were developed to extract the model parameters from the steady-state data are discussed in detail, and the vibration data from the Ithaco wheels is used to validate the model. The subjects of Chapter 4 are the analytical and extended models. The development of the models are presented and a parameter matching methodology that fits the analytical model parameters to RWA disturbance data is developed. The Ithaco E Wheel is used to validate the analytical model through comparison with data and the empirical model. Chapter 5 discusses the coupling of a RWA disturbance model to a spacecraft model. Preliminary analyses of the coupling effects and a testing plan for development and validation of a coupling model are presented. In the final chapter of the thesis, Chapter 6, the work is summarized and recommendations are made for future work.



Comments

(a) from isolated vibration tests.
generally steady-state.

Chapter 2

(b) physical wheel parameters
from manufacturer.

(c) from RWA DADM toolbox.
wheel harmonic only.
steady-state model.
discrete wheel speeds.

Chapter 3

(d) physical model.
fundamental harmonic and
structural wheel modes.
steady-state or transient

Chapter 4

(e) assumes wheel speed is a
random variable.

broadband disturbances over
range of speeds.

by J. Melody

(f) combines empirical and
analytical models.

all harmonics and
structural wheel modes
steady-state or transient

Chapter 4

(g) multiple wheel model.
 n wheels at specified
orientations.

spacecraft reference frame
by H. Gutierrez

Figure 1-4: RWA Disturbance Models

Chapter 2

RWA Vibration Testing

RWA vibration data are used throughout this thesis to illustrate modeling and parameter matching methodologies and to validate the disturbance models. Both the form and parameters of the empirical model are based solely on vibration data, and the analytical model parameters are determined using such data. The data are obtained from isolated tests in which the RWA is hardmounted to a fairly rigid test fixture and either spun at discrete speeds or allowed to spin through a range of speeds. Time histories of the disturbances that result are obtained through load cells mounted at the interface of the wheel and the test fixture. Spectral analysis techniques are used to process the time histories into frequency domain data and gain insight into the nature of RWA disturbances through examination of their frequency content.

The data that will be used for model validation were obtained from wheels manufactured by Ithaco Space Systems and tested at Orbital Sciences Corp. and NASA Goddard Space Flight Center (GSFC). This chapter begins with a discussion of the spectral analysis techniques used to process the data. Then, the details of the RWA vibration tests performed by Orbital and GSFC, and the data that were obtained, are presented. It will be shown that the data contain disturbance amplifications resulting from flexibility within the wheel. The chapter concludes with a discussion of the structural dynamics of the wheel and its dominant vibration modes.

2.1 Spectral Analysis

In general, a signal can be characterized as either purely deterministic or stochastic (random). A deterministic signal is one that is exactly predictable over the time period of interest, such as $x(t) = 10 \sin(2\pi t)$. A stochastic signal, on the other hand, is one that has some random element associated with it. One example of a stochastic process is a sine wave with random phase: $X(t) = 10 \sin(2\pi t + \alpha)$ where α is evenly distributed between 0 and 2π [20]. In addition, a stochastic signal can be further characterized as deterministic or non-deterministic. The example, $X(t)$, given above is a deterministic stochastic process because it is deterministic in form, but has some random element. Pure white noise, on the other hand, is a nondeterministic stochastic process, since it is purely determined by chance and has no particular structure at all.

RWA disturbances are generally modeled as deterministic random processes similar to the second example given above. Such a process can be characterized by its autocorrelation function, which describes how well the process is correlated with itself at two different times and is defined as:

$$R_X(\tau) = R_X(t, t + \tau) = E[X(t)X(t + \tau)] \quad (2.1)$$

where $X(t)$ is a stationary random process and $E[\cdot]$ is the expectation operator. A random process is described as stationary if its probability density functions are time invariant. The autocorrelation function contains information about the frequency content of the process. If $R_X(\tau)$ decreases rapidly with time, then the process changes rapidly with time, and conversely if $R_X(\tau)$ decreases slowly with time, the process is changing slowly [20]. Taking the Fourier transform of Equation 2.1 produces the power spectral density function, $S_X(\omega)$ and transforms the time domain signal to the frequency domain:

$$\begin{aligned} S_X(\omega) &= \mathcal{F}[R_X(\tau)] \\ &= \int_{-\infty}^{+\infty} R_X(\tau) e^{-i\omega\tau} d\tau \end{aligned} \quad (2.2)$$

where $\mathcal{F}[\cdot]$ indicates Fourier transform. Conversely, the autocorrelation can be recovered from the spectral density:

$$R_X(\tau) = \mathcal{F}^{-1}[S_X(\omega)]$$

$$= \frac{1}{2\pi} \int_{-\infty}^{+\infty} S_X(\omega) e^{i\omega\tau} d\omega \quad (2.3)$$

Note that the factor $\frac{1}{2\pi}$ appears in the definition of the inverse Fourier transform. There is an alternative definition that includes this factor in the Fourier transform [21]. Both definitions are correct and will yield the same results if used consistently. The power spectral density (PSD) provides information about the frequency content of the random signal, and is generally plotted versus frequency.

Another useful frequency domain representation of a stochastic process is the amplitude spectrum. It provides an estimate of the signal amplitude as a function of frequency and is defined as:

$$A_X(\omega) = \frac{1}{2\pi T} \left| \int_0^T X(t) e^{-i\omega t} dt \right| \quad (2.4)$$

where T is the length of the time history. The units of $A_X(\omega)$ are the same as those of $X(t)$. If the random signal is $X(t) = A_1 \sin(\omega_0 t + \alpha)$ the value of the amplitude spectrum at the frequency of the sinusoid is equal to the amplitude of the sinusoid: $A_X(\omega_0) = A_1$. In engineering practice both the power spectral density and the amplitude spectrum are generally plotted against a frequency axis in units of hertz (Hz). Therefore the following transformations are made:

$$S_X(f) = 2\pi S_X(\omega) \quad (2.5)$$

$$A_X(f) = 2\pi A_X(\omega) \quad (2.6)$$

where $S_X(f)$ and $A_X(f)$ are the power spectral density and amplitude spectra in hertz and have units of $x(t)^2/\text{Hz}$ and $x(t)$, respectively.

2.1.1 Root Mean Square

The mean, $\mu_X(t)$, and variance, $\sigma_X(t)$ of a random process, $X(t)$, are defined as

$$\mu_X(t) = E[X(t)] \quad (2.7)$$

$$\sigma_X^2(t) = E[\{X(t) - \mu_X(t)\}^2] \quad (2.8)$$

The mean square, r_X^2 is defined as the expected value of the square of the random process and can be expressed in terms of the mean and variance through Equation 2.8:

$$\begin{aligned} r_X^2 &= E[X(t)^2] \\ &= \sigma_X^2 + \mu_X^2 \end{aligned} \quad (2.9)$$

The square root of the mean square is referred to as the root mean square (RMS) and is a useful metric for validating the disturbance models through data comparison. It is easy to see from Equation 2.9 that for a zero-mean process the RMS is simply equal to the square root of the variance. For simplicity, the assumption is made that all stochastic disturbances presented in this thesis are zero-mean.

The mean square can also be obtained from the autocorrelation function. Evaluating Equation 2.1 at $\tau = 0$ and using the relationship in Equation 2.9 results in:

$$R_X(0) = E[X(t)^2] = \sigma_X^2 \quad (2.10)$$

An alternative definition for $R_X(0)$ can be obtained by substituting $\tau = 0$ into Equation 2.3 and transforming $S_X(\omega)$ to $S_X(f)$:

$$R_X(0) = \int_{-\infty}^{+\infty} S_X(f)df \quad (2.11)$$

Equations 2.10 and 2.11 suggest a relationship between the variance of a random process and its PSD:

$$\sigma_X^2 = \int_{-\infty}^{+\infty} S_X(f)df \quad (2.12)$$

Therefore, the RMS of a zero-mean, stationary process is simply the square root of the area under the PSD over the frequency band of interest. Equation 2.12 is a powerful result and is used extensively throughout the RWA disturbance modeling and validation processes.

Another metric that is useful in the model validation process is the cumulative RMS, $\sigma_{X_c}(f_0)$. It is defined as:

$$\sigma_{X_c}(f_0) = \left(2 \int_{f_{min}}^{+f_0} S_X(f)df \right)^{\frac{1}{2}} \quad (2.13)$$

where $f_0 \in [f_{min}, f_{max}]$ and f_{min} and f_{max} are the upper and lower limits of the frequency band of interest [19]. These limits are generally set by the frequency range of the measured

Table 2.1: Frequencies and Amplitudes of X(t)

Harmonic	Frequency (Hz)	Amplitude (N)
1	10	1
2	25	1.5
3	40	4

PSD. In practice, the cumulative RMS of a signal is calculated by dividing its PSD into smaller segments. The RMS of each of these PSD segments is calculated by integrating over the frequency bandwidth of each segment to obtain the variance of the segment. A running total of the segment variances is computed, and the cumulative RMS is the square root of this total. The cumulative RMS curve is most useful when plotted with the corresponding PSD or amplitude spectra of the signal. It allows identification of the frequencies at which significant contributions to the total RMS occur.

2.1.2 Example

A simple example is used to illustrate the concepts presented above and demonstrate their application. Consider a random process, $X(t)$, that consists of three harmonics:

$$X(t) = \sum_{i=1}^3 A_i \sin(\omega_i t + \alpha_i) \quad (2.14)$$

where A_i is the amplitude of the i^{th} harmonic in Newtons (N), ω_i is the frequency in rad/s, and α_i is a random phase uniformly distributed between 0 and 2π . The signal frequencies and amplitudes used for this example are listed in Table 2.1. The time history of the signal is created in MATLAB using a time vector of length 2048 with a resolution of .01 seconds. This time spacing corresponds to a sampling rate of 100 Hz. A portion of the resulting signal is shown in Figure 2-1(a). It is difficult to determine the frequencies and amplitudes of the sinusoids that generated this signal from the time history. Therefore the signal is transformed to the frequency domain using Equations 2.2 and 2.4.

The resulting amplitude spectra and PSD are plotted in Figure 2-1(b). In this form the frequency content of the signal is obvious. Both functions consist of peaks at the frequencies listed in Table 2.1. Note that the magnitudes of the peaks in A_X correspond to the magnitudes of the sinusoids at each of the frequencies. The magnitudes of the peaks in the PSD, S_X , on the other hand, do not directly present any information about the

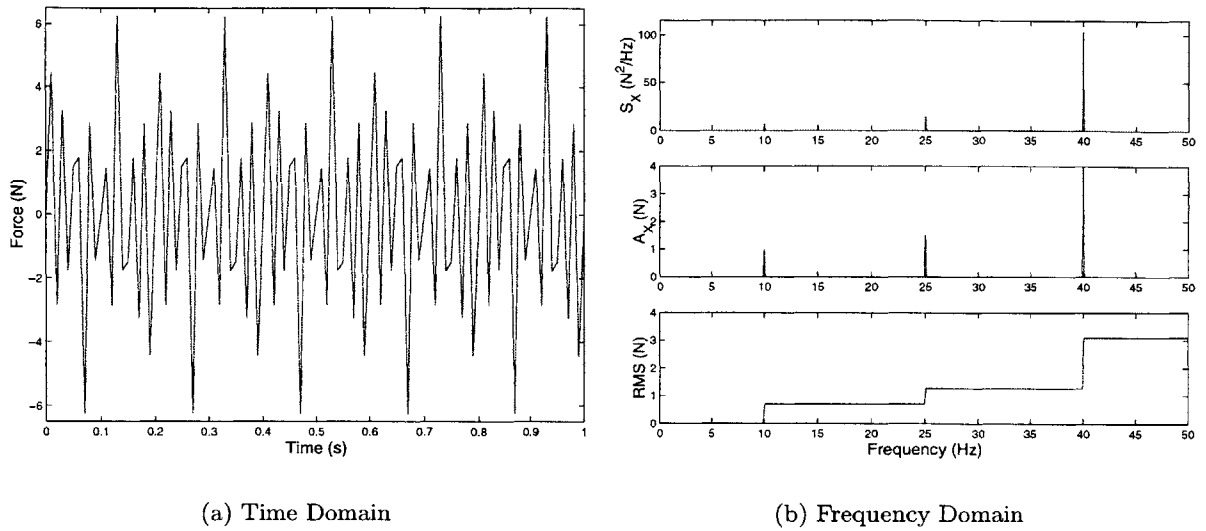


Figure 2-1: Time and Frequency Domain Representations of Stochastic Process, $X(t)$

amplitudes of $X(t)$. The PSD does however, allow calculation of the RMS of the signal through integration. The bottom plot in Figure 2-1(b) is the cumulative RMS of the signal. Note that the curve is a series of “steps” and that each step occurs at one of the frequencies listed in Table 2.1. Also note that the largest step is at 40 Hz, which is the frequency of the sinusoid with the greatest amplitude. The cumulative RMS can be used in this manner to identify the dominant frequencies in a signal. The final value of the cumulative RMS in this example is 3.1024 N. This value also results from taking the square root of the area under the PSD and is the total RMS of the signal.

2.2 Ithaco RWA Disturbance Data

RWA vibration data from two types of wheels manufactured by Ithaco Space Systems are used in this thesis to illustrate the parameter extraction methodologies for both the empirical and analytical model and to validate the models through data comparison. The wheels that were tested are type B and E Ithaco TORQWHEELS, with model numbers TW-16B32 and TW-50E300. In both cases the wheels were off-the shelf standard catalog products that had not yet been balanced for minimum vibration operation. Pictures of typical Ithaco B and E wheels are shown in Figures 1-1 and 1-2 and the design specifications for the models that were tested are listed in Table 2.2. Notice that the Ithaco E Wheel can

Table 2.2: Ithaco TORQWHEEL Design Specifications

	Model Number	
	TW-16B32	TW-50E300
Speed Range (rpm)	± 5100	± 3850
Momentum Capacity (N·m·s)	> 16.6	> 50
Reaction Torque (mN·m)	> 32.0	> 300
Tachometer (Pulses/Rev)	72	72
Static Imbalance (g·cm)	< 1.5	< 1.8
Dynamic Imbalance (g·cm ²)	< 40	< 60
Peak Power (W)	< 50.0	< 280
Mass Reaction Wheel (kg)	< 5.9	< 10.6
Mass Motor Driver (kg)	included	< 3.3
Wheel Diameter (cm)	< 25.5	< 39.3
Wheel Height (cm)	< 9.3	< 16.6
Motor Driver (cm)	included	$< 21 \times 18 \times 9$

provide a significantly greater reaction torque than the Ithaco B Wheel. However, it is also a much larger and much heavier wheel. Both the pictures and the information listed in the table were obtained from the Ithaco Space Systems website (www.ithaco.com).

2.2.1 B Wheel

An Ithaco B Wheel, model TW-16B32, was tested at Orbital Sciences Corp. in Germantown, MD in February and April of 1997. Vibration tests were run on two wheels, an engineering and a flight unit for the FUSE mission. Only the data from the flight unit will be presented in this thesis. Vibration data were obtained from a Kistler 9253A force/torque table, which is a steel plate containing four 3-axis load cells. The table was mounted directly to a large granite block that sat upon foam rubber pads. The reaction wheel was mounted to the Kistler table such that the z-axis of the table corresponded to the spin axis of the wheel. The output signals of the load cells were combined to derive the six disturbance forces and torques at the mounting interface between the wheel and the table. Data were taken for approximately 8 seconds once the wheel had reached steady-state spin at every 100 rpm from 500 to 3400. A sampling rate of 1kHz was used, and anti-aliasing filters were set at 480 Hz. In addition, data was taken with the wheel actively controlled to 0 rpm to provide a measure of sensor and electrical noise.

The data were processed using MATLAB to obtain PSDs and amplitude spectra of the time histories of the wheel disturbances at each speed and the noise data. Figure 2-

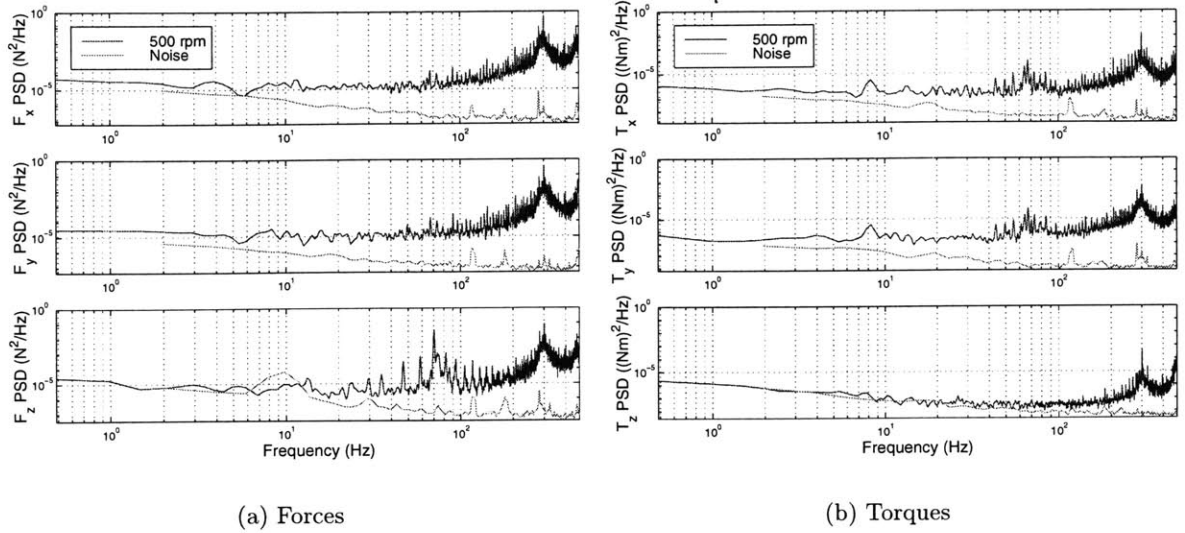


Figure 2-2: Comparison of Noise and Disturbance Data (at 500 rpm) for Ithaco B Wheel (FUSE Flight Unit)

2 compares the noise data to the disturbance data taken at the lowest wheel speed (500 rpm). The three forces, F_x , F_y and F_z are shown in Figure 2-2(a) and the three torques, T_x , T_y and T_z are shown in Figure 2-2(b). Note that in general, the noise data is well below the disturbance data at frequencies greater than 10 Hz. The only case for which this observation is not true is the T_z data. This torque is the axial disturbance torque and is negligible. Therefore, the T_z disturbance lies very close to the noise floor. Since the wheel disturbances increase as the wheel speed increases, it can be concluded that the noise floor has a negligible effect on the five significant disturbances, F_x , F_y , F_z , T_x , and T_y .

Frequency domain data can be plotted side-by-side in a 3-dimensional plot called a waterfall plot. Plotting the data in this form allows the identification of disturbance trends across both frequency and wheel speed. An example of a waterfall plot is shown in Figure 2-3(a). The data shown are the Ithaco B Wheel F_x , or radial force, disturbances. Note that the dominant disturbances appear as ridges at around 300 Hz and 460 Hz. These disturbances are independent of wheel speed and occur at frequencies corresponding to the resonances of the test fixture. Since these effects are caused by amplification of wheel harmonics by the test fixture dynamics they should not be included in a disturbance model. The second plot, Figure 2-3(b), shows the same data plotted to 200 Hz. Note that now diagonal ridges of disturbances are visible in the data. The frequencies of these disturbances are linearly

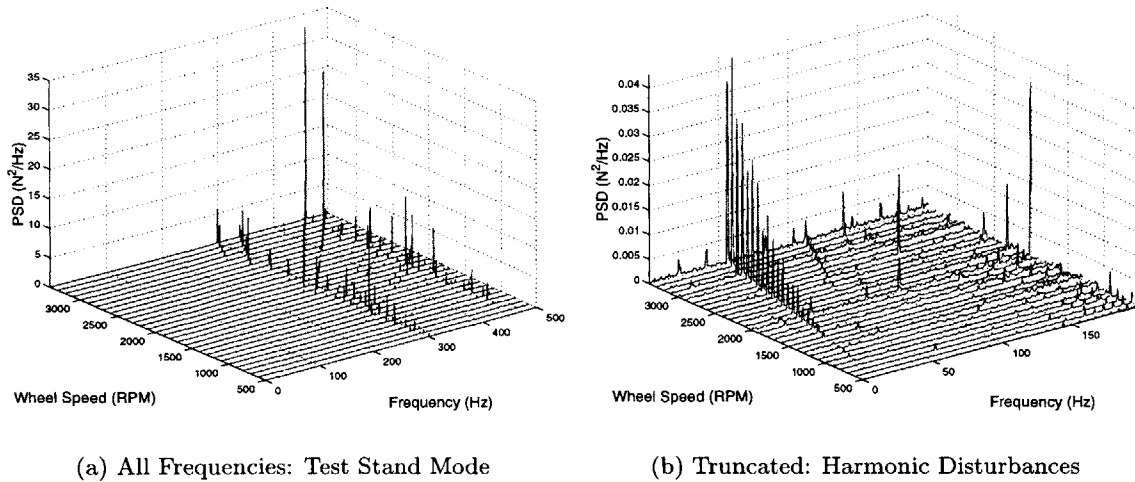
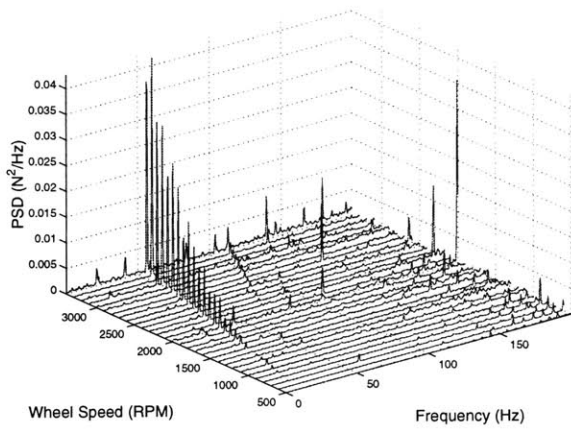


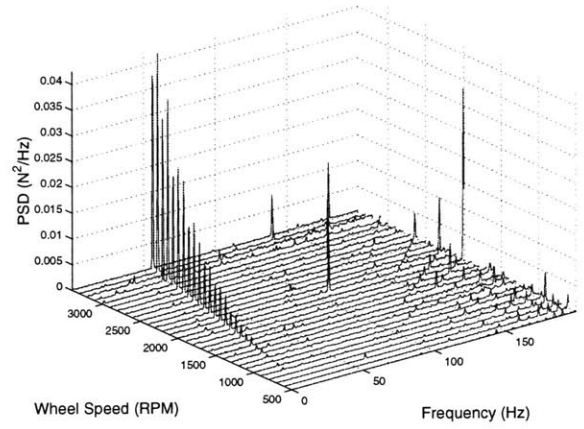
Figure 2-3: Waterfall Plot of Ithaco B Wheel F_x Disturbance Data

dependent on the wheel speed. As the speed of the wheel increases the disturbances slide along the frequency axis. These disturbances are the wheel harmonics that were introduced in Section 1.2. The largest ridge visible in this plot is the fundamental harmonic. Recall that the fundamental harmonic corresponds to disturbances that occur once per revolution and is caused by static and dynamic imbalance of the flywheel. Also note that smaller diagonal ridges are visible. These are super-harmonics caused by bearing imperfections and other disturbance sources within the wheel.

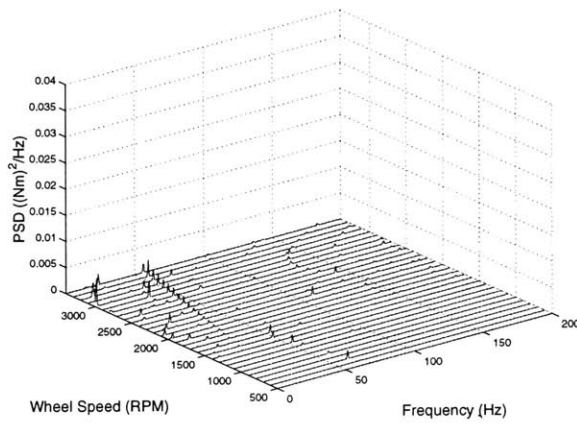
Waterfall plots of all six Ithaco B Wheel disturbance PSDs are presented in Figure 2-4. The signals are truncated at 200 Hz to remove the effects of the test stand resonance and the z-axis on all the plots is kept at the same scale to allow comparison among the directions. The F_x and F_y data are both radial force disturbances and differ only by 90° of phase. The PSD contains no phase information so, since the RWA is axi-symmetric, the data from these two disturbance directions are nearly identical. Figures 2-4(c) and 2-4(d) are the radial torque disturbances, T_x and T_y . These disturbances are also identical due to the symmetry of the wheel. The final two sub-figures, Figure 2-4(e) and 2-4(f) are the axial force and torque disturbances, respectively. Note that all of the disturbances in the F_z data are amplified around 70 Hz. The source of these amplifications will be discussed in Section 2.3. Also it is clear from Figure 2-4(f) that the axial torques are insignificant in comparison to the other disturbances. The waterfall plot supports the earlier claim that disturbance torques in this direction can be neglected.



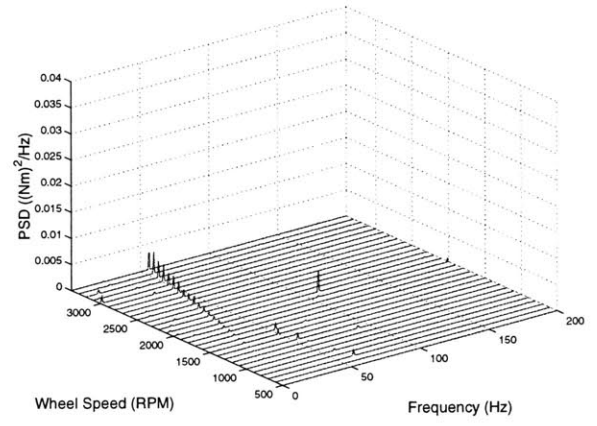
(a) Radial Force, x-direction



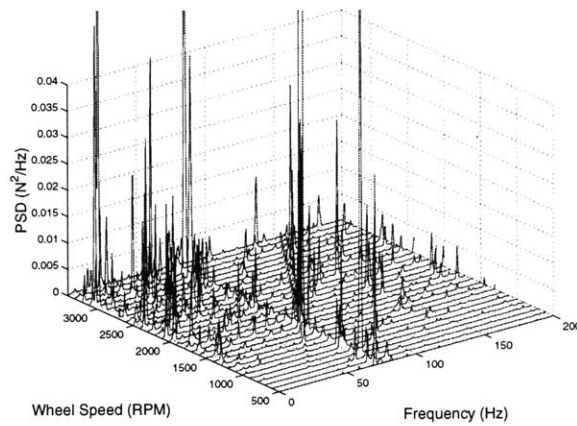
(b) Radial Force, y-direction



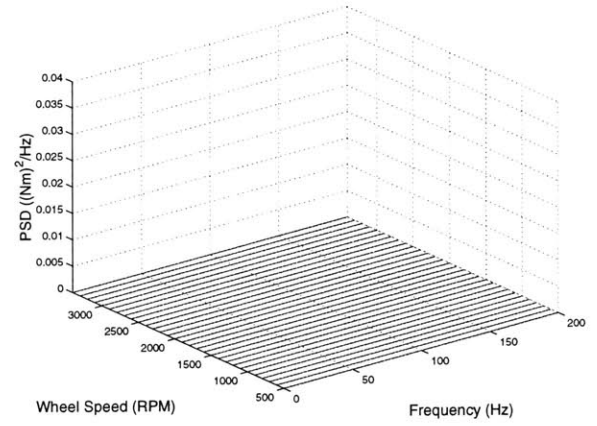
(c) Radial Torque, x-direction



(d) Radial Torque, y-direction



(e) Axial Force, z-direction



(f) Axial Torque, z-direction

Figure 2-4: RWA Disturbance Data - Ithaco B Wheel

2.2.2 E Wheel

An Ithaco E Wheel, model TW-50E300 was tested at the NASA Goddard Space Flight Center (GSFC). The wheel was integrated into a stiff cylindrical test fixture and hard-mounted to a 6-axis Kistler force/torque table. In this test, the wheel was started at 0 rpm and full torque voltage was applied to the motor until the wheel saturated around 2400 rpm. The data was sampled at 3840 Hz for 390 seconds and 8 channels of load cell data were obtained. These channels were combined to derive the disturbance forces and torques at the mounting interface between the wheel and the table. Note that this vibration test was not conducted at steady-state speeds like the Ithaco B Wheel test performed at Orbital. Therefore, in order to use the data to obtain a steady-state empirical model, a technique was developed to obtain steady-state frequency domain data from the continuous time histories.

The spin-up of the wheel occurred at a relatively slow rate, so the resulting time history can be subdivided into time slices that are considered to be quasi-steady state. Each time slice has a sample length of 2.133 seconds and contains 8192 points. These time histories are then transformed to the frequency domain through the PSD and amplitude spectra. The frequency content of the signal is used to determine the average wheel speed of each time slice by assuming that the fundamental harmonic causes the most significant disturbance. Based on this assumption, the frequency at which the maximum disturbance occurs in a given time slice is also the average speed of the wheel. In Figure 2-5 the average wheel speeds are plotted versus the time slice number. The data were processed into 120 time slices, and the curve indicates that the assumption used to identify the wheel speeds is a valid one. As the time slice index increases the wheel speed also increases until the wheel saturates around 2400 rpm [22].

When processed as described above, the Ithaco E Wheel data can be treated as steady-state data similar to the Ithaco B Wheel data. The waterfall plots of the six disturbance PSDs are shown in Figure 2-6. The test fixture that the Ithaco E Wheel was mounted to is stiffer than that used for the Ithaco B Wheel. Therefore, the data are not corrupted by test stand resonances and can be plotted up to 300 Hz. The orientation of the wheel was such that F_x and F_y are the radial forces, T_x and T_y are the radial torques, and F_z and T_z are the axial forces and torques, respectively. The fundamental harmonic is clearly visible in the

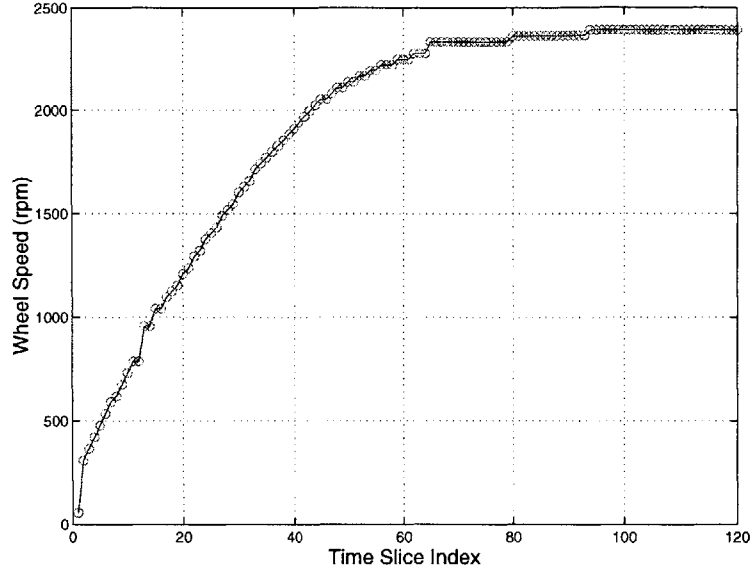
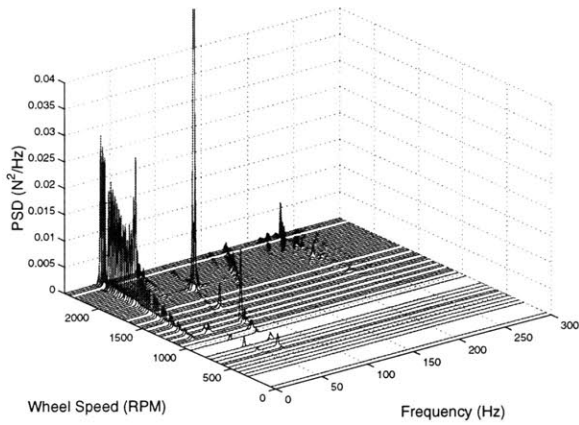


Figure 2-5: Wheel Speeds Corresponding to Quasi-Steady State Time Slices

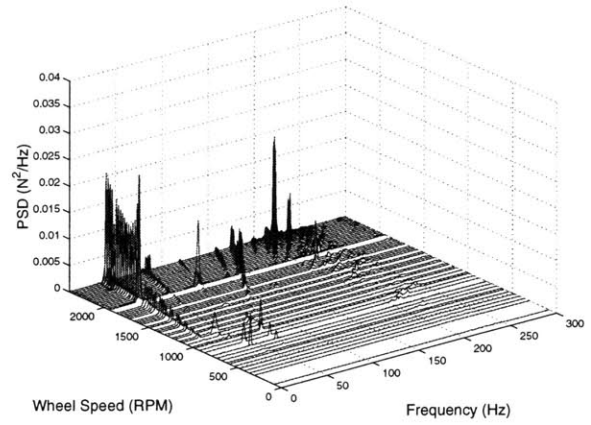
radial forces and torques and the axial force. The two radial force plots, Figures 2-6(a) and 2-6(b), show that the number and shape of the harmonics visible in these disturbances are similar. The same observation can be made with regard to the radial torques, Figures 2-6(c) and 2-6(d). Also note that, like the Ithaco B Wheel data, the axial torque (Figure 2-6(f)) is negligible when compared to the other disturbances. Finally, similar to the Ithaco B Wheel F_z data, there are regions of disturbance amplification visible at low frequencies in all five of the Ithaco E Wheel disturbances. Since the test stand resonance was greater than 300 Hz for this test, another explanation for the amplifications must be found. These resonant effects are the subject of the following section.

2.3 Structural Wheel Modes

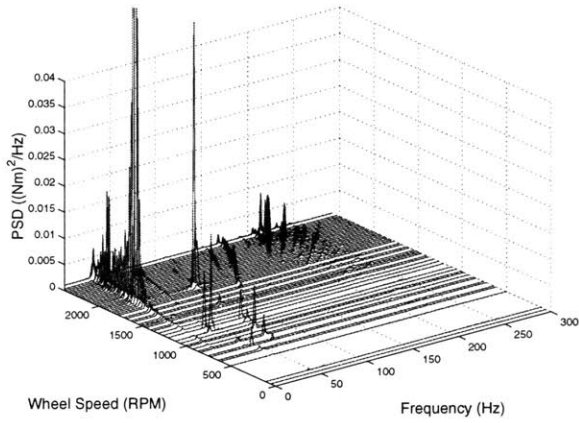
The RWA can be modeled as having five degrees of freedom, translation in the axial direction, translation in the two radial directions and rotation about the two radial axes. This model results in three dominant vibration modes: axial translation, radial translation and radial rocking. These modes are depicted schematically in Figure 2-7. The natural frequencies of the three modes reported by Ithaco for type B and E TORQWHEELS are listed in Table 2.3 [16]. The radial rocking mode consists of two whirl modes, the positive whirl and the negative whirl, which have natural frequencies that are dependent on the speed of



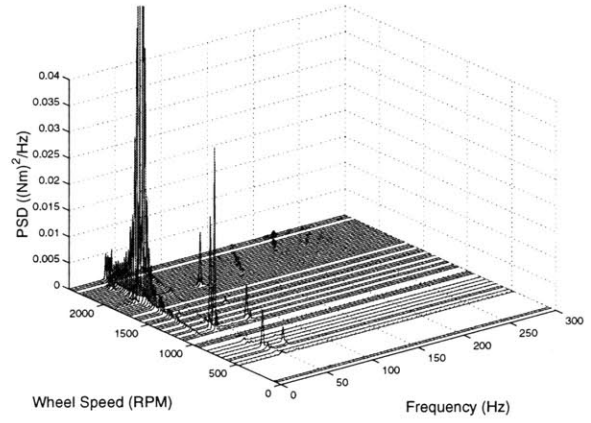
(a) Radial Force, x-direction



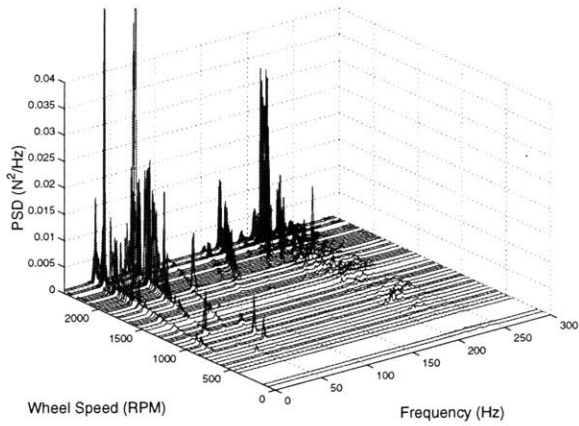
(b) Radial Force, y-direction



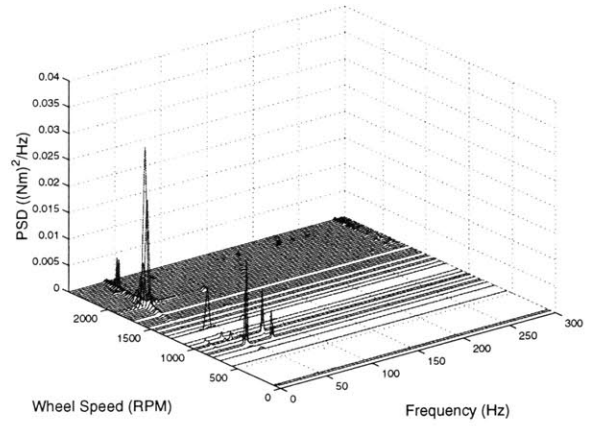
(c) Radial Torque, x-direction



(d) Radial Torque, y-direction



(e) Axial Force, z-direction



(f) Axial Torque, z-direction

Figure 2-6: RWA Disturbance Data - Ithaco E Wheel

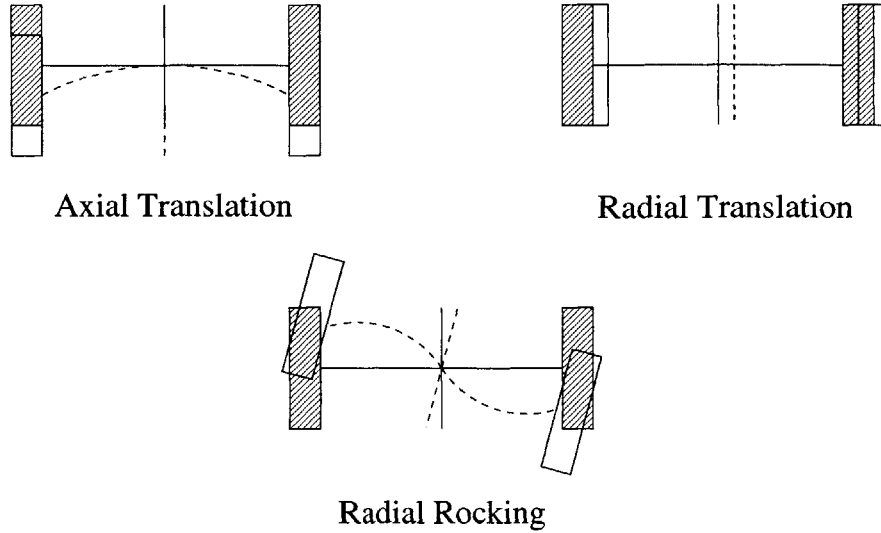


Figure 2-7: Structural Wheel Modes

Table 2.3: Frequencies of Ithaco Structural Wheel Modes

Mode	Frequency (Hz)	
	Type B	Type E
Rocking (Nominal)	85	60
Axial Translation	65	70
Radial Translation	200	250

the wheel. The natural frequency listed for the rocking mode in Table 2.3 is the natural frequency at zero wheel speed and is the same for both the positive and negative whirls. The rocking mode and its whirl will be discussed in more detail when the analytical model is presented in Section 4.1.1.

The structural wheel modes provide an explanation for the disturbance amplifications seen in the Ithaco B and E Wheel data. Recall that a ridge of disturbance amplification was observed in the Ithaco B Wheel F_z data at approximately 70 Hz across all wheel speeds. This frequency is close to the reported natural frequency of the axial translation mode of the Ithaco B Wheel listed in Table 2.3. Therefore, it can be concluded that the disturbance amplification is caused by the excitation of the axial translation mode by the wheel harmonics. Figure 2-8(a) is the waterfall plot of the Ithaco B Wheel F_z data with the location of this mode highlighted with a heavy solid line. Note that at 1600 rpm, when a harmonic crosses the mode, there is large amplification in the disturbance magnitude. Similar amplifications can be observed at this frequency when other harmonics pass through

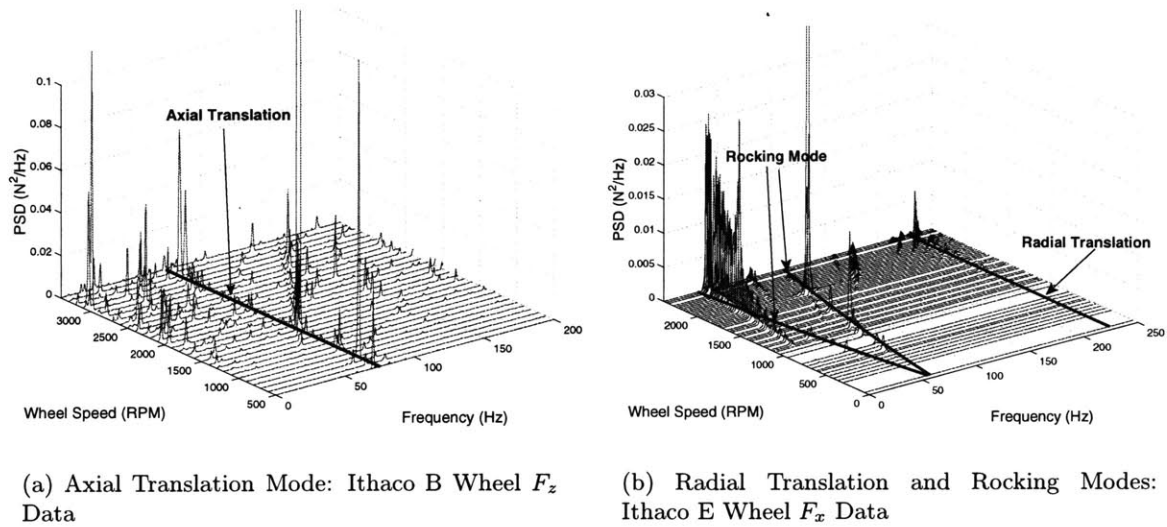


Figure 2-8: Disturbance Amplification from Structural Wheel Modes

the solid line.

Disturbance amplifications are also visible in the Ithaco E Wheel data as shown in Figure 2-8(b). Note that disturbance amplifications occur at approximately 230 Hz. This frequency is highlighted with a solid black line and is very close to the reported value of the Ithaco E Wheel radial translation mode listed in Table 2.3. In addition, there are disturbance amplifications that form a V-shaped ridge across wheel speeds in the lower frequencies. The V-shape is also marked with a solid black line and represents the positive and negative whirls of the rocking mode. Note that the point of the “V” is at 60 Hz, which is the frequency listed as the nominal natural frequency of the rocking mode in Table 2.3. Therefore, it can be concluded that the amplification of the harmonics at 230 Hz are a result of excitation of the radial translation mode, and that the amplifications at lower frequencies are due to excitation of the two whirls of the rocking mode. The effects of the radial translation mode are most clearly seen in the higher wheel speeds while the effects of the rocking mode are most visible between 1500 and 2000 rpm.

2.4 Summary

This chapter began with an overview of spectral analysis. Information about the frequency content of a random process can be obtained through transformation from the time domain to the frequency domain into power or amplitude spectra. Power spectral densities (PSDs)

are a measure of the energy in a signal as a function of frequency and provide a simple method of obtaining the signal RMS. Amplitude spectra are another type of frequency domain representation which give an estimate of the signal amplitude with respect to its frequency. These frequency domain representations were used to process RWA disturbance data. The vibration data were obtained from isolated RWA tests conducted on Ithaco B and E type Wheels at Orbital Sciences Corp. and NASA GSFC. In both tests, the wheels were hardmounted to a fairly rigid test stand and the disturbance forces and torques induced by the spinning of the wheel at the interface of the wheel and the test fixture were measured with load cells. The resulting disturbance data for both wheels were presented. It was shown that wheel harmonics occur in the data at frequencies that are linearly dependent on wheel speed. In addition, amplifications of the wheel harmonics due to excitation of the three structural wheel modes: the radial translation mode, the axial translation mode and the radial rocking mode are, also visible in the data. In the following chapter, an empirical model is introduced, and the vibration data is used to extract the model parameters to fit the experimentally measured results.

Chapter 3

Empirical Model

The first type of disturbance model that will be presented is an empirical model. The model was initially created to assess the effects of RWA vibrations on the performance of the Hubble Space Telescope (HST). HST had very tight requirements for target pointing accuracy and mechanical stability when acquiring science data. Therefore, characterization of RWA vibrations was important in the early stages of spacecraft design to allow prediction of performance degradation due to the operation of the wheels. To accomplish this goal, the HST RWA flight units were subject to a series of induced vibration tests. The results of these tests indicated that RWA disturbances are tonal in nature; i.e. waterfall plots of the frequency domain data show distinct ridges of disturbances occurring at frequencies that are a linear function of wheel speed [15]. The empirical model captures this feature by assuming that the disturbances consist of discrete harmonics of the reaction wheel speed with amplitudes proportional to the square of the wheel speed:

$$m(t) = \sum_{i=1}^n C_i \Omega^2 \sin(2\pi h_i \Omega t + \alpha_i) \quad (3.1)$$

where $m(t)$ is the disturbance force or torque in Newtons (N) or Newton-meters (Nm), n is the number of harmonics included in the model, C_i is the amplitude of the i th harmonic in N^2/Hz (or $(\text{Nm})^2/\text{Hz}$), Ω is the wheel speed in Hz, h_i is the i th harmonic number and α_i is a random phase (assumed to be uniform over $[0, 2\pi)$) [23]. The harmonic numbers are non-dimensional frequency ratios that describe the relationship between the i th disturbance

frequency, $\bar{\omega}_i$ and the wheel's spin rate, Ω :

$$h_i = \frac{\bar{\omega}_i}{\Omega} \quad (3.2)$$

Note that the empirical model (Equation 3.1) yields disturbance forces and torques as a function of the wheel speed. It is a steady-state model only; transient effects induced from changing wheel speeds are not considered.

The model parameters, h_i , C_i and n , are wheel dependent. As discussed in Chapter 1, the two largest sources of RWA disturbances are flywheel imbalance and bearing imperfections. RWAs made by different manufacturers will not have the same designs and specifications. As a result, each wheel will induce a unique set of disturbances. For example, a large wheel, which can provide high reaction torque, may produce larger amplitude disturbances than a RWA with a small flywheel. Also, flywheel imbalance and bearing imperfections are clearly not part of the RWA design. These anomalies occur during the manufacturing process and cannot be controlled during operation. Therefore, each RWA has its own characteristic set of harmonic numbers and amplitude coefficients. As a result, in order to properly model a given wheel, a vibration test, such as those described in Section 2.2, should be performed and the empirical model parameters determined from the test data. To facilitate this modeling process, a MATLAB toolbox which analyzes steady-state RWA disturbance data and extracts the harmonic numbers and amplitude coefficients for the empirical model has been developed. This chapter describes the formulation of an empirical RWA model by first describing the process in terms of the MATLAB functions in the toolbox (Section 3.1.1) and then illustrating each step through a series of examples. In addition empirical models created with the RWA DADM from the Ithaco RWA vibration data are presented and used to validate the modeling process.

3.1 RWA Data Analysis and Disturbance Modeling Toolbox

The RWA Data Analysis and Disturbance Modeling (DADM) toolbox creates steady-state disturbance models of the form show in Equation 3.1 from steady-state reaction wheel disturbance data. The analysis tools extract the model parameters, h_i and C_i , from frequency domain data using the following functions:

1. `iden_harm.m` - identifies harmonics, h_i .
2. `find_coeff.m` - calculates amplitude coefficients, C_i .
3. `remove_mode.m` - removes effects of structural wheel modes and recalculates amplitude coefficients.
4. `comp_model.m` - compares model to experimental data.

The following section will discuss the disturbance modeling process. Each of the functions in the toolbox will be explored in detail. First, the algorithm used to identify the harmonic numbers is explained. Then, the calculation of the amplitude coefficients and the effects of the structural wheel modes on the disturbance amplitudes is discussed. Finally, methods of model validation are presented and compared. The development of a radial force disturbance model from the Ithaco B Wheel F_x and F_y data will be used as an example throughout the section.

3.1.1 Overview

Typical test results from one wheel include data for six disturbances: x-axis force, F_x , y-axis force, F_y , z-axis force, F_z , x-axis torque, T_x , y-axis torque, T_y , and z-axis torque, T_z . Assuming the z-axis is the spin axis of the wheel, the F_x and F_y data are both radial force disturbances and should be nearly identical. They are used in combination to create the radial force disturbance model. Similarly, T_x and T_y are both radial torque data, and are used to create the radial torque model. The axial force disturbance model is created from the F_z , or axial force data. The T_z data is the disturbance torque about the spin axis. This disturbance is very small and can be neglected.

The RWA DADM toolbox requires that experimental data from a given wheel be processed and stored in five data sets, one for each of the relevant disturbances, which include the following information:

S: A row vector of disturbance PSDs arranged such that $\mathbf{S} = [S_1 \dots S_m]$. The discretized version used for implementation in MATLAB is an $n_f \times m$ matrix, where n_f is the number of frequency points and m is the number of wheel speeds at which data was taken. The matrix is arranged such that the j^{th} column corresponds to the PSD of the disturbance taken at the j^{th} wheel speed, S_j .

A: A row vector of disturbance amplitude spectra arranged such that $\mathbf{A} = [A_1 \dots A_m]$. The discretized version used for implementation in MATLAB is an $n_f \times m$ matrix arranged such that the j^{th} column corresponds to the amplitude spectrum of the disturbance taken at the j^{th} wheel speed, A_j .

Ω : A vector of wheel speeds (in rpm) at which data was taken.

f: frequency vector (in Hz) corresponding to the frequency domain data.

f_{Lim} : Upper frequency limit of good disturbance data (Hz).

In general, the vectors Ω and \mathbf{f} and the frequency f_{Lim} are identical across the disturbance directions for a given wheel. However, \mathbf{S} and \mathbf{A} are direction dependent. In this thesis, subscripts will be used to differentiate between the five disturbance directions. Individual PSDs (or amplitude spectra) within the matrices will be subscripted to indicate both the wheel speed at which the data was taken and, if necessary, the disturbance direction. For example, the vector of F_x PSDs is \mathbf{S}_{F_x} , and the F_x disturbance PSD taken at the first wheel speed in Ω is $(S_1)_{F_x}$.

The methodologies used to create the three disturbance models, radial force, radial torque and axial force, are quite similar. Figure 3-1 summarizes the axial force modeling procedure. The method used to model the radial forces and torques is simply an extension of this process, as shown in Figure 3-2. The radial force model will be used in the following discussion to illustrate the end-to-end analysis and modeling procedure.

In the initial stages of the analysis process, the F_x and F_y data sets are run through the toolbox separately. The following discussion will refer only to the F_x data set, but in application the same procedure is followed with the F_y data set (see Figure 3-2). The first step in the analysis is running the function `iden_harm.m` using \mathbf{A}_{F_x} , Ω , \mathbf{f} and f_{Lim} . This function outputs two matrices, a list of harmonic numbers, $(\mathbf{h}_{F_x})_1$ and a matrix of normalized peak frequencies, $(\mathbf{M}_{peak})_{F_x}$, which will both be discussed in greater detail in Section 3.1.2. These outputs then become inputs to the function `find_coeff.m`, and the amplitude coefficients, $(\mathbf{C}_{F_x})_1$ are calculated (see Section 3.1.3).

$(\mathbf{h}_{F_x})_1$ and $(\mathbf{C}_{F_x})_1$ are the first generation of model parameters and are input into the function `comp_model.m` for comparison with the experimental data. The plots generated by `comp_model.m` allow refinement of the first generation harmonics, $(\mathbf{h}_{F_x})_1$. A second

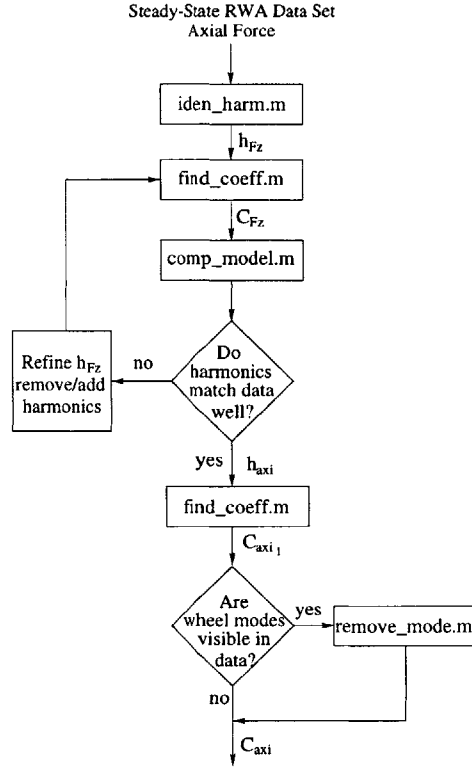


Figure 3-1: RWA Data Analysis Process for Axial Force Disturbance

generation of harmonic numbers, $(\mathbf{h}_{F_x})_2$ is created by removing the “bad” harmonic numbers from $(\mathbf{h}_{F_x})_1$ and adding any that may have been missed in the first iteration. Then, `find_coeff.m` is run again to obtain the corresponding second generation of amplitude coefficients, $(\mathbf{C}_{F_x})_2$. The second generation of model parameters are then run through `comp_model.m` for validation. Additional iterations are performed until the final generation of harmonic numbers, \mathbf{h}_{F_x} , which match the experimental data to the user’s satisfaction, are obtained.

At this point in the analysis process there are two separate sets of model parameters, \mathbf{h}_{F_x} and \mathbf{C}_{F_x} and \mathbf{h}_{F_y} and \mathbf{C}_{F_y} . The harmonic numbers, \mathbf{h}_{F_x} and \mathbf{h}_{F_y} , are combined to create a set of radial harmonic numbers, \mathbf{h}_{rad} . If a number is found in both lists (or if two numbers are close to each other) their average is included in \mathbf{h}_{rad} . Otherwise, \mathbf{h}_{rad} is simply the union of \mathbf{h}_{F_x} and \mathbf{h}_{F_y} . Once \mathbf{h}_{rad} has been determined it is input into `find_coeff.m` along with both the F_x and F_y data sets to calculate the amplitude coefficients for the radial disturbance model, \mathbf{C}_{rad} .

The radial amplitude coefficients are validated with curve fit plots that are generated

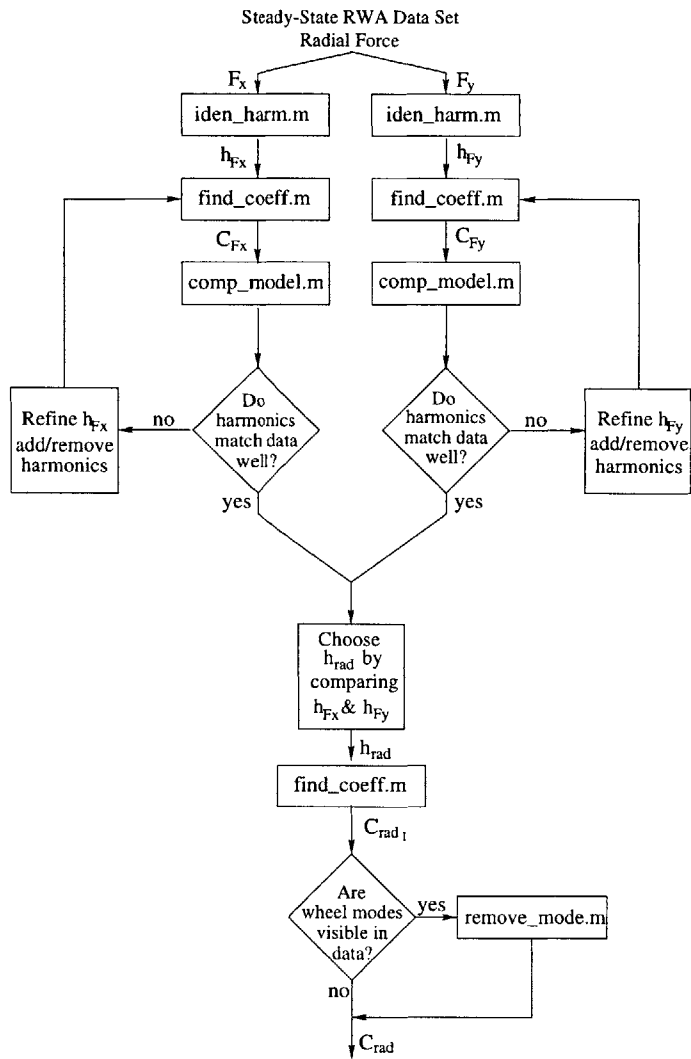


Figure 3-2: RWA Data Analysis Process for Radial Force Disturbance

Table 3.1: Ithaco B Wheel F_x Data Set

Name	Description	Size/Value
m	# of wheel speeds	30
n_f	# of frequency points	1025
\mathbf{f}	Frequency vector	1025 x 1
f_{Lim}	Upper frequency limit	200 (Hz)
$\mathbf{\Omega}$	Wheel speed vector	1 x 30
\mathbf{A}_{F_x}	amplitude spectra	1025 x 30
\mathbf{S}_{F_x}	PSDs	1025 x 30

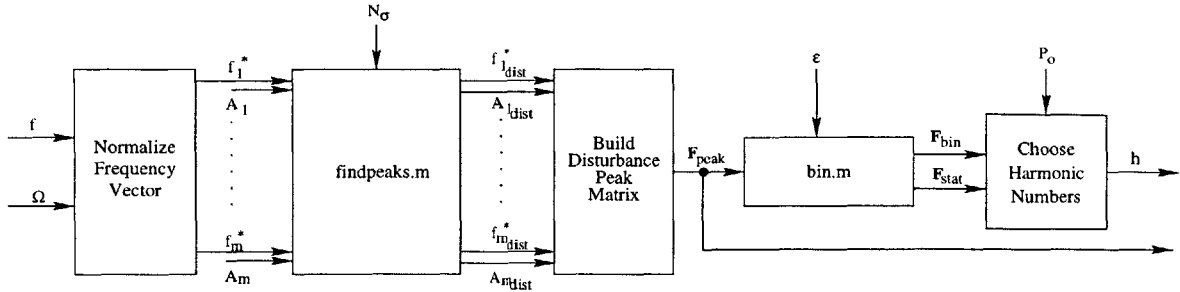
by `find_coeff.m`. If interactions between the structural wheel modes and harmonics are visible in the curve fits, the coefficients are run through the final function, `remove_modes.m`. In addition, if the curve fit for a particular amplitude coefficient shows that it was calculated from a small number of data points, the associated harmonic is removed from the model. This part of the modeling process will be discussed in detail in Section 3.1.3. Finally, `comp_model.m` is run once more as a final check between the radial model parameters and both the F_x and F_y experimental data. The final radial model parameters should fit both data sets well.

The radial force disturbance modeling procedure is described in detail in the following sections using the Ithaco B Wheel F_x data set as an example. The data set consists of 30 time histories, one taken every 100 rpm from 500-3400 rpm, that were each sampled at 1000 Hz for approximately eight seconds. The time data was then processed into amplitude spectra, \mathbf{A} , and PSDs, \mathbf{S} , using a hanning window with 2048 FFT points. The windows were overlapped by 1024 points so that eight averages were obtained per time history. A waterfall plot of this data set is shown in Figure 2-4(a), and the components of the data set are listed in Table 3.1.

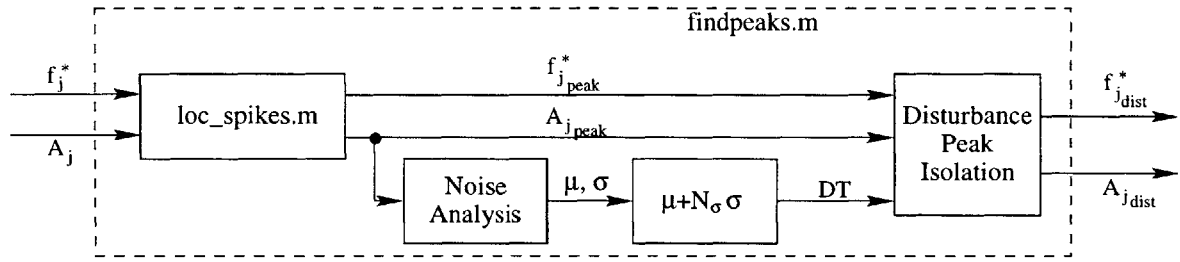
3.1.2 Identifying Harmonic Numbers

The first step in the empirical modeling process is the extraction of the harmonic numbers, h_i , from the experimental data. The MATLAB function, `iden_harm.m` and its sub-functions individually examine all the amplitude spectra in a data set and locate peaks which are due to the wheel harmonics. Figure 3-3 presents a graphical representation of the harmonic number identification process and will be referred to throughout the following discussion.

In order to identify the harmonic numbers from the data, the frequency vector, \mathbf{f} , must



(a) Sub-functions of iden_harm.m



(b) Detail of Sub-Function findpeaks.m

Figure 3-3: RWA DADM Toolbox Function iden_harm.m and Sub-functions

be normalized. m vectors of non-dimensional frequency ratios, \mathbf{f}_j^* , are obtained by dividing the frequency vector by the speeds (in Hz) in the wheel speed vector. Figure 3-4 shows an example for $\Omega_{30} = 3400$ rpm. In the upper plot, the amplitude spectrum, A_{30} , is plotted versus frequency. In the lower plot the same data is plotted as a function of the non-dimensional, normalized frequency, \mathbf{f}_{30}^* . Note that the largest peak in the amplitude spectra occurs at $f_{30}^* = 1.0$. This peak is caused by the fundamental harmonic disturbance ($h_i = 1$).

The amplitude spectra, A_j , and normalized frequencies, \mathbf{f}_j^* are input to a MATLAB sub-function called `findpeaks.m` that identifies the normalized frequencies of disturbance peaks in the data. A detail of this sub-function is shown in Figure 3-3(b). The figure shows the flow of the function for one set of amplitude spectra and normalized frequencies. However, within `iden_harm.m`, `findpeaks.m` is called m times as shown in Figure 3-3(a).

The first block in Figure 3-3(b) represents another sub-function called `loc_spikes.m` that identifies peaks by differencing A_j and searching for sign changes in the differenced data. The outputs are a vector of normalized peak frequencies, $\mathbf{f}_{j_{peak}}^*$ and a vector of peak

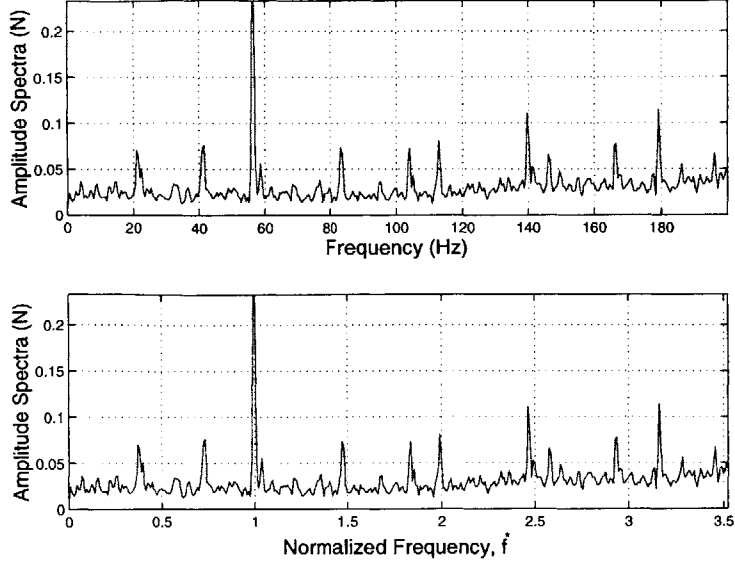


Figure 3-4: Frequency Normalization of Ithaco B Wheel F_x Data (3400 rpm)

amplitudes, $\mathbf{A}_{j_{peak}}$. The peaks identified by `loc_spikes.m` in A_{30} are shown in Figure 3-5(a) with stars, “*”. Note that *all* of the peaks in the data are marked. It is highly unlikely that all of these peaks are a result of harmonic disturbances. Some may be due to noise or may be a result of performing an FFT on the time history data. Therefore, a method was developed to discriminate between disturbance peaks and “noisy” peaks.

Noise is isolated from the disturbance harmonics in the block labeled “Noise Analysis.” The MATLAB function `hist.m` is used to bin the elements of $\mathbf{A}_{j_{peak}}$ according to amplitude. Assuming that the “noisy” spikes all have roughly the same amplitude and therefore account for the largest bin in the histogram allows a disturbance amplitude threshold, DT , to be determined. All spike amplitudes that fall in or below the largest histogram bin are considered noise. The remaining spikes are considered possible harmonic disturbances. See Figure 3-5(b) for an example. The disturbance amplitude threshold is then defined as:

$$DT = \mu_{noise} + N_{\sigma}\sigma_{noise} \quad (3.3)$$

where μ_{noise} and σ_{noise} are the mean and standard deviation of the spike amplitudes identified with the histogram. The parameter N_{σ} is a user-defined tolerance level. Its default value is 3, but should be adjusted according to the signal to noise ratio of the data. All peaks with an amplitude below the disturbance amplitude threshold are not included in the

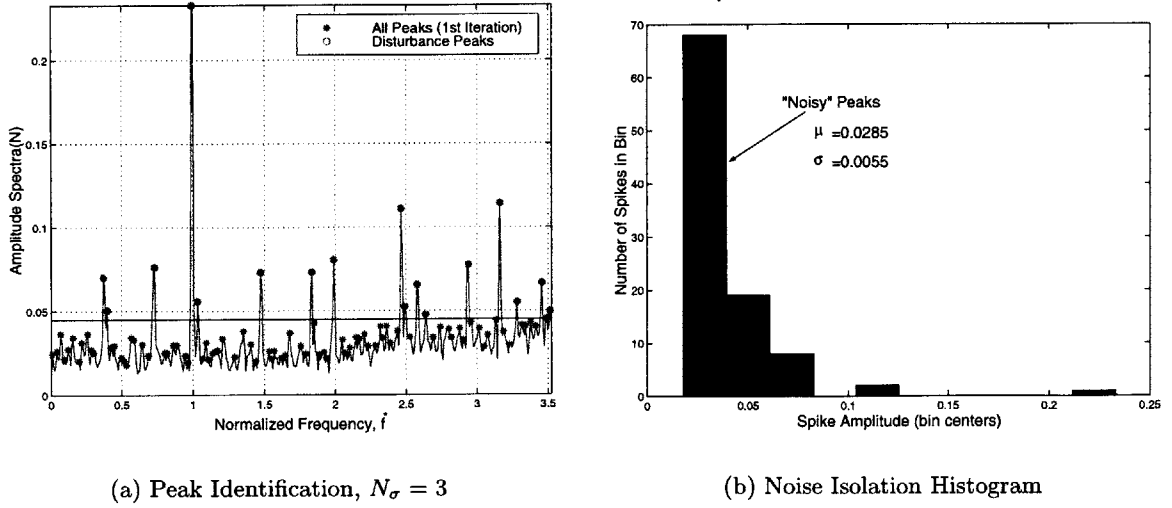


Figure 3-5: Disturbance Peak Identification in Ithaco B Wheel F_x Data (3400 rpm)

final vector of disturbance peaks. This part of the function is represented in the diagram by the block labeled “Disturbance Peak Isolation.” The final outputs of `findpeaks.m` are a vector of normalized disturbance peak frequencies, $\mathbf{f}_{j_{dist}}^*$ and a vector of disturbance peak amplitudes, $\mathbf{A}_{j_{dist}}$. The results of running the Ithaco B Wheel data through the function is shown in Figure 3-5(a). The disturbance threshold is indicated by the horizontal line, and the dark circles indicate peaks that were identified as disturbances. Note that the majority of the the smaller “noisy” peaks lie below the disturbance threshold and were not selected in the final iteration. Once all m sets of amplitude spectra and normalized frequencies vectors have been run through `findpeaks.m` a matrix of normalized peak frequencies, \mathbf{F}_{peak} , with each column corresponding to a different wheel speed, is built. This matrix is then used to identify the harmonic numbers.

A true harmonic disturbance should occur at the same normalized frequency over all wheel speeds. Therefore, a binning algorithm, `bin.m`, is used to search \mathbf{F}_{peak} for matching frequencies across wheel speeds. Initially, the first column of the matrix is used as the baseline case, \mathbf{f}_{base}^* . The first entry in the baseline column is denoted the “test entry”, f_o^* , and placed into a bin. All of the other columns are then searched for normalized frequencies, f^* , that are within $\pm\epsilon$ of the test entry (where ϵ is a user-defined tolerance):

$$f_o^* - \epsilon \leq f^* \leq f_o^* + \epsilon \quad (3.4)$$

All f^* satisfying Equation 3.4 are placed into the bin with f_o^* and their locations in \mathbf{F}_{peak} are set to zero. If two or more normalized frequencies in the same column satisfy Equation 3.4 their average is placed in the bin, and both entries are set to zero. Averaging ensures that a possible harmonic will only be accounted for once in each wheel speed. When the entire matrix has been searched, the second element of \mathbf{f}_{base}^* becomes the test entry and a new bin is created. The process continues until all elements of \mathbf{f}_{base}^* have been considered. At this point, the second column becomes \mathbf{f}_{base}^* and the search is repeated. The algorithm continues in this manner until all non-zero elements of \mathbf{F}_{peak} are binned.

The outputs of `bin.m` are a matrix of the binned normalized frequencies, \mathbf{F}_{bin} (with the k^{th} column corresponding to the k^{th} bin) and a second matrix containing the statistics for each bin, \mathbf{F}_{stat} . The first row of \mathbf{F}_{stat} is the average, or center, of the bins, $\bar{f}_{bin_k}^*$, and the second row contains the number of elements in the bins, N_{bin_k} .

The final block in Figure 3-3(a) represents the choosing of the harmonic numbers from \mathbf{F}_{stat} . A metric, P_k , is defined as the percentage of possible wheel speeds in which a given normalized peak frequency was found:

$$P_k = \frac{N_{bin_k}}{N_{poss_k}} 100\% \quad (3.5)$$

where N_{poss_k} is the total possible number of elements in the k^{th} bin. In general, N_{poss_k} should be equal to the number of wheel speeds in the data set. However, this assumption does not always hold depending on the frequency range of the data set. Recall from Section 2.2 that a test stand resonance may corrupt the data above a given frequency. If such a resonance is visible, only the data in the frequency range $[0, f_{Lim}]$ should be used in the model parameter extraction (where f_{Lim} is the upper frequency limit of uncorrupted data). The value of f_{Lim} may limit the number of wheel speeds in which a given normalized peak frequency is visible. For example, as shown in Figure 2-3(a), a test stand resonance corrupts the Ithaco B Wheel data above 200 Hz. The normalized frequency 1.0 corresponds to 8.3 Hz when the wheel is spinning at 500 rpm and to 56.7 Hz at 3400 rpm. Since both frequencies lie within the frequency range $[0, 200]$ a disturbance at $f^* = 1.0$ can be observed at all wheel speeds and $N_{poss} = 30$. The normalized frequency 5.98, on the other hand, corresponds to 49.8 Hz at 500 rpm and 339 Hz at 3400 rpm. In this case, f^* lies within the specified frequency range for only a subset of the wheel speeds and $N_{poss} = 16$. Table 3.2

Table 3.2: Bin Statistics for Ithaco B Wheel Radial Harmonics($f_{Lim} = 200$ Hz)

$f_{bin_k}^*$	Frequency (Hz)		Wheel Speed	N_{poss_k}	P_k
	500 rpm	3400 rpm	Limit (rpm)		
0.99	8.25	56.10	3400	30	93.3
1.99	16.58	112.8	3400	30	56.7
2.46	20.50	139.4	3400	30	50.0
3.16	26.33	179.1	3400	30	53.3
3.87	32.25	219.3	3100	27	34.6
4.56	38.00	258.4	2600	22	36.4
5.28	44.00	299.2	2200	18	44.4
5.98	49.83	338.9	2000	16	31.2
8.09	67.42	458.4	1500	11	40.0
8.83	73.58	500.4	1300	9	55.6
9.54	79.50	540.6	1200	8	37.5
10.25	85.42	580.8	1100	7	28.6

lists the bin statistics, N_{poss_k} and P_k for selected bins that resulted from analysis of the Ithaco B Wheel F_x data.

The metric P_k can be considered a measure of the strength of a disturbance across wheel speeds, and is used to identify wheel harmonics from the list of bin centers, $\bar{f}_{bin_k}^*$ in \mathbf{M}_{stat} . If P_k is greater than a user defined threshold, P_o , then $\bar{f}_{bin_k}^*$ is defined to be a harmonic number and placed into a new vector, \mathbf{h} . The outputs of `iden_harm.m` are this vector of harmonic numbers, \mathbf{h} , and the matrix of normalized disturbance peak frequencies, \mathbf{F}_{peak} that was returned by `findpeaks.m`. Both outputs are necessary for the next step of the modeling process.

To create a complete wheel model, the harmonic number identification process described above is performed on the three force and two torque disturbances. Then, the radial force and radial torque model harmonic numbers, \mathbf{h}_{rad} and \mathbf{h}_{tor} , are determined by comparing and combining the harmonic numbers extracted from the F_x and F_y data and the T_x and T_y data, respectively. The axial force harmonic numbers, \mathbf{h}_{axi} are the harmonic numbers extracted from the F_z data.

3.1.3 Calculating Amplitude Coefficients

The next step in the empirical modeling process is the extraction of the amplitude coefficients, C_i , from the experimental data. Figure 3-6 presents a graphical representation of the MATLAB code, `find_coeff.m`, that calculates the amplitude coefficients given a steady-

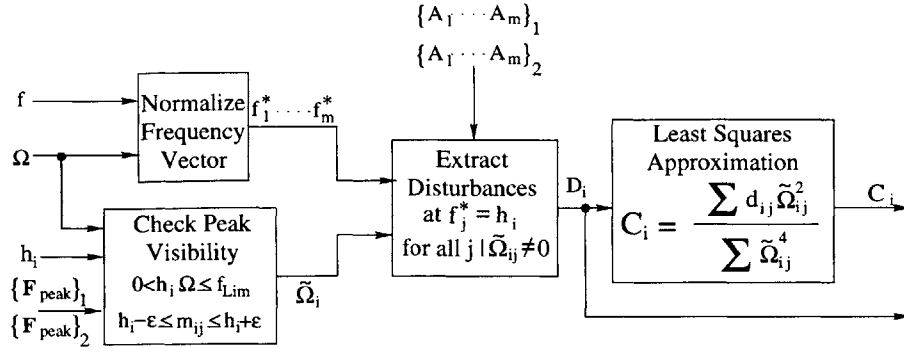


Figure 3-6: RWA DADM Toolbox Function find_coeff.m

state RWA data set, and the harmonic numbers and matrix of normalized disturbance peak frequencies, \mathbf{M}_{peak} returned by `iden_harm.m`. The block diagram details the process for one harmonic number and its corresponding amplitude coefficient, but the function can accept a vector of harmonic numbers and will calculate a vector of corresponding amplitude coefficients by repeating the algorithm for each harmonic.

Least squares approximation methods were used to calculate the amplitude coefficients for the HST RWA disturbance model [15]. The magnitude of the disturbance force (or torque) is assumed to be related to the wheel speed as follows:

$$\tilde{d}_{ij} = K\Omega_j^2 \quad (3.6)$$

where \tilde{d}_{ij} is the expected disturbance force (or torque) at the frequency corresponding to the i^{th} harmonic at the j^{th} wheel speed and K is a constant. The error between the actual disturbance and the expected disturbance at the i^{th} harmonic and the j^{th} wheel speed, e_{ij} is then:

$$e_{ij} = d_{ij} - K\Omega_j^2 \quad (3.7)$$

where d_{ij} is the experimentally measured disturbance force at the i^{th} harmonic and j^{th} wheel speed. The amplitude coefficient, C_i , is defined as the value of K which minimizes this error. An expression for C_i is obtained by first squaring Equation 3.7 and summing over the wheel speeds:

$$\sum_{j=1}^m e_{ij}^2 = \sum_{j=1}^m d_{ij}^2 - 2K \sum_{j=1}^m \Omega_j^2 d_{ij} + K^2 \sum_{j=1}^m \Omega_j^4 \quad (3.8)$$

The squared error, e_{ij}^2 , is minimized at values of K for which its derivative equals zero. The partial derivative of Equation 3.8 with respect to K is:

$$\frac{\partial}{\partial K} e_{ij}^2 = -2 \sum_{j=1}^m \Omega_j^2 d_{ij} + 2K_i \sum_{j=1}^m \Omega_j^4 \quad (3.9)$$

Then, an expression for C_i is obtained by setting Equation 3.9 equal to zero and solving for K :

$$C_i = \frac{\sum_{j=1}^m d_{ij} \Omega_j^2}{\sum_{j=1}^m \Omega_j^4} \quad (3.10)$$

The MATLAB function `find_coeff.m` calculates the amplitude coefficients using Equation 3.10. The function can determine the amplitude coefficients based on a single data set or multiple data sets as shown in Figure 3-6. Single data set calculations are necessary for the axial force model and during the initial modeling stages of the radial forces and torques. When run in this mode, the quantities $\{A_1 \dots A_m\}_2$ and $\{\mathbf{F}_{peak}\}_2$ are zero. However, calculation of the final radial force and torque amplitude coefficients requires two data sets (see Figures 3-2 and 3-1). The algorithm used in both cases is similar. The only differences are in the size and number of the inputs. In the following discussion, multiple data set extraction of radial force amplitude coefficients from the Ithaco B Wheel F_x and F_y data will be used to describe the function algorithm.

The first block in Figure 3-6 represents the normalization of the frequency vector, \mathbf{f} . The resulting non-dimensional frequency vectors, $\{\mathbf{f}_1^* \dots \mathbf{f}_m^*\}$ are used along with \mathbf{A} , \mathbf{F}_{peak} , $\mathbf{\Omega}$ and \mathbf{h} to determine the disturbance forces, d_{ij} , at each harmonic number over all wheel speeds. It is important to note that a disturbance at the i^{th} harmonic may not be visible in all of the amplitude spectra in the dataset. A disturbance peak can be undetectable for one of two reasons. If the frequency corresponding to h_i for a given wheel speed, Ω_j is not within the frequency range of good data, $[0, f_{Lim}]$, the disturbance amplitude at this frequency may be corrupted and is not included in the calculation of the amplitude coefficient. In addition, not all disturbances that fall within the frequency range are visible at all wheel speeds. For example, disturbances are often more difficult to identify in data taken at low wheel speeds due to a low signal to noise ratio. Therefore, the data must meet certain peak detection conditions to be included in the calculation of C_i .

Recall that both the matrix of amplitude spectra, \mathbf{A} , and \mathbf{F}_{peak} contain m columns, each corresponding to one wheel speed. Defining the quantity \mathcal{D}_j which contains the amplitude

spectra, wheel speed, normalized frequency vector, normalized peak locations, and upper frequency limit of good data associated with one wheel speed, $\mathcal{D}_j(A_j, \mathbf{f}_j^*, \mathbf{F}_{peak_j}, \Omega_j, f_{Lim})$ allows the peak detection conditions to be written as follows:

$$\mathcal{D}_j = \{0 < h_i \Omega_j \leq f_{Lim}\} \cap \left\{ f^* \in \mathbf{F}_{peak_j} \mid h_i - \epsilon \leq f^* \leq h_i + \epsilon \right\} \quad (3.11)$$

The first condition in Equation 3.11 ensures that the frequency corresponding to the harmonic for Ω_j is within the frequency range of good data. The second condition uses the matrix of detected normalized peak frequencies, \mathbf{F}_{peak} , obtained from `iden_harm.m` to ensure that a disturbance peak at $f^* = h_i$ is detectable in the amplitude spectra.

The extraction of disturbance amplitudes for use in the amplitude coefficient calculation is done one wheel speed at a time. Recall from Section 2.1 that the amplitude spectrum provides an estimation of the signal amplitude over frequency. Therefore, if \mathcal{D}_j satisfies both of the above conditions the magnitude of the disturbance force/torque at the frequency corresponding to the i^{th} harmonic is simply the value of A_j at the normalized frequency $f^* = h_i$. The disturbance magnitude is assigned to d_{ij} , and the wheel speed is assigned to $\tilde{\Omega}_{ij}$. However, if one or both of the conditions are not satisfied, the data for that wheel speed is not included in the calculation and both d_{ij} and $\tilde{\Omega}_{ij}$ are set to zero. This process is continued for all wheel speeds, and two vectors of length m , one of disturbance amplitudes, \mathbf{D}_i and one of corresponding wheel speeds, $\tilde{\Omega}_i$, are created. In general, $\tilde{\Omega}_i$ would be equal to the input vector Ω , but since all of the wheel speeds may not be included in the amplitude coefficient calculation for a given harmonic due to lack of disturbance peak visibility, each C_i is computed using a distinct subset of wheel speeds, $\tilde{\Omega}_i$. The vectors \mathbf{D}_i and $\tilde{\Omega}_i$ are manipulated and summed as shown in Equation 3.10 to obtain C_i .

The function `find_coeff.m` also generates plots that show the quality of the fit between the data and the disturbance force predicted by C_i . The plots for the 1.0 and 3.87 harmonics of the Ithaco B Wheel data (F_x and F_y) are shown in Figure 3-7. The circles represent the force amplitudes of the experimental data over the different wheel speeds. Note that some of the circles lie on the x-axis. These points are from wheel speeds which did not meet the conditions in Equation 3.11. The solid line is the curve generated using the calculated C_i and Equation 3.6.

These coefficient curve fit plots are useful for a number of reasons. First, they allow

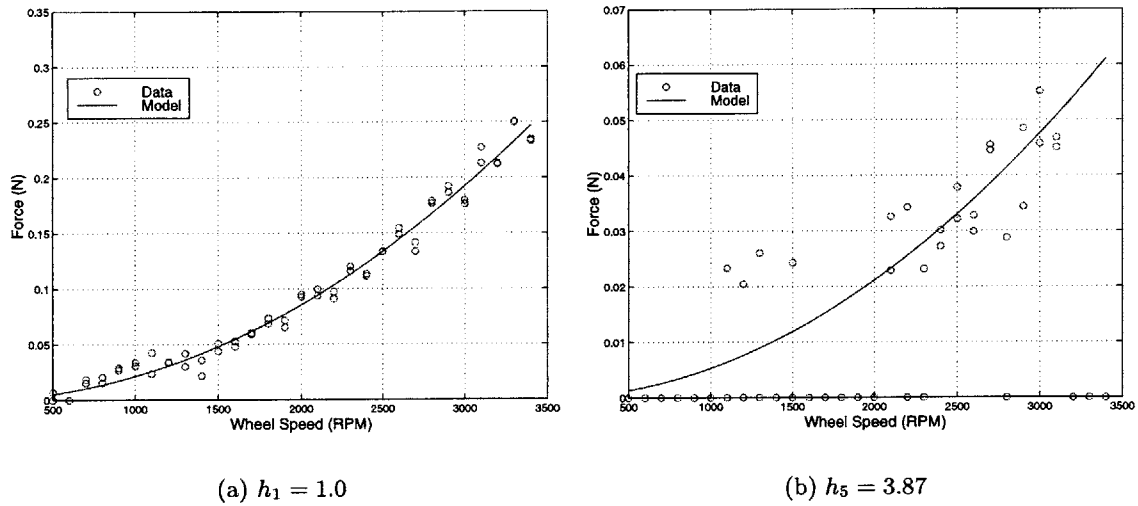


Figure 3-7: Amplitude Coefficient Curve Fits for Ithaco B Wheel Radial Force Data

assessment of the assumption in Equation 3.6. In Figure 3-7(a) the data points lay right along the theoretical curve. This result suggests that the assumption of Equation 3.6 is a good one for the fundamental harmonic. In contrast, the curve fit for $h_5 = 3.87$, Figure 3-7(b), is not quite as good. This curve follows the general trend of the data at higher wheel speeds, but at low speeds the disturbance amplitude is under-predicted by at least a factor of 2. It is possible that Equation 3.6 may not hold for the higher harmonics or that some other disturbance source is dominating at low wheel speeds.

The curve fit plots can also be used to eliminate harmonics from the model. If a curve fit is not based on enough data points there cannot be a high degree of confidence in the resulting amplitude coefficient, and the harmonics are removed from the model. An example from the Ithaco B Wheel radial force model is shown in Figure 3-8. The plot shows that the amplitude coefficient was only calculated based on three data points from low wheel speeds. The data from the high wheel speeds could not be included in the curve fit because the frequencies corresponding to this harmonic are not within the frequency range of good data. It is often difficult to predict the amplitude coefficients for the higher harmonics for this reason.

In some cases, the effects of the structural modes of the wheel on the harmonic disturbances can be observed in the coefficient curve fit plots. Figure 3-9 shows the coefficient curve fit for the second radial torque harmonic, $h_2 = 1.99$ of the Ithaco B Wheel. The

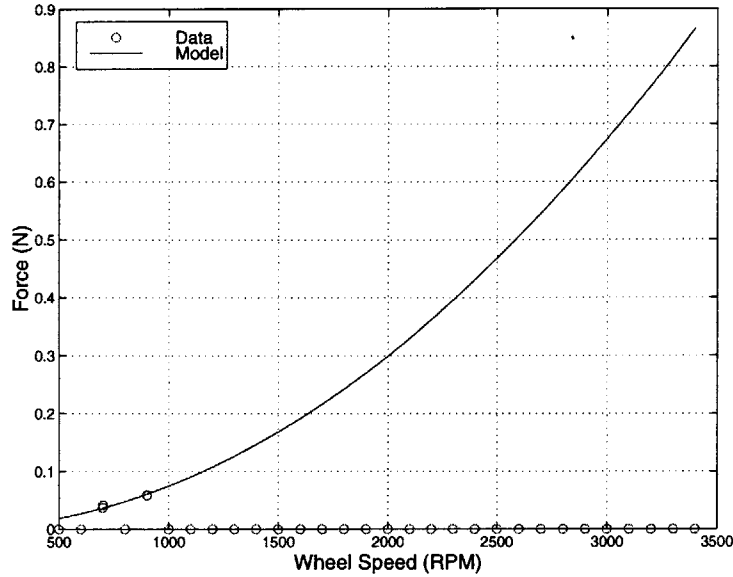


Figure 3-8: Amplitude Coefficient Curve Fit Showing Low Confidence Fit: $h_i = 12.38$ (Ithaco B Wheel Radial Force)

lighter circles and dashed curve are the initial results of the amplitude coefficient calculation. Note that there is a large increase in force amplitude in the data between 1300 and 1900 rpm. This amplitude increase occurs when the frequency of the harmonic approaches the frequency of one of the structural wheel modes. The form of the empirical model does not present a convenient method of accounting for these modal excitations. Therefore the empirical model will be used to model only the wheel harmonics, and the disturbance amplifications will be incorporated into a new model which is the subject of Chapter 4. As a result, the modal interactions seen in the figure should not be included in the calculation of the amplitude coefficient.

Another MATLAB function, `remove_mode.m`, was created to isolate the effects of the structural mode from the harmonic disturbances. Figure 3-10 shows a block diagram representation of this function. The original outputs from `find_coeff.m` are denoted \bar{C}_i and \bar{D}_i to differentiate between coefficients calculated with and without modal effects. These quantities are input to `remove_mode.m` along with Ω , the harmonic index, i , and the wheel speed range affected by the structural mode, $[\Omega_l, \Omega_h]$. For example, considering the second harmonic of the Ithaco B Wheel radial force model shown in Figure 3-9, $i = 2$ and the affected wheel speed range is $[1300, 1900]$. Data points associated with speeds in this range are removed from \bar{D}_i and a new disturbance magnitude vector, D_i , and corresponding wheel

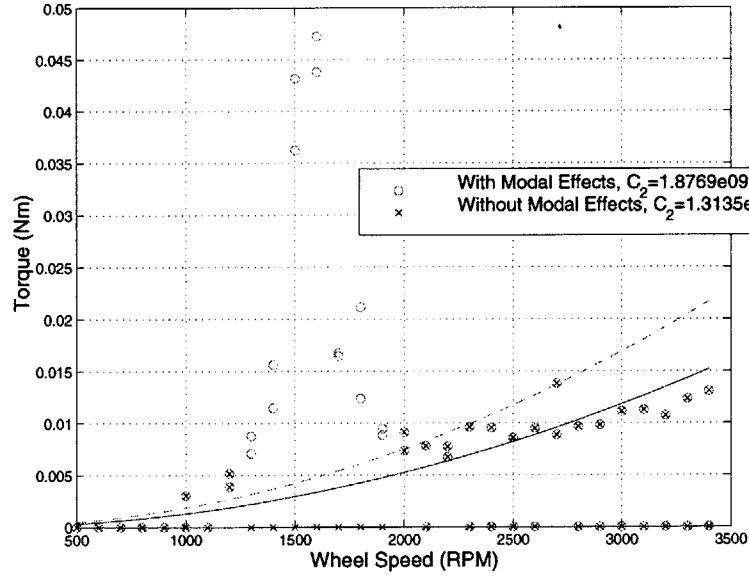


Figure 3-9: Effects of Internal Wheel Modes on Amplitude Coefficient Curve Fit: $h_2 = 1.99$ (Ithaco B Wheel Radial Torque)

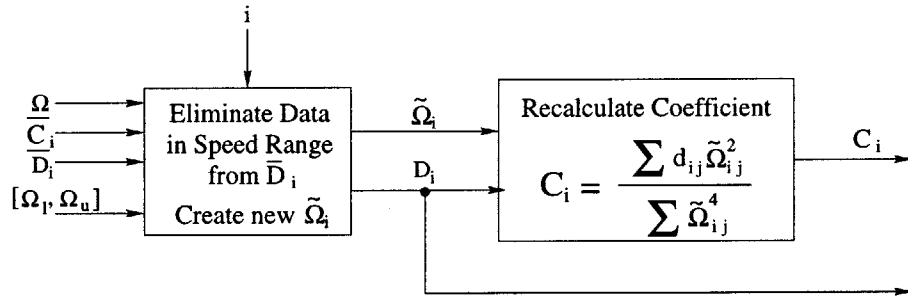


Figure 3-10: RWA DADM Toolbox Function remove_mode.m

speed vector, $\tilde{\Omega}_i$ are created and used to calculate the corrected amplitude coefficient, C_i .

The results of running `remove_mode.m` on the second harmonic of the Ithaco B Wheel radial torque data is shown along with the original coefficient calculation results (\bar{C}_i , \bar{D}_i) in Figure 3-9. The dark x's and the solid curve correspond to D_2 and C_2 and do not include the resonance points, while the lighter circles and dashed curve correspond to the original coefficient calculation based on all points, \bar{D}_2 and \bar{C}_2 . Note that including data with the resonance behavior causes an over-estimation of the disturbance force at higher wheel speeds (dashed curve). When the resonant data are removed from the coefficient calculation (solid curve) the amplitude coefficient is decreased and there is a much better fit between the theoretical curve and the data above 2000 rpm. These interactions between the harmonics and the internal wheel modes will be explored in more detail in Chapter 4.

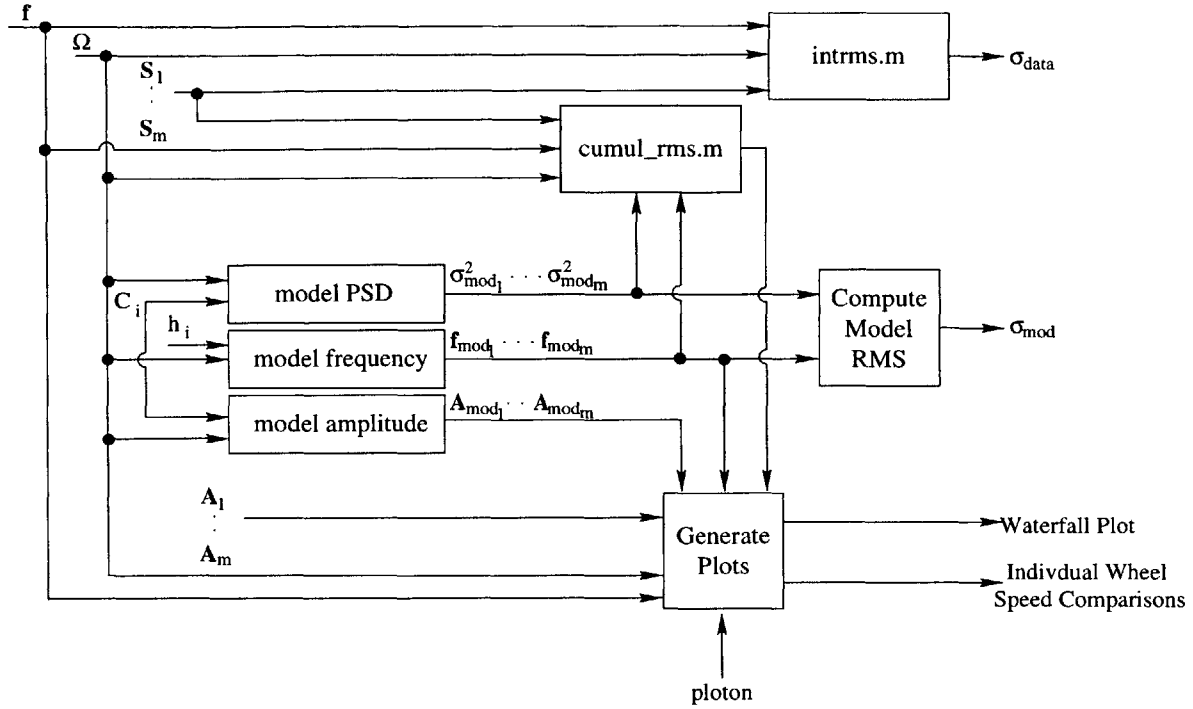


Figure 3-11: RWA DADM Toolbox Function `comp_model.m`

3.1.4 Model Validation: Comparing to Data

The model parameters should be validated through comparison of the empirical model to the experimental data. The final function in the RWA DADM toolbox, `comp_model.m`, performs this task. A block diagram representation of the function is shown in Figure 3-11. The inputs to the function include the vectors of model parameters, \mathbf{h} and \mathbf{C} , and the data set components, \mathbf{S} , \mathbf{A} , \mathbf{f} , Ω and f_{Lim} . The function outputs are a series of plots, the number and type of which depend on the value of a plotting flag, and vectors of length m containing the RMS of the model, σ_{mod} , and the data, σ_{data} , at each of the wheel speeds.

The empirical model is created using the model parameters extracted by `iden_harm.m`, `find_coeff.m` and `remove_mode.m` and Ω . Recall from Equation 3.1 that the forces and torques are modeled as discrete harmonic disturbances at frequencies dependent upon h_i and with amplitudes proportional to the wheel speed squared. The disturbance frequencies for a given wheel speed, $\bar{\omega}_j$ are determined by:

$$\bar{\omega}_j = \mathbf{h}\Omega_j \quad (3.12)$$

The vector $\bar{\omega}_j$ is a vector of discrete disturbance frequencies for the j^{th} wheel speed and is

the same length as \mathbf{h} . Similarly, vectors of disturbance amplitudes, \mathbf{A}_{mod_j} , corresponding to $\bar{\omega}_j$ are created based on the assumption that the disturbance amplitude from the i^{th} harmonic at the j^{th} wheel speed is:

$$A_{mod_{ij}} = C_i \Omega_j^2 \quad (3.13)$$

The matrices \mathbf{A}_{mod} and $\bar{\omega}$, which are analogous to the experimental quantities \mathbf{A} and \mathbf{f} , are used to generate model/data comparison plots.

In addition, the PSD of the model, \mathbf{S}_{mod_j} , is calculated for comparison to the experimental data. An expression for the model PSD as a function of frequency and wheel speed was derived by first finding the autocorrelation, $R_m(\tau)$ of Equation 3.1. Substituting $m(t)$ (Equation 3.1) for $\mathbf{X}(t)$ in the definition of the autocorrelation (Equation 2.1) and assuming that α_i is a random variable uniformly distributed between 0 and 2π and that α_i and α_j are statistically independent, the expression for the autocorrelation of the empirical model is:

$$R_m(\tau) = \sum_{i=1}^n \frac{C_i^2 \Omega_j^4}{2} \cos(\Omega_j h_i \tau) \quad (3.14)$$

See Appendix B for the full derivation of $R_m(\tau)$. Recall from Section 2.1.1 that the mean square of a random process is equal to its autocorrelation evaluated at $\tau = 0$. Then, assuming that $m(t)$ is both stationary and zero mean, the variance of the empirical model is:

$$\sigma_{mod_j}^2 = R_m(0) = \sum_{i=1}^n \frac{C_i^2 \Omega_j^4}{2} \quad (3.15)$$

Equations 3.14 and 3.15 are then be used to derive the spectral density function of the empirical model. The autocorrelation function of a single harmonic process and its corresponding spectral density are given in [21] as:

$$R_{\mathbf{X}}(\tau) = \sigma_{\mathbf{X}}^2 \cos(\omega_0 \tau) \quad (3.16)$$

$$S_{\mathbf{X}}(\omega) = \sigma_{\mathbf{X}}^2 \left[\frac{1}{2} \delta(\omega + \omega_0) + \frac{1}{2} \delta(\omega - \omega_0) \right] \quad (3.17)$$

Substituting Equation 3.15 into Equation 2.1 and setting $h_i \Omega_j = \omega_0$ results in an autocorrelation of the same form as that in Equation 3.16. Therefore, the PSD of the empirical model is of the same form as that in Equation 3.17. After making the necessary substitutions the

one-sided PSD of the empirical model, $S_{mod_j}(\omega)$, is:

$$S_{mod_j}(\omega) = \sum_{i=1}^n \frac{C_i^2 \Omega_j^4}{2} \delta(\omega - \bar{\omega}_j) \quad (3.18)$$

Note that the empirical model PSD consists of a series of discrete impulses occurring at frequencies, $h_i \Omega_j$, with amplitudes equal to the variances of the harmonics, $\sigma_{mod_{ij}}^2$. The vectors $[\sigma_{mod_1}^2 \dots \sigma_{mod_m}^2]$, which are outputs of the “model PSD” block in Figure 3-11, consist of the PSD amplitudes for the discrete harmonics at all m wheel speeds. The matrix of these vectors, σ_{mod}^2 is analogous to \mathbf{S} and is used for model/data comparison.

The RMS values of the model and data are calculated for each wheel speed. It was shown in Section 2.1.1 that the area under the PSD of a random process is equal to the mean square. Therefore, the data RMS for a given wheel speed, σ_{data_j} , is simply the square root of the area under the PSD, S_j . The MATLAB function `intrms.m` is used to perform the integration across frequency and obtain this value for each wheel speed. The RMS of the model is calculated using the assumption that the random process $m(t)$ is stationary and zero mean. Recall from Section 2.1 that the RMS of a zero mean process is simply the square root of its variance:

$$\sigma_{mod_j} = \sqrt{\sum_{i=1}^n \frac{C_i^2 \Omega_j^4}{2}} \quad (3.19)$$

The vectors of RMS values, σ_{mod} and σ_{data} are used to compare the model and the data and assess model validity.

Two different types of plots are generated by the function `comp_model.m`. The first is a waterfall plot overlaying the model PSDs and the data PSDs as shown in Figure 3-12. In this figure, the Ithaco B Wheel F_x data PSDs are plotted as continuous lines and the radial force empirical model PSDs are represented with circles. It is important to note that the units of amplitude (z-axis) for the data and model are not equivalent. The data PSDs are continuous over frequency and have amplitudes with units of N^2/Hz , but the model PSDs consist of series of discrete impulses with amplitudes which have units of N^2 and are equal to the variance, or the area under the corresponding peak in the continuous PSD, of the harmonic disturbance. Therefore this type of plot should not be used to validate the amplitude coefficients of the model. Instead, the waterfall plot is useful for validating the harmonic numbers. Note in Figure 3-12 that the diagonal lines of circles lie on top of the

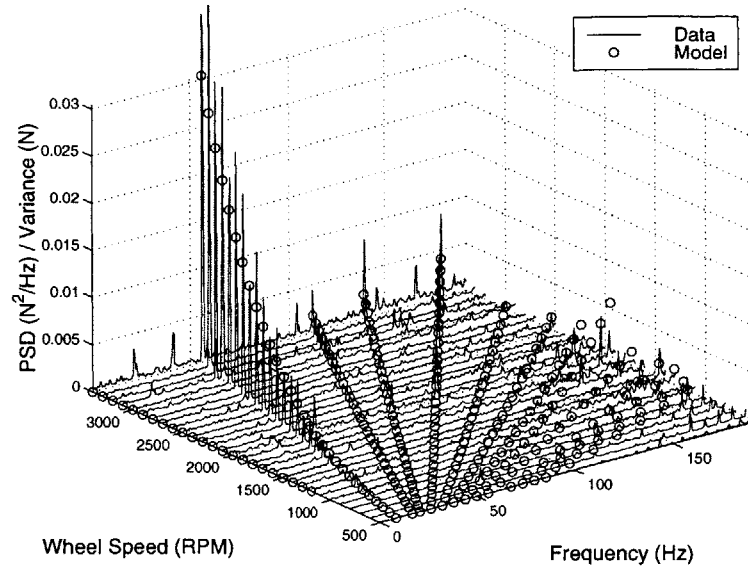


Figure 3-12: Waterfall Plot Comparison of Radial Force Model to F_x Data (Ithaco B Wheel)

diagonal ridges seen in the data. The plot indicates that the location of the harmonics have been identified correctly. During the first iterations of the modeling process such plots are extremely useful for finding harmonics which may have been either missed by `iden_harm.m` or erroneously identified. In general, it is more practical to view the PSD comparison when validating the harmonic numbers with waterfall plots. The square operation involved in computing the power spectral density tends to make the noise floor appear smaller which results in better defined ridges of harmonics in the waterfall plot.

The second type of plot generated by `comp_model.m` is shown in Figure 3-13. The lower plot compares the amplitude spectra of the data and model for one wheel speed (3000 rpm in this example). The continuous curve is the data amplitude spectrum, and the discrete impulses, marked with circles, are the radial force model amplitudes. In this form, both data and model amplitudes have the same units and can be compared directly allowing validation of the amplitude coefficients. Note that the amplitude of the first harmonic, which is the fundamental, matches the amplitude of the data quite well. The comparison of the higher harmonics, on the other hand, is not as good. This discrepancy is most likely due to the assumption that the disturbance force is proportional to the wheel speed squared (Equation 3.6). As mentioned earlier, this assumption seems valid for the fundamental harmonic but begins to break down with the higher harmonics.

The cumulative RMS curves, which represent the RMS as a function of frequency (see

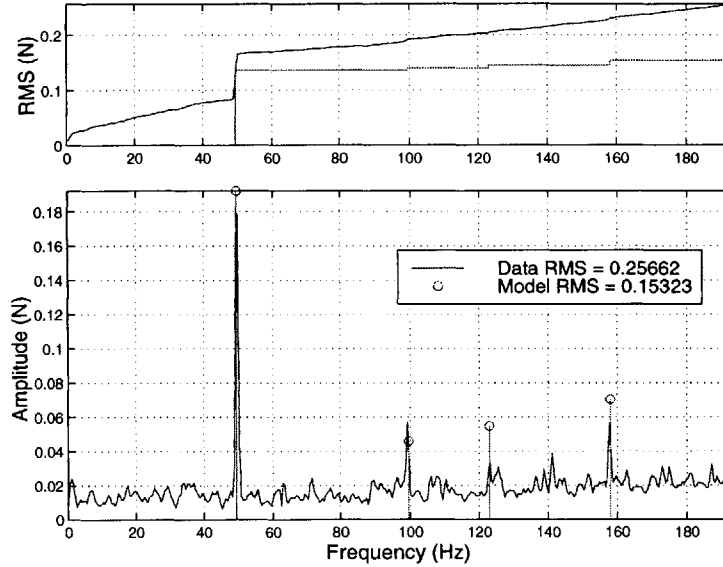


Figure 3-13: PSD Comparison of Radial Force Model to F_x Data (Ithaco B Wheel) with Cumulative RMS at 3000 rpm

Section 2.1.1), for both the model and the data, are plotted above the amplitude spectra. These curves offer another way to check the amplitude coefficients. Ideally the model RMS will be close to the data RMS and the contributions to the RMS from the harmonics will be comparable. For this example, the contribution of the fundamental harmonic accounts for a large portion of the RMS in both the data and the model. However, the model underpredicts the RMS over all frequencies. The data shows energy at frequencies below the wheel speed which are not captured in the model. The RMS curves at frequencies greater than the wheel speed both exhibit a “staircase” behavior resulting from the addition of energy by the higher harmonics, but the cumulative RMS of the data is as much as a factor of 2 greater than that of the model. Such discrepancies between the model and the data may indicate errors in the amplitude coefficient calculation. However, the lower plot shows that although the amplitudes of the higher harmonics are not predicted exactly, a reasonable estimate has been obtained. Therefore other possible explanations for the poor data/model comparison are considered and will be discussed in Section 3.2.3.

3.2 Examples

The RWA vibration data discussed in Section 2.2 was run through the RWA DADM toolbox to create disturbance models for the Ithaco type B and E wheels. Five sets of data for each

Table 3.3: Empirical Model Parameters for Ithaco B Wheel

Radial Force, $n_{rad} = 13$		Radial Torque, $n_{tor} = 11$		Axial Force, $n_{axi} = 4$	
Harmonic Number, h_i	Amplitude Coefficient, C_i N/rpm ² x10e ⁻⁷	Harmonic Number, h_i	Amplitude Coefficient, C_i N/rpm ² x10e ⁻⁷	Harmonic Number, h_i	Amplitude Coefficient, C_i N/rpm ² x10e ⁻⁷
0.99	0.2134	0.99	0.0630	0.99	0.0727
1.99	0.0510	1.99	0.0314	1.41	0.0497
2.46	0.0609	3.16	0.0089	2.82	0.0975
3.16	0.0783	4.56	0.0119	5.95	0.1989
3.87	0.0528	5.28	0.0261		
4.56	0.0905	5.97	0.0372		
5.28	0.1752	6.23	0.0237		
5.98	0.3040	6.68	0.0276		
6.71	0.2053	7.38	0.0335		
8.09	0.3246	8.09	0.0477		
8.83	0.3517	8.80	0.0400		
9.54	0.2991				
10.25	0.3183				

wheel, F_x , F_y , F_z , T_x , and T_y , were used to obtain three disturbance models per wheel: radial force, radial torque and axial force. The results of the data analysis, the model parameters and comparisons between the models and data are presented in the following sections.

3.2.1 Ithaco B Wheel Empirical Model

The model parameters extracted from the Ithaco B Wheel data are listed in Table 3.3. The number of harmonics included in each model are indicated in the column heading by the parameter n . The creation of the three models will be discussed separately and in detail in this section.

Radial Forces

The harmonic numbers for the Ithaco B Wheel radial force model were identified using the function `iden_harm.m` and then refined through data comparison. The function was run twice, once with \mathbf{A}_{F_x} and once with \mathbf{A}_{F_y} . The wheel speed and frequency vectors for both cases are identical, and the upper frequency limit, f_{Lim} was set at 200 Hz due to the effects of the test stand resonance on the data. The noise isolation, binning and bin percentage tolerances, N_σ , ϵ , and P_0 , were set to 3, .02 and 25, respectively. In addition, the data

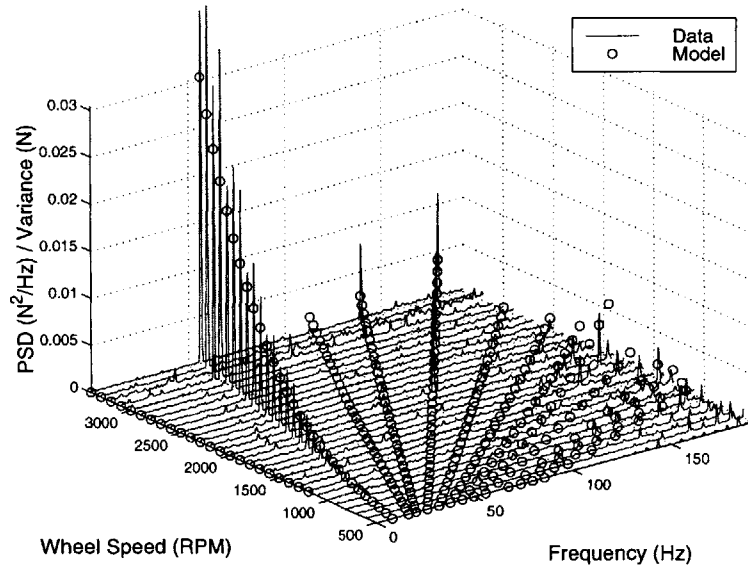


Figure 3-14: Waterfall Comparison of Radial Force Model and Ithaco B Wheel F_y Data

splicing option was turned on due to the poor quality of the data.

Both waterfall plots and amplitude coefficient curve fit plots aided in choosing harmonic numbers. The waterfall plots were used to find extraneous harmonics that were incorrectly identified by `iden_harm.m` or harmonics that were visible in the data but were missed by the function. Then the coefficient curve fit plots, created with the combination of the F_x and F_y data sets, provided a filter for harmonics with low confidence amplitude coefficients. Harmonics with numbers greater than 10.25 were removed from the model for this reason. No structural wheel mode resonances could be clearly identified in the radial force data so the function `remove_mode.m` was not necessary. The resulting radial model consists of 13 harmonics. Their numbers and amplitude coefficients are listed in Table 3.3 and the coefficient curve fits are presented in Appendix A.1.1.

Waterfall comparisons of the final radial force model and the F_x and F_y data are shown in Figures 3-12 and 3-14, respectively. Both plots indicate that the disturbance frequencies have been captured by the model quite well. The first four harmonics are clearly visible in the data and the model frequencies lie right along the data peaks. The higher harmonics are difficult to see in the data at low frequencies (probably because of a low signal to noise ratio), but at higher frequencies a good correlation between model and data can be observed.

A second type of model/data comparison is shown in Figure 3-15. Here, the RMS values of the data and the model are plotted as a function of wheel speed. In effect, this plot is

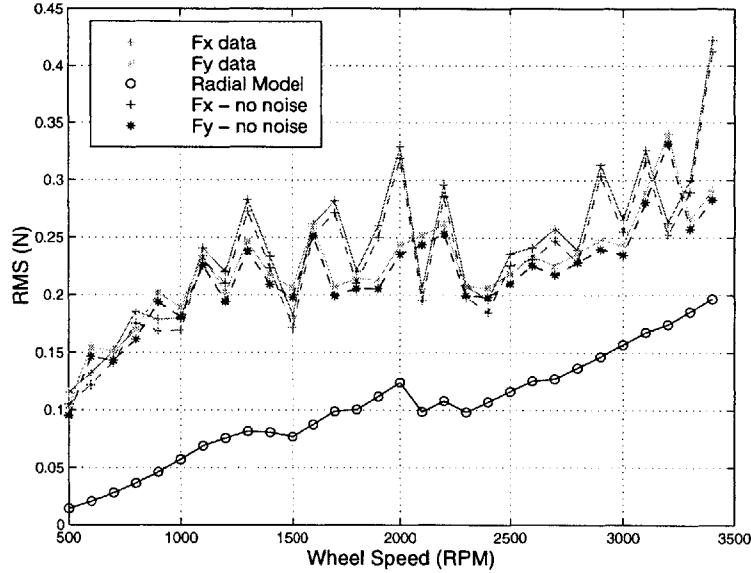


Figure 3-15: RMS Comparison of Empirical Model and Ithaco B Wheel Data: Radial Force (with and without noise floor)

simply an integration of the waterfall plot across frequency. The solid curves, marked with “+” and “*” are the RMS values for the F_x and F_y data, respectively, and are quite similar, as is expected. The dotted curves are the RMS values for the F_x and F_y data minus the RMS of the noise floor obtained from the Ithaco B Wheel noise data (see Section 2.2.1). Note that the measured noise contributes very little to the energy of the signal. The solid line marked with circles is the RMS of the radial force model. The plot clearly shows that the radial force model under-predicts the actual disturbance across all wheel speeds. One thing to note is that there is quite a bit of energy at low wheel speeds that is not captured by the model. In fact, the model RMS is lower by more than a factor of 2 at 500 rpm. The model gets closer to the data as the wheel speed increases, but is consistently lower. This discrepancy will be addressed in detail in Section 3.2.3, after both the complete Ithaco B and E Wheel models have been presented.

Radial Torques

The procedure for developing the radial torque model closely parallels that of the radial forces. The wheel speed vector, frequency vector, f_{Lim} and tolerances are unchanged, but the data sets used are \mathbf{A}_{T_x} and \mathbf{A}_{T_y} . The waterfall plots provided a check on the early generations of harmonic numbers, and higher harmonics (above 10.25) were eliminated due

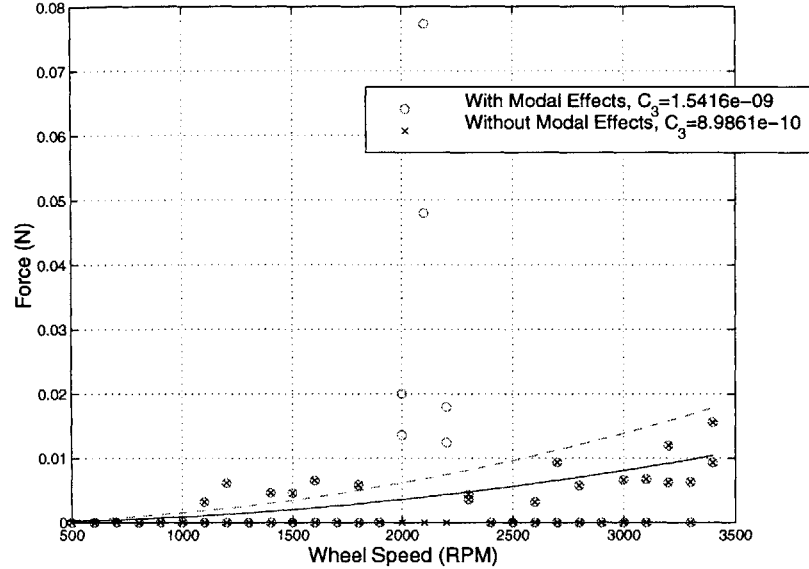


Figure 3-16: Elimination of Rocking Mode Disturbance Amplification from Calculation of C_3 ($h_3 = 3.16$)

to low confidence amplitude coefficient curve fits.

The initial coefficient curve fits for the final harmonic numbers are presented in Appendix A.1.2. Note that the curve fits for \bar{C}_2 ($h_2 = 1.99$) and \bar{C}_3 ($h_3 = 3.16$) show distinct disturbance amplifications in the ranges 1200 – 1900 rpm and 2000 – 2300 rpm, respectively. These amplifications are due to the excitation of the positive and negative whirls of the rocking mode (see Section 2.3). The function `remove_mode.m` was used to remove the modal effects from the amplitude coefficient calculation for these harmonics. The results are plotted in Figures 3-9 and 3-16. Note that removing the modal disturbance amplification lowered the value of the amplitude coefficient for both harmonics. The final harmonic numbers and amplitude coefficients for the radial torque model are listed in Table 3.3.

Waterfall comparisons of the Ithaco B Wheel radial torque model are shown in Figure 3-17. The first three harmonics are clearly visible in the data and occur at frequencies which are accurately captured by the model. The higher harmonics are more difficult to identify, but the high frequencies show a relatively good correlation between the model and the data.

The RMS comparison for the radial torque model is shown in Figure 3-18. The solid curves, marked with “+” and “*” are the RMS values for the T_x and T_y data, respectively, and are quite similar, as is expected. The dotted curves are the RMS values for the T_x and T_y data minus the RMS of the noise floor. Note that the noise floor contributes very little

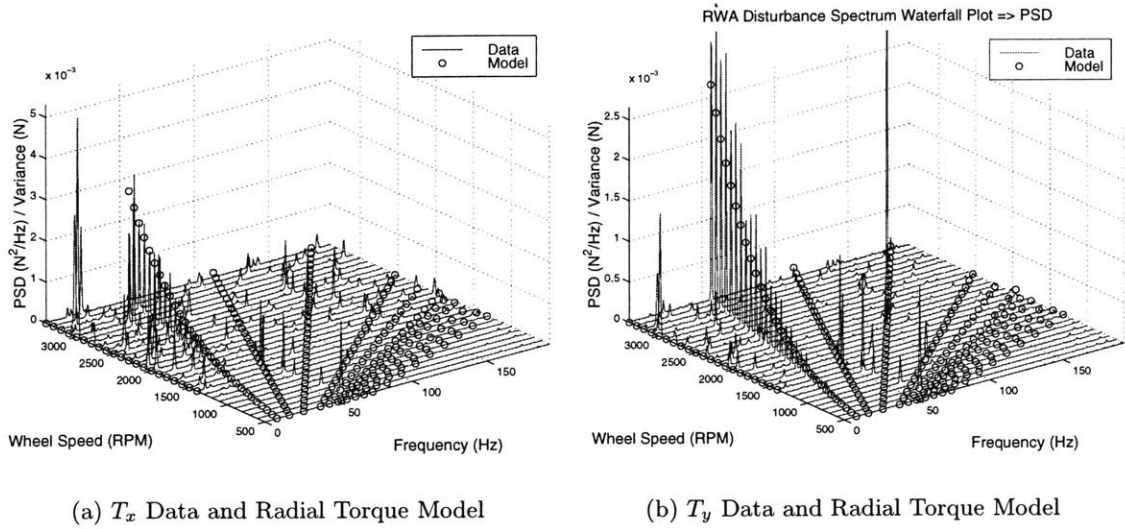


Figure 3-17: Waterfall Comparisons of Radial Torque Model and Ithaco B Wheel Data

to the energy of these signals as was the case with the radial force data. The radial torque model RMS is plotted as a solid line with data points marked by circles.

The RMS comparison indicates that the radial torque model, like the radial force model, severely under predicts the disturbances. Note the peaks in the data RMS around 1600 rpm and 2100 rpm. Recall that these wheel speeds correspond to the middle of the wheel speed ranges over which disturbance amplifications from the rocking modes were visible in some of the coefficient curve fits. It can be concluded then that these large RMS values are due to the effects of the structural modes on the wheel disturbance and are not expected to be seen in the empirical model. However, all the additional energy in the data cannot be attributed to interactions with the structural wheel modes since the model RMS is consistently much lower than the data RMS over all wheel speeds, not only those speeds at which disturbance amplification occurs. Therefore other possible sources of error must be considered, as is the case with the radial forces, and will be discussed after the presentation of the Ithaco E Wheel model in Section 3.2.3.

Axial Forces

The axial force model was created from \mathbf{A}_{F_z} and the same $\mathbf{\Omega}$, \mathbf{f} , f_{Lim} and tolerances used for the radial force and torque models. Notice from Figure 2-4 that the waterfall plot of the F_z data looks much different from the radial force and torque data. Distinct ridges of

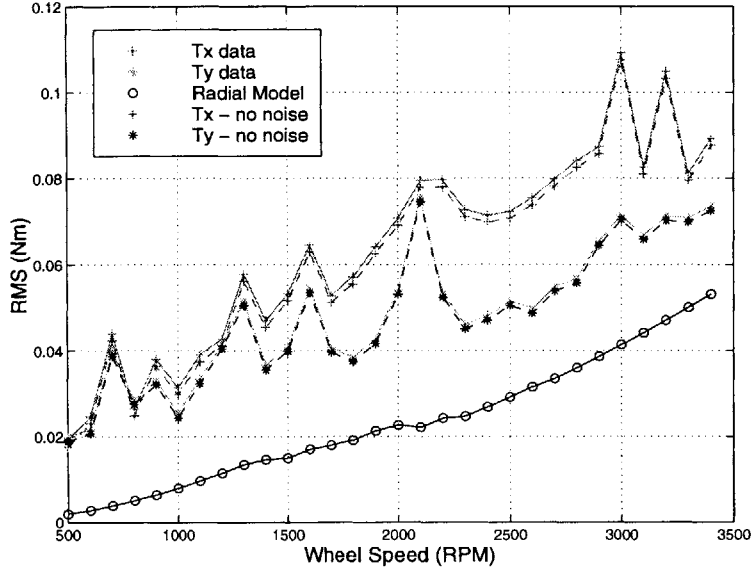
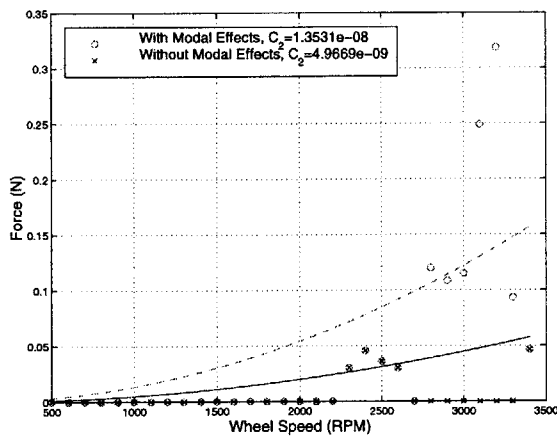


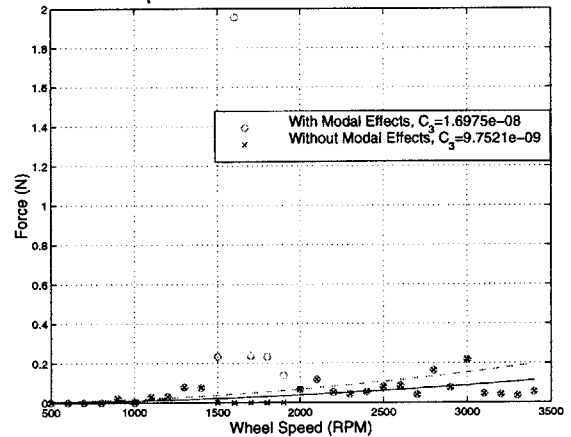
Figure 3-18: RMS Comparison of Empirical Model and Ithaco B Wheel Data: Radial Torque (with and without noise floor)

harmonic disturbances are very difficult to see and there is a constant frequency ridge at about 75 Hz. Note from Table 2.3 that this frequency is close to the reported frequency of the axial mode of the Ithaco B Wheel [16]. Therefore it appears that the dominant disturbances in the F_z data are a result of excitation of the axial translation mode. In addition, there are quite a few dynamics visible in the waterfall plot below 50 Hz. These disturbances do not seem to be wheel speed dependent and their source is unknown.

The axial mode resonances and low frequency disturbances dominate the F_x data and cause difficulties in the identification of the harmonic numbers. The function `iden_harm.m` is unable to effectively isolate harmonic disturbances from the data. Therefore, the resulting axial model is of poor quality. Most of the harmonics identified with `iden_harm.m` had to be removed from the model due to low confidence amplitude coefficient curve fits. The coefficient curve fit plots for the remaining four harmonics, which are presented in Appendix A.1.3, show that none of the coefficient curves fit the data very well. Even the fit for the fundamental harmonic, $h_1 = 0.99$, is not particularly good. The second and third harmonics, $h_2 = 1.41$ and $h_3 = 2.82$, both contain disturbance amplification from the axial mode between 1500 and 1900 rpm and 2800 and 3000 rpm, respectively. The function `remove_mode.m` was used to eliminate the modal effects from the coefficient calculation as shown in Figure 3-19.



(a) $h_2 = 1.41$



(b) $h_3 = 2.82$

Figure 3-19: Elimination of Axial Mode Disturbance Amplification from Amplitude Coefficient Calculations: Ithaco B Wheel Axial Force

The waterfall plot comparison of the axial force model and the F_z data is shown in Figure 3-20. As was discussed earlier, harmonic disturbances are not clearly visible in the data and can only be observed when the disturbance frequency equals that of the axial mode. Even the fundamental harmonic, which was the most significant harmonic in the radial forces and torques, is not clearly defined in the axial force data. Therefore, the correlation between the model and the data is not very good. It is possible that the axial force disturbances are not a series of discrete harmonics like the radial forces and torques. The correlation between the Ithaco E Wheel data and model can be used to test this hypothesis and the model/data fit discussion will be continued in Section 3.2.3.

The final plot is the RMS comparison between the axial force model and the data. The solid line marked with “+” represents the RMS values of the F_z data and the dashed line is the data RMS minus the noise RMS. Note that the noise RMS does not contribute very much to the data RMS. This result is consistent with those seen for the radial forces and torques. The axial force model RMS is plotted with a solid line with data points marked by circles. The dominant feature in this plot is the peak in RMS between 1500 and 1700 rpm. This wheel speed range corresponds to the range over which disturbance amplifications from the axial mode were present in the coefficient curve fit for the third harmonic (Figure 3-19(b)). In the waterfall plot of the F_z data (Figure 3-20) a very large peak is visible at about 65 Hz and 1600 rpm. This amplified disturbance adds a large amount of energy to

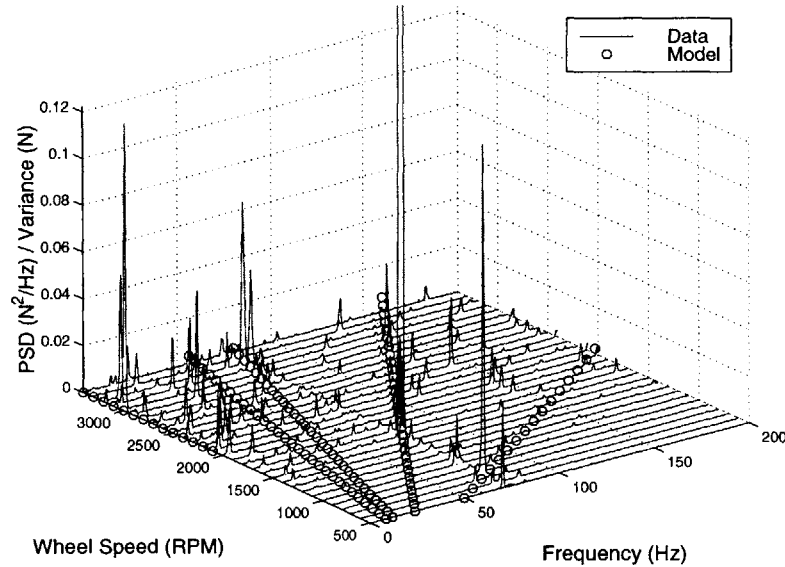


Figure 3-20: Waterfall Comparison of Axial force Model and Ithaco B Wheel F_z Data

the RMS at this wheel speed resulting in the large peak RMS value in Figure 3-21. It should also be noted that the axial force model lies consistently below the data over all speeds. As discussed earlier, this result is only expected at wheel speeds in which the disturbances are amplified by the internal wheel modes. This discrepancy will be discussed in more detail in Section 3.2.3 after the Ithaco E Wheel model is presented.

3.2.2 Ithaco E Wheel Empirical Model

The model parameters extracted from the Ithaco E Wheel data are listed in Table 3.4. The number of harmonics included in each model are indicated in the column heading by the parameter n . The creation of the three models will be discussed separately and in detail in this section.

Radial Forces

The radial force model parameters were extracted using the inputs listed in Table 3.5. Note that there are two wheel speed vectors, one corresponding to each of the radial force data sets. The vibration tests conducted on the Ithaco E Wheel were actually wheel speed sweeps, and the data for each disturbance direction had to be pre-processed, as described in Section 2.2.2, into “steady-state” data sets. As a result of the pre-processing, there is a distinct wheel speed vector for each data set. The Ithaco E Wheel data was sampled at

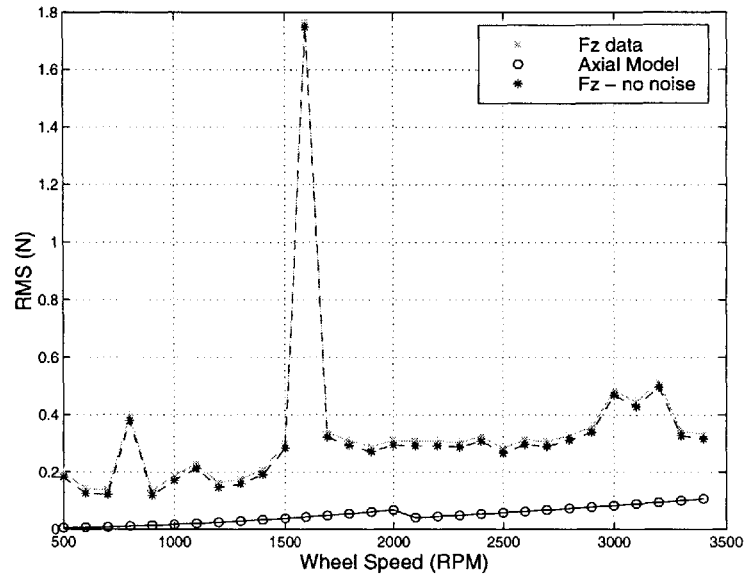


Figure 3-21: RMS Comparison of Empirical Model and Ithaco B Wheel Data: Axial Force (with and without noise floor)

Table 3.4: Empirical Model Parameters for Ithaco E Wheel

Radial Force, $n_{rad} = 7$		Radial Torque, $n_{tor} = 6$		Axial Force, $n_{axi} = 5$	
Harmonic Number, h_i	Amplitude Coefficient, C_i N/rpm ² x10e ⁻⁷	Harmonic Number, h_i	Amplitude Coefficient, C_i N/rpm ² x10e ⁻⁷	Harmonic Number, h_i	Amplitude Coefficient, C_i N/rpm ² x10e ⁻⁷
1.00	0.4155	1.00	0.2205	1.00	0.3038
2.00	0.0832	2.00	0.0609	1.98	0.2818
3.00	0.0543	3.00	0.0242	2.96	0.0719
4.00	0.0621	4.00	0.0243	4.00	0.0685
4.42	0.1097	4.42	0.0485	4.33	0.1011
5.37	0.0542	5.58	0.0498		
5.57	0.0690				

Table 3.5: Inputs for Ithaco E Wheel Radial Force Modeling

Name	Description	Size/Value
m	# of wheel speeds	120
n_f	# of frequency points	640
\mathbf{f}	Frequency vector	640 x 1
f_{Lim}	Upper frequency limit	300 (Hz)
$\mathbf{\Omega}_{F_x}$	Wheel speeds	1 x 120
$\mathbf{\Omega}_{F_y}$	Wheel speeds	1 x 120
\mathbf{A}_{F_x}	Amplitude spectra	640 x 120
\mathbf{A}_{F_y}	Amplitude spectra	640 x 120
\mathbf{S}_{F_x}	PSDs	640 x 120
\mathbf{S}_{F_y}	PSDs	640 x 120
N_σ	Noise isolation tolerance	2
ϵ	Binning tolerance	0.02
P_0	Bin percentage threshold	25%

a relatively high frequency (3840 Hz) and for a long time. Therefore, a small frequency resolution and good signal to noise ratio were obtained, which allows the use of a low noise isolation tolerance, $N_\sigma = 2$ for the identification of the harmonic numbers.

The harmonic numbers were identified with `iden_harm.m` and refined through waterfall comparisons and amplitude coefficient curve fits. A harmonic at $h_i = 5.00$ and those greater than 5.57 were eliminated from the model due to low confidence amplitude coefficient curve fits. In most of these cases the only significant peaks were a result of disturbance amplification by structural modes. Once the affected points were removed from the calculation there were not enough data left to accurately predict the amplitude coefficient. The fact that these harmonics could not be observed at low wheel speeds indicates that the disturbances at these frequencies are most likely small relative to the identified harmonics. Therefore, their omission from the model should not have a large effect on the degree of correlation between the model and the data. The harmonic numbers corresponding to the seven harmonics that are included in the radial force model are listed in Table 3.4.

The curve fit for the first harmonic, $h_1 = 1.0$, is shown in Figure 3-22. Notice that the data points are not distributed evenly across wheel speeds, but are clustered at high wheel speeds. Recall from Section 2.2.2 that when the vibration tests were conducted, full torque was applied to the wheel and it was allowed to spin up until it reached saturation around 2300 rpm. As a result, a large portion of the data was taken while the wheel was saturated at its maximum speed. Therefore, when the data was processed into quasi-steady state data

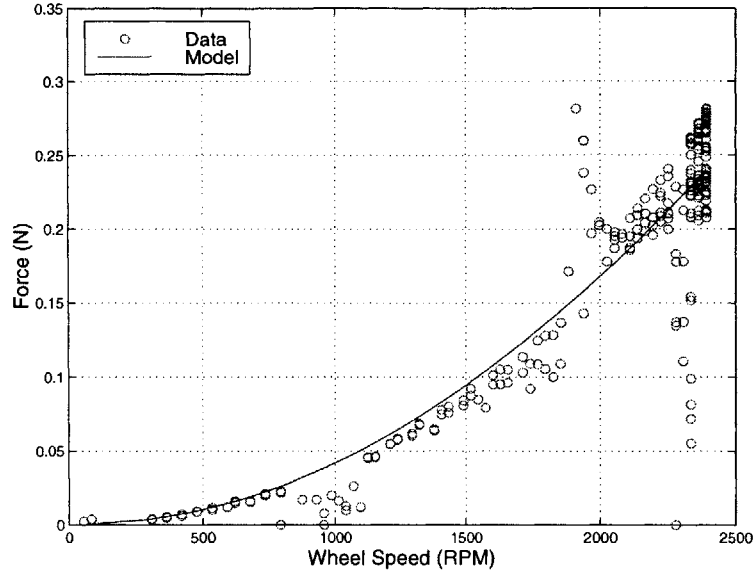


Figure 3-22: Amplitude Coefficient Curve Fit for Radial Force Harmonic, $h_1 = 1.0$

sets, the highest wheel speed was represented multiple times in the wheel speed vector and frequency domain data matrices. The algorithm used in `find_coeff.m` ensures that the uneven wheel speed distribution does not result in an unequal weighting of the data points when the amplitude coefficient is calculated. If a data point from a given wheel speed is included more than once in the vector \mathbf{D}_i , it is also included an equal number of times in $\tilde{\mathbf{\Omega}}_i$.

The coefficient curve fits for the other six harmonics are presented in Appendix A.2.1. Note that disturbance amplifications are clearly visible in all of the curve fits. Some of the curves show amplifications over multiple wheel speed ranges. For example, disturbance amplifications occur in the fit for $h_5 = 4.42$ (Figure A-8(d)) between 900 and 1100 rpm and then again between 1800 and 2150 rpm. The function `remove_mode.m` was used to isolate the amplifications and recalculate the amplitude coefficients. The results of this analyses are presented both in graphical, Figures 3-24 and 3-25, and tabular, Table 3.6, form.

Table 3.6 lists the affected speed ranges, probable amplification sources and amplitude coefficients (with and without amplification) for each of the affected harmonics. The amplification source was determined by examining the waterfall plot comparison of the radial force data and model, Figure 3-23. In this plot, the frequencies of the radial translation and rocking modes are labeled and highlighted with solid dark lines. The modal frequencies were determined using the values in Table 2.3 as a guide. The coefficient curve fit plot for

Table 3.6: Disturbance Amplification in Radial Force Harmonics

h_i	Wheel Speed Range (rpm)	Amplification Source	C_i N/rpm ² x10e ⁻⁷	C_i N/rpm ² x10e ⁻⁷
1.0	1900-2000	radial rocking (negative whirl)	0.4200	0.4155
2.0	800-1300 2200+	radial rocking (negative whirl) unknown	0.0846	0.0832
3.0	1800-2000	radial rocking (positive whirl)	0.0734	0.0543
4.0	1150-1400 2100+	radial rocking (positive whirl) unknown	0.0629	0.0621
4.42	900-1100 1800-2150	radial rocking (positive whirl) unknown	0.1188	0.1100
5.37	2200+	radial translation	0.0780	0.0524
5.57	2200+	radial translation	0.1729	0.0690

the first harmonic shows a disturbance amplification around 2000 rpm. This amplification is also visible in the waterfall plot at the same wheel speed. Note that the amplification occurs at the point where the harmonic crosses the negative whirl of the rocking mode. This observation suggests that the disturbance amplification is due to the excitation of the radial rocking mode by the first harmonic. The sources of the other amplifications are determined in this manner and listed in Table 3.6. In some cases the amplification source is listed as “unknown.” These harmonics show disturbance amplifications at high wheel speeds and frequencies that do not correspond to either of the radial modes; one example is the fifth harmonic ($h_5 = 4.42$). The source of disturbance amplification is unclear in these cases.

The data/model waterfall and RMS comparison plots are shown in Figures 3-26 and 3-27, respectively. Both the F_x and F_y waterfall plots show a very good correlation between the disturbance frequencies of the data and the model indicating that the harmonic numbers were identified accurately. It does appear that there may be some higher harmonics which were not included in the model (due to large uncertainty in the amplitude coefficients), but the most significant disturbances were captured. Figure 3-27 shows that there is a relatively good correlation between the RMS of the model and data at a majority of the wheel speeds. The RMS of the F_x data is represented by the “+” symbol, that of the

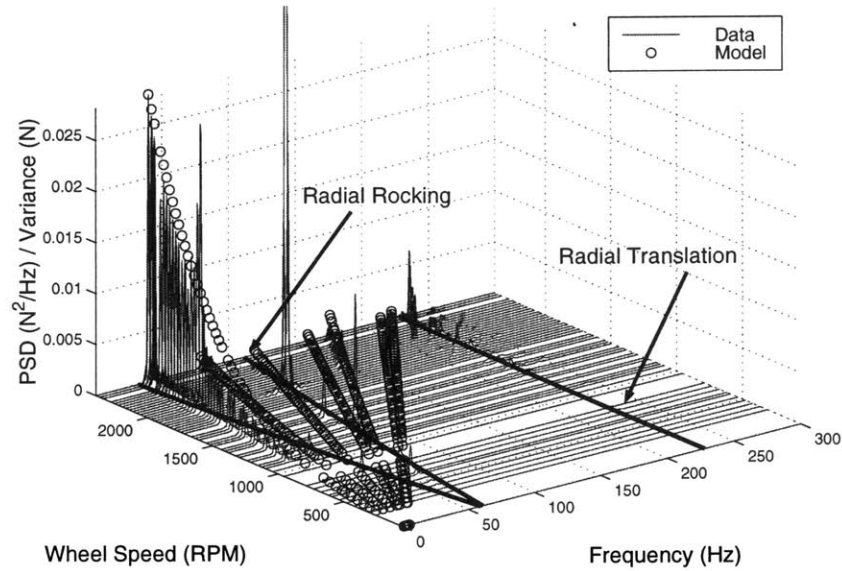
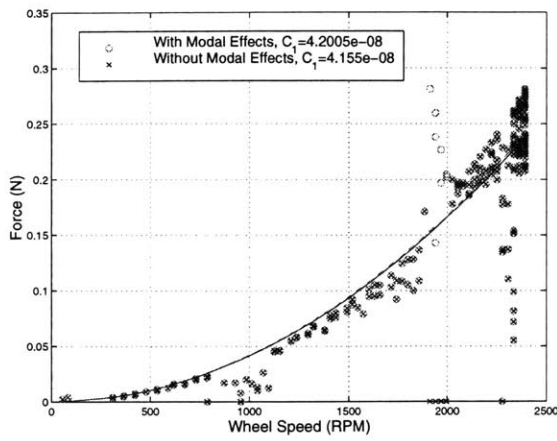


Figure 3-23: Waterfall Comparison of Radial Force Model and Ithaco E Wheel F_x Data Showing Modal Excitation

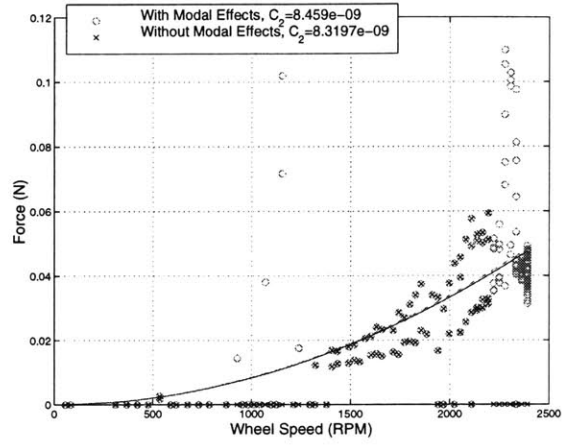
F_y data by the “*” and that of the model by circles. There was no noise data available for the Ithaco E Wheel data so the RMS of the data minus the noise could not be calculated. For most wheel speeds the model under-predicts the data slightly, but not by a significant amount. However, there is also a large amount of energy in the data between 1800 and 2000 rpm which was not captured in the model. Referring to Table 3.6, it is clear that both the first and third harmonic excite the positive whirl of the rocking mode in this wheel speed range. Therefore, a discrepancy between the data and the model in this range exists because the empirical model does not account for the structural modes of the wheel. The smaller peaks in the data RMS between 800 and 1200 rpm can also be attributed to the structural wheel modes by the same reasoning.

Radial Torques

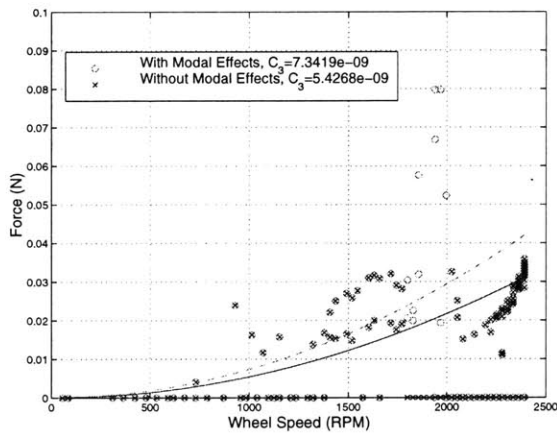
The radial torque model parameters were extracted using inputs similar to those listed in Table 3.5, with T_x substituted for F_x and T_y substituted for F_y in the subscripts. The radial torque data are similar to the radial force data so identical tolerance parameters could be used for both models. Harmonic numbers were identified with `iden_harm.m` and validated with waterfall comparisons and coefficient curve plots. A harmonic at $h_i = 5.4$ and those above 5.8 were removed from the model due to low confidence curve fits. The amplitude



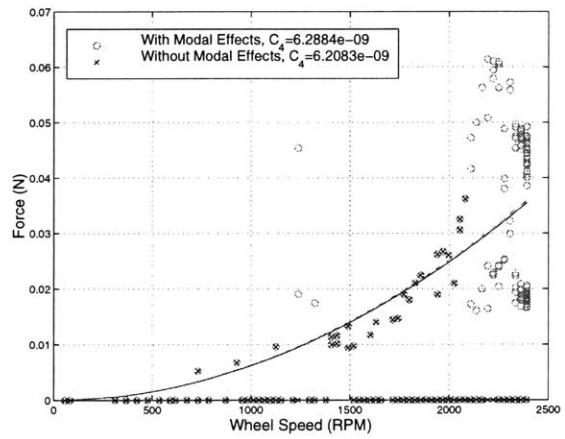
(a) $h_1 = 1.00$



(b) $h_2 = 2.00$

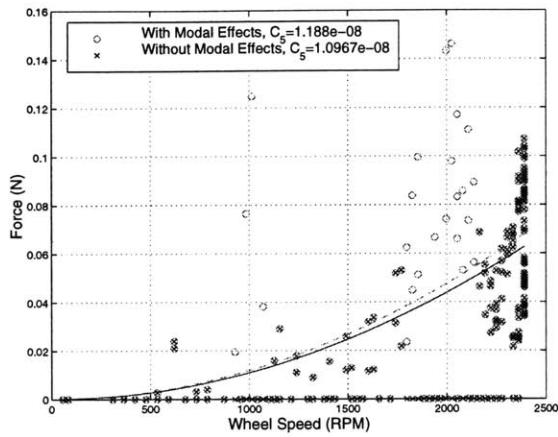


(c) $h_3 = 3.00$

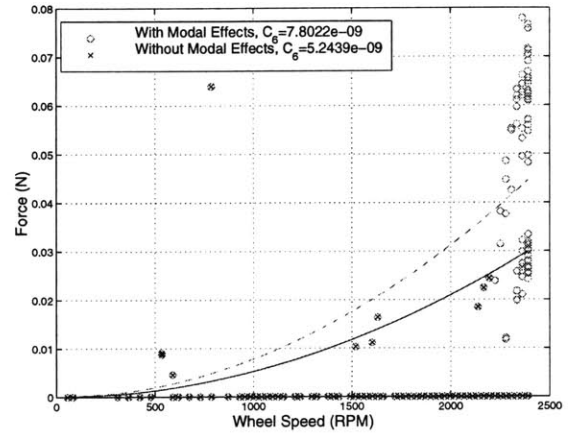


(d) $h_4 = 4.00$

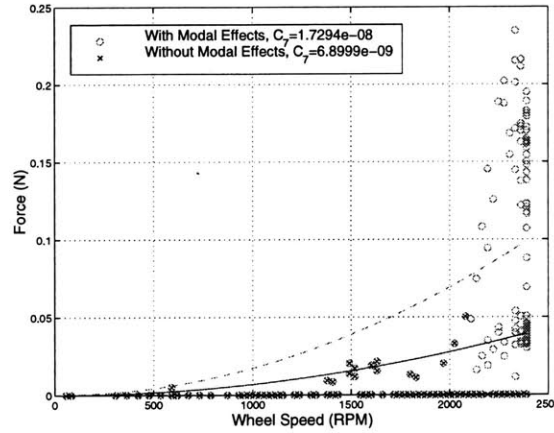
Figure 3-24: Elimination of Disturbance Amplification from Amplitude Coefficient Calculations: Ithaco E Wheel Radial Force (1)



(a) $h_5 = 4.42$



(b) $h_6 = 5.37$



(c) $h_7 = 5.57$

Figure 3-25: Elimination of Disturbance Amplification from Amplitude Coefficient Calculations: Ithaco E Wheel Radial Force (2)

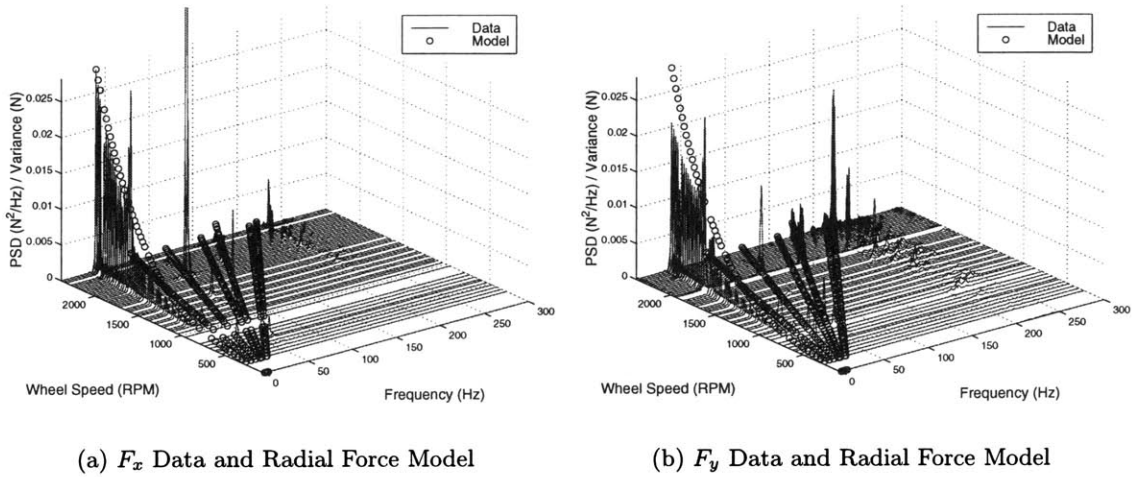


Figure 3-26: Waterfall Comparison of Radial Force Model and Ithaco E Wheel Data

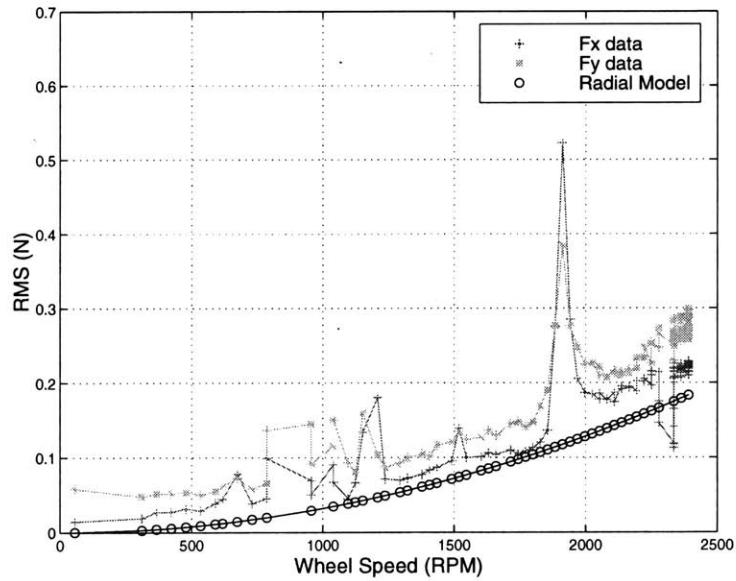


Figure 3-27: RMS Comparison of Empirical Model and Ithaco E Wheel Data: Radial Force

coefficient calculations for these harmonics are only based on a limited number of points, all of which are at high wheel speeds, as is the case with the higher radial force harmonics. The harmonic numbers for the six harmonics that are included in the radial torque model are listed in Table 3.4.

The coefficient curve fits for the initial amplitude coefficients, \bar{C}_i , are presented in Appendix A.2.2. As was the case with the radial force curve fits there is an uneven distribution of data points across wheel speeds due to the conditions of the vibration test and the pre-processing of the time histories. Also, disturbance amplification is visible in all of the harmonics, and the fifth harmonic, $h_5 = 4.42$ shows amplification over two distinct wheel speed ranges. The function `remove_mode.m` was used to isolate these disturbance amplifications and calculate new amplitude coefficients that do not include the effects of modal excitation. The results are presented in both tabular, Table 3.7, and graphical, Figure 3-29, form. Figure 3-28 is the waterfall comparison plot used to determine the sources of disturbance amplification listed in Table 3.7. It is clear from the figure that disturbance amplifications at low wheel speeds are due to excitation of the rocking mode, and that the amplification of the sixth harmonic at high wheel speeds can be attributed to excitation of the radial translation mode. There are also some unidentified dynamics occurring at high wheel speeds in the fourth and fifth harmonics. These results parallel those obtained for the radial force model.

The data/model waterfall and RMS comparison plots are shown in Figures 3-30 and 3-31. The correlation between the model and the data for the radial torques is quite similar to that observed for the radial forces. The waterfall plots show that the model harmonics lie directly on the disturbance ridges in the data indicating that the harmonic numbers were identified accurately. A few unidentified higher harmonics are visible in the data, but do not appear to be significant. In addition, Figure 3-31 shows a good correlation between the data and model RMS values across most wheel speeds. As was the case with the radial force, there are discrete wheel speed ranges over which the data RMS is much greater than the model. However, Table 3.7 confirms that these speed ranges correspond to excitations of the radial wheel modes by one or more harmonics. For example, the large peak in data RMS around 1800 rpm can be attributed to the excitation of the negative and positive whirls of the radial rocking mode by the first and third harmonics, respectively.

Table 3.7: Disturbance Amplification in Radial Torque Harmonics

h_i	Wheel Speed Range (rpm)	Amplification Source	\bar{C}_i Nm/rpm ² x10e ⁻⁷	C_i Nm/rpm ² x10e ⁻⁷
1.0	1750-2000	radial rocking (negative whirl)	0.2716	0.2205
2.0	1150-1350	radial rocking (negative whirl)	0.0624	0.0609
3.0	1800-2000	radial rocking (positive whirl)	0.0411	0.0242
4.0	2100-2375	unknown	0.0348	0.0243
4.42	900-1100 1750-2250	rocking mode (positive whirl) unknown	0.0624	0.0485
5.58	2150+	radial translation	0.0902	0.0498

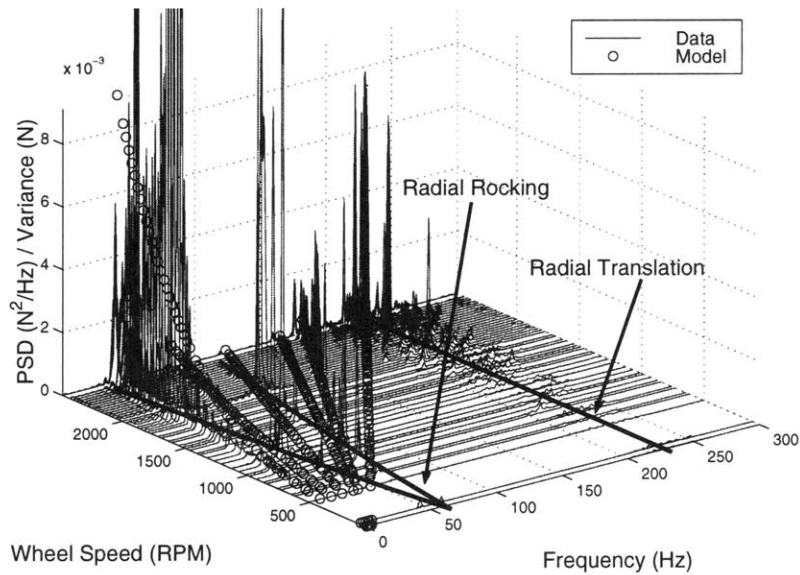
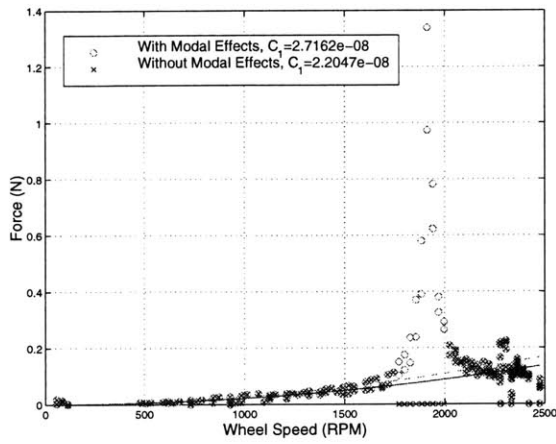
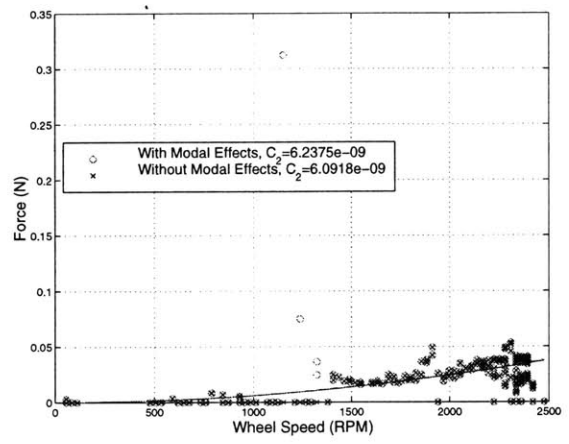


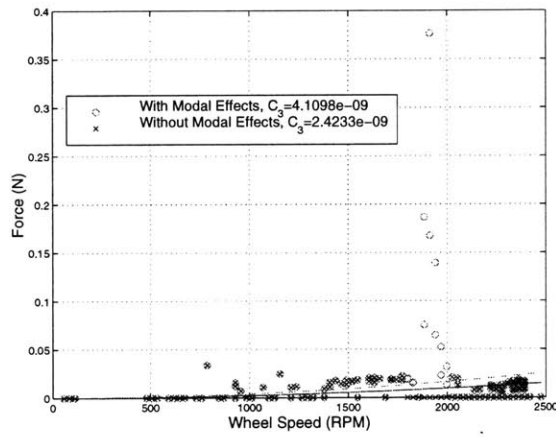
Figure 3-28: Waterfall Comparison of Radial Torque Model and Ithaco E Wheel T_x Data Showing Modal Excitation



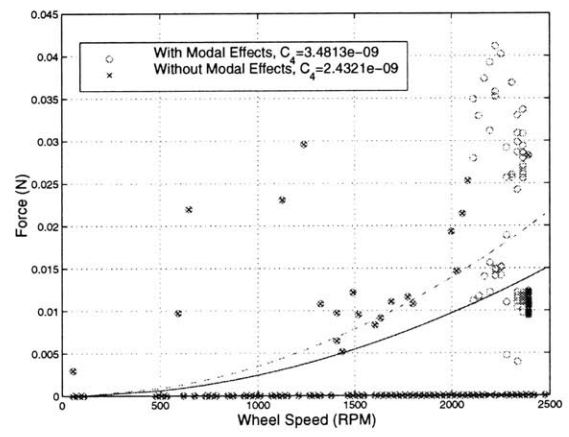
(a) $h_1 = 1.00$



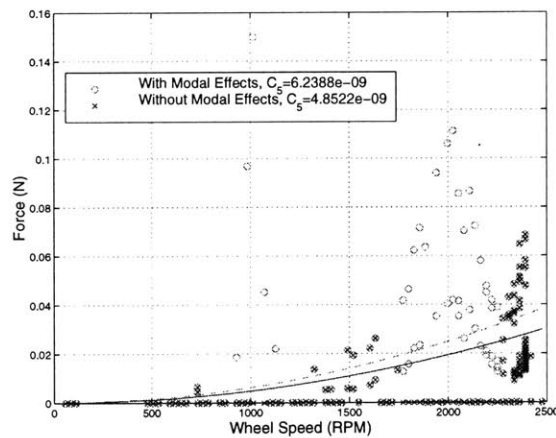
(b) $h_2 = 2.00$



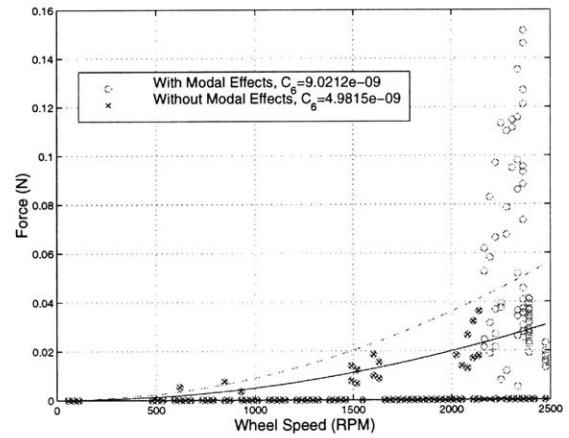
(c) $h_3 = 3.00$



(d) $h_4 = 4.00$



(e) $h_5 = 4.42$



(f) $h_6 = 5.58$

Figure 3-29: Elimination of Disturbance Amplification from Amplitude Coefficient Calculations: Ithaco E Wheel Radial Torque

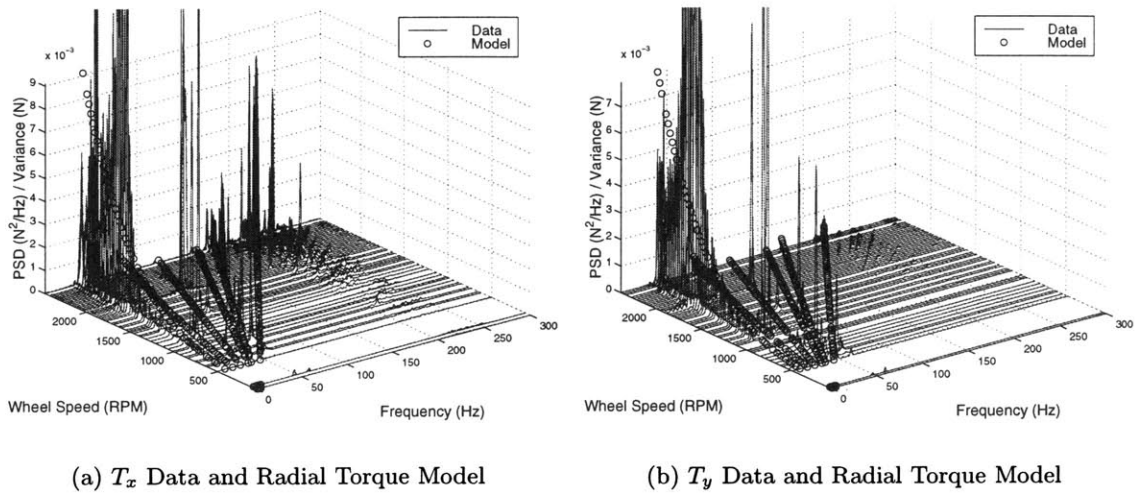


Figure 3-30: Waterfall Comparison of Radial Torque Model and Ithaco E Wheel Data

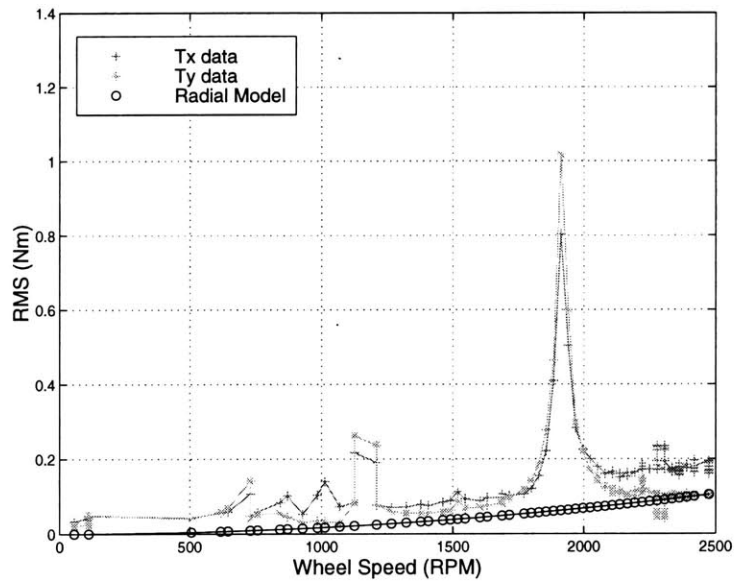


Figure 3-31: RMS Comparison of Empirical Model and Ithaco E Wheel Data: Radial Torque

Table 3.8: Inputs for Ithaco E Wheel Axial Force Modeling

Name	Description	Size/Value
m	# of wheel speeds	120
n_f	# of frequency points	640
\mathbf{f}	Frequency vector	640 x 1
f_{Lim}	Upper frequency limit	300 (Hz)
Ω_{F_z}	Wheel speeds	1 x 120
\mathbf{A}_{F_z}	Amplitude spectra	640 x 120
\mathbf{S}_{F_z}	PSDs	640 x 120
N_σ	Noise isolation tolerance	2
ϵ	Binning tolerance	0.02
P_0	Bin percentage threshold	20%

Axial Forces

The analysis of the axial force data and parameter extraction for the model closely parallels those for the radial forces and torques. The only major difference is that only one set of data is used as an input as shown in Table 3.8. Also, the bin percentage threshold, P_0 , had to be lowered to 20% in order to capture all of the harmonics. Waterfall plots and coefficient curve fits were used to choose the harmonic numbers from the list of normalized frequencies generated by `iden_harm.m`. Harmonics with numbers greater than 4.33 were eliminated from the model due to low confidence curve fits. Many of the higher harmonics only became visible when their amplitude was increased due to excitation of the radial translation mode. As a result only five harmonic numbers could be positively identified. These harmonic numbers are listed in Table 3.4.

The coefficient curve fits for the amplitude coefficients, C_i are presented in Appendix A.2.3. Disturbance amplification is visible in four of the five harmonics: 1.0, 2.0, 2.96 and 4.33. The function `remove_mode.m` was used to isolate the disturbance amplifications and recalculate the amplitude coefficients. Both the original coefficients and those resulting from `remove_mode.m` are listed in Table 3.9 along with the speed range of the amplification and its probable source. The amplification source was determined using a waterfall comparison plot such as the one in Figure 3-32. This figure is similar to those used in the modeling of the radial forces and torques (Figures 3-23 and 3-28 however now all *three* structural wheel modes, including the axial translation, are labeled in the figure and highlighted with heavy, solid lines. The frequencies of the axial translation mode was determined from Table 2.3. Disturbance amplifications due to excitation of the radial rocking and axial translation

Table 3.9: Disturbance Amplification in Axial Force Harmonics

h_i	Wheel Speed Range (rpm)	Amplification Source	C_i N/rpm ² x10e ⁻⁷	C_i N/rpm ² x10e ⁻⁷
1.0	1850-2050	radial rocking (negative whirl)	0.3335	0.3038
2.0	2100-2350	axial translation	0.3497	0.2818
2.96	1900-2000	radial rocking (positive whirl)	0.0839	0.0719
4.33	2300+	unknown	0.0218	0.0101

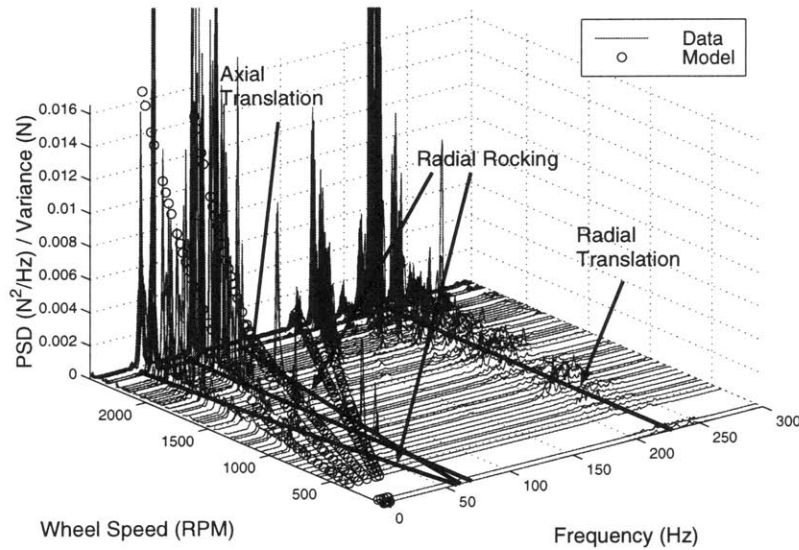
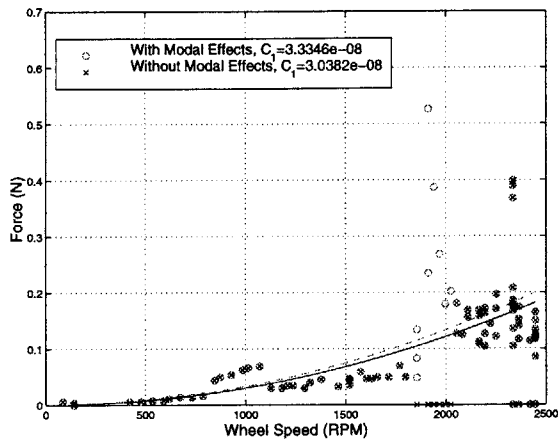


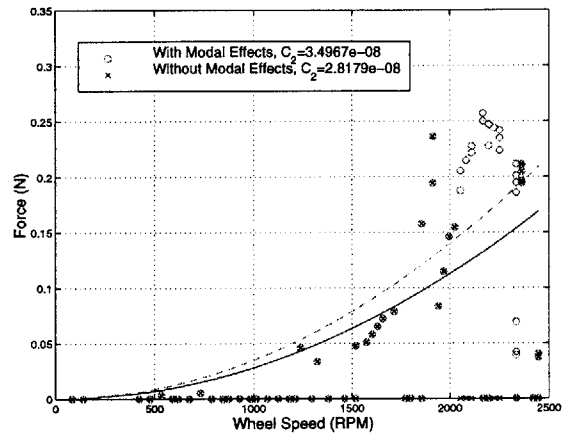
Figure 3-32: Waterfall Comparison of Axial Force Model and Ithaco E Wheel F_z Data Showing Modal Excitation

modes are clearly visible in the waterfall plot. In addition, unidentified amplifications at high speeds in the fifth harmonic $h_5 = 4.33$ are also present. These “extra” dynamics were also observed in the radial forces and torques at a similar wheel speed/frequency combination. The results listed in Table 3.9 are also presented graphically in Figure 3-33.

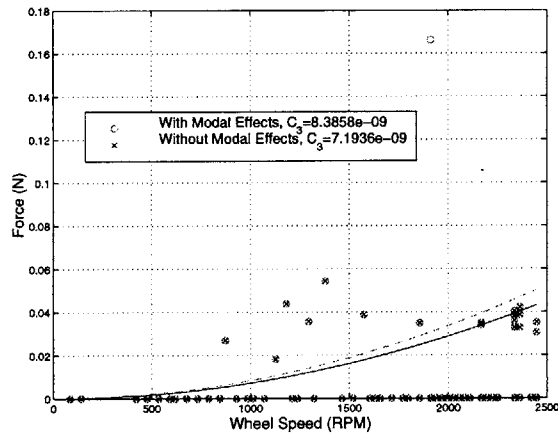
The data/model waterfall and RMS comparison plots are shown in Figures 3-34 and 3-35. The waterfall plots show good correlation between the data and model disturbance frequencies indicating that the harmonic numbers were identified accurately. As was true for both the radial forces and torques as well, there are some unidentified higher harmonics visible in the data. One difference between the axial force and the radial force/torque models is that there seems to be a very significant disturbance amplification resulting from



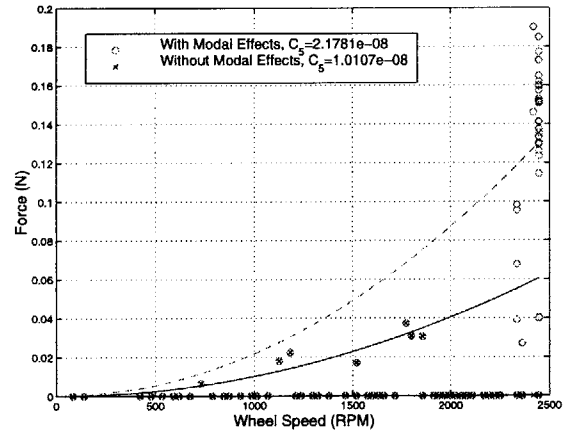
(a) $h_1 = 1.00$



(b) $h_2 = 2.00$



(c) $h_3 = 2.96$



(d) $h_4 = 4.43$

Figure 3-33: Elimination of Disturbance Amplification from Amplitude Coefficient Calculations: Ithaco E Wheel Axial Force

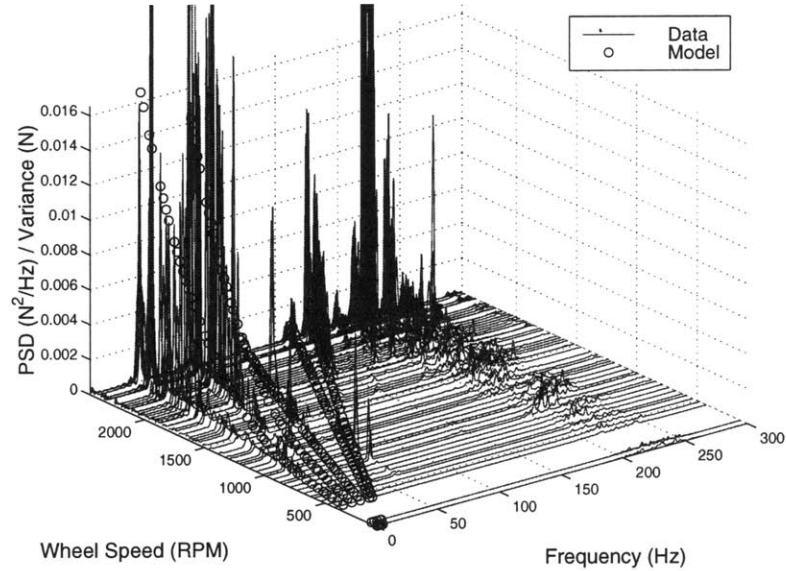


Figure 3-34: Waterfall Comparison of Axial force Model and Ithaco E Wheel F_z Data

the excitation of the radial translation mode an *unmodeled* harmonics. This discrepancy should result in a model which under-predicts the data. These results are supported by the RMS comparison, Figure 3-35. The data RMS, plotted with “*” symbols, is significantly larger than the model RMS, plotted with circles, across all wheel speeds. Note that at speeds higher than 1700 rpm this discrepancy increases. The peak in the data RMS at 1800 rpm is expected to be unmatched by the model since it is a direct result of excitation of the positive and negative whirls of the rocking mode (see Table 3.9). The additional energy after this peak is most likely due to the excitation of the radial translation mode by the unmodeled harmonics discussed earlier. The consistent discrepancy in RMS values cannot be attributed to the wheel flexibility, however, and will be examined in more detail in the next section.

3.2.3 Observations

Recall from section 3.2.1 that the RMS comparisons of the Ithaco B Wheel data and empirical model show a large discrepancy across all wheel speeds for all three disturbance directions (Figures 3-15, 3-18 and 3-21). One possible explanation for this discrepancy is disturbance amplification from interaction with the structural wheel modes, as was the case for the Ithaco E Wheel (Section 3.2.2). Since the wheel modes are not accounted for in the empirical model, it is expected that the data RMS would be higher than the model at

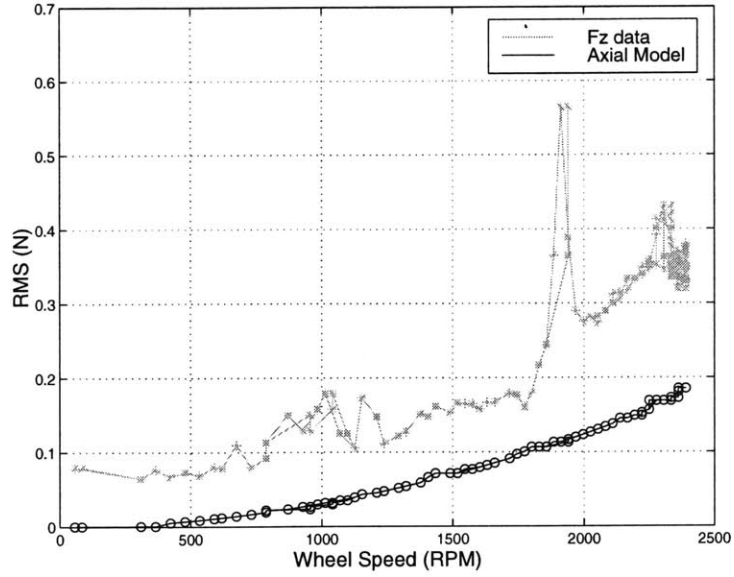
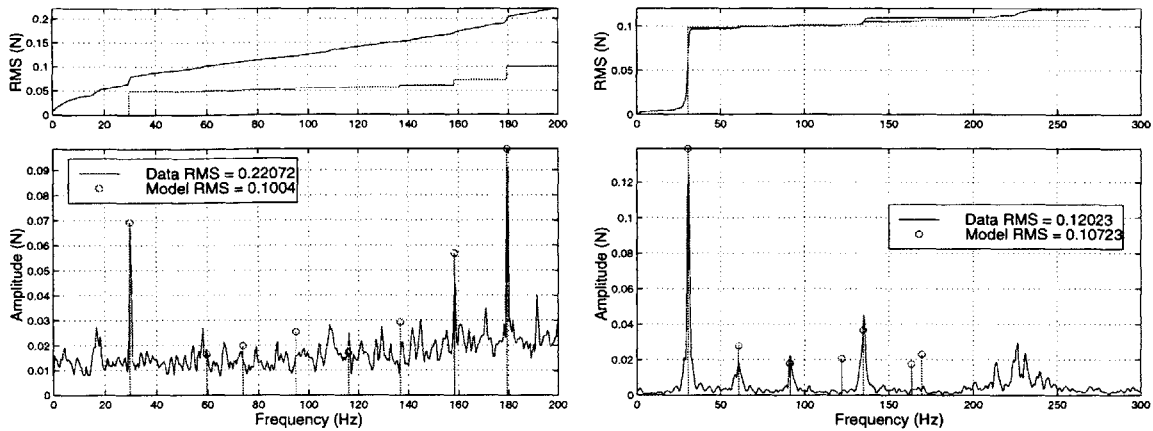


Figure 3-35: RMS Comparison of Empirical Model and Ithaco E Wheel Data: Axial Force

wheel speeds at which disturbance amplification occurs. However, that does not seem to be the case for the Ithaco B Wheel models because no significant disturbance amplification is visible in the data (besides the test stand resonance) and there is a significant difference in RMS at all wheel speeds, not just within a specific range.

A second likely source of the error is the presence of unmodeled dynamics in the data. The poor frequency resolution of the Ithaco B Wheel data makes identifying harmonics with the RWA DADM toolbox difficult in general, and disturbance harmonics that are not accounted for in the model can cause a discrepancy between the data and the model RMS values. The coefficient curve fit plots in Appendix A.1 show that for some harmonics the model curve resulting from the least squares approximation does indeed lie below the data. For an example, consider the radial force model plots in Appendix A.1.1. The fit for C_4 ($h_4=3.16$) is particularly bad, especially at high wheel speeds, while the curve fit for C_5 ($h_5 = 3.87$) severely under-predicts the data at low wheel speeds. These curve fits support the poor results shown in the RMS comparison, indicating that there are unmodeled disturbances present in the data. However, since the amplitude of the dominant harmonic, the fundamental, has been captured quite accurately (as shown in Figure 3-7(a)), it is unlikely that the omission of a few less significant harmonics would cause an error as large as those seen in the RMS plots.

The model/data correlation obtained for the Ithaco E Wheel empirical model should be



(a) Ithaco B Wheel Radial Force: 1800 rpm

(b) Ithaco E Wheel Radial Force: 1828 rpm

Figure 3-36: Model/Data Comparison Plots with Cumulative RMS Curves

considered to determine if the unmodeled disturbances are characteristic of reaction wheels, and should be incorporated into the model, or are simply the result of the conditions of the Ithaco B Wheel vibration test. If the RMS discrepancy is indeed due to a modeling oversight, a similar trend should be observable in the Ithaco E Wheel data/model comparisons. However recall from Section 3.2.2 and Figures 3-27, 3-31 and 3-35 that the model/data correlation for the Ithaco E Wheel RMS values was actually quite good over most wheel speeds. The only large discrepancies occur over speeds at which the wheel harmonics excited the structural modes. This result is a good indication that the poor model/data correlation seen in the B Wheel model is vibration test related and not due to the empirical model.

Model/data comparisons at about 1800 rpm for both the B and E wheels are shown in Figure 3-36. The cumulative RMS curves in the upper plots allow a good comparison of the data correlation for the two different wheels. Note that although the amplitude spectra for the Ithaco B Wheel model and data, Figure 3-36(a), show a reasonable matching of the harmonic disturbances, the cumulative RMS curves are widely different. The large amount of energy present in the data at low frequencies could be the result of load cell drift that may have occurred during data acquisition. However, it should also be noted that the difference between the two curves increases with frequency indicating that a broadband noise or disturbance component may be contributing to the data RMS. The source of this additional energy and its relationship to the wheel speed (if any) is unknown. In contrast both the amplitude spectra comparison and cumulative RMS curves for the Ithaco E Wheel,

Figure 3-36(b), match well. The first harmonic is the largest contributor to the RMS in both the data and the model and its amplitude has been captured in the model quite accurately. There is a slight discrepancy in the RMS values at high frequencies which is most likely due to harmonics which could not be included in the model due to low confidence amplitude coefficient curve fits. These results indicate that the empirical model captures the harmonic RWA disturbances reasonably well.

3.3 Summary

An empirical RWA disturbance model that was developed for the HST RWA and assumes that RWA disturbances are a series of discrete harmonics with amplitudes proportional to the wheel speed squared has been reviewed. A MATLAB tool for extracting the model parameters, harmonic numbers and amplitude coefficients, from steady-state RWA vibration data has been developed and presented in detail. The toolbox consists of four main functions and allows the creation of an empirical model for any reaction wheel for which vibration data exists. The toolbox was used to create empirical models for two different Ithaco wheels: a B type and an E type. The model/data correlation for the Ithaco B Wheel shows the presence of broadband dynamics in the disturbance data which were not captured by the empirical model, but are believed to be specific to this data set and possibly due to the conditions under which the vibration test was conducted. The Ithaco E Wheel model, on the other hand, correlates well with the data over all frequencies except those at which disturbance amplifications are caused by excitation of the structural wheel modes. In some cases, these amplifications can be quite large causing the empirical model to severely under-predict the disturbance. Therefore, in order to obtain an accurate disturbance model the internal flexibility of the RWA must be taken into account. In the next chapter a second, physical model is developed to capture the interactions between the harmonic disturbances and the structural wheel modes.

Chapter 4

Analytical Model

It has been shown that the empirical model captures the harmonic quality of reaction wheel disturbances and a MATLAB toolbox has been developed which accurately identifies the disturbance frequencies and provides an estimate for the amplitudes. The Ithaco E Wheel data was used to validate the model, and it was shown that the empirical model correlated well to the data over most wheel speeds. However, large discrepancies were seen between the model and data at particular wheel speeds. It was found that the model severely under-predicts the data for speeds at which interactions occur between the harmonics and the structural wheel modes. This discrepancy occurs because the empirical model does not account for the internal flexibility in the wheel. Therefore, a non-linear, analytical RWA disturbance model which captures the structural modes of the wheel and the effects of the fundamental harmonic has been developed. This model is then extended to include all the wheel harmonics using the amplitude coefficients and harmonic numbers from the empirical model.

The development of the analytical model is presented in the following sections. First the modeling methodology is discussed in detail and the equations of motion are derived and solved to obtain the steady state solutions for the spinning wheel. Then the model is extended to include the higher harmonics obtained with the RWA DADM. Finally preliminary simulation results are presented and methods of choosing the model parameters to fit the data are discussed. Further development is needed to complete the analytical model. At the end of the chapter modeling issues are presented and recommendations are made for future work.

4.1 Model Development

The RWA is modeled as a balanced flywheel rotating on a rigid shaft. Linear springs and dampers are added to model shaft and bearing flexibility. The most significant disturbance source, flywheel imbalance, is modeled with lumped masses that are positioned strategically on the wheel. The equations of motion of the full system are solved using energy methods in a series of stages. First, the problem of a balanced, rotating flywheel on flexible supports is solved. Then, the static and dynamic imbalance masses are added to the flywheel to complete the model.

4.1.1 Balanced Wheel: Rocking and Radial Modes

The problem of a balanced flywheel on flexible supports, shown in Figure 4-1, is considered first to capture the radial modes (translation and rocking) and gyroscopic stiffening of the wheel. The flywheel of mass, M , and radius, R , is centered axially on a shaft of length, $2d$. Flexibility in the shaft and bearings is modeled with four linear springs of stiffness $\frac{k}{2}$ located at a distance d_k from the center of the wheel. Damping is added by linear dashpots, with damping coefficient $\frac{c}{2}$ placed in parallel with the springs at a distance d_c from the center of the wheel. This model is also used in rotor dynamics and is discussed in detail in [24].

Euler angles are used to define the rigid body rotations of the wheel and relate one coordinate frame to another. The wheel is free to rotate about three different axes as shown in Figure 4-2. The first rotation, ϕ , is about the \mathbf{Y} -axis of the ground-fixed, inertial frame, \mathbf{XYZ} and defines the intermediate reference frame, \mathbf{abc} . The next rotation, θ , which is about the \mathbf{a} -axis, defines the rocking frame, $\mathbf{x'y'z'}$, which is rotating in both ϕ and θ with respect to ground. The final rotation, ψ , is about the \mathbf{z}' -axis. This rotation represents the spinning of the wheel and defines the final, body-fixed frame, \mathbf{xyz} . These coordinate frames and the transformations between them are presented in tabular form as well in Figure 4-2

Energy methods require that expressions for the kinetic and potential energies of the system and the external work done on the system be obtained in terms of the generalized coordinates, ξ_i . Kinetic energy is defined as:

$$T = \frac{1}{2}\omega^T \mathbf{I}\omega + \frac{1}{2}M\mathbf{v}^T \mathbf{v} \quad (4.1)$$

where \mathbf{I} is the inertia tensor and ω and v are angular and translational velocities, respec-

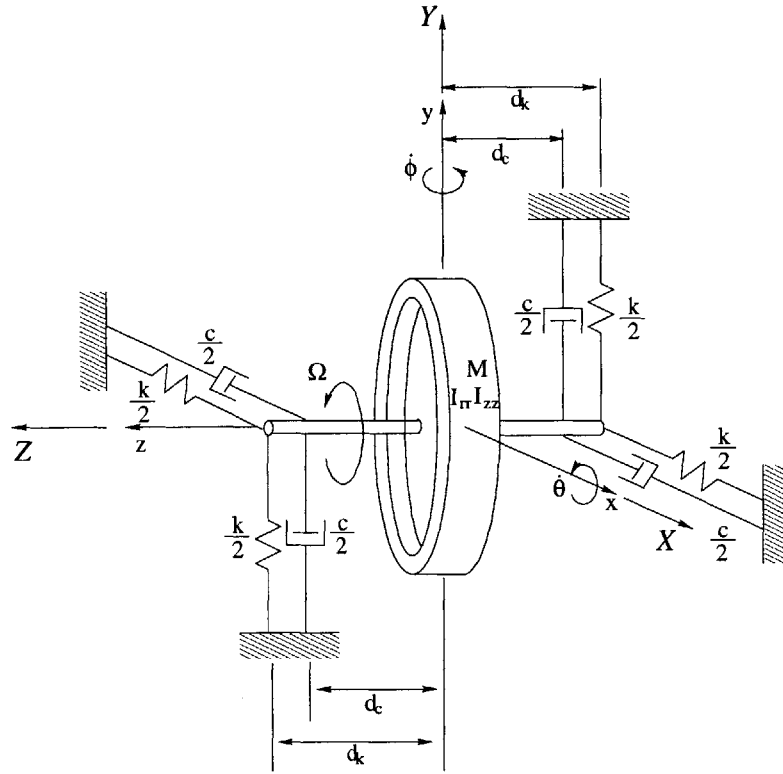
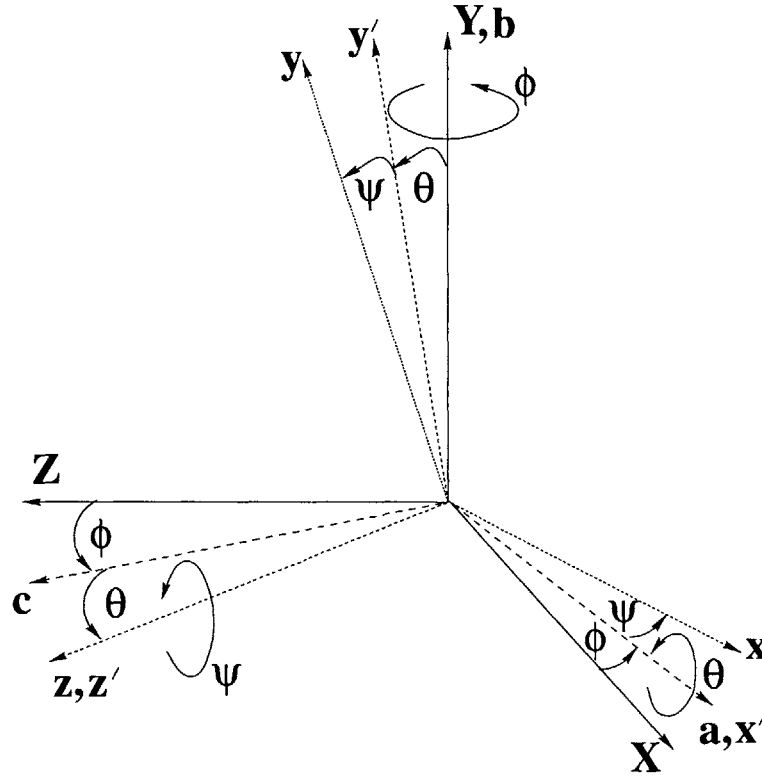


Figure 4-1: Model of Balanced Flywheel on Flexible Supports

tively. As discussed above, the wheel has three rotational degrees of freedom, θ , ϕ and ψ . However, it is assumed that the wheel is spinning about its spin axis, \mathbf{z}' , with a constant angular velocity, $\dot{\psi} = \Omega$. Therefore, there are only two generalized rotations, θ and ϕ . The angular velocity of the wheel in terms of the generalized rotations and the constant spin rate is obtained by inspection from the Euler angle rotations shown in Figure 4-2:

$$\boldsymbol{\omega} = \dot{\theta} \hat{\mathbf{u}}_{\mathbf{a}} + \dot{\phi} \hat{\mathbf{u}}_{\mathbf{Y}} + \Omega \hat{\mathbf{u}}_{\mathbf{z}'} \quad (4.2)$$

Note that Equation 4.2 contains components from multiple coordinate frames. In order to properly find the kinetic energy of the system, the angular velocity must be written in terms of only one coordinate frame. Since the balanced flywheel is axisymmetric, the kinetic energy can be written in the rocking frame, $\mathbf{x}'\mathbf{y}'\mathbf{z}'$. The transformations listed in Figure 4-2



Reference Frame	Description	Transformation		
		x	y	z
XYZ	Ground-fixed, inertial frame	\hat{u}_X	\hat{u}_Y	\hat{u}_Z
abc	Intermediate frame	$c\phi\hat{u}_X - s\phi\hat{u}_Z$	\hat{u}_Y	$s\phi\hat{u}_X + c\phi\hat{u}_Z$
x'y'z'	Rocking frame	\hat{u}_a	$c\theta\hat{u}_b + s\theta\hat{u}_c$	$c\theta\hat{u}_c - s\theta\hat{u}_b$
xyz	Body-fixed frame	$c\psi\hat{u}_{x'} + s\psi\hat{u}_{y'}$	$c\psi\hat{u}_{y'} - s\psi\hat{u}_{x'}$	$\hat{u}_{z'}$

\hat{u} = unit vector, $c = \cos$, $s = \sin$

Figure 4-2: Euler Angle Rotations and Coordinate Frame Transformations for Balanced Wheel

are substituted into Equation 4.2 to obtain, in vector form:

$$\omega_{\mathbf{x}'\mathbf{y}'\mathbf{z}'} = \begin{pmatrix} \dot{\theta} \\ \dot{\phi} \cos \theta \\ \Omega - \dot{\phi} \sin \theta \end{pmatrix} \quad (4.3)$$

The inertia tensor of the flywheel in the rocking frame can be written in terms of the principle moments of inertial of the wheel:

$$\mathbf{I}_{\mathbf{x}'\mathbf{y}'\mathbf{z}'} = \begin{bmatrix} I_{rr} & 0 & 0 \\ 0 & I_{rr} & 0 \\ 0 & 0 & I_{zz} \end{bmatrix} \quad (4.4)$$

where I_{rr} and I_{zz} are the radial and polar moments of inertia, and for a uniform disc:

$$I_{rr} = \frac{1}{2}MR^2 \quad I_{zz} = \frac{1}{4}MR^2 \quad (4.5)$$

The flywheel also has two translational degrees of freedom, x and y , which describe the motion of the center of mass of the wheel in the \mathbf{X} and \mathbf{Y} directions as shown in Figure 4-1. The translational velocity in terms of the generalized translations is:

$$\mathbf{v}_{\mathbf{x}'\mathbf{y}'\mathbf{z}'} = \begin{pmatrix} \dot{x} \\ \dot{y} \\ 0 \end{pmatrix} \quad (4.6)$$

Finally, the kinetic energy of the flywheel is obtained by substituting Equations 4.3-4.6 into Equation 4.1:

$$T_w = \frac{1}{2} \left[(\dot{\theta}^2 + \dot{\phi}^2 \cos^2 \theta) I_{rr} + (\Omega - \dot{\phi} \sin \theta)^2 I_{zz} + M (\dot{x}^2 + \dot{y}^2) \right] \quad (4.7)$$

The potential energy of the flywheel is stored in the springs and can be written by inspection:

$$V = \frac{k}{4} \left[(x + d_k \sin \phi)^2 + (x - d_k \sin \phi)^2 + (y + d_k \sin \theta)^2 + (y - d_k \sin \theta)^2 \right] \quad (4.8)$$

However, since the wheel is centered axially on the shaft, Equation 4.8 reduces to:

$$V = \frac{k}{2} \left[d_k^2 (\sin^2 \theta + \sin^2 \phi) + x^2 + y^2 \right] \quad (4.9)$$

The external work done on the wheel by the dashpots must also be taken into account. It can be written in terms of the generalized coordinates and their variations:

$$\begin{aligned} \delta W = & -\frac{c}{2} \left[(\dot{y} + \dot{\theta} d_c \cos \theta)(\delta y + \delta \theta d_c \cos \theta) + (\dot{y} - \dot{\theta} d_c \cos \theta)(\delta y - \delta \theta d_c \cos \theta) \right. \\ & \left. + (\dot{x} + \dot{\phi} d_c \cos \phi)(\delta x + \delta \phi d_c \cos \phi) + (\dot{x} - \dot{\phi} d_c \cos \phi)(\delta x - \delta \phi d_c \cos \phi) \right] \end{aligned} \quad (4.10)$$

which, due to symmetry reduces to:

$$\delta W = -c \left[\dot{y} \delta y + \dot{x} \delta x + d_c^2 (\dot{\theta} \cos^2 \theta \delta \theta + \dot{\phi} \cos^2 \phi \delta \phi) \right] \quad (4.11)$$

The equations of motion are derived using Equations 4.7, 4.9, 4.11 and Lagrangian methods. First the Lagrangian:

$$\mathcal{L} (\xi_1 \dots \xi_n, \dot{\xi}_1 \dots \dot{\xi}_n, t) = T - V \quad (4.12)$$

is formed:

$$\begin{aligned} \mathcal{L}_w = & \frac{1}{2} \left\{ (\dot{\theta}^2 + \dot{\phi}^2 \cos^2 \theta) I_{rr} + (\Omega - \dot{\phi} \sin \theta)^2 I_{zz} + M (\dot{x}^2 + \dot{y}^2) \right. \\ & \left. - k \left[d_k^2 (\sin^2 \theta + \sin^2 \phi) + x^2 + y^2 \right] \right\} \end{aligned} \quad (4.13)$$

where the subscript w indicates that this is the Lagrangian for the balanced wheel only. The equations of motion are then obtained by differentiating \mathcal{L}_w with respect to the generalized coordinates and their derivatives and accounting for the external work.

$$\frac{d}{dt} \left(\frac{\partial \mathcal{L}_w}{\partial \dot{x}} \right) - \frac{\partial \mathcal{L}_w}{\partial x} = -c\dot{x} \quad (4.14)$$

$$\frac{d}{dt} \left(\frac{\partial \mathcal{L}_w}{\partial \dot{y}} \right) - \frac{\partial \mathcal{L}_w}{\partial y} = -c\dot{y} \quad (4.15)$$

$$\frac{d}{dt} \left(\frac{\partial \mathcal{L}_w}{\partial \dot{\theta}} \right) - \frac{\partial \mathcal{L}_w}{\partial \theta} = -cd_c^2 \dot{\theta} \cos^2 \theta \quad (4.16)$$

$$\frac{d}{dt} \left(\frac{\partial \mathcal{L}_w}{\partial \dot{\phi}} \right) - \frac{\partial \mathcal{L}_w}{\partial \phi} = -cd_c^2 \dot{\phi} \cos^2 \phi \quad (4.17)$$

The equations of motion resulting from Equations 4.14-4.17 can be linearized assuming small motion about x , y , θ and ϕ . The translational and rotational degrees of freedom are decoupled (due to the assumed symmetry in the model) and can be considered separately. The equations of motion for the generalized translations are:

$$\begin{bmatrix} M & 0 \\ 0 & M \end{bmatrix} \begin{Bmatrix} \ddot{x} \\ \ddot{y} \end{Bmatrix} + \begin{bmatrix} c & 0 \\ 0 & c \end{bmatrix} \begin{Bmatrix} \dot{x} \\ \dot{y} \end{Bmatrix} + \begin{bmatrix} k & 0 \\ 0 & k \end{bmatrix} \begin{Bmatrix} x \\ y \end{Bmatrix} = \mathbf{0} \quad (4.18)$$

and those for the generalized rotations are:

$$\begin{bmatrix} I_{rr} & 0 \\ 0 & I_{rr} \end{bmatrix} \begin{Bmatrix} \ddot{\theta} \\ \ddot{\phi} \end{Bmatrix} + \begin{bmatrix} c_\theta & \Omega I_{zz} \\ -\Omega I_{zz} & c_\theta \end{bmatrix} \begin{Bmatrix} \dot{\theta} \\ \dot{\phi} \end{Bmatrix} + \begin{bmatrix} kd^2 & 0 \\ 0 & kd^2 \end{bmatrix} \begin{Bmatrix} \theta \\ \phi \end{Bmatrix} = \mathbf{0} \quad (4.19)$$

where k_θ and c_θ are the torsional stiffness and damping, respectively:

$$k_\theta = kd_k^2 \qquad c_\theta = cd_c^2 \quad (4.20)$$

The natural frequencies of the balanced wheel can be determined from the homogeneous solutions of the equations of motion. The natural frequency of the radial translation mode, $\omega_T = \sqrt{\frac{k}{M}}$, is obtained by setting $c = 0$ and solving for the eigenvalues in Equation 4.18.

The frequencies of the rotational modes are found by assuming that the solutions to Equation 4.19 are of the form, $\theta = Ae^{i\omega t}$ and $\phi = Be^{i\omega t}$. Substituting into Equation 4.19, setting $c_\theta = 0$, and solving for ω gives two rotational natural frequencies:

$$\omega_{1,2} = \mp \frac{\Omega I_{zz}}{2I_{rr}} + \sqrt{\left(\frac{\Omega I_{zz}}{2I_{rr}}\right)^2 + \frac{kd_k^2}{I_{rr}}} \quad (4.21)$$

Note that $\omega_{1,2}$ are dependent on the spin rate of the wheel, Ω . The gyroscopic precession of the flywheel and the flexibility of the shaft creates a rocking mode which splits into the two frequencies shown in Equation 4.21. When the precession of the wheel is opposed to its rotation, this mode will destiffen as the wheel speed increases (ω_1). This branch of the rocking mode is called the counter-rotating, or negative whirl mode. However, if the precession is in the same direction as the spin, the mode stiffens with increasing wheel speed, (ω_2) creating the co-rotating, or positive whirl, mode [24]. This effect, called gyroscopic stiffening, is responsible for the V-shaped mode that is visible in the low frequency Ithaco

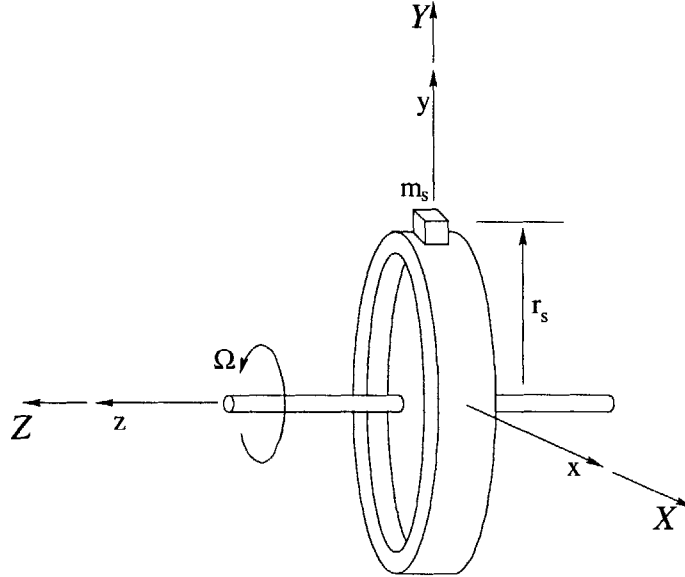


Figure 4-3: Model of Static Wheel Imbalance

E Wheel data (Figure 2-8(b)).

4.1.2 Static Imbalance

The balanced wheel and flexible shaft model (Figure 4-1) captures the radial translation and rocking modes of the wheel. The static imbalance must be added to model the radial force disturbances of the rotating wheel. Static imbalance is caused by the offset of the center of mass of the wheel from the axis of rotation. It is most easily modeled as a small mass, m_s , placed at a radius, r_s , on the wheel as shown in Figure 4-3 [16].

Assuming that the mass, m_s is a point mass, its kinetic energy, T_{m_s} , is defined only in terms of its translational velocity, \mathbf{v}_{m_s} with respect to ground (see Equation 4.1). An expression for \mathbf{v}_{m_s} is obtained by first determining the position of the mass on the wheel in the \mathbf{XYZ} frame. The mass is located on the \mathbf{y} -axis of the body-fixed frame as shown in Figure 4-3, and its position in this frame can be written as:

$$\mathbf{u}_{m_s} = \left\{ \begin{matrix} 0 & r_s & 0 \end{matrix} \right\}^T \quad (4.22)$$

The direction cosine matrix that transforms a point from the wheel-fixed frame to the inertial, ground-fixed frame is derived using the Euler angle rotation transformations listed

in Figure 4-2:

$$\Phi = \begin{bmatrix} s\phi s\theta s(\Omega t) + c\phi c(\Omega t) & s\phi s\theta c(\Omega t) - c\phi s(\Omega t) & c\theta s\phi \\ c\theta s(\Omega t) & c\theta c(\Omega t) & -s\theta \\ -s\phi c(\Omega t) + s\theta c\phi s(\Omega t) & s\phi s(\Omega t) + s\theta c\phi c(\Omega t) & c\theta c\phi \end{bmatrix} \quad (4.23)$$

where $c = \cos$, and $s = \sin$. Recall that the center of the wheel is also free to translate in the \mathbf{X} and \mathbf{Y} directions, as described by the vector Δ :

$$\Delta = \left\{ \begin{matrix} x & y & 0 \end{matrix} \right\}^T \quad (4.24)$$

Since the static imbalance mass is attached to the wheel, it also undergoes these translations, and its position in the inertial reference frame, \mathbf{U}_{m_s} , can be fully described by:

$$\mathbf{U}_{m_s} = \Phi \mathbf{u}_{m_s} + \Delta \quad (4.25)$$

Substituting Equations 4.22, 4.23 and 4.24 into Equation 4.25, results in the following expression for \mathbf{U}_{m_s} in terms of the generalized coordinates:

$$\mathbf{U}_{m_s} = \left\{ \begin{matrix} r_s(\sin \phi \sin \theta \cos(\Omega t) - \cos \phi \sin(\Omega t)) + x \\ r_s \cos \theta \cos(\Omega t) + y \\ r_s(\sin \phi \sin(\Omega t) + \cos \phi \sin \theta \cos(\Omega t)) \end{matrix} \right\} \quad (4.26)$$

Then, the velocity of the static imbalance mass in the inertial reference frame, \mathbf{v}_{m_s} is obtained by differentiating \mathbf{U}_{m_s} . Substitution of the resulting vector into Equation 4.1 gives the following expression for the kinetic energy:

$$\begin{aligned} T_{m_s} &= \frac{m_s}{2} \left\{ \dot{x}^2 + \dot{y}^2 + r_s^2 \left[\dot{\phi}^2 \left(1 - \cos^2 \theta \cos^2(\Omega t) \right) + \dot{\theta}^2 \cos^2(\Omega t) + \Omega^2 \right] \right. \\ &\quad - 2r_s \dot{y} \left(\dot{\theta} \sin \theta \cos(\Omega t) + \Omega \cos \theta \sin(\Omega t) \right) + 2r_s^2 \dot{\phi} \left(-\Omega \sin \theta + \dot{\theta} \cos \theta \cos(\Omega t) \sin(\Omega t) \right) \\ &\quad + 2r_s \dot{x} \left[\dot{\theta} \sin \phi \cos \theta \cos(\Omega t) - \Omega (\cos \phi \cos(-\Omega t) + \sin \phi \sin \theta \sin(\Omega t)) \right. \\ &\quad \left. \left. + \dot{\phi} (\cos \phi \sin \theta \cos(\Omega t) + \sin \phi \sin(\Omega t)) \right] \right\} \quad (4.27) \end{aligned}$$

The kinetic energy of the static imbalance mass, Equation 4.27, is combined with that of the wheel, Equation 4.7, to obtain the kinetic energy of the complete system. The

Lagrangian of the system, \mathcal{L}_{m_s} , is found using Equation 4.12:

$$\begin{aligned}
\mathcal{L}_{m_s} = & \frac{1}{2} \left\{ (M + m_s) (\dot{x}^2 + \dot{y}^2) + \dot{\theta}^2 (r_s^2 \cos^2(\Omega t) + Irr) + \dot{\phi}^2 (r_s^2 (1 - \cos^2(\Omega t) \cos^2 \theta) \right. \\
& + I_{zz} \sin^2 \theta) + (r_s^2 + I_{zz}) \Omega^2 - 2r_s \dot{y} (\dot{\theta} \sin \theta \cos(\Omega t) + \Omega \cos \theta \sin(\Omega t)) \\
& + 2r_s \dot{x} (\dot{\theta} \sin \phi \cos \theta \cos(\Omega t) - \Omega (\cos \phi \cos(\Omega t) + \sin \phi \sin \theta \sin(\Omega t))) + \\
& + \dot{\phi} (\cos \phi \sin \theta \cos(\Omega t) + \sin \phi \sin(\Omega t)) \left. \right\} + 2\dot{\phi} (r_s^2 (\dot{\theta} \cos \theta \cos(\Omega t) \sin(\Omega t) \\
& - \Omega \sin \theta) - I_{zz} \Omega \sin \theta) - k [d^2 (\sin^2 \theta + \sin^2 \phi) + x^2 + y^2] \left. \right\} \quad (4.28)
\end{aligned}$$

where the subscript m_s indicates that the Lagrangian corresponds to the model of the wheel and static imbalance mass. The equations of motion for the statically imbalanced flywheel are derived by substituting \mathcal{L}_{m_s} for \mathcal{L}_w in Equations 4.14-4.17 and linearizing about small translations and rotations. The generalized translations are described by:

$$\begin{bmatrix} \tilde{M} & 0 \\ 0 & \tilde{M} \end{bmatrix} \begin{Bmatrix} \ddot{x} \\ \ddot{y} \end{Bmatrix} + \begin{bmatrix} c & 0 \\ 0 & c \end{bmatrix} \begin{Bmatrix} \dot{x} \\ \dot{y} \end{Bmatrix} + \begin{bmatrix} k & 0 \\ 0 & k \end{bmatrix} \begin{Bmatrix} x \\ y \end{Bmatrix} = \mathcal{U}_s \Omega^2 \begin{Bmatrix} -\sin(\Omega t) \\ \cos(\Omega t) \end{Bmatrix} \quad (4.29)$$

where $\tilde{M} = M + m_s$ and the static imbalance is defined as:

$$\mathcal{U}_s = m_s r_s \quad (4.30)$$

The addition of the static imbalance to the model results in a driving term in the translational equations of motion which is proportional to the wheel speed squared, Ω^2 . Recall that the rotational and translational degrees of freedom are decoupled for this model. As a result, the addition of the static imbalance mass does not affect the generalized rotations since the inertia of the flywheel is not changed significantly and the principle axis of maximum inertia remains aligned with the spin axis of the flywheel.

4.1.3 Dynamic Imbalance

Recall from Chapter 1 that a flywheel can be both statically and dynamically imbalanced. To complete the analytical model, dynamic imbalance must be added to the wheel to capture the radial torque disturbances. Physically, dynamic imbalance is caused by angular misalignment of the principle axis of the wheel and the spin axis. It is modeled as two equal

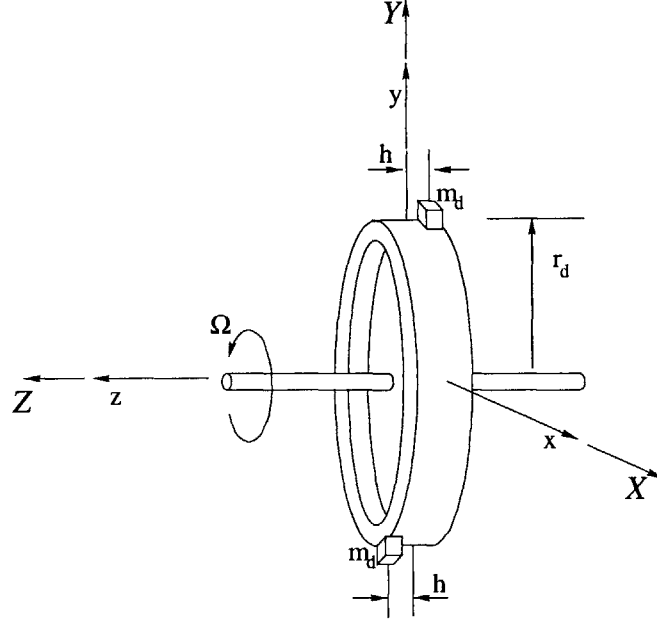


Figure 4-4: Model Dynamic Wheel Imbalance

masses, m_d , placed 180° apart at a radial distance, r_d , and an axial distance, h from the center of the flywheel as shown in Figure 4-4 [16]. The dynamic imbalance is incorporated into the model with the same methods used for the static imbalance.

The dynamic imbalance masses are point masses, and their kinetic energy can be fully described by their translational velocities, $\mathbf{v}_{m_{d_1}}$ and $\mathbf{v}_{m_{d_2}}$. Expressions for the velocities are obtained from the positions of the two masses in \mathbf{XYZ} . As shown in Figure 4-4 the dynamic imbalance masses are located on the y -axis of the wheel, and their positions in the body-fixed frame are:

$$\mathbf{u}_{m_{d_1}} = \left\{ \begin{array}{ccc} 0 & r_d & -h \end{array} \right\}^T \quad (4.31)$$

$$\mathbf{u}_{m_{d_2}} = \left\{ \begin{array}{ccc} 0 & -r_d & h \end{array} \right\}^T \quad (4.32)$$

The transformation matrix, Φ (Equation 4.23), and the translational motion of the center of mass of the wheel, Δ (Equation 4.24), is used to determine the positions of the imbalance masses in the ground-fixed reference frame:

$$\mathbf{U}_{m_{d_1}} = \Phi \mathbf{u}_{m_{d_1}} + \Delta \quad (4.33)$$

$$\mathbf{U}_{m_{d_2}} = \Phi \mathbf{u}_{m_{d_2}} + \Delta \quad (4.34)$$

Substituting Equations 4.31-4.32 and 4.24 into Equations 4.33-4.34 results in expressions for $\mathbf{U}_{m_{d_1}}$ and $\mathbf{U}_{m_{d_2}}$ in terms of the generalized coordinates:

$$\mathbf{U}_{m_{d_1}} = \begin{Bmatrix} r_d(\sin \phi \sin \theta \cos(\Omega t) - \cos \phi \sin(\Omega t)) - h \cos \theta \sin \phi + x \\ r_d \cos \theta \cos(\Omega t) + h \sin \theta + y \\ r_d(\sin \phi \sin(\Omega t) + \cos \phi \sin \theta \cos(\Omega t)) - h \cos \phi \cos \theta \end{Bmatrix} \quad (4.35)$$

$$\mathbf{U}_{m_{d_2}} = \begin{Bmatrix} -r_d(\sin \phi \sin \theta \cos(\Omega t) - \cos \phi \sin(\Omega t)) + h \cos \theta \sin \phi + x \\ -r_d \cos \theta \cos(\Omega t) - h \sin \theta + y \\ -r_d(\sin \phi \sin(\Omega t) + \cos \phi \sin \theta \cos(\Omega t)) + h \cos \phi \cos \theta \end{Bmatrix} \quad (4.36)$$

Then, the velocity of the dynamic imbalance masses, $\mathbf{v}_{m_{d_1}}$ and $\mathbf{v}_{m_{d_2}}$, are obtained by differentiating Equations 4.35 and 4.36. The kinetic energy added to the system by the dynamic imbalance masses is:

$$T_{m_d} = \frac{1}{2} m_d \mathbf{v}_{m_{d_1}}^T \mathbf{v}_{m_{d_1}} + \frac{1}{2} m_d \mathbf{v}_{m_{d_2}}^T \mathbf{v}_{m_{d_2}} \quad (4.37)$$

Differentiating $\mathbf{U}_{m_{d_1}}$ and $\mathbf{U}_{m_{d_2}}$ and substituting the results into Equation 4.37 gives:

$$\begin{aligned} T_{m_d} = & m_d \left\{ \dot{\phi}^2 \left[h^2 \cos^2 \theta + r_d^2 \left(1 - \cos^2 \theta \cos^2(\Omega t) \right) - r_d h \sin(2\theta) \cos(\Omega t) \right] \right. \\ & + \dot{\theta}^2 \left(r_d^2 \cos^2(\Omega t) + h^2 \right) - 2r_d \dot{\theta} \sin(\Omega t) \left[h\Omega - \dot{\phi} (r_d \cos \theta \cos(\Omega t) + h \sin \theta) \right] \\ & \left. - 2r_d \dot{\phi} \Omega (r_d \sin \theta - h \cos \theta \cos(\Omega t)) + \dot{x}^2 + \dot{y}^2 + r_d^2 \Omega^2 \right\} \end{aligned} \quad (4.38)$$

The modeling of the dynamic imbalance mass completes the analytical model which is shown in Figure 4-5. The kinetic energy of the dynamic imbalance masses, T_{m_d} is combined with the kinetic energies of the balanced wheel, T_w , and the static imbalance masses, T_{m_s} , to obtain the total kinetic energy of the system.

$$T = T_w + T_{m_s} + T_{m_d} \quad (4.39)$$

The Lagrangian of the full model, \mathcal{L}_{mod} is formed by substituting Equations 4.7, 4.27 and 4.38 into Equation 4.39 and then substituting the resulting kinetic energy and the potential energy, Equation 4.9 into Equation 4.12. The result is a complex expression in terms of the generalized coordinates and their derivatives.

where $c = \cos$, $s = \sin$, the inertia terms are:

$$I_\theta = I_{rr} + 2m_d h^2 + \tilde{I} \cos^2(\Omega t) \quad (4.42)$$

$$I_\phi = I_{rr} + 2m_d h^2 + \tilde{I} \sin^2(\Omega t) \quad (4.43)$$

$$\tilde{I} = 2m_d r_d^2 + m_s r_s^2 \quad (4.44)$$

and the dynamic imbalance is defined as:

$$\mathcal{U}_d = 2m_d r_d h. \quad (4.45)$$

Equations 4.40-4.41 fully describe the motion of the analytical model. Note that the driving terms of the right-hand side of the equations corresponding to both the translations and rotations, are harmonic functions with a frequency equal to the wheel spin rate. The translations and rotations resulting from these forcing functions generate the fundamental wheel harmonic in the radial force and torque data.

4.1.4 Extended Model: Additional Harmonics

The analytical model shown in Figure 4-5 captures the radial modes of the RWA and flywheel imbalance, which causes disturbance forces and torques at the frequency of the wheel's spin, as seen in the right sides of Equations 4.40 and 4.41. However, it has been shown that additional disturbances occur at frequencies corresponding to many different ratios of the wheel's spin rate (see Figure 3-12 for an example). These disturbances are captured in the empirical model and a MATLAB toolbox has been developed that facilitates the extraction of the model parameters from data (Chapter 3). Therefore, the analytical model, as it stands now, does not fully capture the dynamics of RWA disturbances. The additional harmonic disturbances must be incorporated into the analytical model. The empirical model parameters are used to create an extended analytical model, as shown in Figure 4-6, which includes the radial wheel modes, and *all* the harmonic disturbances identified by the RWA DADM toolbox.

Recall from Chapter 1 that disturbances occurring at frequencies other than the wheel's spin rate are generally attributed to components of the RWA other than the flywheel such as, bearing imperfections, motor disturbances, and dynamic lubricant behavior. Capturing the

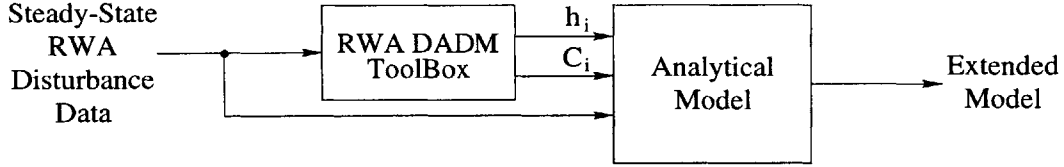


Figure 4-6: Incorporation of Harmonic Disturbances into Analytical Model

dynamic behavior of all of the RWA components would require a very complex, high-fidelity model. Therefore, for simplicity the parameters of the empirical model are used to capture the frequencies and amplitudes of the additional harmonic disturbances without modeling their sources physically. The equations of motion of the extended model are obtained by adding the additional disturbances as harmonic forcing functions at frequencies, $h_i\Omega$, and with amplitudes of $C_i\Omega^2$, to the right hand side of Equations 4.40 and 4.41. The resulting generalized translations and rotations are described by:

$$\begin{bmatrix} M_t & 0 \\ 0 & M_t \end{bmatrix} \begin{Bmatrix} \ddot{x} \\ \ddot{y} \end{Bmatrix} + \begin{bmatrix} c & 0 \\ 0 & c \end{bmatrix} \begin{Bmatrix} \dot{x} \\ \dot{y} \end{Bmatrix} + \begin{bmatrix} k & 0 \\ 0 & k \end{bmatrix} \begin{Bmatrix} x \\ y \end{Bmatrix} = \sum_{i=1}^n C_{rad_i} \Omega^2 \begin{Bmatrix} -\sin(h_{rad_i} \Omega t) \\ \cos(h_{rad_i} \Omega t) \end{Bmatrix} \quad (4.46)$$

and:

$$\begin{bmatrix} I_\theta & \frac{1}{2} \tilde{I} s(2\Omega t) \\ \frac{1}{2} \tilde{I} s(2\Omega t) & I_\phi \end{bmatrix} \begin{Bmatrix} \ddot{\theta} \\ \ddot{\phi} \end{Bmatrix} + \Omega \begin{bmatrix} \frac{c_\theta}{\Omega} - \tilde{I} s(2\Omega t) & I_{zz} + 2\tilde{I} c^2(\Omega t) \\ -I_{zz} - 2\tilde{I} s^2(\Omega t) & \frac{c_\phi}{\Omega} + \tilde{I} s(2\Omega t) \end{bmatrix} \begin{Bmatrix} \dot{\theta} \\ \dot{\phi} \end{Bmatrix} + \begin{bmatrix} k_\theta & 0 \\ 0 & k_\phi \end{bmatrix} \begin{Bmatrix} \theta \\ \phi \end{Bmatrix} = \sum_{i=1}^n C_{tor_i} \Omega^2 \begin{Bmatrix} c(h_{tor_i} \Omega t) \\ s(h_{tor_i} \Omega t) \end{Bmatrix} \quad (4.47)$$

where I_θ , I_ϕ , \tilde{I} , c and s are defined in the previous section. The parameter pairs, h_{rad_i} and C_{rad_i} , and h_{tor_i} and C_{tor_i} correspond to the harmonics numbers and amplitude coefficients of the radial force and torque disturbances, respectively. Since the fundamental harmonic is physically accounted for in the model by the static and dynamic imbalance masses, the amplitude coefficients, C_{rad_i} and C_{tor_i} corresponding to this harmonic, $h_{rad_i} = h_{tor_i} = 1$, are equal to the static imbalance, U_s , and the dynamic imbalance, U_d , respectively:

$$C_{rad_i} = U_s \text{ when } h_{rad_i} = 1.0 \quad (4.48)$$

$$C_{tor_i} = U_d \text{ when } h_{tor_i} = 1.0 \quad (4.49)$$

All other harmonic numbers and amplitude coefficients are equal to those obtained through the empirical modeling process (see Chapter 3).

4.2 Model Simulation

The disturbance forces and torques predicted by the extended analytical model are obtained by simulating the equations of motion presented in Equations 4.46 and 4.47 with MATLAB. In this section, the methods used to obtain the time histories of the disturbances are presented, and the results of a preliminary simulation are discussed. It will be shown that the extended analytical model captures interactions between the harmonics and the internal wheel mode. However, problems are encountered modeling both the positive and negative whirls of the rocking mode. This modeling issue is explored in detail and a preliminary solution is proposed.

4.2.1 Analytical Solutions of EOM

In order to simulate the extended analytical model, the solutions of the second order differential equations governing the motion of the system (Equations 4.46-4.47) are obtained using the method of undetermined coefficients [25]. In general, an n^{th} order linear equation:

$$a_n w^{(n)} + a_{n-1} w^{(n-1)} + \dots + a_1 w' + a_0 w = f(t) \quad (4.50)$$

has a general solution of the form:

$$w(t) = w_h(t) + w_p(t) \quad (4.51)$$

where $w_h(t)$ is the solution of the homogeneous equations associated with Equation 4.50 and $w_p(t)$ is a single particular solution of Equation 4.50. Therefore, in order to find the complete analytical solutions for the generalized translations $x(t)$ and $y(t)$, and generalized rotations, $\theta(t)$ and $\phi(t)$, both the homogeneous and particular solutions of Equations 4.46-4.47 must be obtained.

Generalized Translations

Homogeneous Solutions The generalized translations will be considered first. The solutions of the homogeneous equations:

$$M_t \ddot{x} + c \dot{x} + kx = 0 \quad (4.52)$$

$$M_t \ddot{y} + c \dot{y} + ky = 0 \quad (4.53)$$

are found by assuming solutions of the form:

$$x_h(t) = \bar{A}e^{rt} \quad (4.54)$$

$$y_h(t) = \bar{B}e^{rt} \quad (4.55)$$

and substituting into Equations 4.53 to obtain the characteristic equation:

$$M_t r^2 + cr + k = 0 \quad (4.56)$$

Dividing Equation 4.56 by M_t and using:

$$\omega_T = \sqrt{\frac{k}{M_t}} \quad (4.57)$$

$$\zeta_T = \frac{c}{2\omega_T M_t} \quad (4.58)$$

results in the following general form:

$$r^2 + 2\zeta_T \omega_T r + \omega_T^2 = 0 \quad (4.59)$$

where ω_T is the natural frequency of the radial translation mode and ζ_T is the damping ratio. Then, solving for r :

$$r = -\zeta_T \omega_T \pm i\omega_T \sqrt{1 - \zeta_T^2} \quad (4.60)$$

substituting Equation 4.60 into Equation 4.55, and assuming that the system is underdamped ($0 < \zeta_T < 1$), expressions for $x_h(t)$ and $y_h(t)$ are obtained:

$$x_h(t) = e^{-\zeta_T \omega_T t} (\bar{A}_1 \cos(\omega_d t) + \bar{A}_2 \sin(\omega_d t)) \quad (4.61)$$

Equations 4.57 and 4.58:

$$\begin{aligned} x_{p_i}(t) &= \frac{C_i \Omega^2 / M_t}{(\bar{\omega}_i^2 - \omega_T^2)^2 + (2\bar{\omega}_i \zeta_T \omega_T)^2} \left[(\bar{\omega}_i^2 - \omega_T) \sin(\bar{\omega}_i t) + 2\bar{\omega}_i \omega_T \zeta_T \cos(\bar{\omega}_i t) \right] \\ y_{p_i}(t) &= \frac{C_i \Omega^2 / M_t}{(\bar{\omega}_i^2 - \omega_T^2)^2 + (2\bar{\omega}_i \zeta_T \omega_T)^2} \left[2\bar{\omega}_i \omega_T \zeta_T \sin(\bar{\omega}_i t) - (\bar{\omega}_i^2 - \omega_T) \cos(\bar{\omega}_i t) \right] \end{aligned} \quad (4.66)$$

where $\bar{\omega}_i$ is the disturbance frequency corresponding to the i^{th} harmonic: $\bar{\omega}_i = h_i \Omega$. The denominator of the solution has two roots, or poles, at which resonance occurs:

$$\bar{\omega}_i^2 = \omega_T^2 (1 - 2\zeta_T^2) \pm 2\zeta_T \omega_T^2 \sqrt{\zeta_T^2 - 1} \quad (4.67)$$

For a lightly damped system, the right-hand side of Equation 4.67 reduces to simply the natural frequency of the radial translation mode, ω_T . Therefore disturbance amplification occurs at wheel speeds in which a disturbance frequency is approximately equal to the radial translation frequency.

Complete Solutions Finally, the complete solutions for the generalized translations are defined by:

$$\begin{aligned} x(t) &= x_h(t) + \sum_{i=1}^n x_{p_i}(t) \\ y(t) &= y_h(t) + \sum_{i=1}^n y_{p_i}(t) \end{aligned} \quad (4.68)$$

where the coefficients, \bar{A}_1 , \bar{A}_2 , \bar{B}_1 , and \bar{B}_2 , are determined by the initial conditions.

Generalized Rotations

The complete solutions for the generalized rotations are found with the same methods used for the generalized translations. The mass of the flywheel, M , is much larger than the imbalance masses, which are generally on the order of .01 grams (g). Therefore, it can be concluded that:

$$I_{rr}, I_{zz} \gg \tilde{I} \quad (4.69)$$

This relationship can be used to simplify some of the terms in Equation 4.47:

$$I_\theta = I_{rr} + 2m_d h^2 + \tilde{I} \cos^2(\Omega t) \approx I_{rr}$$

$$\begin{aligned}
I_\phi &= I_{rr} + 2m_d h^2 + \tilde{I} \sin^2(\Omega t) \approx I_{rr} \\
I_{zz} &+ 2\tilde{I} \cos^2(\Omega t) \approx I_{zz}
\end{aligned} \tag{4.70}$$

The analytical solutions of the full EOM of the generalized rotations were derived, and the results obtained are equivalent to those presented here for the simplified EOM. Therefore, for simplicity of presentation, the following simplified EOM for the generalized rotations are used in the remained of this chapter:

$$\begin{aligned}
\begin{bmatrix} I_{rr} & \frac{1}{2}\tilde{I} \sin(2\Omega t) \\ \frac{1}{2}\tilde{I} \sin(2\Omega t) & I_{rr} \end{bmatrix} \begin{Bmatrix} \ddot{\theta} \\ \ddot{\phi} \end{Bmatrix} + \Omega \begin{bmatrix} \frac{c_\theta}{\Omega} - \tilde{I} \sin(2\Omega t) & I_{zz} \\ -I_{zz} & \frac{c_\theta}{\Omega} + \tilde{I} \sin(2\Omega t) \end{bmatrix} \begin{Bmatrix} \dot{\theta} \\ \dot{\phi} \end{Bmatrix} + \begin{bmatrix} k_\theta & 0 \\ 0 & k_\theta \end{bmatrix} \begin{Bmatrix} \theta \\ \phi \end{Bmatrix} \\
= \sum_{i=1}^n C_{tor_i} \Omega^2 \begin{Bmatrix} \cos(h_{tor_i} \Omega t) \\ \sin(h_{tor_i} \Omega t) \end{Bmatrix}
\end{aligned} \tag{4.71}$$

Homogeneous Solutions The homogeneous equations for the generalized rotations using the simplified equations of motion are:

$$\begin{aligned}
I_{rr} \ddot{\theta} + \frac{1}{2} \tilde{I} \sin(2\Omega t) \ddot{\phi} + (c_\theta - \Omega \tilde{I} \sin(2\Omega t)) \dot{\theta} + \Omega I_{zz} \dot{\phi} + k_\theta \theta &= 0 \\
\frac{1}{2} \tilde{I} \sin(2\Omega t) \ddot{\theta} + I_{rr} \ddot{\phi} - \Omega I_{zz} \dot{\theta} + (c_\theta + \Omega \tilde{I} \sin(2\Omega t)) \dot{\phi} + k_\theta \phi &= 0
\end{aligned} \tag{4.72}$$

Assuming solutions, $\theta_h(t)$ and $\phi_h(t)$, of the form:

$$\begin{aligned}
\theta_h(t) &= \bar{C} e^{rt} \\
\phi_h(t) &= \bar{D} e^{rt}
\end{aligned} \tag{4.73}$$

substituting into Equation 4.72, and collecting like terms results in the following system of equations:

$$\begin{bmatrix} I_{rr} r^2 + (c_\theta - \Omega \tilde{I} \sin(2\Omega t)) r + k_\theta & \frac{1}{2} \tilde{I} r^2 \sin(2\Omega t) + \Omega I_{zz} r \\ \frac{1}{2} \tilde{I} r^2 \sin(2\Omega t) - \Omega I_{zz} r & I_{rr} r^2 + (c_\theta + \Omega \tilde{I} \sin(2\Omega t)) r + k_\theta \end{bmatrix} \begin{Bmatrix} \bar{C} \\ \bar{D} \end{Bmatrix} = \mathbf{0} \tag{4.74}$$

Setting the determinant of this matrix equal to zero and using Equation 4.69 to simplify the terms, the characteristic equation is obtained:

$$I_{rr}^2 r^4 + 2I_{rr} c_\theta r^3 + \left(2I_{rr} k_\theta + \Omega^2 I_{rr}^2 + c_\theta^2\right) r^2 + 2c_\theta k_\theta r + k_\theta^2 = 0 \quad (4.75)$$

The polynomial in Equation 4.75 has four roots of the form:

$$r_{1,2} = -a \pm ib \quad r_{3,4} = -c \pm id \quad (4.76)$$

where $r_{1,2}$ correspond to the negative whirl of the rocking mode and $r_{3,4}$ to the positive whirl. The parameters a , b , c and d are difficult to obtain symbolically, but can easily be found numerically when the simulation is run. The general form of the homogeneous solutions assuming an underdamped system are then:

$$\begin{aligned} \theta_h(t) &= e^{-at} (\bar{C}_1 \cos(bt) + \bar{C}_2 \sin(bt)) + e^{-ct} (\bar{C}_1 \cos(dt) + \bar{C}_2 \sin(dt)) \\ \phi_h(t) &= e^{-at} (\bar{D}_1 \cos(bt) + \bar{D}_2 \sin(bt)) + e^{-ct} (\bar{D}_1 \cos(dt) + \bar{D}_2 \sin(dt)) \end{aligned} \quad (4.77)$$

Particular Solutions The particular solutions, $\theta_p(t)$ and $\phi_p(t)$ are found using the method of undetermined coefficients and the principle of superposition, as in the case of the generalized translations. Note that both the original and the simplified equations of motion, Equations 4.47 and 4.71, contain $\sin(2\Omega t)$ terms. The presence of these terms suggests that the solutions corresponding to the i^{th} disturbance harmonic, θ_{p_i} and ϕ_{p_i} , may themselves be combinations of multiple integer harmonics. Therefore, it was initially assumed that the solutions of the rotations are Fourier series expansions:

$$\begin{aligned} \theta_{p_i}(t) &= \sum_{k=1}^{\infty} \tilde{A}_{i_k} \sin(kh_i \Omega t) + \tilde{B}_{i_k} \cos(kh_i \Omega t) \\ \phi_{p_i}(t) &= \sum_{k=1}^{\infty} \tilde{C}_{i_k} \sin(kh_i \Omega t) + \tilde{D}_{i_k} \cos(kh_i \Omega t) \end{aligned} \quad (4.78)$$

The derivation of the analytical solution assuming this form is shown in Appendix C. The results show that coefficients for $k > 1$ are negligible. Therefore, for simplicity the solutions corresponding to the i^{th} harmonic disturbance, θ_{p_i} and ϕ_{p_i} , can be assumed to be of the

form:

$$\begin{aligned}\theta_{p_i}(t) &= \tilde{A}_i \sin(h_i \Omega t) + \tilde{B}_i \cos(h_i \Omega t) \\ \phi_{p_i}(t) &= \tilde{C}_i \sin(h_i \Omega t) + \tilde{D}_i \cos(h_i \Omega t)\end{aligned}\quad (4.79)$$

Substituting Equation 4.79 into the two equations in Equation 4.71 and setting like terms equal results in the following system of equations:

$$\begin{bmatrix} k_\theta - (h_i \Omega)^2 I_{rr} & -h_i \Omega c_\theta & 0 & -h_i \Omega^2 I_{zz} \\ h_i \Omega c_\theta & k_\theta - (h_i \Omega)^2 I_{rr} & h_i \Omega^2 I_{zz} & 0 \\ 0 & h_i \Omega^2 I_{zz} & k_\theta - (h_i \Omega)^2 I_{rr} & -h_i \Omega c_\theta \\ -h_i \Omega^2 I_{zz} & 0 & h_i \Omega c_\theta & k_\theta - (h_i \Omega)^2 I_{rr} \end{bmatrix} \begin{bmatrix} \tilde{A}_i \\ \tilde{B}_i \\ \tilde{C}_i \\ \tilde{D}_i \end{bmatrix} = \begin{bmatrix} 0 \\ -C_i \Omega^2 \\ C_i \Omega^2 \\ 0 \end{bmatrix}\quad (4.80)$$

Then, solving for the coefficients, \tilde{A}_i , \tilde{B}_i , \tilde{C}_i and \tilde{D}_i and substituting the results into Equation 4.79, the particular solutions of the generalized rotations for the i^{th} disturbance harmonic are obtained:

$$\begin{aligned}\theta_{p_i}(t) &= \frac{C_i \Omega^2}{(h_i \Omega^2 I_{eff} - k_\theta)^2 + (h_i \Omega c_\theta)^2} \left[h_i \Omega c_\theta \sin(h_i \Omega t) - (h_i \Omega^2 I_{eff} - k_\theta) \cos(h_i \Omega t) \right] \\ \phi_{p_i}(t) &= \frac{-C_i \Omega^2}{(h_i \Omega^2 I_{eff} - k_\theta)^2 + (h_i \Omega c_\theta)^2} \left[(h_i \Omega^2 I_{eff} - k_\theta) \sin(h_i \Omega t) + h_i \Omega c_\theta \cos(h_i \Omega t) \right]\end{aligned}\quad (4.81)$$

where:

$$I_{eff} = h_i I_{rr} - I_{zz}\quad (4.82)$$

Note that the solutions are of equal amplitude but are 90° out of phase from each other. Since θ and ϕ are both angles about the radial axes, this result is expected.

Recall from Section 4.1.1 that the natural frequencies of the rocking mode are a function of the wheel speed. Therefore, the frequencies at which the i^{th} harmonic excites the two whirls of the rocking mode are dependent upon the harmonic number h_i . Since the static and dynamic imbalances are very small compared to the mass of the wheel, the rocking mode frequencies of the imbalanced wheel are about the same as those of the balanced wheel (Equation 4.21). The natural rocking frequencies for the i^{th} disturbance can be

found by solving for the frequency at which $\bar{\omega}_i$ satisfies Equation 4.21:

$$\bar{\omega}_{r_i} = h_i \Omega = \mp \frac{\Omega I_{zz}}{2I_{rr}} + \sqrt{\left(\frac{\Omega I_{zz}}{2I_{rr}}\right)^2 + \frac{k d_k^2}{I_{rr}}} \quad (4.83)$$

After some algebraic manipulation the following two frequencies are obtained:

$$\begin{aligned} (\omega_{r_i}^-)^2 &= \frac{h_i k_\theta}{h_i I_{rr} + I_{zz}} \\ (\omega_{r_i}^+)^2 &= \frac{h_i k_\theta}{h_i I_{rr} - I_{zz}} \end{aligned} \quad (4.84)$$

where the minus superscript indicates the interaction frequency of the i^{th} harmonic and the negative whirl and the plus superscript indicates that of the i^{th} harmonic and the positive whirl. In addition, damping ratios for the i^{th} disturbance and the two whirls can be defined:

$$\begin{aligned} \zeta_{r_i}^- &= \frac{h_i c_\theta}{2\omega_{r_i}^- (h_i I_{rr} + I_{zz})} \\ \zeta_{r_i}^+ &= \frac{h_i c_\theta}{2\omega_{r_i}^+ (h_i I_{rr} + I_{zz})} \end{aligned} \quad (4.85)$$

The quantities in Equations 4.84-4.85 can be used to put the particular solutions in Equation 4.81 into a more convenient form:

$$\begin{aligned} \theta_{p_i}(t) &= \frac{h_i C_i \Omega^2 / (h_i I_{rr} - I_{zz})}{(\bar{\omega}_i^2 - (\omega_{r_i}^+)^2)^2 + (2\omega_{r_i}^+ \zeta_{r_i}^+ \bar{\omega}_i)^2} \left[2\omega_{r_i}^+ \zeta_{r_i}^+ \bar{\omega}_i \sin(\bar{\omega}_i t) - (\bar{\omega}_i^2 - (\omega_{r_i}^+)^2) \cos(\bar{\omega}_i t) \right] \\ \phi_{p_i}(t) &= \frac{h_i C_i \Omega^2 / (h_i I_{rr} - I_{zz})}{(\bar{\omega}_i^2 - (\omega_{r_i}^+)^2)^2 + (2\omega_{r_i}^+ \zeta_{r_i}^+ \bar{\omega}_i)^2} \left[(\bar{\omega}_i^2 - (\omega_{r_i}^+)^2) \sin(\bar{\omega}_i t) + 2\omega_{r_i}^+ \zeta_{r_i}^+ \bar{\omega}_i \cos(\bar{\omega}_i t) \right] \end{aligned} \quad (4.86)$$

Note that the only frequency which appears in the particular solutions other than the disturbance frequency is $\omega_{r_i}^+$, which is the natural frequency of the positive whirl of the rocking mode for the i^{th} disturbance. However, it has been shown that the rocking mode has two natural frequencies, one for each whirl and that, in general, the disturbance harmonics excite both of them (see Figure 2-8(b) for an example in the Ithaco E Wheel data). Therefore, the extended analytical model is not capturing the full rocking behavior of the wheel. An entire mode is lost. This discrepancy between the model and the data must be investigated before the complete solution of the generalized rotations can be obtained.

Pole-Zero Cancellation The particular solution obtained for the generalized rotations can be explored using a simplified version of the analytical model. Consider the equations of motion for a balanced flywheel (Equation 4.19) with no damping, driven by only one harmonic excitation at the wheel's spin rate that is of the same form as that resulting from the dynamic imbalance (Equation 4.41):

$$\begin{bmatrix} I_{rr} & 0 \\ 0 & I_{rr} \end{bmatrix} \begin{Bmatrix} \ddot{\theta} \\ \ddot{\phi} \end{Bmatrix} + \Omega \begin{bmatrix} 0 & I_{zz} \\ -I_{zz} & 0 \end{bmatrix} \begin{Bmatrix} \dot{\theta} \\ \dot{\phi} \end{Bmatrix} + \begin{bmatrix} k_{\theta} & 0 \\ 0 & k_{\theta} \end{bmatrix} \begin{Bmatrix} \theta \\ \phi \end{Bmatrix} = F \begin{Bmatrix} \cos(\Omega t) \\ \sin(\Omega t) \end{Bmatrix} \quad (4.87)$$

The solutions of these equations are found by assuming that θ and ϕ are of the form shown in Equation 4.79 (assuming that $h_1 = 1$) and substituting into Equation 4.87. Then, after collecting like terms, the following set of equations is obtained:

$$\begin{bmatrix} k_{\theta} - \Omega^2 I_{rr} & 0 & 0 & \Omega^2 I_{zz} \\ 0 & k_{\theta} - \Omega^2 I_{rr} & \Omega^2 I_{zz} & 0 \\ 0 & \Omega^2 I_{zz} & k_{\theta} - \Omega^2 I_{rr} & 0 \\ \Omega^2 I_{zz} & 0 & 0 & k_{\theta} - \Omega^2 I_{rr} \end{bmatrix} \begin{Bmatrix} \tilde{A} \\ \tilde{B} \\ \tilde{C} \\ \tilde{D} \end{Bmatrix} = \begin{Bmatrix} 0 \\ F \\ F \\ 0 \end{Bmatrix} \quad (4.88)$$

It is easy to see from Equation 4.88 that the coefficients, \tilde{A} and \tilde{D} , are zero. Solving for the remaining two coefficients, the following result is obtained:

$$\tilde{B} = \tilde{C} = \frac{F}{I_{rr} - I_{zz}} \left\{ \frac{(\omega_{r_1}^-)^2 - \Omega^2}{((\omega_{r_1}^+)^2 - \Omega^2)((\omega_{r_1}^-)^2 - \Omega^2)} \right\} \quad (4.89)$$

It is clear from these coefficients that two distinct poles exist at which resonant behavior occurs, $\omega_{r_1}^-$ and $\omega_{r_1}^+$, which are the interaction frequencies of the negative and positive rocking mode whirls and the fundamental harmonic. However, also note that the numerator of Equation 4.89 contains a pair of zeros at $\omega_{r_1}^-$, which cancels a pair of poles, effectively eliminating the resonant behavior due to the negative whirl and results in the following solutions for the generalized rotations:

$$\theta(t) = \frac{F}{I_{rr} - I_{zz}} \left\{ \frac{1}{\omega_{r_1}^+ - \Omega^2} \right\} \cos(\Omega t) \quad (4.90)$$

$$\phi(t) = \frac{F}{I_{rr} - I_{zz}} \left\{ \frac{1}{\omega_{r_1}^+ - \Omega^2} \right\} \sin(\Omega t) \quad (4.91)$$

These final solutions, like those obtained for the extended model (Equation 4.86), only contain one pole, $\omega_{r_1}^+$. Only the disturbance amplification due to the positive whirl mode remains in the model.

It can be concluded from the results of this simple analysis that only the natural frequency of the positive whirl mode is present in the partial solutions for the generalized rotations because a pole-zero cancellation occurs which eliminates the effects of the negative whirl of the rocking mode. One possible explanation for these results may be found in the rotations defined at the beginning of the modeling process. Recall from Section 2.3 that the positive whirl mode, also called the co-rotating precessional mode, results when the wheel's spin and precession are in the same direction. Note that in Figure 4-2 the positive directions of Ω and the two radial angles, θ and ϕ , are defined as positive rotations about the axes. Also, note that the precession of the wheel (about the \mathbf{Z} -axis) is a combination of θ and ϕ . Therefore, for this model, the precession and spin of the wheel are defined in the same directions, and the co-rotating (positive) whirl mode is captured.

The counter-rotating, or negative, whirl results when the wheel's precession and spin are in opposing directions. Therefore, one way to capture the negative whirl in the mode is to reverse the directions of θ and ϕ , so that the precession is defined opposite its spin. The equations of motion for this version of the model are:

$$\begin{aligned} \begin{bmatrix} I_{rr} & \frac{1}{2}\tilde{I}\sin(2\Omega t) \\ \frac{1}{2}\tilde{I}\sin(2\Omega t) & I_{rr} \end{bmatrix} \begin{Bmatrix} \ddot{\theta} \\ \ddot{\phi} \end{Bmatrix} + \Omega \begin{bmatrix} \frac{c\theta}{\Omega} - \tilde{I}\sin(2\Omega t) & -I_{zz} \\ I_{zz} & \frac{c\phi}{\Omega} + \tilde{I}\sin(2\Omega t) \end{bmatrix} \begin{Bmatrix} \dot{\theta} \\ \dot{\phi} \end{Bmatrix} + \begin{bmatrix} k_\theta & 0 \\ 0 & k_\theta \end{bmatrix} \begin{Bmatrix} \theta \\ \phi \end{Bmatrix} \\ = -\sum_{i=1}^n C_{tor_i} \Omega^2 \begin{Bmatrix} \cos(h_{tor_i} \Omega t) \\ \sin(h_{tor_i} \Omega t) \end{Bmatrix} \end{aligned} \quad (4.92)$$

Solving this set of equations using the same methods detailed in the preceding section, the particular solutions are:

$$\begin{aligned} \theta_{p_i}^- (t) &= \frac{h_i C_i \Omega^2 / (h_i I_{rr} - I_{zz})}{(\bar{\omega}_i^2 - (\omega_{r_i}^-)^2)^2 + (2\omega_{r_i}^- \zeta_{r_i}^- \bar{\omega}_i)^2} \left[2\omega_{r_i}^- \zeta_{r_i}^- \bar{\omega}_i \sin(\bar{\omega}_i t) - (\bar{\omega}_i^2 - (\omega_{r_i}^-)^2) \cos(\bar{\omega}_i t) \right] \\ \phi_{p_i}^- (t) &= \frac{h_i C_i \Omega^2 / (h_i I_{rr} - I_{zz})}{(\bar{\omega}_i^2 - (\omega_{r_i}^-)^2)^2 + (2\omega_{r_i}^- \zeta_{r_i}^- \bar{\omega}_i)^2} \left[(\bar{\omega}_i^2 - (\omega_{r_i}^-)^2) \sin(\bar{\omega}_i t) + 2\omega_{r_i}^- \zeta_{r_i}^- \bar{\omega}_i \cos(\bar{\omega}_i t) \right] \end{aligned} \quad (4.93)$$

The negative superscript on $\theta_{p_i}(t)$ and $\phi_{p_i}(t)$ indicate that the solutions are for the counter-rotating case.

Recall from Section 2.3 that amplification of harmonic disturbances by both the positive and negative whirl modes are visible in the Ithaco E Wheel data shown (Figure 2-8(b)). Therefore the effects of both whirls of the rocking mode must be captured by the analytical model. One way to do accomplish this goal is through superposition of the particular solutions obtained assuming both co-rotating and counter-rotating conditions:

$$\begin{aligned}\theta_{p_i} &= C_i \Omega^2 (\theta_{p_i}^- + \theta_{p_i}^+) \\ \phi_{p_i} &= C_i \Omega^2 (\phi_{p_i}^- + \phi_{p_i}^+)\end{aligned}\tag{4.94}$$

where $(\theta_{p_i})_+$ and $(\phi_{p_i})_+$ are the particular solutions for the co-rotating mode (Equations 4.86) and $(\theta_{p_i})_-$ and $(\phi_{p_i})_-$ are the particular solutions for the counter-rotating mode (Equations 4.93).

Complete Solutions The complete solutions for the generalized rotations are slightly more complex than those for the generalized translations since both the co-rotating and counter-rotating solutions must be included for each harmonic disturbance:

$$\begin{aligned}\theta(t) &= \theta_h(t) + \sum_{i=1}^n (\theta_{p_i}^-(t) + \theta_{p_i}^+(t)) \\ \phi(t) &= \phi_h(t) + \sum_{i=1}^n (\phi_{p_i}^-(t) + \phi_{p_i}^+(t))\end{aligned}\tag{4.95}$$

The coefficients \bar{C}_1 , \bar{C}_2 , \bar{D}_1 and \bar{D}_2 are determined by the initial conditions. These solutions, together with those for the generalized translations are used to simulate the extended analytical model with MATLAB.

4.2.2 Preliminary Simulation Results

Preliminary simulations were run using the equations for the generalized translations and rotations derived in the previous sections. The homogeneous parts of the complete solutions account for the transient behavior of the wheel as it changes wheel speed. Since this thesis deals exclusively with steady-state RWA disturbances, only the particular solutions are considered at this time. MATLAB is used to simulate the spinning reaction wheel

and obtain the time histories of the translations and rotations. The disturbance forces and torques are calculated from the translational and angular displacements through the following relationships:

$$\begin{aligned} F_x(t) &= kx(t) & F_y(t) &= ky(t) \\ T_x(t) &= k_\theta\theta(t) & T_y(t) &= k_\theta\phi(t) \end{aligned} \tag{4.96}$$

Figure 4-7(a) is a waterfall plot of the simulated radial force disturbance. The steady-state solutions were found at wheel speeds ranging from 0 to 3000 rpm and the PSDs of the time histories were calculated. Twelve radial harmonics in addition to the fundamental were included in the model and all are visible in the simulation results. Also, note that interaction between the higher harmonics and the radial translational mode (which was set at 200Hz) is captured. The amount of disturbance amplification can be controlled by changing the damping coefficient, c , as will be discussed in the following sections.

The simulated radial torque disturbance is shown in Figure 4-7(b). Ten higher harmonics and the fundamental were included in the model. All harmonics are visible in the waterfall plot and the interactions between both the positive and negative whirl modes are captured. The heavy dark lines in the wheel speed/frequency plane represent the natural frequencies of the rocking modes as a function of wheel speed. Note that whenever the harmonics, which appear as diagonal ridges across wheel speed and frequency, cross these black lines the mode is excited, and an amplification in the disturbance results.

Figure 4-7, also demonstrates the decoupling of the rotations and translations that was discussed during the modeling process. Note that the radial translation mode only appears in the radial forces and the rocking mode only appears in the radial torques. Such perfect decoupling does not match the experimental data. Recall from Figures 3-23 and 3-28 that both the radial translation and rocking modes were observed in the radial force and radial torque data for the Ithaco E Wheel. The coupling between translations and rotations in the data may be due to the location of the load cell with respect to the center of the wheel. The translations and rotations in the model are all measured from the center of the wheel, but the data was taken at the interface of the wheel and the mounting point. It is possible that a decoupling matrix based on the geometry of the test setup can be used to obtain the pure translations and rotations of the wheel. Further investigation into this issue is necessary.

These preliminary simulation results indicate that the analytical model does indeed cap-

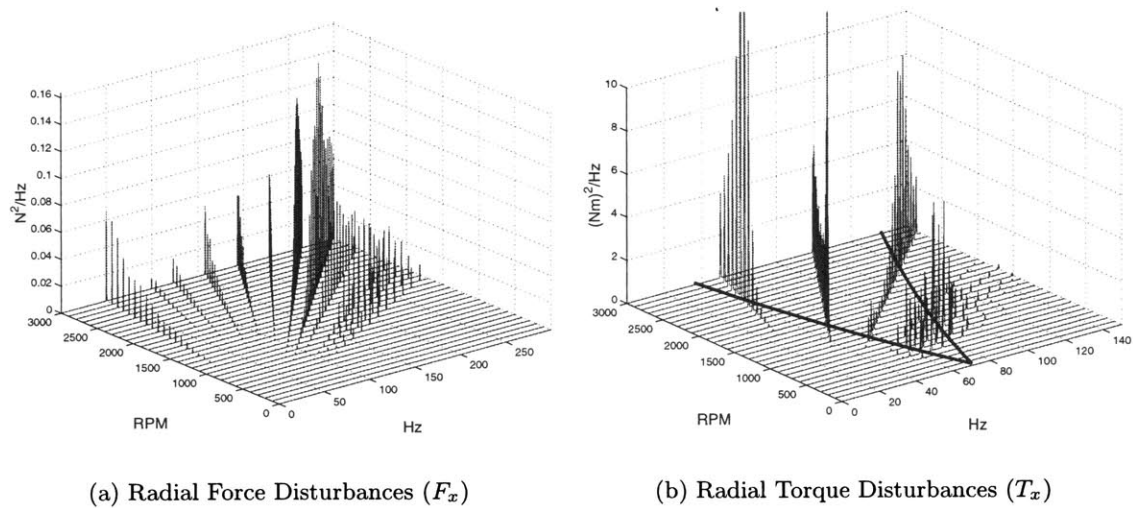


Figure 4-7: Extended Analytical Model Simulation

ture the effects of the structural wheel modes on the harmonic disturbances. The empirical and analytical modeling techniques have been combined to produce a model which includes the trends visible in RWA disturbance data. However, these results are not correlated to RWA data. In the following section a methodology is developed which uses steady-state RWA data to set the model parameters such that the resulting simulation captures the disturbance behavior of a particular RWA.

4.3 Choosing Model Parameters

The schematic of the analytical model shown in Figure 4-5 contains many model parameters, including: M , R , m_d , r_d , h , k , and d_k which control different features of the model. For example, the frequency of the structural wheel modes depend on k and d_k , and the amplitude of the fundamental harmonic is governed by m_d , m_s , r_d , r_s , and h . A complete list of parameters and their descriptions can be found in Table 4.1. Choosing specific values for these parameters allows the analytical model to be fit to steady-state RWA disturbance data from any given wheel. A methodology to facilitate the parameter fitting process is in the preliminary stages of development and is presented in this section. The Ithaco E Wheel data is used to illustrate the methodology and provides preliminary validation of the analytical model. The methodology is still under development, and the following discussion will refer to the analytical model, not the extended analytical model. Only the

Table 4.1: Model Parameters and Fitting Methodologies

Parameter	Description	Source	Equation
M_t	Total mass of RWA	Manufacturer	-
R	Radial of RWA	Manufacturer	-
I_{zz}	Polar moment of inertia	Calculated	$\frac{M_t R^2}{2}$
I_{rr}	Radial moment of inertia	Calculated	$\frac{M_t R^2}{4}$
r_s	Radial position of static imbalance mass	Calculated	R
r_d	Radial position of dynamic imbalance mass	Calculated	R
h	Axial position of dynamic imbalance mass	Manufacturer (thickness of RWA, t_w)	$\frac{t_w}{2}$
k	Spring Stiffness	Frequency of radial translation mode: radial force data	$\omega_t^2 M_t$
d_k	Distance from wheel c.g. to springs	Nominal radial rocking frequency: radial torque data	$\frac{I_{rr} \omega_r^2}{k}$
m_s	Static imbalance mass	Amplitude of fundamental harmonic: empirical model, radial force data	$\frac{u_s}{r_s}$
m_d	Dynamic imbalance mass	Amplitude of fundamental harmonic: empirical model, radial torque data	$\frac{u_d}{2r_d h}$
c	Damping coefficient	Amplification of harmonics by radial translation mode: radial force data	-
d_c	Distance from wheel c.g. to dashpots	Amplification of harmonics by radial rocking mode: radial torque data	-
h_i	Harmonic number	Empirical model	-
C_i	Amplitude coefficient	Empirical model	-

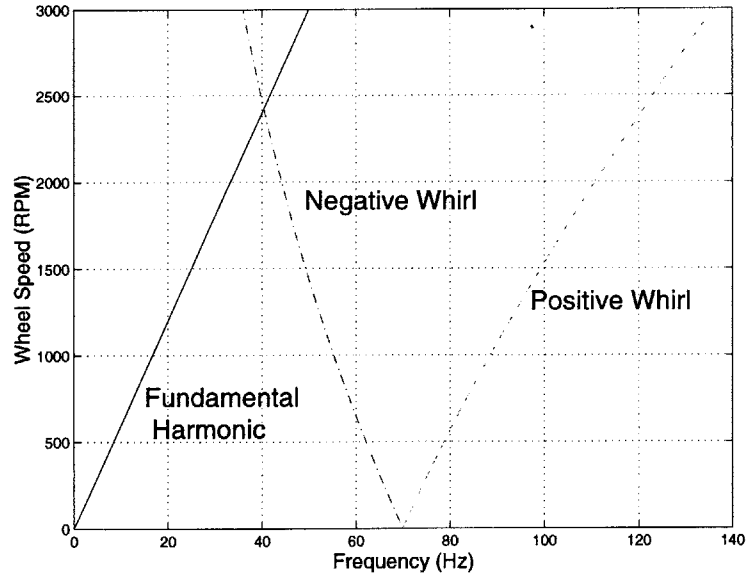


Figure 4-8: Frequency of Rocking Mode Whirls and Fundamental Harmonic as Function of Wheel Speed, $\omega_r=70$ Hz

effects of the fundamental harmonic are considered. Recall that this harmonic is the most significant in the Ithaco E Wheel data. Therefore, accurately capturing the disturbances due to this harmonic provides a good approximation to the complete wheel disturbance. The methodology presented in the following sections can easily be extended and applied to the extended analytical model.

It was shown in the previous section that a pole-zero cancellation occurs when obtaining the solution for the generalized rotations which results in the elimination of the effects of the negative whirl of the rocking mode from the model. One possible solution for this issue, which uses superposition to capture both whirls, has been presented. However, this solution affects the amplitude of the disturbance torques and makes the parameter fitting process more difficult. Therefore, in the following discussion only the solution that captures the negative whirl of the rocking mode is considered. The negative whirl is chosen since, as shown in Figure 4-8, no interaction occurs between the fundamental harmonic and the positive whirl. In the figure, the positive and negative whirl frequencies are represented with dashed lines, and the fundamental harmonic is shown with a solid line. It is easy to see that the fundamental harmonic only interacts with the negative whirl. The slope of the positive whirl frequency curve is such that its frequency is always greater than the spin rate.

Table 4.1 lists the sources used to fit each parameter. Note that the first seven parameters are all either obtained from the manufacturer or calculated. The mass and radius of the wheel are easily obtained from the manufacturer of the wheel and do not need to be fit to the data. These parameters for the Ithaco E Wheel are available on the Ithaco web page (www.ithaco.com). The mass of the wheel is listed as 10.6 kg and its radius as 19.68 cm. The next two parameters, I_{zz} and I_{rr} are calculated from the mass and radius of the wheel using the equations shown in the table. The radial and axial positions of the static and dynamic imbalance masses on the wheel, r_s , r_d , and h , can not be obtained directly from the wheel manufacturer, but can be set by other given wheel properties. Since the inertia of the imbalance masses does not contribute significantly to the inertia of the flywheel, these quantities only appear in the model along with m_s and m_d as part of the static and dynamic imbalances, \mathcal{U}_s and \mathcal{U}_d . Therefore these parameters can be set arbitrarily, reducing the number of parameters that must be fit to data and allowing m_s and m_d to govern the static and dynamic imbalance fits. To ensure that practical values for the parameters are chosen, the radii are set to the radius of the wheel, $r_s = r_d = R$, and the axial offset is assumed to be equal to half of the wheel's thickness, $h = t_w/2$. The thickness, t_w , is generally provided by the manufacturer. The remaining parameters in Table 4.1 must all be fit using RWA data (with the exception of C_i and h_i , which are empirical model parameters and correspond to higher harmonics that are not considered in this discussion). The following sections will discuss the methods used to choose values for the stiffness parameters, k and d_k , the imbalance masses, m_s and m_d , and the damping parameters, c and d_c .

4.3.1 Stiffness Parameters

The stiffness parameters control the natural frequencies of the radial translation and rocking modes. It is clear from Equation 4.57 that the natural frequency of the radial translation is a function of only k , and Equation 4.21 shows that the natural frequencies of the rocking mode are a function of k_θ , which is a combination of both k and d_k . Therefore, the parameter k can be set by the frequency of the radial translation mode and then d_k can be set by the frequencies of the rocking mode and the value obtained for k .

Rearranging Equation 4.57 results in the following expression for k :

$$k = \omega_T^2 M_t \tag{4.97}$$

The natural frequency, ω_T , is extracted from the steady-state radial force disturbance data with MATLAB. Recall that when the disturbance harmonics are at the same frequency as that of the radial translation mode, disturbance amplification occurs. These amplifications are used to determine ω_T . An initial guess for ω_T is provided, and the frequencies at which maximum disturbance occurs in the neighborhood of this guess are identified and binned in a histogram. The mean frequency of the maximum disturbances is identified as the natural frequency of the radial translation mode. This process is illustrated with the E Wheel data in Figure 4-9(a). The lower plot shows the maximum disturbance frequencies for each wheel speed. User interaction is required to choose an upper and lower bound of clustered points as indicated by the dashed lines. The mean of the points that fall within this range is calculated and returned as ω_T . In the upper plot, the histogram of the maximum disturbance frequencies is presented as a check. Note that there is a cluster of maximum points around 227 Hz. This frequency is the natural frequency of the radial translation mode. Figure 4-9(b) shows the identified value of ω_T plotted on the Ithaco E Wheel radial force data for comparison. Note that disturbance amplifications are indeed visible when the harmonics cross the solid line marking the natural frequency of the mode.

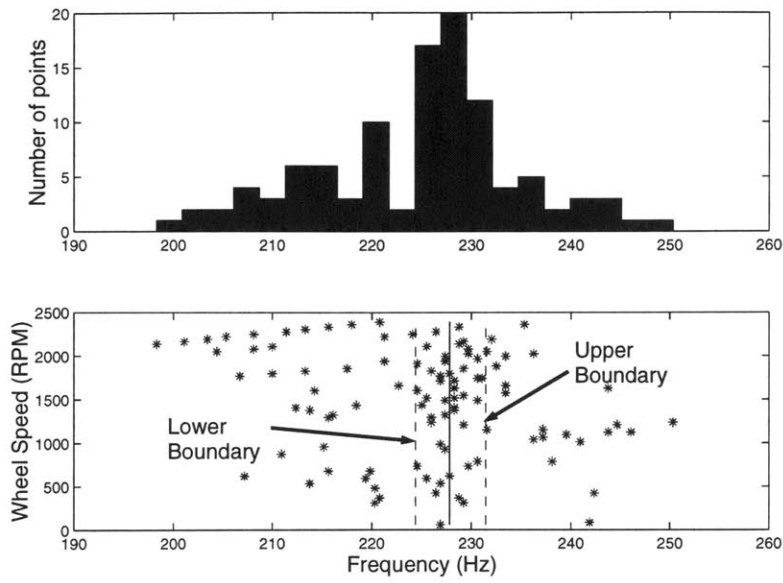
The parameter d_k is set using the natural frequencies of the rocking mode. Recall that the rocking mode contains two branches, a positive and negative whirl, that have natural frequencies which are a function of wheel speed. The frequencies of the positive and negative whirl are the same when the wheel is at rest, $\Omega = 0$:

$$\omega_{r0} = \sqrt{\frac{k_\theta}{I_{rr}}} \quad (4.98)$$

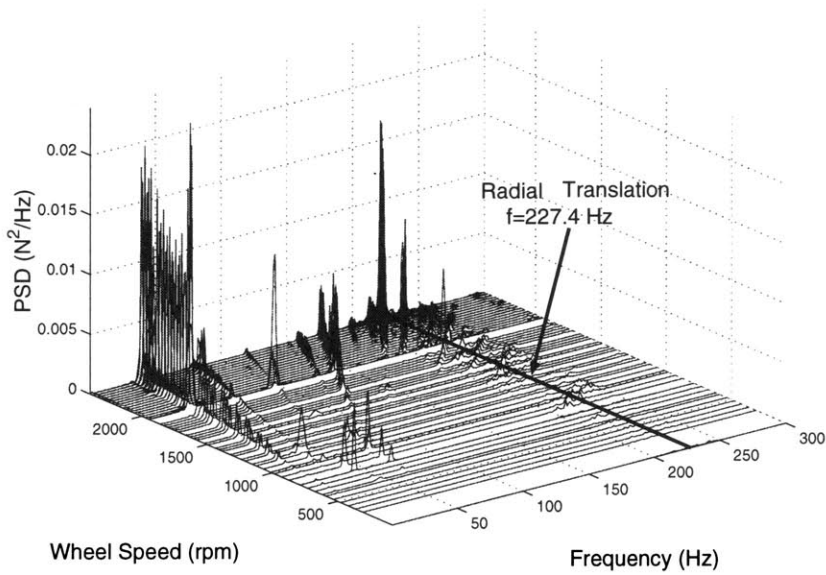
This frequency will be referred to as the nominal rocking mode frequency. Substituting the expression for k_θ into Equation 4.98 and rearranging, an expression for d_k in terms of k is obtained:

$$d_k = \sqrt{\frac{\omega_{r0}^2 I_{rr}}{k}} \quad (4.99)$$

The nominal rocking mode frequency is extracted from the radial torque data by finding the frequencies at which disturbance amplifications occur. Figure 4-10(a) illustrates the extraction procedure using the Ithaco E Wheel. Given an initial guess for ω_{r0} , a MATLAB function is used to plot the frequencies of maximum disturbance amplitude at each wheel speed. These points are represented by "*" in the figure. The frequencies corresponding



(a) Matching Frequency to Radial Force Data



(b) Frequency Comparison with F_y Data

Figure 4-9: Setting Analytical Model Parameter, k , Using Ithaco E Wheel Radial Force Data

to the fundamental harmonic are also plotted on the figure and labeled along with the rocking mode frequencies corresponding to the initial guess (dashed lines). Note that all of the maximum frequency points lie along the fundamental harmonic line or in a “v” shape similar to that generated by the initial guess, but translated a bit on the frequency axis. It can be assumed that any maximum amplification points that do not lie along the fundamental harmonic line are due to the radial rocking mode. The user is asked if the initial guess fit is sufficient. If it is not, a new nominal rocking mode frequency is picked off the plot using the mouse until a good match, like the one shown with the solid V-shaped curve, is obtained. The nominal rocking mode frequency associated with the final match is returned as ω_{r_0} . Figure 4-10(b) shows the rocking mode frequencies extracted from the Ithaco E Wheel radial torque data plotted against the data for comparison. The rocking mode frequencies are represented with heavy black lines. The plot confirms that the value of ω_{r_0} extracted with the method described above is correct. Disturbance amplifications are visible in the data whenever a harmonic crossed the heavy black lines, as is expected.

4.3.2 Static and Dynamic Imbalance Parameters

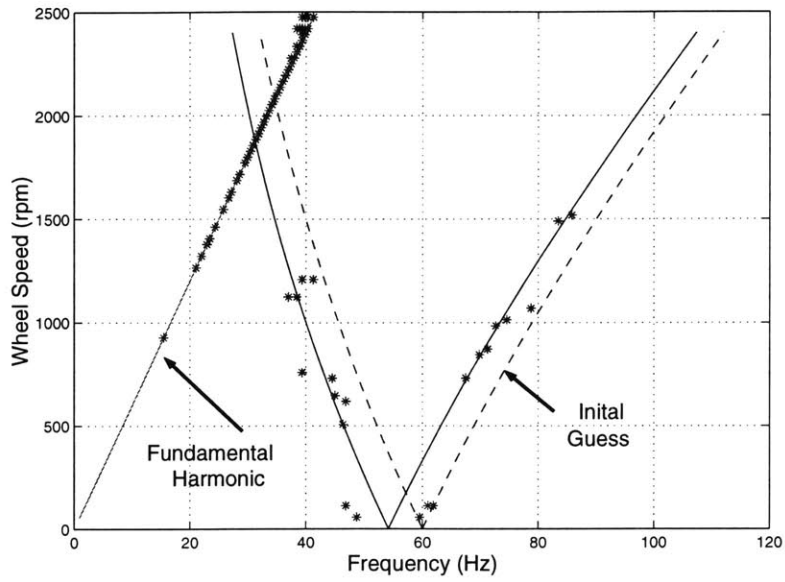
The static and dynamic imbalance mass parameters, m_s and m_d , are set using the amplitude coefficients corresponding to the fundamental harmonic ($h_i = 1.0$) obtained with the RWA DADM. The equations of motion for the analytical model, Equations 4.40 and 4.41, show that the radial forces are a result of the static imbalance and that the radial torques are due to the dynamic imbalance. Then, the expressions for the imbalance masses, obtained by rearranging Equations 4.30 and 4.45, are:

$$m_s = \frac{U_s}{r_s} = \left(\frac{60}{2\pi}\right)^2 \frac{C_{rad1}}{r_s} \quad (4.100)$$

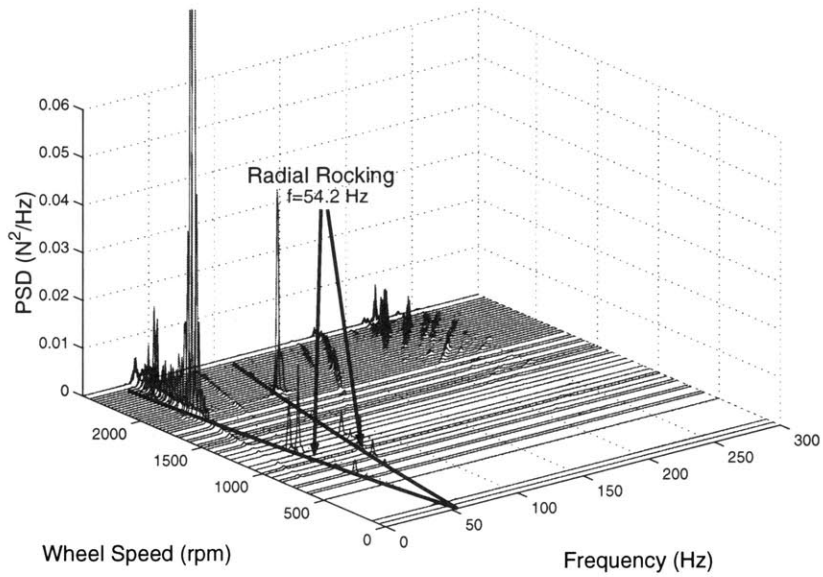
$$m_d = \frac{U_d}{2r_d h} = \left(\frac{60}{2\pi}\right)^2 \frac{C_{tor1}}{2r_d h} \quad (4.101)$$

where C_{rad1} and C_{tor1} are the amplitude coefficients corresponding to the fundamental harmonic for the radial force and torque disturbances, respectively. It is assumed that the coefficients are provided in units of N/rpm² and that $h_1 = 1.0$, as is the case for the Ithaco E Wheel.

Figure 4-11 shows the disturbance amplitudes of the fundamental harmonic plotted as a function of wheel speed from both the simulated model and the data. The simulation was



(a) Matching Frequency to Radial Torque Data



(b) Frequency Comparison with T_x Data

Figure 4-10: Setting Analytical Model Parameter, d_k , Using Ithaco E Wheel Radial Torque Data

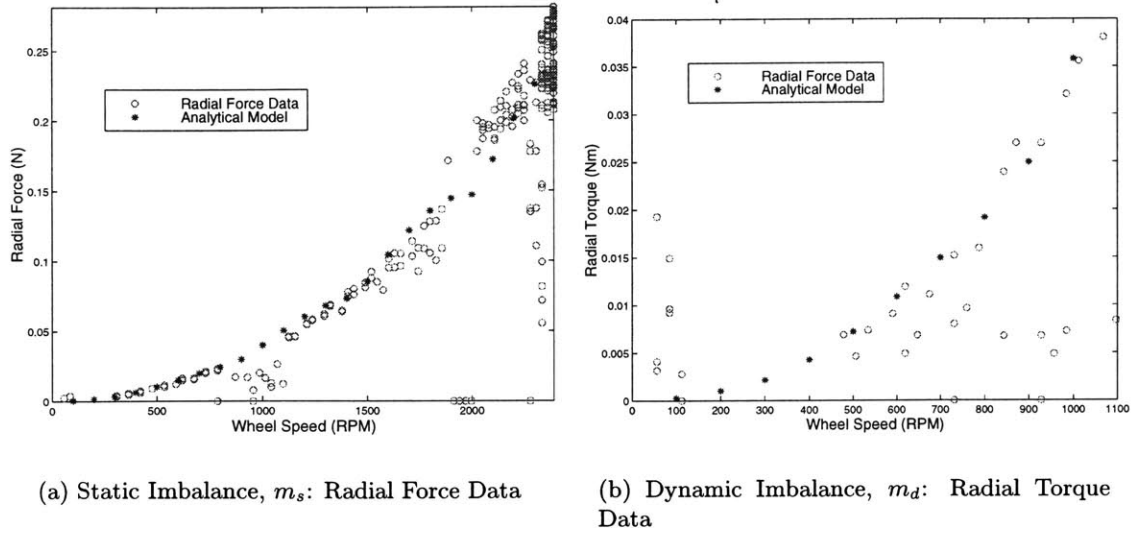


Figure 4-11: Setting Imbalance Parameters for Analytical Model Using Ithaco E Wheel Data for Fundamental Harmonic

run with the imbalance masses calculated with Equations 4.100 and 4.101, the stiffness parameters obtained through the methods presented in the preceding section and zero damping. The left plot, Figure 4-11(a), is from the radial force model and data and is used to check the value of m_s . Note that the model amplitudes, marked with “*” lie directly along the data (“o”). The right plot, Figure 4-11(b), is from the radial torque model and data and is used to check the value of m_d . In this plot, the data is only shown up to 1100 rpm because interactions between the fundamental harmonic and the negative whirl mode affects the disturbance amplitudes at the higher wheel speeds. Since the damping parameters are not being considered at this point in the parameter fitting process, the affected data should not be used to validate the imbalance mass, m_d . The figure shows that, for the low wheel speeds, the data and model correlate quite well.

4.3.3 Damping Parameters

The final model parameters which must be set are the damping parameters, c and d_c . A good methodology for choosing these parameters is still under development. In general, the disturbance amplification of the harmonics by the radial translation could be used to set c , and the disturbance amplification of the harmonics by the radial rocking modes can then be used to set the value of d_c ($c_\theta = cd_c^2$). However, for the example case being considered here,

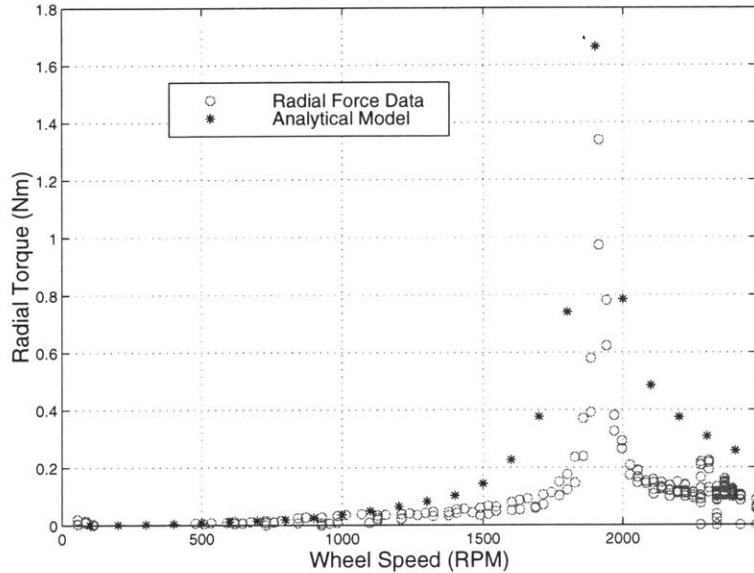


Figure 4-12: Setting Damping Parameters for Analytical Model Using Ithaco E Wheel Radial Torque Data for Fundamental Harmonic

the fundamental harmonic of the Ithaco E Wheel, no interaction between the harmonic and the radial translation mode occurs within the wheel speed range of the data. Therefore, d_c is set equal to d_k and the interaction between the fundamental harmonic and the negative whirl of the rocking mode is used to fit c .

The disturbance magnitude of the fundamental harmonic for the radial torque data and model are compared and c is set through trial and error. A reasonable initial guess is obtained using $\zeta_{r_i}^-$ from Equation 4.85 to set the negative rocking whirl damping ratio between 0 and 1. Figure 4-12 shows the resulting model/data correlation for the interaction between the fundamental harmonic and the negative rocking whirl for the Ithaco E Wheel. Note that although the wheel frequencies at which amplification occurs have been captured quite well, there is some discrepancy in the damping effects. The model overbounds the data in the neighborhood of the amplification. It was not possible, given the model parameters, to capture both the width and height of the disturbance peak in the data. As the c is reduced to capture the width of the peak, the maximum amplitude gets larger, severely over predicting the data. One possible explanation for the discrepancy may be the fact that linear damping was assumed in the model. The use of non-linear damping functions may improve the quality of the fit. It is also possible that there are unmodeled dynamics in the data that are causing the mismatch or that other model parameters, besides those associated

Table 4.2: Parameters for Analytical Model of Ithaco E Wheel

Parameter	Value		Units
	Model	Ithaco	
M_t	10.6	10.6	kg
R	19.65	19.65	cm
r_s	19.65	-	cm
r_d	19.65	-	cm
h	8.30	-	cm
k	21.7	-	N/ μm
d_k	2.37	-	cm
m_s	0.019	-	g
m_d	0.062	-	g
c	5067	-	kg/s
d_c	2.37	-	cm
ω_T	227.7	250	Hz
ω_r	54.9	60	Hz
\mathcal{U}_s	0.38	< 1.8	g-cm
\mathcal{U}_d	24.77	< 60	g-cm ²

with damping, affect the disturbance amplification. Therefore, it may be necessary to use additional model parameters to capture the disturbance amplification correctly.

4.3.4 Preliminary Results: Ithaco E Wheel

The resulting parameters for the analytical model of the Ithaco E Wheel (including only the fundamental harmonic) obtained through the methodologies described above are listed in Table 4.2. The second column contains the parameter values fit from the data, and the third column contains the values reported by Ithaco (when available). The first two parameters, M_t and R were taken straight from the Ithaco web site is indicated by the identical values in columns two and three. The final four values, the two modal frequencies and the imbalances, were calculated from model parameters obtained through data fitting. Comparison of these values (column 2) with those in column three shows that the model parameters which were extracted from the data seem to be on the correct order of magnitude.

The parameter values listed in the table were used to simulate the analytical model of the Ithaco E Wheel at 30 wheel speeds ranging from 100 to 3000 rpm. The RMS values of the modeled radial torque disturbance at each wheel speed were obtained and compared to the RMS values from the data and the empirical model. Recall that only the fundamental harmonic was accounted for in the analytical model considered for this

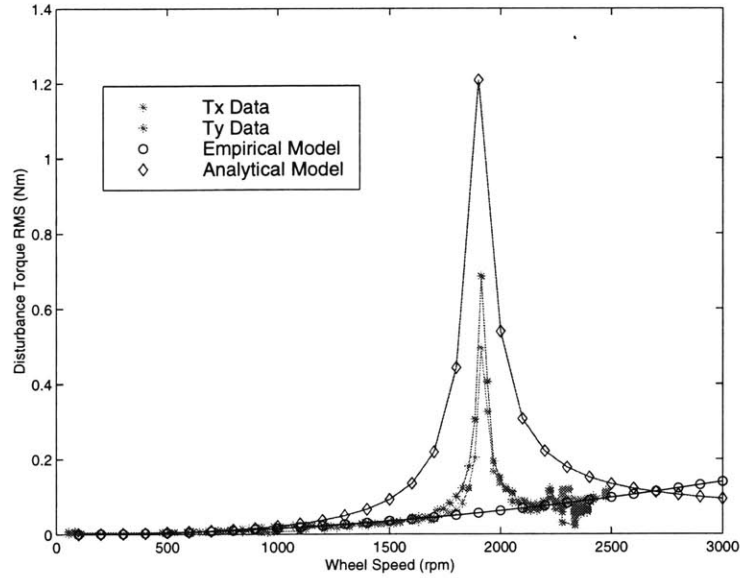


Figure 4-13: RMS Comparison of Ithaco E Wheel Radial Torque Data and RWA disturbance Models, frequency bandwidth: $[0, 1.3\Omega]$

example. Therefore, the RMS values of the data and the empirical model were calculated over the frequency bandwidth $[0, 1.3\Omega]$. Since the second harmonic of the Ithaco E Wheel is at 2.0Ω (Table 3.4) this frequency band only contains the fundamental harmonic and provides a good comparison between the data and the two models.

The result of this RMS comparison is plotted in Figure 4-13. The radial torque data (T_x and T_y) is marked with “*” and the empirical and analytical models are marked with circles and diamonds, respectively. The empirical model captures the disturbance behavior of the Ithaco E Wheel at low frequencies, but severely under-predicts the data at for wheel speeds at which interaction occurs between the fundamental harmonic and the radial rocking mode, as was discussed in Section 3.2.2. The analytical model, on the other hand, does well at low wheel speeds, but also captures the disturbance amplification due to the rocking mode. In this particular example, the rocking mode over-predicts the data by as much as a factor of two around the amplified disturbances. This discrepancy is due to the problems that were encountered when fitting the damping parameters. The correlation between the analytical model and the data should improve with the development of more accurate techniques to model and fit the disturbance amplifications.

4.4 Summary

An analytical RWA model that captures the fundamental harmonic disturbance and the radial rocking and translation modes of the RWA has been developed. The model is based on the physical behavior of the wheel and was derived using Lagrangian energy methods. It consists of a balanced flywheel on flexible supports with small masses strategically placed on it to model imbalances. The system has five degrees of freedom, two generalized rotations, which capture the radial rocking mode and the dynamic imbalance, two generalized translations, which capture the radial translation mode and the static imbalance, and the rotation of the wheel, which is assumed to be constant. Only the flywheel imbalance, which is the source of the fundamental harmonic, is physically included in the model, so the analytical model is extended to capture the additional harmonic disturbances that are visible in steady-state RWA data. These disturbances are incorporated into the model as harmonic forcing functions with frequencies and amplitudes based on the parameters of the empirical model that are extracted from steady-state data with the RWA DADM toolbox. The complete solutions of the generalized translations and rotations are obtained and simulated with MATLAB.

The extended analytical model is still under development. Modeling problems were encountered in the generalized rotations. A pole-zero cancellation occurs when solving for the particular solutions which eliminates the effects of one of the rocking mode whirls. This issue has been investigated in some detail and a temporary solution was proposed. In addition, a parameter fitting methodology which sets the analytical model parameters based on steady-state reaction wheel data in order to accurately capture the disturbance behavior of any given wheel is being developed. The preliminary framework for such a parameter fitting process has been presented along with an analytical model of the Ithaco E Wheel. The model presented contains only the fundamental harmonic and the interactions with the negative whirl of the rocking mode. The results show that the analytical model correlates to the disturbance data much better than the empirical. The interactions between the harmonics and the structural wheel mode are captured and an over-bound of the disturbances across all wheel speeds results. There are some discrepancies between the disturbance amplification that results in the model and that observed in the data which may be due to non-linear damping in the RWA or an error in the parameter matching methodology. A

closer model/data correlation should be obtained through investigation of the disturbance amplification and determination of the model parameters which control it.

Chapter 5

Model Coupling

The two types of disturbance models presented in this thesis, empirical and analytical, rely heavily on experimental disturbance data (forces and torques) obtained from isolated RWA vibration tests to determine model parameters. The vibration tests are conducted by mounting the RWA on a “rigid” test stand and using load cells to measure the disturbance forces that result from the motion of the wheel. Therefore, the disturbance models are based on a fixed boundary condition assumption. In effect, the disturbances captured are those induced by the wheels when attached to a fairly rigid structure. However, this boundary condition is not the same as that under which the wheels will actually be operated, since in application, the wheels are mounted on a flexible spacecraft, such as SIM. In addition, it has been shown that the RWA contains a significant degree of internal flexibility (see Sections 2.3, 3.2.1, and 3.2.2). It is highly likely that the flexibility of the RWA and the spacecraft will produce some degree of dynamic coupling between the two structures during operation. The wheel disturbances will induce vibrations in the spacecraft, exciting its flexible modes. The spacecraft vibrations will then drive the wheel, creating more disturbances. Since the models will be used to assess the performance of SIM in the presence of disturbances, it is necessary to accurately capture the nature of these disturbances, including any such coupling effects.

The following sections address the issue of dynamic coupling between the RWA and the spacecraft. First a simple example is used to demonstrate the effects of dynamic coupling on flexible systems. Then, a modeling technique is presented that was developed by Carl Blaurock and is based on the concept of acceleration feedback [26]. The technique is applied

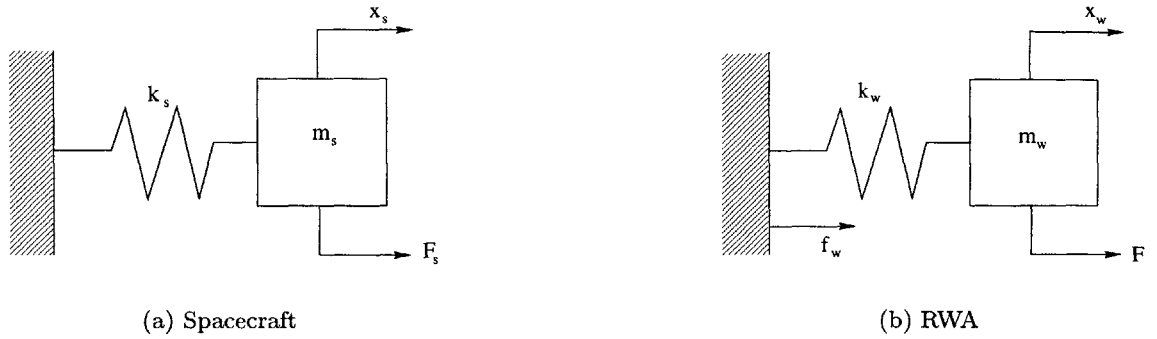


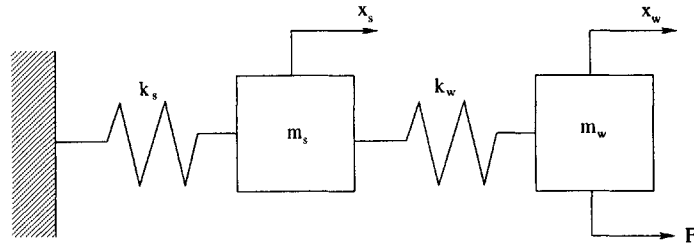
Figure 5-1: Spring Mass Models

to the problem of coupling a RWA disturbance model to a model of a flexible spacecraft and capturing the dynamics of the fully coupled system. The results of a simple analysis are presented for two different RWA compliance conditions and recommendations are made for future work. In addition, a laboratory experiment is designed to assess the degree of coupling between a representative RWA and a flexible structure and to explore and validate modeling and testing techniques that will allow accurate prediction of the fully coupled dynamics.

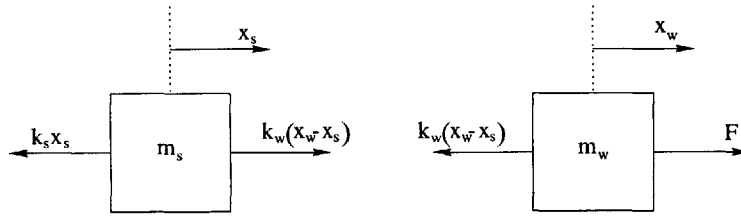
5.1 Motivating Example

A simple example with spring mass models is considered to illustrate the effects of dynamic coupling on flexible systems. Figure 5-1(b) represents the RWA mounted to a rigid structure, as it is during the isolated vibration tests. The forces, F and f_w , are the disturbance force on the wheel due to its motion and the force measured by the load cells at the interface of the wheel and the test fixture, respectively. Figure 5-1(a) represents a spacecraft subjected to a disturbance force, F_s . Both components are assumed to have internal compliance, k_w and k_s , and the fixture used to test the reaction wheel is assumed to be completely rigid.

The effects of coupling on the dynamics of a coupled spacecraft/RWA system, such as that shown in Figure 5-2(a), can be assessed by solving for the equations of motion of the coupled system in two ways. First, the two components are considered separately as shown in Figure 5-1. The measured RWA disturbance force, f_w , is determined from the EOM of the RWA model and applied to the spacecraft model as F_s , allowing the displacement of the spacecraft, x_s , to be obtained in terms of F . Then this same metric, x_s , is obtained



(a)



(b) Free-Body Diagrams

Figure 5-2: Coupled spacecraft and RWA system

by directly solving the EOM of the fully coupled system (Figure 5-2(a)). Comparing the results of the two models demonstrates the degree of coupling in the system. If the coupling of the two models has no effect on the dynamics of the system the two results should be equivalent.

It is clear from Figure 5-1(b) that the measured RWA disturbance force, f_w , is:

$$f_w = k_w x_w \quad (5.1)$$

The EOM of the RWA is obtained by summing the forces on the wheel:

$$m_w \ddot{x}_w = F - k_w x_w \quad (5.2)$$

Then, the measured disturbance force is found by taking the Laplace transform of Equation 5.2, solving for x_w and substituting the result into Equation 5.1:

$$f_w = \frac{k_w F}{m_w s^2 + k_w} \quad (5.3)$$

Similarly, the EOM of the spacecraft is:

$$m_s \ddot{x}_s = F_s - k_s x_s \quad (5.4)$$

The measured RWA disturbance force, f_w is applied to the spacecraft and the resulting displacement, x_s , is obtained by substituting Equation 5.3 for F_s in Equation 5.4, taking the Laplace transform and solving for x_s :

$$x_s = \frac{k_w F}{m_w m_s s^4 + (m_w k_s + m_s k_w) s^2 + k_w k_s} \quad (5.5)$$

For comparison, Newton's method is used to obtain the equations of motion of the coupled system (Figure 5-2(a)). Summing the forces acting on each mass (see Figure 5-2(b)) gives the following:

$$\begin{aligned} m_s \ddot{x}_s &= -(k_w + k_s) x_s + k_w x_w \\ m_w \ddot{x}_w &= k_w x_s - k_w x_w + F \end{aligned} \quad (5.6)$$

Then, the equations of motion are, in matrix form:

$$\begin{bmatrix} m_s & 0 \\ 0 & m_w \end{bmatrix} \begin{Bmatrix} \ddot{x}_s \\ \ddot{x}_w \end{Bmatrix} + \begin{bmatrix} k_s + k_w & -k_w \\ -k_w & k_w \end{bmatrix} \begin{Bmatrix} x_s \\ x_w \end{Bmatrix} = \begin{Bmatrix} 0 \\ F \end{Bmatrix} \quad (5.7)$$

An expression for the displacement, x_s , is obtained by solving the second equation for x_w , substituting the result into the first equation, and taking the Laplace transform:

$$x_s = \frac{k_w F}{m_w m_s s^4 + (m_w k_s + m_w k_w + m_s k_w) s^2 + k_w k_s} \quad (5.8)$$

Note that Equation 5.8 is not equivalent to Equation 5.5. The denominator of Equation 5.8 contains an extra s^2 term, $m_w k_w$. Note, however, that if:

$$m_s \gg m_w; \quad k_s \gg k_w \quad (5.9)$$

the additional term becomes negligible and Equation 5.8 becomes equivalent to Equation 5.5. This result suggests that there are coupling effects on the dynamics of a system

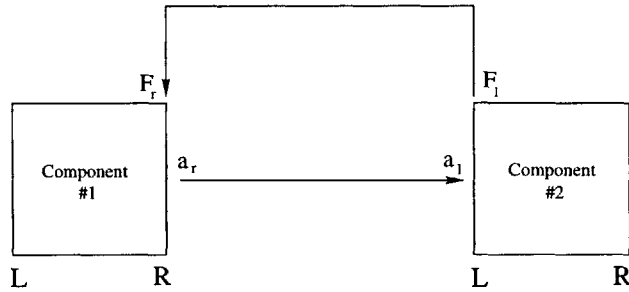


Figure 5-3: Connection of two components through feedback

consisting of flexible components, such as a RWA and spacecraft, which can be neglected under certain stiffness and mass conditions. However, the spring-mass models are greatly simplified versions of the RWA and spacecraft models, and there is no guarantee that meeting the condition of Equation 5.9 will ensure that the coupling effects are negligible for higher fidelity models. Therefore, it is necessary to find a way to account for dynamic coupling effects in the RWA disturbance model and/or the disturbance analysis process. One technique that may offer a solution, is component modeling, an acceleration feedback technique used for robotics, which allows the assembly of isolated components into the coupled system and fully captures the dynamic coupling of any system.

5.2 Component Modeling

Acceleration feedback, which is developed and described in detail in [26], allows the separation of a multi-body system into multiple subsystems. This modeling technique was initially developed for modeling robotic manipulators explicitly for control. An input/output description of the interconnection of components at each joint is used, and the attachment of two components is described as a feedback interconnection between the two subsystems. This technique is shown schematically in Figure 5-3. At the connection interface, the force on the right of the first component, F_r , is equal and opposite to the force on the left of the second component, F_l , and the acceleration on the left of the second component, a_l , is equal to the acceleration on the right of the first component, a_r .

The modeling algorithm consists of five steps:

- (i) Determine the number, type and arrangement of components.
- (ii) Model each component as a free-free body, with force inputs and acceleration outputs

at each attachment location.

- (iii) Invert the force input and acceleration output of one attachment point per component.
- (iv) Define the boundary conditions between attached components.
- (v) Assemble the system model.

The first step simply involves defining how many components there are in the system, determining which components are attached and locating the attachment points. Once this information is known, the components are modeled in free-free form and the forces at each end are specified. The transfer function matrix of a single component from boundary forces to boundary accelerations is of the form:

$$\begin{Bmatrix} a_l \\ a_r \end{Bmatrix} = \begin{bmatrix} H_{ll}(s) & H_{lr}(s) \\ H_{rl}(s) & H_{rr}(s) \end{bmatrix} \begin{Bmatrix} F_l \\ F_r \end{Bmatrix} \quad (5.10)$$

where $H_{ll}(s)$, $H_{lr}(s)$, $H_{rl}(s)$, and $H_{rr}(s)$ are transfer functions from F_l to a_l , F_r to a_l , F_l to a_r and F_r to a_r , respectively. In the third step, the component model is obtained by inverting the force input and acceleration output of the left attachment:

$$\begin{Bmatrix} F_l \\ a_r \end{Bmatrix} = \begin{bmatrix} H_{ll}^{-1} & -H_{ll}^{-1}H_{lr} \\ H_{rl}H_{ll}^{-1} & H_{rr} - H_{rl}H_{ll}^{-1}H_{lr} \end{bmatrix} \begin{Bmatrix} a_l \\ F_r \end{Bmatrix} \quad (5.11)$$

In this form, the outputs of one component can be fed to an attached component and the inputs driven by the attached component. In the next step, boundary conditions are used to equate forces and moments, and linear and angular accelerations across the joint. If both components contain only translational degrees of freedom (as is the case for the spring-mass models), the boundary conditions reduce to:

$$\begin{aligned} F_{r_{i-1}} &= -R_i^t F_{l_i} \\ a_{l_i} &= R_i a_{r_{i-1}} \end{aligned} \quad (5.12)$$

where R_i is the rotation matrix for the i th component. The final step in the modeling process is the assembly of the system model which is accomplished by using the boundary conditions to append the two individual models producing the EOM for the coupled system.

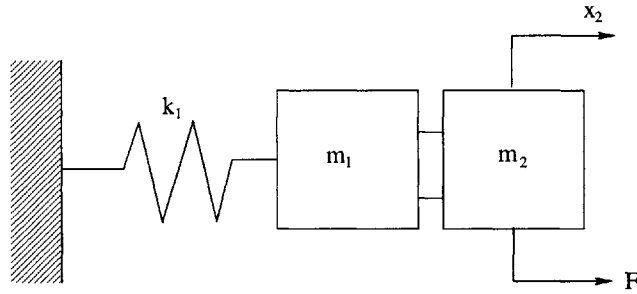


Figure 5-4: Example system containing two subsystems

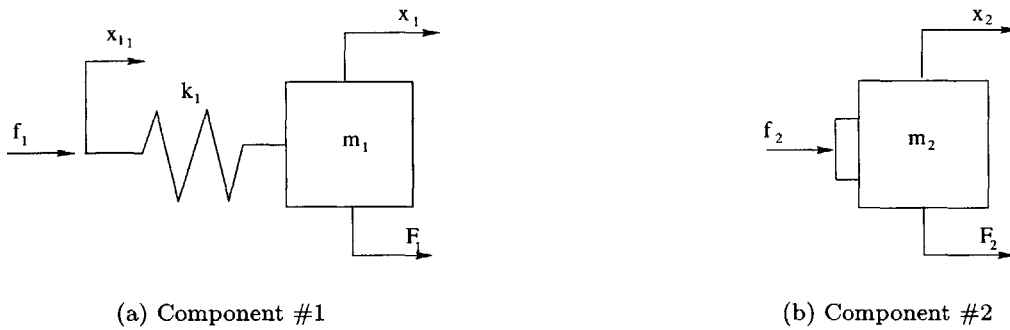


Figure 5-5: Isolated components in free-free form

5.2.1 Example

The coupled system shown in Figure 5-4 is used as an example to clearly illustrate the modeling process.

Step (i): Determine the number, type and arrangement of components.

As illustrated in Figure 5-4, there are two components, and the left side of the second component is attached to the right side of the first.

Step (ii): Model each component as a free-free body, with force inputs and acceleration outputs at each attachment location.

Figure 5-5 shows the two component models in free-free form. The mathematical model of component #1 is obtained by direct application of Newton's laws of motion. The component has two translational degrees of freedom, x_{l_1} and x_1 , and its equations of motion are:

$$m_1 \ddot{x}_1 = F_1 - k_1(x_1 - x_{l_1}) \quad (5.13)$$

$$f_1 = -k_1(x_1 - x_{l_1})$$

Then, through inspection:

$$\begin{aligned} F_{r_1} &= F_1 & a_{r_1} &= \ddot{x}_1 \\ F_{l_1} &= f_1 = -k_1(x_1 - x_{l_1}) & a_{l_1} &= \ddot{x}_{l_1} \end{aligned} \quad (5.14)$$

Finally, by substituting Equations 5.14 into Equation 5.13 and transforming to the Laplace domain, the transfer function matrix from boundary forces to boundary accelerations is obtained:

$$\begin{Bmatrix} a_{l_1} \\ a_{r_1} \end{Bmatrix} = \begin{bmatrix} \frac{m_1 s^2 + k_1}{m_1 k_1} & \frac{1}{m_1} \\ \frac{1}{m_1} & \frac{1}{m_1} \end{bmatrix} \begin{Bmatrix} F_{l_1} \\ F_{r_1} \end{Bmatrix} \quad (5.15)$$

The same modeling process is applied to component #2 (Figure 5-5(b)) which only has one translational degree of freedom, x_2 . Summing the forces on this component gives:

$$m_2 \ddot{x}_2 = F_2 + f_2 \quad (5.16)$$

The boundary forces and accelerations are:

$$\begin{aligned} F_{r_2} &= F_2 & a_{r_2} &= \ddot{x}_2 = s^2 x_2 \\ F_{l_2} &= f_2 & a_{l_2} &= a_{r_2} \end{aligned} \quad (5.17)$$

The transfer function matrix is obtained by substituting Equations 5.17 into Equation 5.16 and solving for the boundary accelerations:

$$\begin{Bmatrix} a_{l_2} \\ a_{r_2} \end{Bmatrix} = \begin{bmatrix} \frac{1}{m_2} & \frac{1}{m_2} \\ \frac{1}{m_2} & \frac{1}{m_2} \end{bmatrix} \begin{Bmatrix} F_{l_2} \\ F_{r_2} \end{Bmatrix} \quad (5.18)$$

Step (iii): Invert the force input and acceleration output of one attachment point per component.

Inversion of the left attachment point of each component is accomplished using Equa-

tion 5.11. The resulting models for components #1 and #2 are, respectively:

$$\begin{Bmatrix} F_{l_1} \\ a_{r_1} \end{Bmatrix} = \begin{bmatrix} \frac{k_1 m_1}{m_1 s^2 + k_1} & -\frac{k_1}{m_1 s^2 + k_1} \\ \frac{k_1}{m_1 s^2 + k_1} & \frac{s^2}{m_1 s^2 + k_1} \end{bmatrix} \begin{Bmatrix} a_{l_1} \\ F_{r_1} \end{Bmatrix} \quad (5.19)$$

$$\begin{Bmatrix} F_{l_2} \\ a_{r_2} \end{Bmatrix} = \begin{bmatrix} m_2 & -1 \\ 1 & 0 \end{bmatrix} \begin{Bmatrix} a_{l_2} \\ F_{r_2} \end{Bmatrix} \quad (5.20)$$

Step (iv): Define the boundary conditions between attached components.

Since both components contain only translational degrees of freedom and are defined in the same coordinate system (i.e. $R_i = 1$) the boundary conditions are:

$$\begin{aligned} F_{r_1} &= -F_{l_2} \\ a_{l_2} &= a_{r_1} \end{aligned} \quad (5.21)$$

Step (v): Assemble the system model.

The component models, Equations 5.19 and 5.20, are used along with the boundary conditions, Equation 5.21, to obtain a model of the coupled system, Figure 5-4. First, the two component models are inverted resulting in the following matrices for components #1 and #2, respectively:

$$\begin{Bmatrix} a_{l_1} \\ F_{r_1} \end{Bmatrix} = \begin{bmatrix} \frac{s^2}{k_1} & 1 \\ -1 & m_1 \end{bmatrix} \begin{Bmatrix} F_{l_1} \\ a_{r_1} \end{Bmatrix} \quad (5.22)$$

$$\begin{Bmatrix} a_{l_2} \\ F_{r_2} \end{Bmatrix} = \begin{bmatrix} 0 & 1 \\ -1 & m_2 \end{bmatrix} \begin{Bmatrix} F_{l_2} \\ a_{r_2} \end{Bmatrix} \quad (5.23)$$

It is clear from Figure 5-4 that the force and acceleration on the right side of the coupled system are equal to those on the right side of component #2 and the force and acceleration of the left side of the coupled system are equal to those on the left side of component #1:

$$\begin{aligned} F_{r_{sys}} &= F_{r_2} & a_{r_{sys}} &= a_{r_2} \\ F_{l_{sys}} &= F_{l_1} & a_{l_{sys}} &= a_{l_1} \end{aligned} \quad (5.24)$$

Therefore, to obtain the equations for the coupled model, the forces and accelerations on the left side of component #2 and the right side of component #1 must be eliminated. Expressions for these boundary forces and accelerations are obtained from the component model matrices and their inverses given in Equations 5.19-5.20 and 5.22-5.23:

$$a_{r_1} = \frac{k_1}{m_1 s^2 + k_1} a_{l_1} + \frac{s^2}{m_1 s^2 + k_1} F_{r_1} \quad (5.25)$$

$$F_{r_1} = -F_{l_1} + m_1 a_{r_1} \quad (5.26)$$

$$a_{l_2} = a_{r_2} \quad (5.27)$$

$$F_{l_2} = m_2 a_{l_2} - F_{r_2} \quad (5.28)$$

Substituting Equation 5.25 into Equation 5.26 results in a relationship for F_{r_1} in terms of only the left attachment of component #1:

$$F_{r_1} = -\frac{m_1 s^2 + k_1}{k_1} F_{l_1} + m_1 a_{l_1} \quad (5.29)$$

Similarly, substituting Equation 5.29 into Equation 5.25 gives the following relationship for a_{r_1} in terms of the left attachment of component #1:

$$a_{r_1} = -\frac{s^2}{k_1} F_{l_1} + a_{l_1} \quad (5.30)$$

Now the boundary conditions in Equation 5.21 are introduced to eliminate the acceleration on the left of component #2 and the force on the right of component #1:

$$a_{r_2} = -\frac{s^2}{k_1} F_{l_1} + a_{l_1} \quad (5.31)$$

$$F_{l_1} = \frac{m_1 k_1}{m_1 s^2 + k_1} a_{l_1} + \frac{m_2 k_1}{m_1 s^2 + k_1} a_{r_2} - \frac{k_1}{m_1 s^2 + k_1} F_{r_2} \quad (5.32)$$

Finally, the force on the left of component #1 is found in terms of the acceleration on the left of #1 and the force on right of #2 by substituting Equation 5.31 into Equation 5.32.

$$F_{l_1} = \frac{k_1(m_1 + m_2)}{(m_1 + m_2)s^2 + k_1} a_{l_1} - \frac{k_1}{(m_1 + m_2)s^2 + k_1} F_{r_2} \quad (5.33)$$

Similarly, the acceleration on the right of component #2 is obtained by substituting Equa-

tion 5.33 into Equation 5.31.

$$a_{r_2} = \frac{k_1}{(m_1 + m_2)s^2 + k_1} a_{l_1} + \frac{s^2}{(m_1 + m_2)s^2 + k_1} F_{r_2} \quad (5.34)$$

The model of the coupled system, in matrix form, is then:

$$\begin{Bmatrix} F_{l_{sys}} \\ a_{r_{sys}} \end{Bmatrix} = \frac{1}{(m_1 + m_2)s^2 + k_1} \begin{bmatrix} k_1(m_1 + m_2) & -k_1 \\ k_1 & s^2 \end{bmatrix} \begin{Bmatrix} a_{l_{sys}} \\ F_{r_{sys}} \end{Bmatrix} \quad (5.35)$$

In this simplified case, the modeling process can be validated by obtaining the coupled system model directly and comparing the result to that obtained through the acceleration feedback technique. Summing the forces on the system shown in Figure 5-4 gives:

$$(m_1 + m_2)\ddot{x}_1 = F - k_1(x_2 - x_{l_1}) \quad (5.36)$$

The boundary forces and accelerations are, by inspection:

$$F_{l_{sys}} = -k_1(x_2 - x_{l_1}) \quad (5.37)$$

$$a_{l_{sys}} = \ddot{x}_{l_1} \quad (5.38)$$

$$F_{r_{sys}} = F \quad (5.39)$$

$$a_{r_{sys}} = \ddot{x}_2 \quad (5.40)$$

After making the appropriate substitutions and performing the necessary algebraic manipulations the the system model is:

$$\begin{Bmatrix} F_{l_{sys}} \\ a_{r_{sys}} \end{Bmatrix} = \frac{1}{(m_1 + m_2)s^2 + k_1} \begin{bmatrix} k_1(m_1 + m_2) & -k_1 \\ k_1 & s^2 \end{bmatrix} \begin{Bmatrix} a_{l_{sys}} \\ F_{r_{sys}} \end{Bmatrix} \quad (5.41)$$

Note that this result is identical to the system model obtained through the component modeling algorithm (Equation 5.35).

Table 5.1: Plant Models

Plant Model	Included in Model		
	Spacecraft	RWA mass	RWA compliance
<i>i</i>	✓		
<i>ii</i>	✓	✓	
<i>iii</i>	✓	✓	✓

Table 5.2: Compliance conditions for RWA Disturbance Models

Disturbance Model	Wheel Compliance	Test Stand Compliance
1		
2	✓	
3		✓
4	✓	✓

5.3 RWA Coupling Analyses

The acceleration feedback technique and simple spring-mass models described above allow the exploration of RWA disturbance modeling and testing methods. First, the acceleration feedback modeling algorithm is used to obtain a model of the coupled spacecraft/RWA system. This coupled model is used to determine the spectral density matrix for the coupled system response to a disturbance from the RWA. Then, a second analysis is performed with isolated RWA disturbance and spacecraft models. A PSD from a RWA disturbance model based on the measured disturbance force obtained from a hard-mounted RWA vibration test is applied to three different “spacecraft,” or plant, models, each containing the spacecraft and some features of the RWA. The features included in each of the three models are listed in Table 5.1. The resulting output spectral density matrix of the plant is compared to that obtained from the coupled system to determine which, if any, of the modeling methods accurately capture the dynamics of the coupled system.

The analysis is performed for four types of RWA disturbance models, each assuming different compliance conditions in the RWA and the test fixture it is mounted to during the vibration tests (see Table 5.2). As a result, the complete analysis will consist of 12 sub-analyses, one for each of the plant/disturbance model combinations. At this time, half of the analyses are completed as shown in Table 5.3. Each row in this table can be considered a separate case. The results presented in the following sections consider disturbance models

Table 5.3: RWA/Spacecraft Coupling Analysis

	Plant Model		
	(i)	(ii)	(iii)
RWA ₁	✓	✓	✓
RWA ₂	✓	✓	✓
RWA ₃			
RWA ₄			

1 and 2 with each of the three plants (rows one and two), or cases #1 and #2.

Throughout this discussion subscripts on model parameters (k,m,a,F,x,y,H) are used to indicate the component number, and superscripts in parentheses denote the case, or disturbance model, number. A superscript (c) on a model parameter or a PSD indicates that the corresponding model has been constrained. All other PSDs and parameters refer to the free-free component models.

5.3.1 Case #1: No Compliance in RWA or Test Fixture

In the first case, both the wheel and the test fixture that supports the wheel during the isolated test are assumed to be rigid. The only compliance in the system is that of the spacecraft. Figure 5-5 shows the spacecraft and wheel models in free-free form. For the remainder of the discussion the spacecraft will be referred to as component #1 and the RWA as component #2.

First, the two component models are obtained with Newton's method:

$$\underbrace{\begin{Bmatrix} F_{l_1} \\ a_{r_1} \end{Bmatrix}}_{y_1} = \underbrace{\frac{1}{m_1 s^2 + k_1} \begin{bmatrix} m_1 k_1 & -k_1 \\ k_1 & s^2 \end{bmatrix}}_{\mathbf{H}_1} \underbrace{\begin{Bmatrix} a_{l_1} \\ F_{r_1} \end{Bmatrix}}_{x_1} \quad (5.42)$$

$$\underbrace{\begin{Bmatrix} F_{l_2} \\ a_{r_2} \end{Bmatrix}}_{y_2^{(1)}} = \underbrace{\begin{bmatrix} m_2 & -1 \\ 1 & 0 \end{bmatrix}}_{\mathbf{H}_2^{(1)}} \underbrace{\begin{Bmatrix} a_{l_2} \\ F_{r_2} \end{Bmatrix}}_{x_2^{(1)}} \quad (5.43)$$

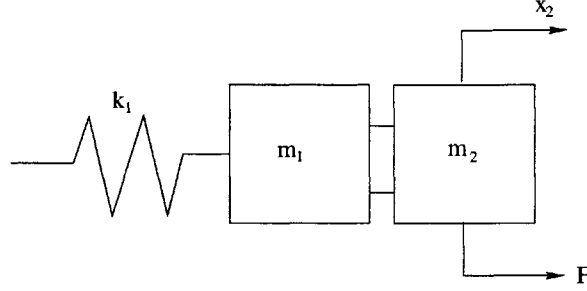


Figure 5-6: Coupled system for Case #1

and acceleration feedback is applied to create a model of the coupled system (Figure 5-6):

$$\underbrace{\begin{Bmatrix} F_{l_1} \\ a_{r_2} \end{Bmatrix}}_{y_{sys}^{(1)}} = \underbrace{\frac{1}{(m_1 + m_2)s^2 + k_1} \begin{bmatrix} k_1(m_1 + m_2) & -k_1 \\ k_1 & s^2 \end{bmatrix}}_{H_{sys}^{(1)}} \underbrace{\begin{Bmatrix} a_{l_1} \\ F_{r_2} \end{Bmatrix}}_{x_{sys}^{(1)}} \quad (5.44)$$

The models in Equations 5.42 and 5.43 are then used to test the three plants. Constraining component #2 at the left end ($a_{l_2} = 0$) ensures that the PSD of the force on the left of the component, $S_{F_{l_2}F_{l_2}}^{(1,c)}$ is analogous to the PSD of the disturbance force measured during the isolated RWA test. Then, the analysis of the first plant model, (i), is performed by applying $S_{F_{l_2}F_{l_2}}^{(1,c)}$ to the right side of component #1 as $S_{F_{r_1}F_{r_1}}$. This analysis is analogous to applying a frequency domain disturbance model based on the fixed isolated test data to a model of the spacecraft alone.

The measured PSD, $S_{F_{l_2}F_{l_2}}^{(1,c)}$, can be written in terms of $S_{F_{r_2}F_{r_2}}$. Recall from Section 2.1 that the PSD of a random process is defined as the Fourier transform of the autocorrelation function. Then the measured PSD is:

$$S_{F_{l_2}F_{l_2}}^{(1,c)} = \int_{-\infty}^{\infty} E [F_{l_2}(t)F_{l_2}(t + \tau)] e^{-i\omega\tau} d\tau \quad (5.45)$$

It is clear from Equation 5.43 that the force on the left of component #2 is related to the force on the right as follows:

$$F_{l_2} = m_2 a_{l_2} - F_{r_2} \quad (5.46)$$

Substituting Equation 5.46 into Equation 5.45, expanding and taking advantage of the

linearity of the expected value gives:

$$S_{F_{l_2}F_{l_2}}^{(1,c)} = m_2^2 S_{a_{l_2}a_{l_2}} - m_2 S_{F_{r_2}a_{l_2}} - m_2 S_{a_{l_2}F_{r_2}} + S_{F_{r_2}F_{r_2}} \quad (5.47)$$

Then, using the fact that component #2 is constrained on the left ($a_{l_2} = 0$) and assuming that F_{r_2} and a_{l_2} are uncorrelated, reduces the expression for the PSD of the measured disturbance:

$$S_{F_{l_2}F_{l_2}}^{(1,c)} = S_{F_{r_2}F_{r_2}} \quad (5.48)$$

The RWA disturbance model is applied to the plant by setting the PSD of the force input to component #1, $S_{F_{r_1}F_{r_1}}$, equal to that of the measured disturbance:

$$S_{F_{r_1}F_{r_1}} = S_{F_{l_2}F_{l_2}}^{(1,c)} = S_{F_{r_2}F_{r_2}} \quad (5.49)$$

The left end of the component is constrained such that $a_{l_1} = 0$, reducing the component model (Equation 5.42):

$$\underbrace{\begin{Bmatrix} F_{l_1} \\ a_{r_1} \end{Bmatrix}}_{\mathbf{y}_1^{(c)}} = \underbrace{\frac{1}{m_1 s^2 + k_1} \begin{bmatrix} -k_1 \\ s^2 \end{bmatrix}}_{\mathbf{H}_1^{(c)}} F_{r_1} \quad (5.50)$$

The spectral density matrices of the inputs and outputs of a system are related as follows [21]:

$$\mathbf{S}_{yy} = \mathbf{H}(\omega) \mathbf{S}_{xx} \mathbf{H}^H(\omega) \quad (5.51)$$

where $\mathbf{H}(\omega)$ is the transfer function matrix from inputs, x , to outputs, y , \mathbf{S}_{xx} is the input spectral density matrix, \mathbf{S}_{yy} is the output spectral density matrix and the notation $(\cdot)^H$ indicates the Hermitian, or complex-conjugate transpose. Since Equation 5.50 is the plant model for this analysis, the output spectral density matrix is $\mathbf{S}_{y_1 y_1}^{(1,c)}$, but for simplicity of notation, the plant model numbers will be used to identify the output spectral density matrices, i.e. : $\mathbf{S}_{y_1 y_1}^{(1,c)} = \mathbf{S}_i^{(1,c)}$ (see Table 5.1). The output PSD matrix of plant model (i) resulting from disturbance model 1 (see Table 5.2) is obtained by substituting $\mathbf{H}_1^{(c)}$ from Equation 5.50 and $S_{F_{r_1}F_{r_1}}$ (Equation 5.49) into Equation 5.51 and transforming from the

Laplace to the frequency domain by substituting $s = i\omega$, where $i = \sqrt{-1}$:

$$\mathbf{S}_i^{(1,c)} = \begin{bmatrix} S_{F_{l_1} F_{l_1}} & S_{F_{l_1} a_{r_1}} \\ S_{a_{r_1} F_{l_1}} & S_{a_{r_1} a_{r_1}} \end{bmatrix} = \frac{1}{(-m_1\omega^2 + k_1)^2} \begin{bmatrix} k_1^2 & k_1\omega^2 \\ k_1\omega^2 & \omega^4 \end{bmatrix} S_{F_{r_2} F_{r_2}} \quad (5.52)$$

The exact solution can be obtained for comparison with Equation 5.52 by assuming that $S_{F_{r_2} F_{r_2}}$ is known and applying it to the coupled system model obtained through acceleration feedback. First Equation 5.44 is simplified by setting $a_{l_1} = 0$, effectively constraining component #1:

$$\underbrace{\begin{Bmatrix} F_{l_1} \\ a_{r_2} \end{Bmatrix}}_{\mathbf{y}_{sys}^{(1,c)}} = \underbrace{\frac{1}{(m_1 + m_2)s^2 + k_1} \begin{bmatrix} -k_1 \\ s^2 \end{bmatrix}}_{\mathbf{H}_{sys}^{(1,c)}} F_{r_2} \quad (5.53)$$

Note that the outputs of the coupled system, $\mathbf{y}_{sys}^{(1,c)}$, are not the same as the outputs of component #1, $\mathbf{y}_1^{(c)}$. The second output of the coupled system is a_{r_2} , while the second output of component #1 is a_{r_1} . This discrepancy in the outputs does not allow comparison between the exact solution and the three plant models (all of which include the component #1 model). Therefore, a new system model that has the same outputs as component #1 is derived. The RWA component model (Equation 5.43) provides an expression for a_{r_2} in terms of a_{l_2} , which is related to a_{r_2} through the boundary conditions (Equation 5.12) at the connection point of the two components :

$$a_{r_2} = a_{l_2} = a_{r_1} \quad (5.54)$$

Then the modified system model is obtained by substituting Equation 5.54 into the original system model (Equation 5.53). For disturbance model 1, the modified system transfer function, $\mathbf{H}_{sys'}^{(1,c)}$, is equivalent to the original, $\mathbf{H}_{sys}^{(1,c)}$

$$\underbrace{\begin{Bmatrix} F_{l_1} \\ a_{r_1} \end{Bmatrix}}_{\mathbf{y}_{sys'}^{(1,c)}} = \underbrace{\frac{1}{(m_1 + m_2)s^2 + k_1} \begin{bmatrix} -k_1 \\ s^2 \end{bmatrix}}_{\mathbf{H}_{sys'}^{(1,c)}} F_{r_2} \quad (5.55)$$

Then, the exact output PSD of the coupled system is obtained by substituting $\mathbf{H}_{sys'}^{(1,c)}$

into Equation 5.51 and transforming from the Laplace to the frequency domain ($s = i\omega$):

$$\mathbf{S}_{y_{sys'} y_{sys'}}^{(1,c)} = \begin{bmatrix} S_{F_{l_1} F_{l_1}} & S_{F_{l_1} a_{r_1}} \\ S_{a_{r_1} F_{l_1}} & S_{a_{r_1} a_{r_1}} \end{bmatrix} = \frac{1}{(-(m_1 + m_2)\omega^2 + k_1)^2} \begin{bmatrix} k_1^2 & k_1\omega^2 \\ k_1\omega^2 & \omega^4 \end{bmatrix} S_{F_{r_2} F_{r_2}} \quad (5.56)$$

The output, $\mathbf{S}_{y_{sys'} y_{sys'}}^{(1,c)}$, correctly captures the coupled dynamics of component #1 and component #2 since it is obtained by applying F_{r_2} directly to the coupled system. Note that the output obtained with plant model (i) (Equation 5.52) does not equal the exact result (Equation 5.56).

The second plant model (ii) includes both component #1 and the mass of component #2, m_2 . When a disturbance model of type 1 is used, this plant model is equivalent to the modified model of the coupled system (Equation 5.55). The output PSD resulting from applying $S_{F_{l_2} F_{l_2}}^{(1,c)}$ to this plant model is obtained by substituting $\mathbf{H}_{sys'}^{(1,c)}$ and the expression for $S_{F_{l_2} F_{l_2}}^{(1,c)}$ (Equation 5.48) into Equation 5.51:

$$\mathbf{S}_{ii}^{(1,c)} = \begin{bmatrix} S_{F_{l_1} F_{l_1}} & S_{F_{l_1} a_{r_1}} \\ S_{a_{r_1} F_{l_1}} & S_{a_{r_1} a_{r_1}} \end{bmatrix} = \frac{1}{(-(m_1 + m_2)\omega^2 + k_1)^2} \begin{bmatrix} k_1^2 & k_1\omega^2 \\ k_1\omega^2 & \omega^4 \end{bmatrix} S_{F_{r_2} F_{r_2}} \quad (5.57)$$

Comparison of Equation 5.57 and Equation 5.56 shows that, for a disturbance model of type 1, plant model (ii) captures the coupled system behavior correctly. Plant model (iii) is not applicable for this disturbance model because the assumption is made that there is no internal wheel compliance. The results of this analysis suggest that if neither the RWA nor the test fixture has internal compliance, a disturbance model created from the results of an isolated, hard-mounted RWA vibration test can be applied to a model of the spacecraft through frequency analysis techniques to accurately predict the dynamics of the coupled system if the mass of the RWA is included in the spacecraft model.

5.3.2 Case #2: Internal Compliance in RWA Only

In the second case, a disturbance model based on vibration data obtained from a flexible RWA hard-mounted to a rigid test fixture is considered. Schematics of the two free-free components are presented in Figure 5-7.

The component model of component #1 is the same as in case #1 (Equation 5.42), but

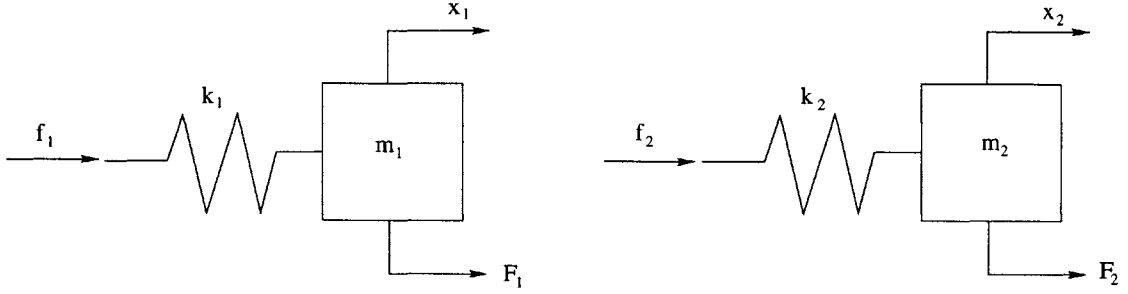


Figure 5-7: Component Models for Case #2

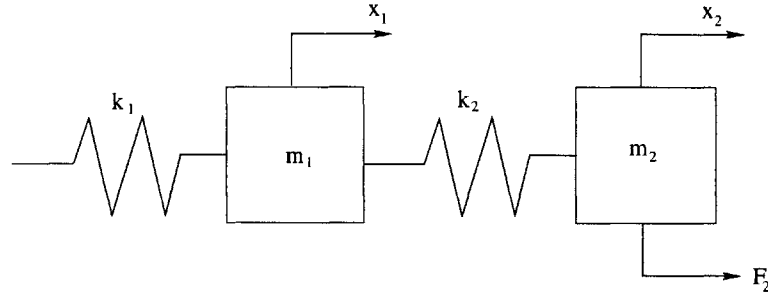


Figure 5-8: System Model for Case #2

the model of component #2 has changed with the addition of internal wheel compliance:

$$\underbrace{\begin{Bmatrix} F_{l2} \\ a_{r2} \end{Bmatrix}}_{y_2^{(2)}} = \underbrace{\frac{1}{m_2 s^2 + k_2} \begin{bmatrix} m_2 k_2 & -k_2 \\ k_2 & s^2 \end{bmatrix}}_{\mathbf{H}_2^{(2)}} \underbrace{\begin{Bmatrix} a_{l2} \\ F_{r2} \end{Bmatrix}}_{x_2^{(2)}} \quad (5.58)$$

Using acceleration feedback methods, the coupled system model (Figure 5-8) is:

$$\underbrace{\begin{Bmatrix} F_{l1} \\ a_{r2} \end{Bmatrix}}_{y_{sys}^{(2)}} = \underbrace{\frac{\begin{bmatrix} k_1(m_1 m_2 s^2 + k_2(m_1 + m_2)) & -k_1 k_2 \\ k_1 k_2 & s^2(m_1 s^2 + k_1 + k_2) \end{bmatrix}}{(m_1 s^2 + k_1)(m_2 s^2 + k_2) + m_2 k_2 s^2}}_{\mathbf{H}_{sys}^{(2)}} \underbrace{\begin{Bmatrix} a_{l1} \\ F_{r2} \end{Bmatrix}}_{x_{sys}^{(2)}} \quad (5.59)$$

The measured force PSD, $S_{F_{l2} F_{l2}}^{(2,c)}$ is written in terms of $S_{F_{r2} F_{r2}}$ using the methods described in the previous section. In this case, the relationship between the forces on the left and right of component #2 includes the RWA compliance:

$$F_{l2} = \frac{1}{m_2 s^2 + k_2} (m_2 k_2 a_{l2} - k_2 F_{r2}) \quad (5.60)$$

Then, by substituting this relationship into Equation 5.45, expanding, and substituting $s = i\omega$ an expression for the measured force PSD is obtained:

$$S_{F_{l_2}F_{l_2}}^{(2,c)} = \frac{k_2^2}{(-m_2\omega^2 + k_2)^2} \left[m_2^2 S_{a_{l_2}a_{l_2}} - m_2 S_{F_{r_2}a_{l_2}} - m_2 S_{a_{l_2}F_{r_2}} + S_{F_{r_2}F_{r_2}} \right] \quad (5.61)$$

This expression can be simplified using the boundary conditions on the left side of the component, $a_{l_2} = 0$, and the assumption that a_{l_2} and F_{r_2} are uncorrelated:

$$S_{F_{l_2}F_{l_2}}^{(2,c)} = \frac{k_2^2}{(-m_2\omega^2 + k_2)^2} S_{F_{r_2}F_{r_2}} \quad (5.62)$$

Plant model (i) is tested by transforming $H_1^{(c)}$ (Equation 5.50) to the frequency domain and substituting the result and Equation 5.62 into Equation 5.51 to obtain the output PSD matrix:

$$\mathbf{S}_i^{(2,c)} = \frac{1}{(-m_1\omega^2 + k_1)^2(-m_2\omega^2 + k_2)^2} \begin{bmatrix} k_1^2 k_2^2 & k_1 k_2^2 \omega^2 \\ k_1 k_2^2 \omega^2 & k_2^2 \omega^4 \end{bmatrix} S_{F_{r_2}F_{r_2}} \quad (5.63)$$

Applying a known force PSD, $S_{F_{r_2}F_{r_2}}$, to the coupled system for comparison with the isolated component analyses is more involved for case #2 than for case #1. As noted earlier the outputs from the coupled system and component #1 are not the same. The elimination of this discrepancy did not change the coupled system model much in case #1 due to the rigidity of both the wheel and test stand. However, since case #2 includes internal wheel compliance the relationship between a_{r_1} and a_{r_2} is more complex and results in the following modified constrained system model:

$$\underbrace{\begin{Bmatrix} F_{l_1} \\ a_{r_1} \end{Bmatrix}}_{\mathbf{y}_{sys'}^{(2,c)}} = \underbrace{\frac{k_2}{(m_1 s^2 + k_1)(m_2 s^2 + k_2) + m_2 k_2 s^2}}_{\mathbf{H}_{sys'}^{(2,c)}} \begin{bmatrix} -k_1 \\ s^2 \end{bmatrix} F_{r_2} \quad (5.64)$$

The exact solution is obtained by transforming $\mathbf{H}_{sys'}^{(2,c)}$ to the frequency domain and substituting the resulting transfer function matrix and the input PSD, $S_{F_{r_2}F_{r_2}}$, into Equation 5.51:

$$\mathbf{S}_{y_{sys'}^{(2,c)}y_{sys'}^{(2,c)}} = \frac{1}{[(-m_1\omega^2 + k_1)(-m_2\omega^2 + k_2) - m_2 k_2 \omega^2]^2} \begin{bmatrix} k_1^2 k_2^2 & k_1 k_2^2 \omega^2 \\ k_1 k_2^2 \omega^2 & k_2^2 \omega^4 \end{bmatrix} S_{F_{r_2}F_{r_2}} \quad (5.65)$$

Note that although the numerator of $\mathbf{S}_i^{(2,c)}$ is equivalent to that of the exact solution, $\mathbf{S}_{y_{sys'}y_{sys'}}^{(2,c)}$, the denominators are quite different. Equation 5.65 contains extra terms that account for the coupling between the two components. Therefore, it can be concluded that the combination of plant model (i) and disturbance model 2 does not accurately capture the dynamics of the coupled system.

The mass of the RWA component is added to the spacecraft component to create plant model (ii). As mentioned earlier, this model for this plant is equivalent to the coupled system model of case #1 (Equation 5.53). The result of applying $S_{F_{l_2}F_{l_2}}^{(2,c)}$ (Equation 5.62) to this model is:

$$\mathbf{S}_{ii}^{(2,c)} = \frac{1}{(-(m_1 + m_2)\omega^2 + k_1)^2(-m_2\omega^2 + k_2)^2} \begin{bmatrix} k_1^2 k_2^2 & k_1 k_2^2 \omega^2 \\ k_1 k_2^2 \omega^2 & k_2^2 \omega^4 \end{bmatrix} S_{F_{r_2}F_{r_2}} \quad (5.66)$$

Again, the numerator matrix of this result is equivalent to that of the exact solution, Equation 5.65, but there are discrepancies in the denominators. Each output spectral density matrix, $\mathbf{S}_i^{(2,c)}$ and $\mathbf{S}_{ii}^{(2,c)}$, contains terms that are not present in the other.

The third plant model, (iii), includes both component #1, the spacecraft, and component #2, the RWA, and is, in effect, the coupled system shown in Figure 5-8. The model for this system is given in Equation 5.64, and the output PSD is obtained by substituting $S_{F_{l_2}F_{l_2}}^{(2,c)}$ and $\mathbf{H}_{sys'}^{(2,c)}$ (with $s = i\omega$) into Equation 5.51:

$$\mathbf{S}_{iii}^{(2,c)} = \frac{S_{F_{r_2}F_{r_2}}}{[(-m_1\omega^2 + k_1)(-m_2\omega^2 + k_2) - m_2 k_2 \omega^2]^2 (-m_2\omega^2 + k_2)^2} \begin{bmatrix} k_1^2 k_2^4 & k_1 k_2^4 \omega^2 \\ k_1 k_2^4 \omega^2 & k_2^4 \omega^4 \end{bmatrix} \quad (5.67)$$

Multiplying Equation 5.65 by k_2^2/k_1^2 simplifies the comparison of $\mathbf{S}_{ii}^{(2,c)}$ and $\mathbf{S}_{y_{sys'}y_{sys'}}^{(2,c)}$. After the output PSDs are manipulated in this manner the matrix numerators are equivalent, but the denominators are not. Equation 5.67 contains extra terms that arise from the fact that the internal compliance of the wheel is accounted for twice in this case: once in $S_{F_{l_2}F_{l_2}}^{(2,c)}$ (see Equation 5.62) and again in the model of the RWA disturbance. It has already been shown that simply applying the PSD of the measured force, $S_{F_{l_2}F_{l_2}}^{(2,c)}$, which includes the effects of the internal compliance of the wheel, to the spacecraft (plant (i)) does not accurately capture the dynamic coupling between the two subsystems. Therefore, it appears that the best way to predict the behavior of the coupled system exactly is to apply $S_{F_{r_2}F_{r_2}}$ to a

model of the coupled system.

Current disturbance modeling efforts fit a model to data measured from the base of the test stand during an isolated RWA vibration test. This model is then input to a finite element model of the spacecraft that includes the mass of the RWA. If the internal wheel compliance is accounted for in the disturbance model, the disturbance analysis is analogous to using plant model (ii) and disturbance model 2. However, it has been shown through comparison of $\mathbf{S}_{ii}^{(2,c)}$ and $\mathbf{S}_{y_{sys'}y_{sys'}}^{(2,c)}$, that this model combination does not accurately capture the dynamics of the coupled system.

Recall from the example in Section 5.1 that if the model parameters, mass and stiffness, satisfy a particular condition, the dynamic coupling effects in the system became negligible. Comparison of one of the output PSDs from the exact output spectral density matrix, $\mathbf{S}_{y_{sys'}y_{sys'}}^{(2,c)}$, to the corresponding PSD from $\mathbf{S}_{ii}^{(2,c)}$, shows that the same is true for plant model (ii) and disturbance model 2. Assuming that the RWA disturbance force is white noise ($S_{F_{r2}F_{r2}} = 1$), Equations 5.65 and 5.66 give the following:

$$S_{a_{r1}a_{r1}exact}^{(2,c)} = \frac{k_2^2\omega^4}{[-(m_1\omega^2 + k_1)(-m_2\omega^2 + k_2) - m_2k_2\omega^2]^2} \quad (5.68)$$

$$S_{a_{r1}a_{r1}ii}^{(2,c)} = \frac{k_2^2\omega^4}{[-(m_1 + m_2)\omega^2 + k_1]^2 (-m_2\omega^2 + k_2)^2} \quad (5.69)$$

where $S_{a_{r1}a_{r1}exact}^{(2,c)}$ is an element of $\mathbf{S}_{y_{sys'}y_{sys'}}^{(2,c)}$, and $S_{a_{r1}a_{r1}ii}^{(2,c)}$ is an element of $\mathbf{S}_{ii}^{(2,c)}$. The upper plot of Figure 5-9 compares the two PSDs for equal model parameters, $m_1 = m_2 = k_1 = k_2 = 1$. Note that PSD obtained from the isolated model analysis is quite different from the exact solution. In the lower plot, the PSDs were obtained using model parameters that satisfy the condition in Equation 5.9 and are representative of the actual spacecraft and RWA. The masses, $m_1 = 1800$ and $m_2 = 6$, and the stiffnesses, $k_1 = 7 \times 10^6$ and $k_2 = 1 \times 10^6$, correspond to natural frequencies of 10 and 65 Hz, which are roughly the frequencies of the first modes for SIM and the RWA, respectively. The plot shows that the two solutions are virtually indistinguishable. In this case, the result from the isolated modeling technique approximates the exact solution quite well. This comparison suggests that although isolated component modeling with plant model (ii) doesn't accurately predict the coupled system dynamics in general, it does produce a very close approximation under specific conditions. In addition, the results shown in the lower plot of Figure 5-9 indicate that these conditions

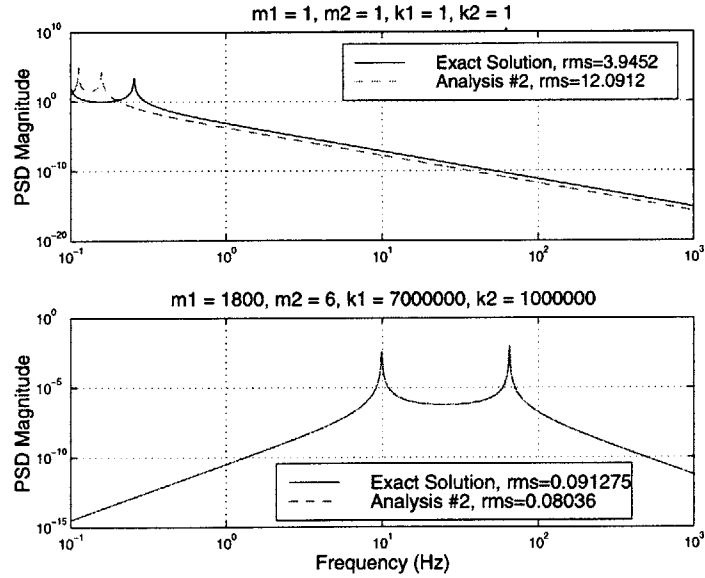


Figure 5-9: Comparison of Exact Solution and Current Methods Using Varying Model Parameters.

may hold for the spacecraft/RWA system and therefore, applying a disturbance model based on force data measured during an isolated RWA test that accounts for the flexibility of the RWA to a model of the spacecraft and RWA mass will capture the dynamics of the coupled system quite accurately. However, it is not clear that the approximation will hold when using more complicated, higher fidelity models in place of the simple spring mass models used to perform this analysis. Therefore it is still necessary to explore other modeling and analysis techniques to predict the behavior of the fully coupled system.

5.3.3 Capturing the Coupled Dynamics

The results of the coupling analyses for disturbance models 1 and 2 indicate that further effort must be devoted to developing a modeling technique that captures the dynamic coupling between the RWA and spacecraft. In the previous section it was shown that applying a model of the wheel disturbances without the effects of the structural wheel modes, $S_{F_{r_2}F_{r_2}}$, to a model of the fully coupled system, which includes the compliance of both the spacecraft and the RWA, accurately predicts the coupled system dynamics. However this approach requires:

1. a method for modeling the disturbance force, $S_{F_{r_2}F_{r_2}}$ from practical measurements taken during isolated tests.

2. an accurate finite element model of the RWA capturing the internal dynamics of the wheel.

Preliminary work on the first item will be presented in this section.

Due to the internal compliance of the wheel it is not possible to directly measure F_{r_2} . The Ithaco data presented earlier (see Section 2.2) show that the effect of the structural wheel modes appears in the measured disturbance data. However, it may be possible to construct F_{r_2} from other measurements and transfer functions. Consider the general form of the component #2 model:

$$\underbrace{\begin{Bmatrix} F_{l_2} \\ a_{r_2} \end{Bmatrix}}_{y_2^{(gen)}} = \underbrace{\begin{bmatrix} H_{11} & H_{12} \\ H_{21} & H_{22} \end{bmatrix}}_{\mathbf{H}_2^{(gen)}} \underbrace{\begin{Bmatrix} a_{l_2} \\ F_{r_2} \end{Bmatrix}}_{x_2^{(gen)}} \quad (5.70)$$

F_{r_2} can be determined if all the entries of the transfer function matrix, $\mathbf{H}_2^{(gen)}$, are known. It may be possible to populate this matrix experimentally by performing two isolated RWA tests with different boundary conditions. The setup for the first test is identical to the one described in the preceding sections. The RWA is mounted on a rigid test fixture effectively constraining it so that $a_{l_2} = 0$. This boundary conditions reduces the model in Equation 5.70 to:

$$\begin{Bmatrix} F_{l_2} \\ a_{r_2} \end{Bmatrix} = \begin{bmatrix} H_{12} \\ H_{22} \end{bmatrix} F_{r_2} \quad (5.71)$$

Then, by exciting F_{r_2} and measuring F_{l_2} and a_{r_2} the following transfer functions can be determined:

$$H_1 = \frac{F_{l_2}}{F_{r_2}} = H_{12} \quad (5.72)$$

$$H_2 = \frac{a_{r_2}}{F_{r_2}} = H_{22} \quad (5.73)$$

The second isolated test requires that the RWA be suspended in a free-free configuration. Consider the inverse of the general component model, Equation 5.70:

$$\begin{Bmatrix} a_{l_2} \\ F_{r_2} \end{Bmatrix} = \frac{1}{H_{11}H_{22} - H_{12}H_{21}} \begin{bmatrix} H_{22} & -H_{12} \\ -H_{21} & H_{11} \end{bmatrix} \begin{Bmatrix} F_{l_2} \\ a_{r_2} \end{Bmatrix} \quad (5.74)$$

If only F_{l_2} is excited (a_{r_2} is constrained to be 0) Equation 5.74 is reduced to:

$$\begin{Bmatrix} a_{l_2} \\ F_{r_2} \end{Bmatrix} = \frac{1}{H_{11}H_{22} - H_{12}H_{21}} \begin{bmatrix} H_{22} \\ -H_{12} \end{bmatrix} F_{l_2} \quad (5.75)$$

and two more transfer functions can be determined by measuring a_{l_2} and F_{r_2} :

$$H_3 = \frac{a_{l_2}}{F_{l_2}} = \frac{H_{22}}{H_{11}H_{22} - H_{12}H_{21}} \quad (5.76)$$

$$H_4 = \frac{F_{r_2}}{F_{l_2}} = \frac{-H_{21}}{H_{11}H_{22} - H_{12}H_{21}} \quad (5.77)$$

Now the measured transfer functions, H_1 , H_2 , H_3 , H_4 , can be used to solve for G_{11} , G_{12} , G_{21} and G_{22} . Using Equations 5.72, 5.73, 5.76 and 5.77:

$$\begin{aligned} H_{11} &= \frac{1-H_1H_4}{H_3} & H_{12} &= H_1 \\ H_{21} &= -\frac{H_2H_4}{H_3} & H_{22} &= H_2 \end{aligned} \quad (5.78)$$

It should be possible to use the results in Equation 5.78 along with the inverse of Equation 5.51 to determine $S_{F_{r_2}F_{r_2}}$. There are some issues, however, that need to be examined in greater detail. The first is the feasibility of the inversion of Equation 5.51. It is unclear whether the PSD of an input can be obtained from measured outputs. Other issues are related to the practicality of the isolated tests described above. In the first test, F_{l_2} and a_{r_2} must be measured. This requires that a load cell be placed at the base of the test stand and an accelerometer be placed on the wheel itself. The location of the accelerometer may be impractical due to the spinning of the wheel. For the second isolated test, it is necessary to hang the wheel in free-free configuration and input F_{l_2} , but keep a_{r_2} at zero. This method requires that F_{l_2} and a_{r_2} be uncorrelated. However, if the wheel is truly in a free-free configuration, application of a force on the left side of the wheel will result in an acceleration on the right. Closer examination of the test conditions and configuration is necessary before any conclusions can be made. Sensor placement may be a problem in this test as well. An accelerometer must be placed on the left side of the wheel and a load cell on the right. Determining the true “left” and “right” sides of the wheel is difficult, and placing any sensor directly on the wheel may not be practical.

5.4 Coupling Experiments

In addition to the coupling analyses described in the preceding section, a series of laboratory experiments are being developed to explore the effects of coupling between two flexible structures, such as a RWA and a spacecraft. A representative reaction wheel and a flexible truss structure will be used to provide the following:

1. Assessment of the degree of coupling between the two flexible components, especially when the wheel is spun at a frequency that excites a structural mode of either the wheel or the truss.
2. Validation of current disturbance modeling efforts.
3. Development and validation of more accurate modeling and RWA testing techniques.

5.4.1 Test Setup

The representative reaction wheel consists of a flywheel that is about 7 inches in diameter and a DC motor with a built-in tachometer. The effects of dynamic coupling on RWA disturbances can be assessed by performing two isolated RWA vibration tests with different boundary conditions, (a) hard-mounted to a rigid structure and (b) hard-mounted to a flexible structure, and comparing the differences in the resulting disturbance data. The setup for test (a) is shown in Figure 5-10. The wheel is mounted to a six-axis load cell through an interface that consists of two metal plates. The load cell is then bolted to an optical isolation table. A signal generator is used to apply a voltage to the motor, spinning the wheel. A data acquisition system samples the disturbance forces measured at the interface of the wheel and the load cell.

In order to collect steady-state disturbance data, the speed of the wheel must be controlled through the tachometer. A simple controller was built to allow the speed of the wheel to be set through the signal generator and maintained at a steady state. The details of the controller design are in Appendix C. Once the loop is closed around the tachometer the voltage corresponding to the desired wheel spin rate can be entered into the signal generator. This voltage is compared to the tachometer output and the control signal is adjusted and drives the wheel until the tachometer output and the desired voltage are equivalent. When the wheel has reached the desired speed the disturbances measured by the load cell

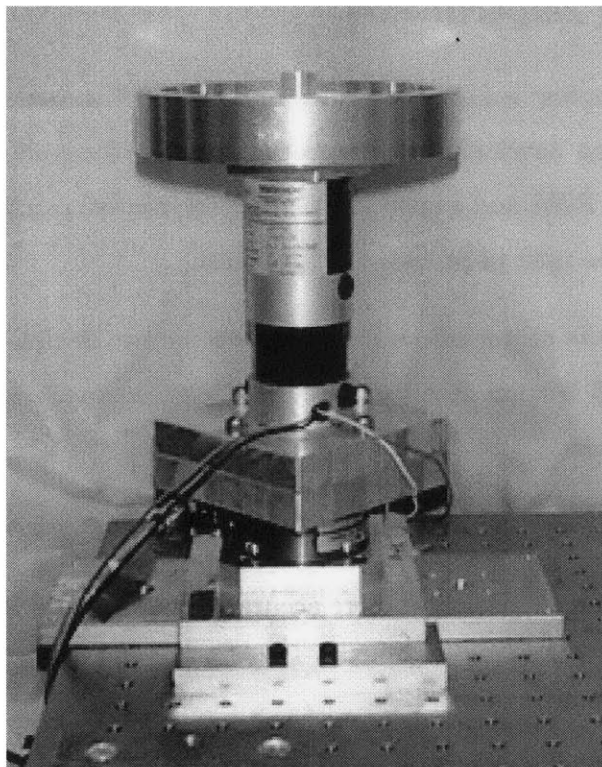


Figure 5-10: Representative Reaction Wheel Hard-mounted to Load Cell

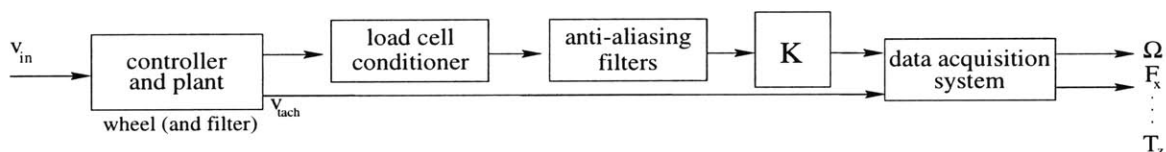


Figure 5-11: Block Diagram Representation Data Acquisition Configuration for Wheel

are sampled at 1 kHz and time histories of the 3 forces and 3 moments are obtained. Low pass filters with corner frequencies of about 480 Hz are used to ensure that aliasing of the data does not occur. A block diagram representation of the testing setup is shown in Figure 5-11.

In the second test, (b), the wheel must be hard-mounted to a flexible structure. A laboratory testbed that was originally designed and constructed to validate a sensitivity analysis methodology will be used for this purpose [19]. A full view of the testbed is shown in Figure 5-12. It is a cantilevered truss-like structure with one appendage bending mode and two truss bending modes, all below 50 Hz. The frequency range of these modes ensures that a wheel spinning up to maximum rate of 3000 rpm will be able to excite the testbed. The wheel and load cell are mounted to a metal plate on top of the truss as shown in Figure 5-

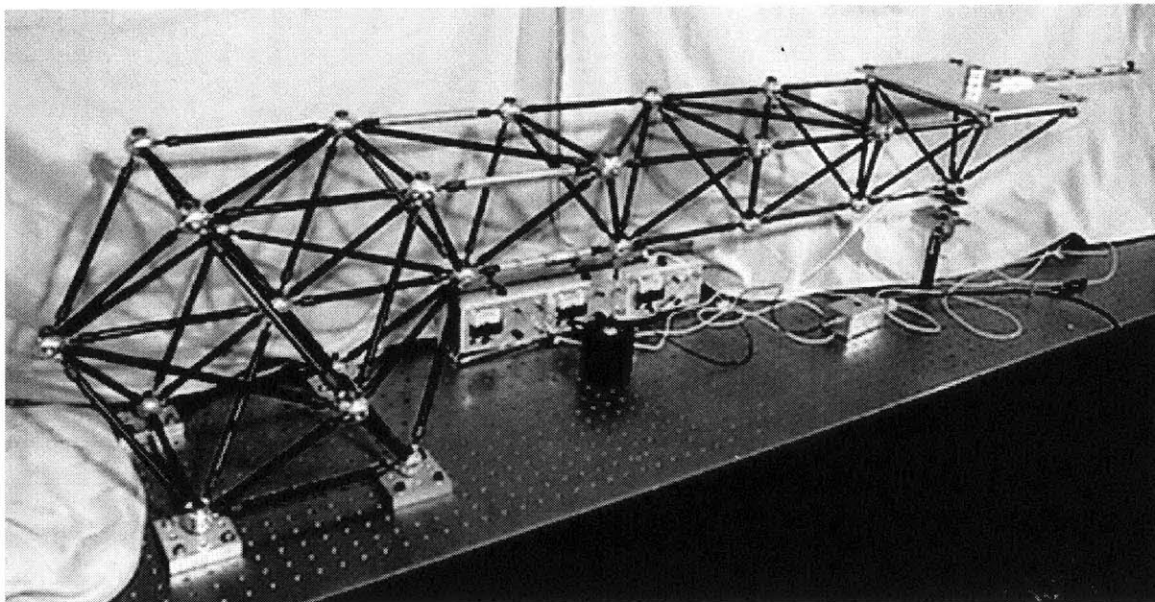


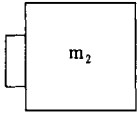
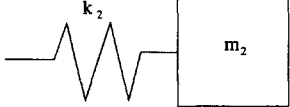
Figure 5-12: Full View of Flexible Truss Testbed

13. Disturbance data from the interface between the wheel and the load cell will be taken in this configuration at the same speeds used in the rigid configuration (a). Comparison of the results from these two tests will provide some insight into the effect that dynamic coupling may have on the RWA and spacecraft. In addition, a FEM model of the testbed can be used to validate current disturbance models by comparing the predicted displacements of the testbed obtained through a disturbance analysis to the actual displacements that occur when the wheel is mounted to the testbed.

5.5 Summary

In this chapter the preliminary efforts of an investigation into the effects that dynamic coupling has on RWA disturbance modeling has been presented. A series of simple analyses using acceleration feedback and spring mass-models have been performed and a summary of the results is presented in Table 5.4. It is clear from comparing the results of the PSD analyses , \mathbf{S}_i , \mathbf{S}_{ii} , and \mathbf{S}_{iii} , to the exact solution that, for disturbance model 1, only the analysis with plant model (ii) accurately captures the coupled dynamics of the two components and, for disturbance model 2, none of the plant models accurately capture the coupled system dynamics. It was shown, however, that if the model parameters satisfy specific conditions, the combination of disturbance model 2 and plant model (ii) results in

Table 5.4: Summary of Results

	Disturbance Model 1	Disturbance Model 2
Component #2		
$S_{F_{l_2} F_{l_2}}^{(c)}$	$S_{F_{r_2} F_{r_2}}$	$\frac{k_2^2}{(-m_2 \omega^2 + k_2)^2} S_{F_{r_2} F_{r_2}}$
$\mathbf{H}_{sys'}^{(c)}$	$\frac{1}{(m_1 + m_2)s^2 + k_1} \begin{bmatrix} -k_1 \\ s^2 \end{bmatrix}$	$\frac{k_2}{(m_1 s^2 + k_1)(m_2 s^2 + k_2) + m_2 k_2 s^2} \begin{bmatrix} -k_1 \\ s^2 \end{bmatrix}$
$S_{y_{sys'} y_{sys'}}$	$\frac{\begin{bmatrix} k_1^2 & k_1 \omega^2 \\ k_1 \omega^2 & \omega^4 \end{bmatrix}}{(-m_1 + m_2)\omega^2 + k_1} S_{F_{r_2} F_{r_2}}$	$\frac{\begin{bmatrix} k_1^2 k_2^2 & k_1 k_2^2 \omega^2 \\ k_1 k_2^2 \omega^2 & k_2^2 \omega^4 \end{bmatrix}}{[(-m_1 \omega^2 + k_1)(-m_2 \omega^2 + k_2) - m_2 k_2 \omega^2]^2} S_{F_{r_2} F_{r_2}}$
S_i	$\frac{\begin{bmatrix} k_1^2 & k_1 \omega^2 \\ k_1 \omega^2 & \omega^4 \end{bmatrix}}{(-m_1 \omega^2 + k_1)^2} S_{F_{r_2} F_{r_2}}$	$\frac{\begin{bmatrix} k_1^2 k_2^2 & k_1 k_2^2 \omega^2 \\ k_1 k_2^2 \omega^2 & k_2^2 \omega^4 \end{bmatrix}}{(-m_1 \omega^2 + k_1)^2 (-m_2 \omega^2 + k_2)^2} S_{F_{r_2} F_{r_2}}$
S_{ii}	$\frac{\begin{bmatrix} k_1^2 & k_1 \omega^2 \\ k_1 \omega^2 & \omega^4 \end{bmatrix}}{(-m_1 + m_2)\omega^2 + k_1} S_{F_{r_2} F_{r_2}}$	$\frac{\begin{bmatrix} k_1^2 k_2^2 & k_1 k_2^2 \omega^2 \\ k_1 k_2^2 \omega^2 & k_2^2 \omega^4 \end{bmatrix}}{(-m_1 + m_2)\omega^2 + k_1)^2 (-m_2 \omega^2 + k_2)^2} S_{F_{r_2} F_{r_2}}$
S_{iii}	N/A	$\frac{\begin{bmatrix} k_1^2 k_2^4 & k_1 k_2^4 \omega^2 \\ k_1 k_2^4 \omega^2 & k_2^4 \omega^4 \end{bmatrix}}{[(-m_1 \omega^2 + k_1)(-m_2 \omega^2 + k_2) - m_2 k_2 \omega^2]^2 (-m_2 \omega^2 + k_2)^2} S_{F_{r_2} F_{r_2}}$

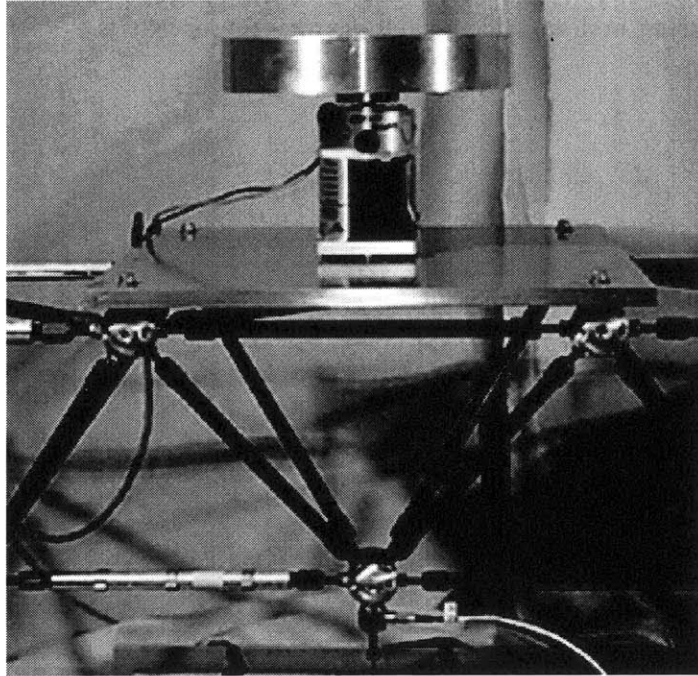


Figure 5-13: Representative Reaction Wheel Mounted to Flexible Testbed

a close approximation to the exact solution. This case is analogous to fitting a disturbance model to the data obtained from an isolated RWA test and using this disturbance model to drive a FEM of the spacecraft and RWA mass. The compliance conditions of disturbance model 2 are similar to the conditions of the low-frequency (< 200 Hz) Ithaco reaction wheel test data. Therefore, the results of this analysis suggests that fitting a model to the low-frequency Ithaco data and using this model to perform a disturbance analysis on a model of the spacecraft (that includes the mass of the RWA) should predict the dynamics of the coupled spacecraft/RWA system. This conclusion is not necessarily correct, however; the above analyses were performed on simple spring mass systems while the RWA and spacecraft are both multi-mode systems that require high-fidelity models to accurately capture their dynamic behavior. It is not clear that the approximation obtained from spring-mass models will hold for more complex models.

Therefore, alternative disturbance modeling and analysis techniques should be investigated. One approach which involves combining data from multiple types of RWA tests to create the disturbance model was briefly outlined, but requires further attention before its feasibility can be assessed and an implementation scheme developed. In addition, a plan for laboratory experiments that can provide insight into the coupling problem and validate

disturbance modeling and analysis techniques was presented.

Chapter 6

Conclusions and Recommendations

6.1 Thesis Summary

Next generation precision space-based telescopes, such as SIM and NGST, require high levels of pointing stability. Small levels of vibration can introduce jitter in the optical train and cause a significant reduction in image quality. Therefore, the success of these missions is highly dependent on the ability of optical control and isolation techniques to keep the large flexible structures stable and the optical elements properly aligned when exposed to a disturbance environment. Vibrations may be induced during operation by orbital environment disturbances such as solar pressure, thermal snap and atmospheric drag, and on-board disturbances from mechanical systems and sensors located on the spacecraft, such as cryo-coolers, optical delay lines, and mirrors. On-board disturbances are expected to dominate the disturbance environment, and the largest anticipated vibration source is the reaction wheel assembly (RWA), a momentum exchange device used to control spacecraft attitude and perform large angle slewing maneuvers.

Due to the large scale of these next generation telescopes, early design decisions must rely on analysis conducted with high fidelity models. A performance assessment and enhancement methodology was developed in [19] to predict the effects of disturbances on these high-performance systems. This methodology depends heavily on the development of an accurate disturbance model. In this thesis, two RWA disturbance models were developed and validated and a third was presented. These models improve on existing RWA disturbance modeling efforts by extending a discrete frequency model to allow the modeling of any RWA given vibration test data and developing a physical model which captures the

flexible modes of the wheel.

Chapter 2 discussed vibration isolation tests that are generally used to characterize RWA disturbances. Two particular experiments performed on Ithaco type B and E RWAs at Orbital Space Systems and the NASA Goddard Space Flight Center were described in detail. In both tests a RWA was hardmounted to a rigid test fixture and load cells were used to measure the six disturbances (three forces and three torques) induced by the spinning of the wheel. The time history data was processed into frequency domain data using the techniques described in Section 2.1. PSDs and amplitude spectra of the disturbances were then plotted in waterfall plots to determine the frequency content of the RWA disturbances across wheel speed. It was found that the disturbance data consists of both wheel harmonics, disturbances occurring at discrete frequency ratios of the wheel speed, and resonant disturbances which occur at the same frequencies across all wheel speeds. These resonances are due to excitation of the test stand fixture and the structural wheel modes by the wheel harmonics. It was concluded that the test stand resonance should not be included in the RWA model and any data corrupted by these resonances could not be used to generate an accurate model. The internal wheel flexibility, on the other hand, must be accounted for in the model, since it will be present when the wheel is mounted on the spacecraft for operation. These structural modes were discussed in detail in Section 2.3.

The first type of disturbance model that was developed is presented in Chapter 3. It is an empirical model that is based solely on system-ID methods. The general form of the model was originally developed to capture the disturbance behavior of the Hubble Space Telescope (HST) RWA [15]. The model assumes that the wheel disturbances are a series of harmonics at discrete frequencies with amplitudes proportional to the wheel speed squared. A set of MATLAB functions has been created to extend the HST model and facilitate the empirical modeling process. These functions, called the Reaction Wheel Assembly Data Analysis and Disturbance Modeling (RWA DADM) toolbox, extract the empirical model parameters from steady-state RWA vibration data allowing the creation of an empirical disturbance model for any given RWA. The toolbox consists of four main functions all of which were described in detail in Section 3.1.

The Ithaco data described in Chapter 2 were used to provide validation for the empirical model. Both the B and E Wheel data were run through the RWA DADM toolbox to create empirical models of the disturbances from the two wheels. Waterfall plots and RMS

comparison plots were used to compare the data and the model to assess the accuracy of the empirical model and the performance of the toolbox. The data correlation for the B Wheel empirical model was rather poor. The frequencies of the harmonics were accurately identified, but their amplitudes were severely under-predicted. The RMS comparison showed a large discrepancy between the model and the data over all wheel speeds. The E Wheel model, on the other hand, had good correlation with the data over most wheel speeds. The waterfall plot comparison indicated that the disturbance frequencies were identified accurately, and the RMS values of the data and model were very close over most wheel speeds. The improved quality in correlation between the data and the E Wheel empirical model suggests that the B Wheel data anomalies are data set specific. The poor B Wheel model correlation is, therefore, most likely due to the conditions under which the vibration data was acquired and not errors in the empirical model.

The Ithaco E wheel model correlation was not exact, however. There were discrete ranges of speeds over which the data RMS was significantly higher than the model. These peaks in RMS were caused by disturbance amplification of the harmonics by the structural wheel modes. Since internal wheel flexibility is not captured in the empirical model, a large discrepancy exists between the data and the model at these speeds. It was concluded that although the empirical model captures the wheel harmonics and identifies the disturbance frequencies well, it is not an accurate RWA disturbance model. Excitation of the structural wheel modes by the harmonics can cause large disturbance amplifications which must be included in the model to accurately predict the effects of the disturbances on the spacecraft during operation. Therefore, a second disturbance model was developed to take the resonant effects into account.

The second model is an analytical model based on the physical behavior of an unbalanced rotating flywheel and was the subject of Chapter 4. The model is developed using Lagrangian energy methods to derive the equations of motion (EOM) of the system. Two of the structural modes of the wheel, radial rocking and translation, were captured by modeling shaft and bearing flexibility with linear springs and dashpots. A balanced flywheel captured the inertia properties of the wheel and gyroscopic stiffening effects. Finally static and dynamic imbalance were added to the model with concentrated masses placed strategically on the flywheel. Although the equations of motion obtained for this model show that the flexible modes of the wheel are captured, the model was not complete. Since

only the flywheel imbalance was physically captured, the fundamental harmonic was the only disturbance in the model. Therefore an extended model was created by combining the analytical model with the empirical. The additional harmonics were incorporated by adding harmonic forcing functions with frequencies and amplitudes defined by the empirical model parameters to the EOM of the analytical model. The EOM of the extended model were solved analytically and preliminary simulations showed that the model captured the wheel harmonics as well as the interactions between the harmonics and the structural wheel modes.

Although the analytical and extended models are physically based, RWA vibration data must be used in combination with manufacturer specifications to choose model parameters for a given wheel. A preliminary methodology was developed to extract these parameters from the vibration data. The stiffness parameters were set based on the natural frequencies of the radial rocking and translation modes. The static and dynamic mass parameters were set using both manufacturer specification of the wheel geometry and the amplitude of the fundamental harmonic in the radial force and torque data. The damping parameters were the final parameters to be set and proved to be the most challenging. The amplification observed in the data at the wheel resonances was used to set these parameters.

The Ithaco E Wheel data was used to validate the analytical model and parameter matching methodology. The frequencies of the radial modes and the amplitude of the fundamental harmonic were captured quite well by the stiffness parameters and imbalance masses. The disturbance amplification was also captured in the model, but an accurate match could not be achieved by adjusting only the damping parameters. However, RMS comparisons of the data (up to the first harmonic), the first harmonic of the empirical model and the analytical model indicated that a good estimate of the modal amplification, and RWA disturbance in general, was obtained. The analytical model matches the data well over most wheel speeds and overbounds the data at speeds in which disturbance amplification occurs. Modeling of damping and the parameter fitting methods are still under development and will be discussed in Section 6.2 as future work.

The final subject of the thesis is an investigation into the dynamic coupling that occurs between the RWA and a spacecraft during operation. Through the empirical modeling process it was discovered that the internal wheel flexibility had a large effect on the RWA disturbances. Therefore, the analytical model was developed to incorporate this effect.

However, the models discussed in this thesis are all based on data taken from RWAs that were hardmounted to a rigid surface. In application, the RWA will be hardmounted to the spacecraft which is quite flexible. Therefore, a series of analyses were performed, using a component modeling technique called acceleration feedback developed in [26] to capture the dynamic coupling between two flexible systems. The results presented in this thesis are from a preliminary study and require further exploration. It was shown, however, that it is highly likely that dynamic coupling will have an effect on the RWA disturbances and the spacecraft performance. Methods of incorporating these effects into the models presented in this thesis should be explored and developed. In addition, a plan for a set of laboratory experiments which could provide insight into the dynamic coupling issue and allow validation of current and future disturbance modeling and analysis techniques was presented.

6.2 Recommendations for Future Work

The recommendations for future work can be grouped into three main areas: empirical model, analytical/extended model, and general RWA disturbance modeling.

Empirical Model

- It was shown in Chapter 3 that the data for the higher harmonics do not generally follow the coefficient curve fits generated using the assumption that the disturbance magnitudes are proportional to the wheel speed squared. Therefore, other possible relationships between the disturbance amplitude and the wheel speed should be considered for these harmonics.
- Further investigation should be made into the large discrepancy observed between the Ithaco B Wheel empirical model and the data. Data from a different vibration test on an Ithaco B Wheel could be used to validate the hypothesis that the discrepancy arises from a source specific to this particular vibration test and not from the Ithaco B Wheel in general.

Analytical/Extended Model

- The investigation of the pole/zero cancellation that occurs when the particular solutions for the generalized rotations in the analytical model are obtained should be

continued. The current technique used to capture both whirls of the rocking mode changes the amplitude of the fundamental harmonic in the radial torque data. A scale factor can be used to compensate for this side effect, but a better solution would be to find a physical explanation for the pole-zero cancellation and develop an alternate method for including both whirls of the rocking mode in the model.

- The current analytical model only contains two of the three structural modes of the wheel. The axial mode must still be accounted for in the model. Preliminary attempts to model the axial mode by adding a translational degree of freedom in the z-direction with linear springs failed to capture a driving term in the equations of motion. One possible solution is to use the empirical model parameters to drive the equation obtained for the z translation.
- The coupling observed among the disturbance data sets (Ithaco E Wheel) must be investigated. Both the radial rocking and translational modes are observed in that radial forces, radial torques and axial forces. It is currently unclear if the coupling is due to the location of the load cells with respect to the center of the wheel and therefore can be removed through a decoupling matrix or if it is a characteristic of the disturbances which should be included in the analytical/extended model.
- The results of the model comparison in Chapter 4 show some discrepancies between the analytical model and data. The current parameter fitting methodology must be examined to find ways of improving this fit. In particular, the methods used to model damping and choose parameters to fit the disturbance amplifications should be investigated.
- Once a good parameter fitting methodology is developed for the analytical model it should be refined as necessary for application to the extended model.
- The RWA DADM toolbox should be extended to include the parameter matching methodology for the analytical/extended model. The result would be a complete set of MATLAB functions that allow a user to choose which type of model to create (empirical, analytical or extended) and return the parameters for that model, given RWA vibration data and user input at key decision-making steps in the modeling processes.

- The extended model should be used to perform a disturbance analysis with the SIM and NGST models. The results can be compared to those obtained with the stochastic broadband model which is the RWA disturbance model that is currently used for these types of analyses.

General RWA Disturbance Modeling

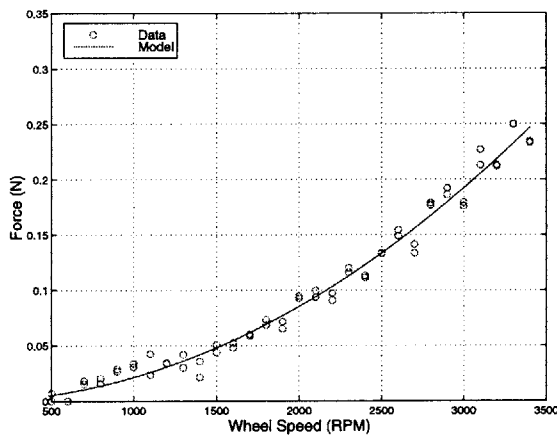
- Some measure of uncertainty should be included in the disturbance models. For example, the amplitude coefficients in the empirical model could be provided with error bars to give some idea of the scatter in the data and the quality of the coefficient curve fit. Other possible areas of uncertainty in the analytical/extended model should be identified and quantified.
- All models presented in this thesis assume that the RWA is spinning at a constant speed. However, during operation the wheels must often spin through a range of speeds. Therefore the transient behavior of the RWAs should be investigated. If a significant difference is found between the steady-state and the transient disturbances, the using analytical/extended models can be used to incorporate transient behavior into the model by removing the constant wheel speed constraint and obtaining new equations of motion.
- The coupling analysis presented in Chapter 5 must be continued. A metric to measure the degree of coupling between RWA and spacecraft should be derived, and the analyses for disturbance models 3 and 4 (including test stand flexibility in the vibration data) should be completed.
- Laboratory experiments exploring RWA to spacecraft coupling issues and validating current disturbance models should be performed. Multiple boundary condition testing should be considered as a method of capturing the coupling dynamics between the RWA and the flexible spacecraft.

Appendix A

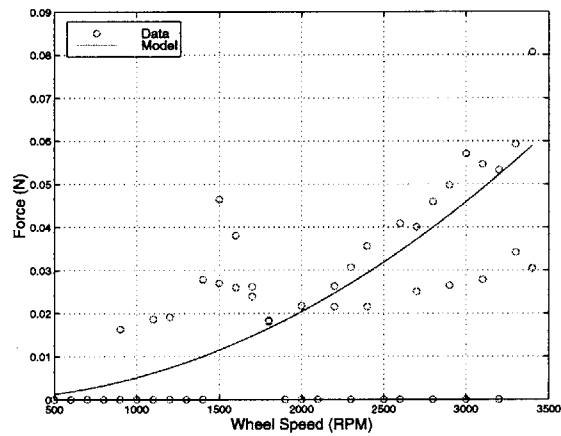
Coefficient Curve Fit Plots

A.1 Ithaco B Wheel

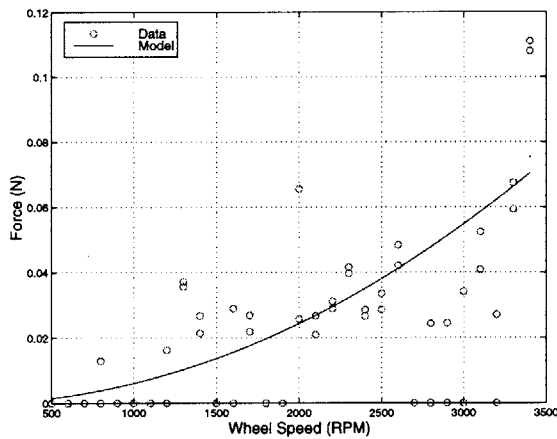
A.1.1 Radial Force



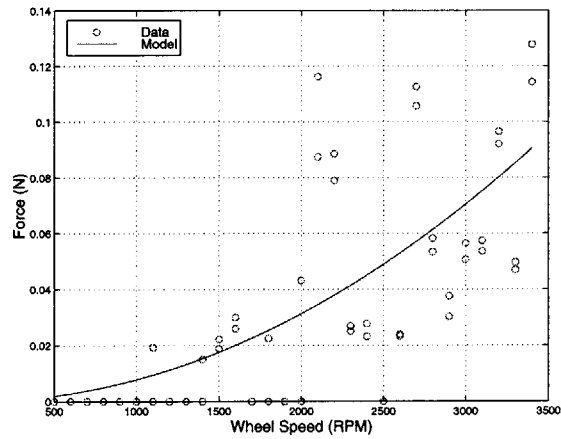
(a) $h_1 = 0.99$



(b) $h_2 = 1.99$

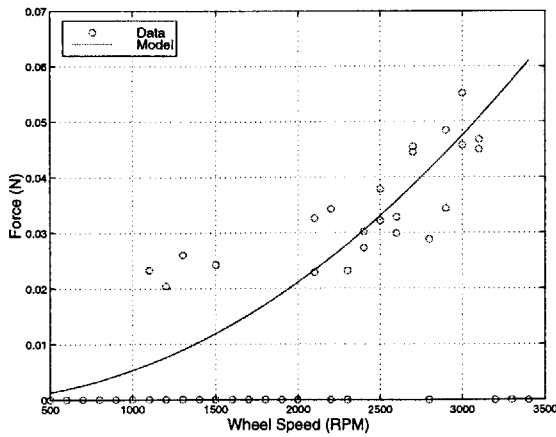


(c) $h_3 = 2.46$

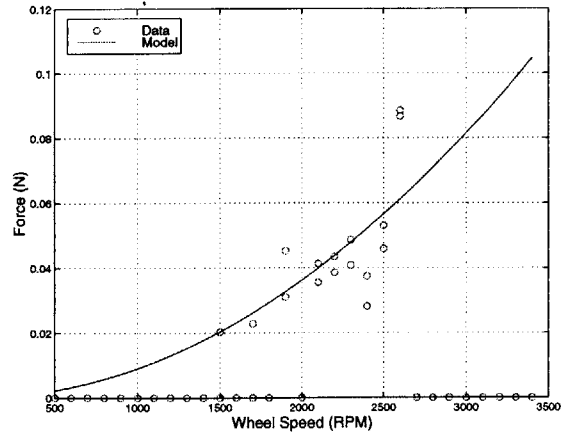


(d) $h_4 = 3.16$

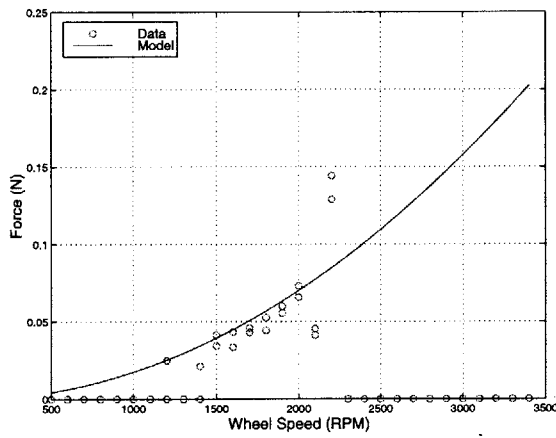
Figure A-1: Coefficient Curve Fits - Ithaco B Wheel Radial Force (1)



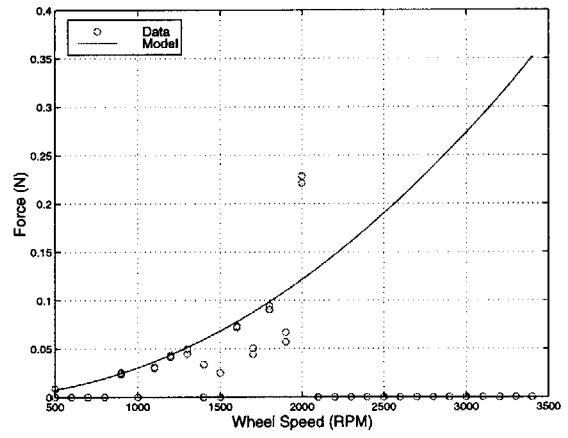
(a) $h_5 = 3.87$



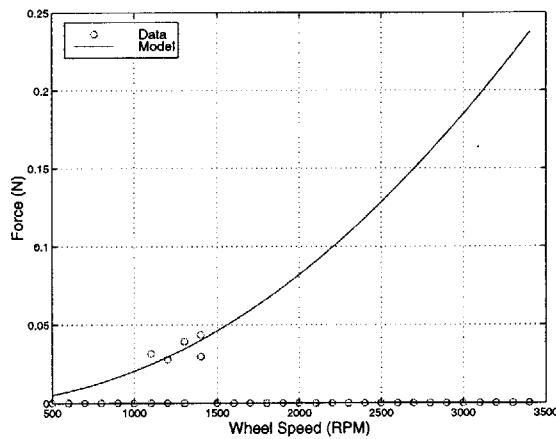
(b) $h_6 = 4.56$



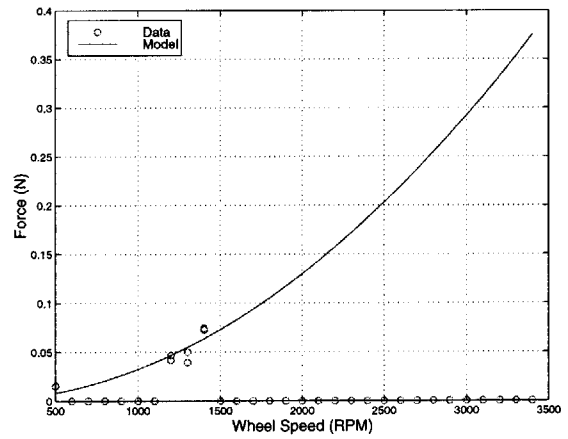
(c) $h_7 = 5.28$



(d) $h_8 = 5.98$

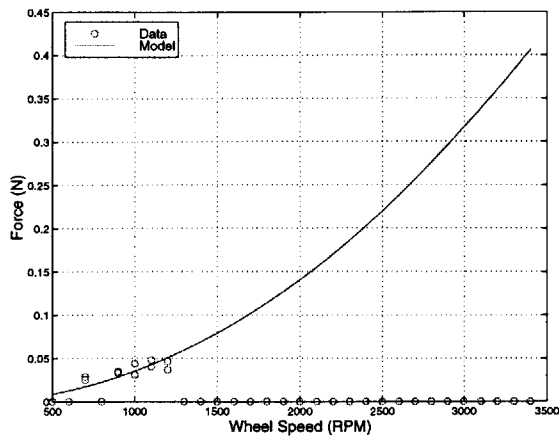


(e) $h_9 = 6.71$

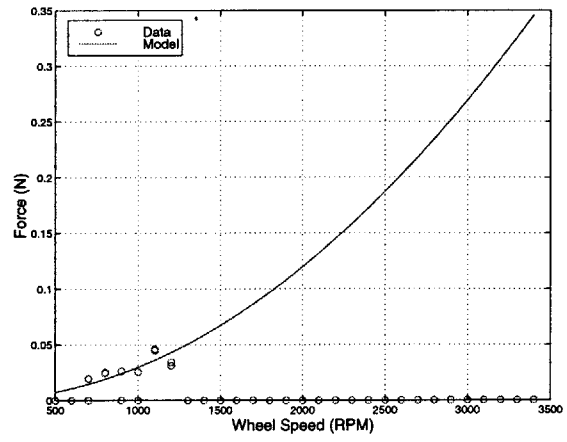


(f) $h_{10} = 8.09$

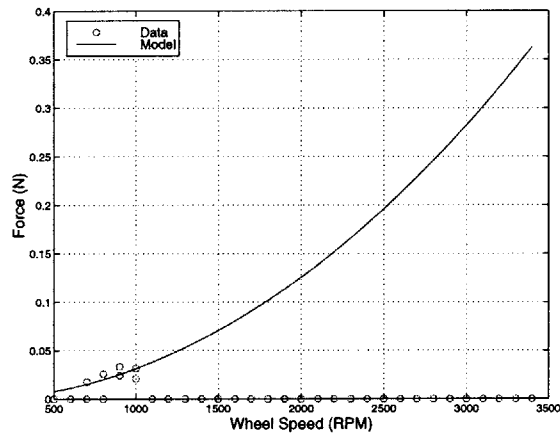
Figure A-2: Coefficient Curve Fits - Ithaco B Wheel Radial Force (2)



(a) $h_{11} = 8.83$



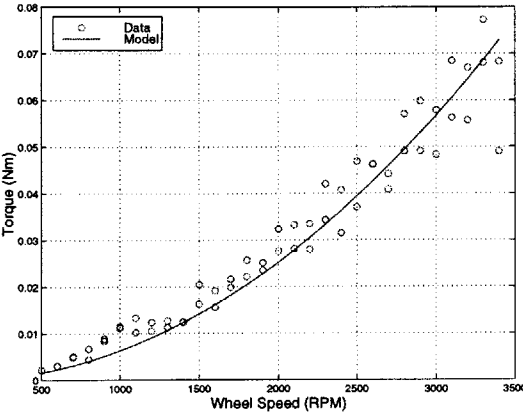
(b) $h_{12} = 9.54$



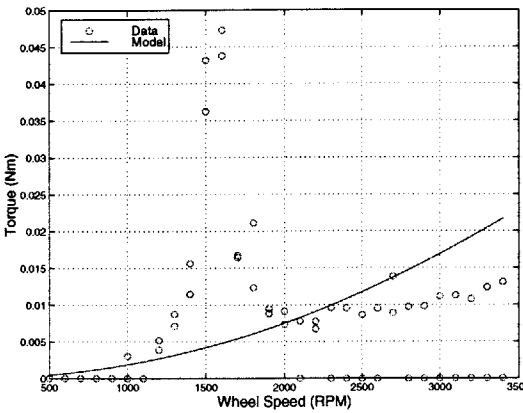
(c) $h_{13} = 10.25$

Figure A-3: Coefficient Curve Fits - Ithaco B Wheel Radial Force (3)

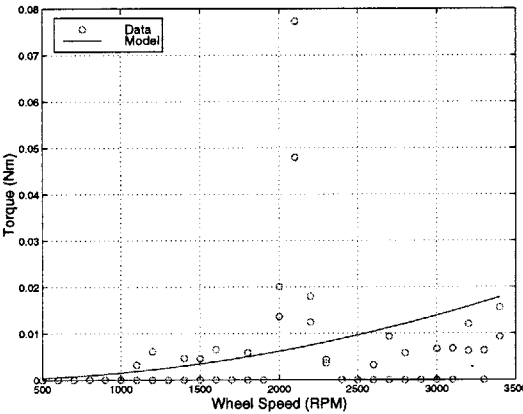
A.1.2 Radial Torque



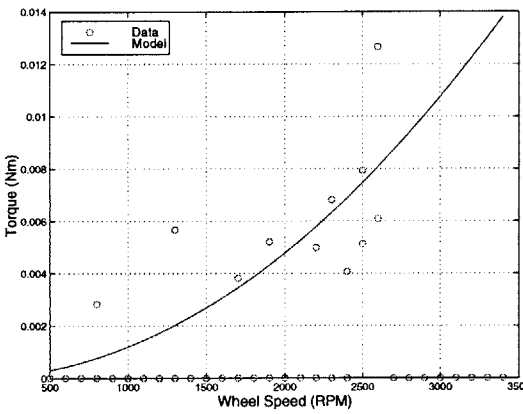
(a) $h_1 = 0.99$



(b) $h_2 = 1.99$

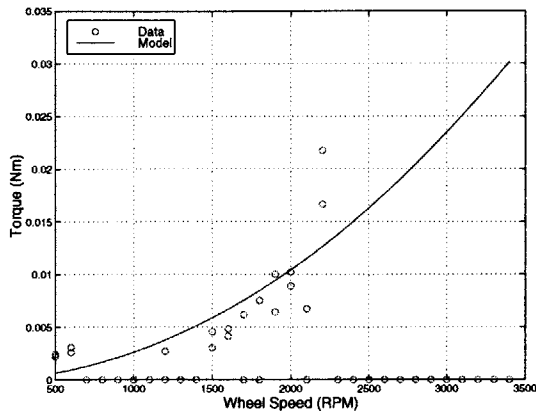


(c) $h_3 = 3.16$

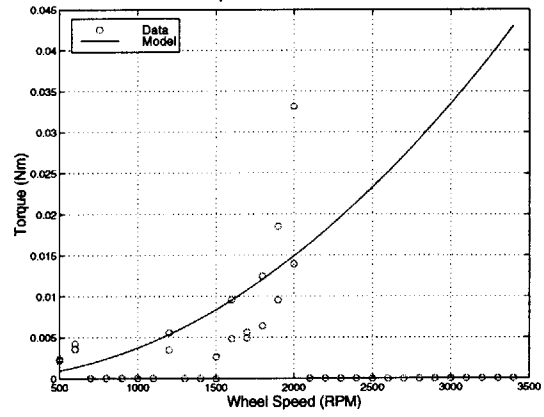


(d) $h_4 = 4.56$

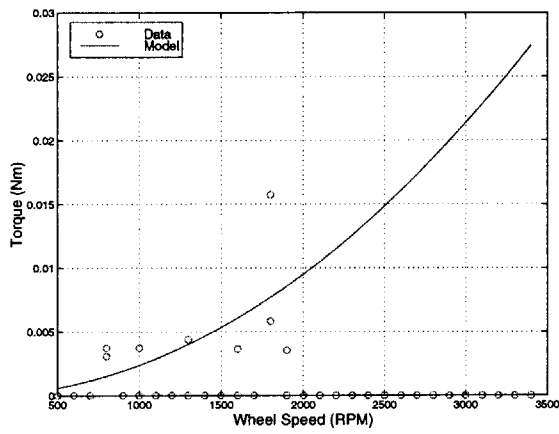
Figure A-4: Coefficient Curve Fits - Ithaco B Wheel Radial Torque (1)



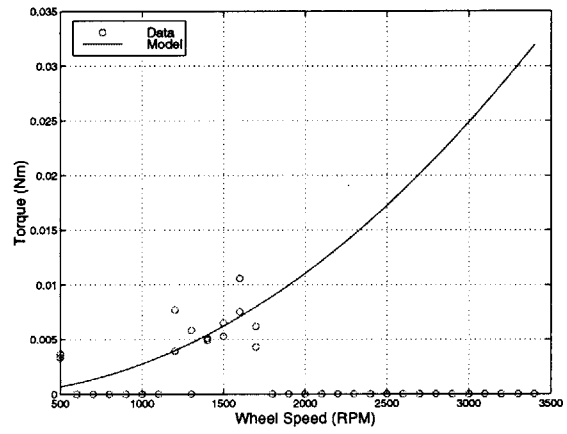
(a) $h_5 = 5.28$



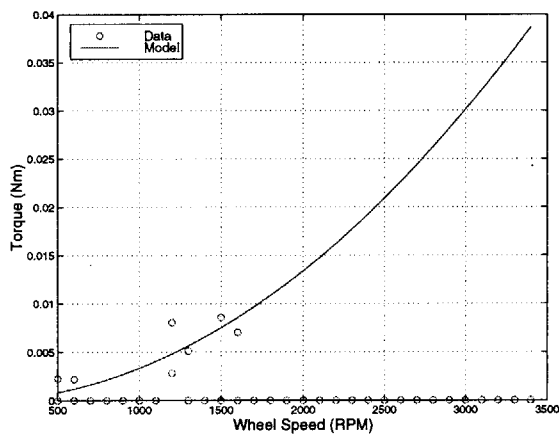
(b) $h_6 = 5.97$



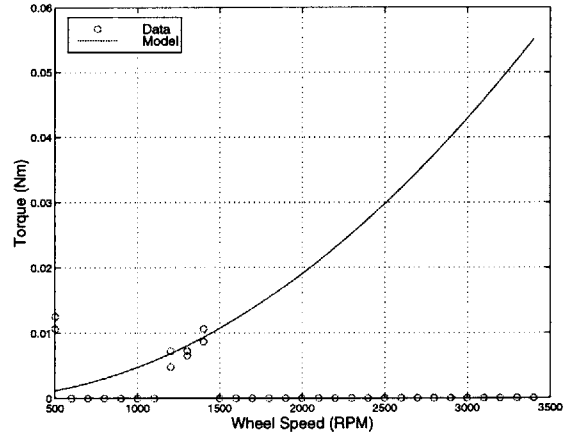
(c) $h_7 = 6.23$



(d) $h_8 = 6.68$

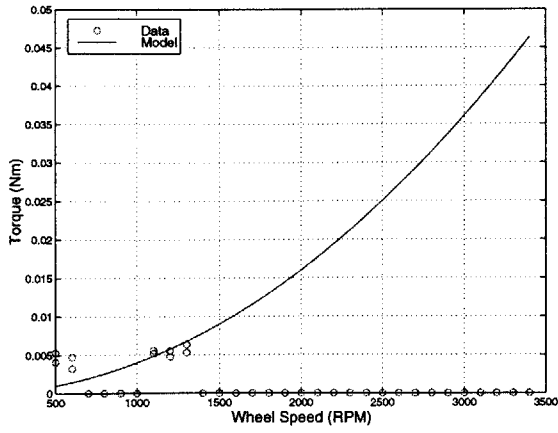


(e) $h_9 = 7.38$



(f) $h_{10} = 8.09$

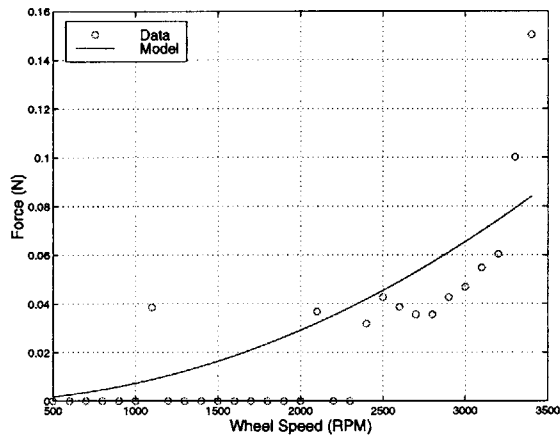
Figure A-5: Coefficient Curve Fits - Ithaco B Wheel Radial Torque (2)



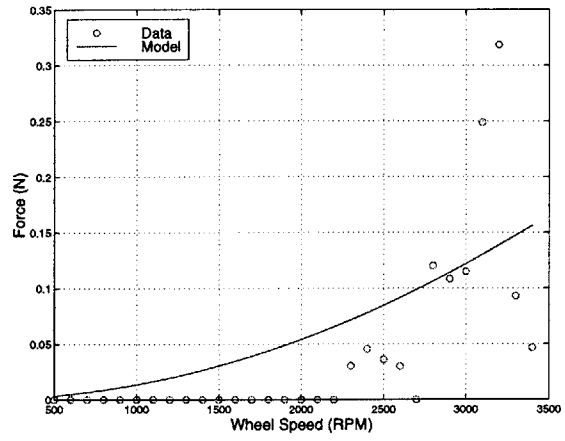
(a) $h_{11} = 8.80$

Figure A-6: Coefficient Curve Fits - Ithaco B Wheel Radial Torque (3)

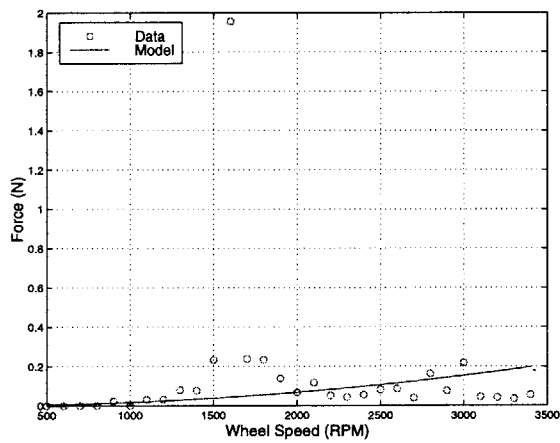
A.1.3 Axial Force



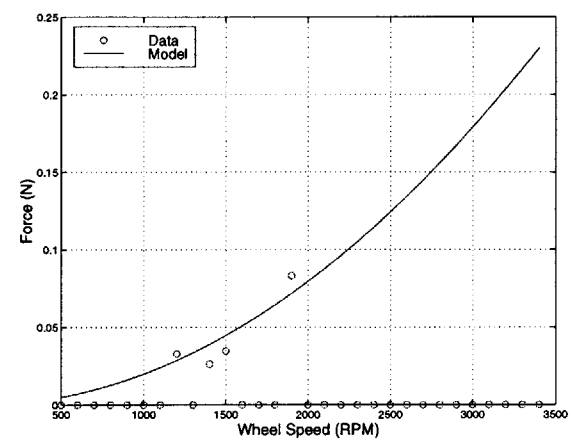
(a) $h_1 = 0.99$



(b) $h_2 = 1.41$



(c) $h_3 = 2.82$

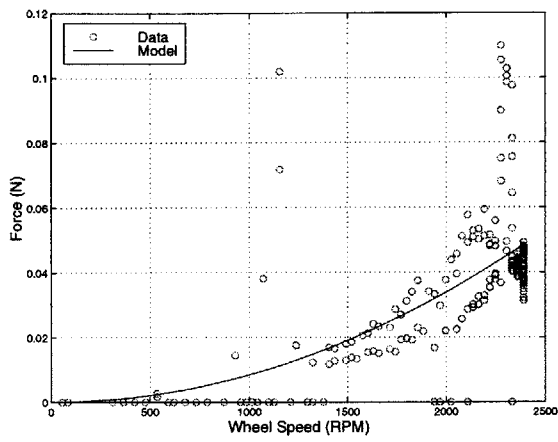


(d) $h_5 = 5.95$

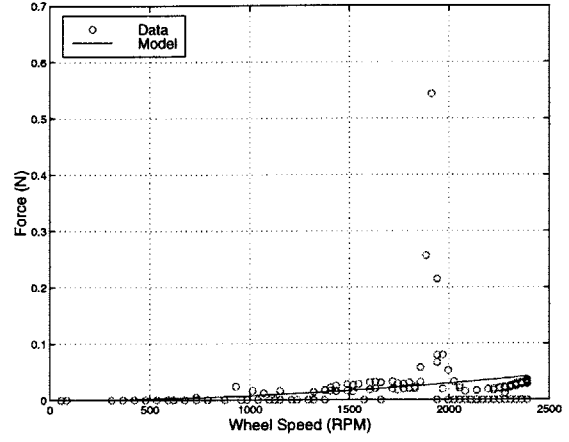
Figure A-7: Coefficient Curve Fits - Ithaco B Wheel Axial Force

A.2 Ithaco E Wheel

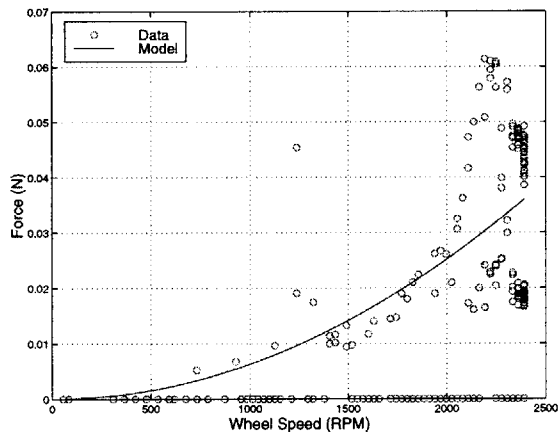
A.2.1 Radial Force



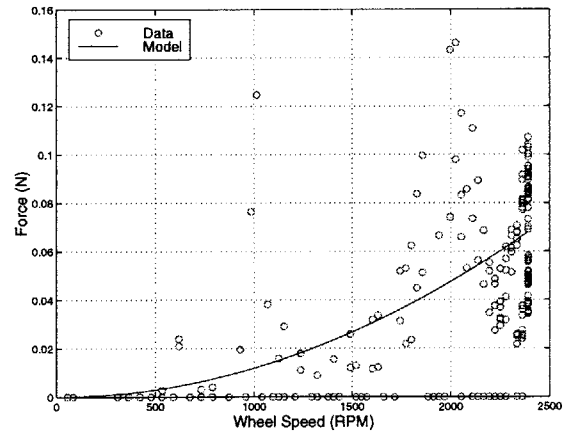
(a) $h_2 = 2.00$



(b) $h_3 = 3.00$

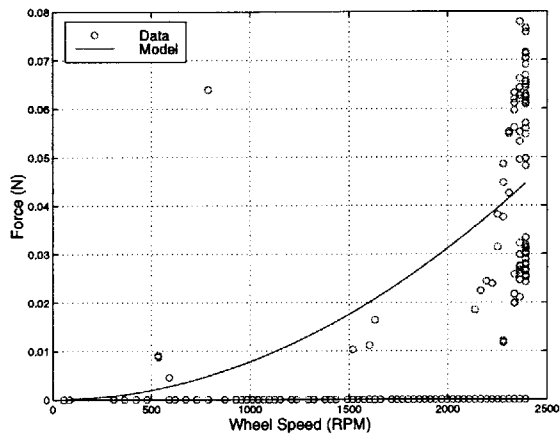


(c) $h_4 = 4.00$

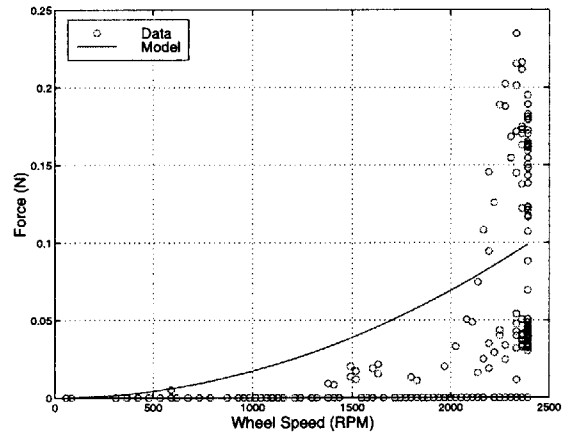


(d) $h_5 = 4.42$

Figure A-8: Coefficient Curve Fits - Ithaco E Wheel Radial Force (1)



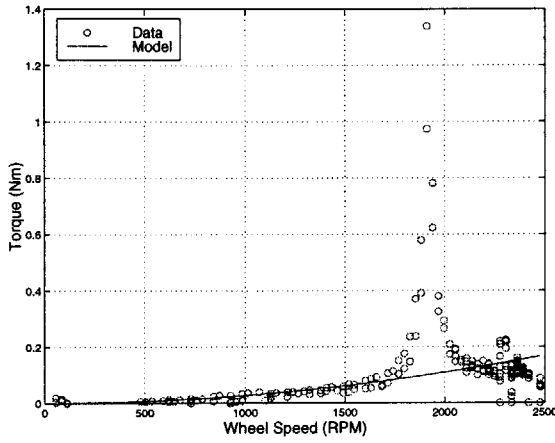
(a) $h_6 = 5.37$



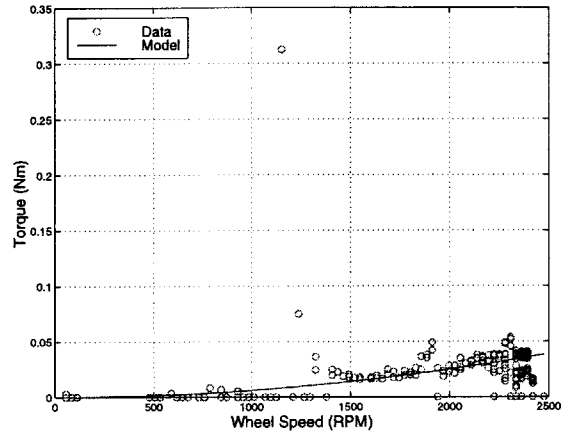
(b) $h_7 = 5.57$

Figure A-9: Coefficient Curve Fits - Ithaco E Wheel Radial Force (2)

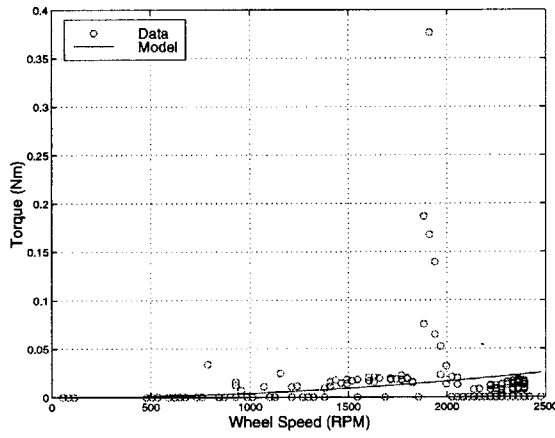
A.2.2 Radial Torque



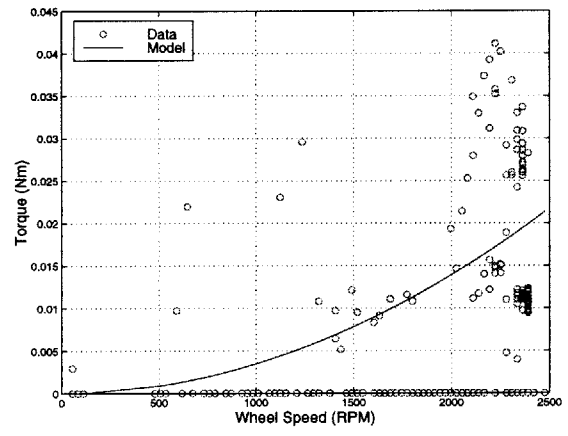
(a) $h_1 = 1.00$



(b) $h_2 = 2.00$

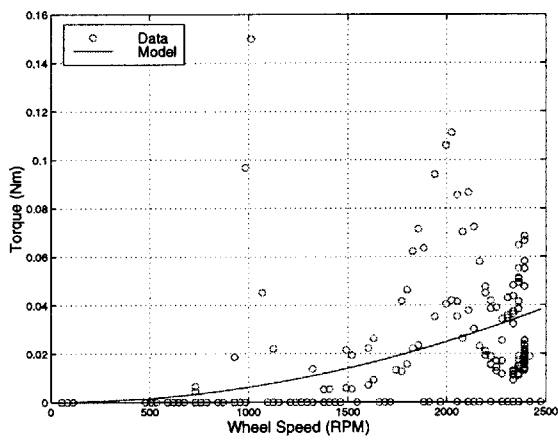


(c) $h_3 = 3.00$

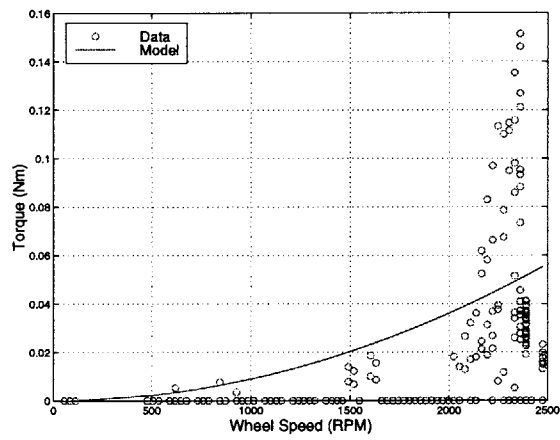


(d) $h_4 = 4.00$

Figure A-10: Coefficient Curve Fits - Ithaco E Wheel Radial Torque (1)



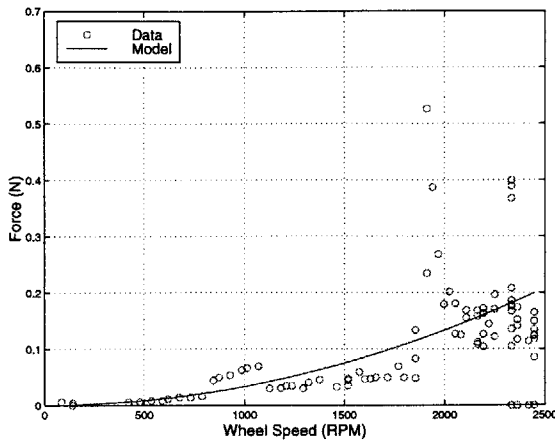
(a) $h_5 = 4.42$



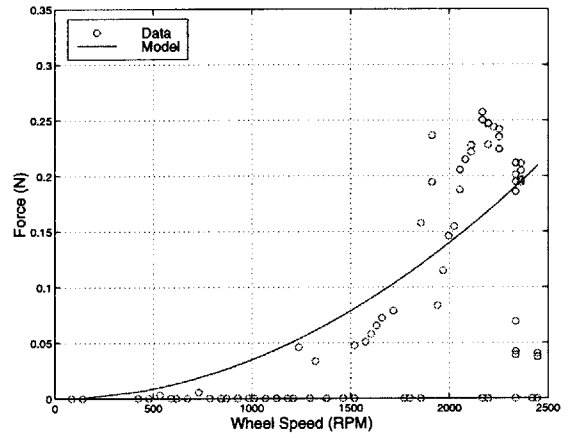
(b) $h_6 = 5.58$

Figure A-11: Coefficient Curve Fits - Ithaco E Wheel Radial Torque (2)

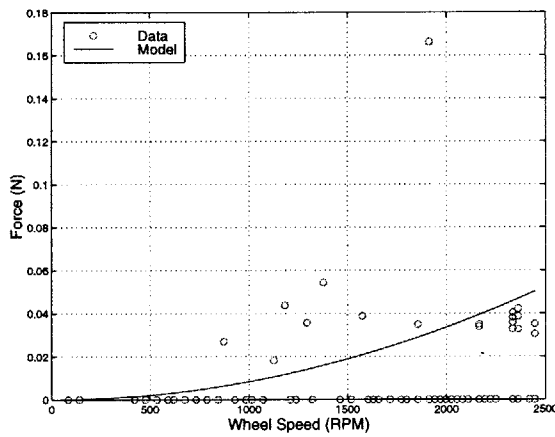
A.2.3 Axial Force



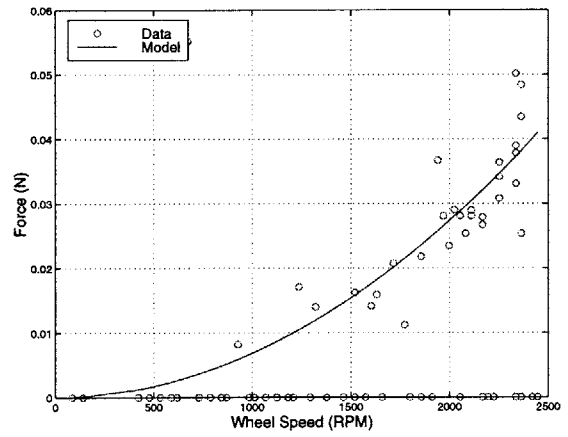
(a) $h_1 = 1.00$



(b) $h_2 = 2.00$

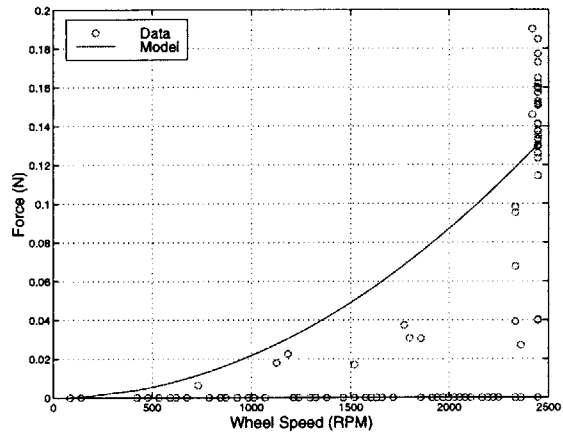


(c) $h_3 = 2.96$



(d) $h_4 = 4.00$

Figure A-12: Coefficient Curve Fits - Ithaco E Wheel Axial Force (1)



(a) $h_5 = 4.43$

Figure A-13: Coefficient Curve Fits - Ithaco E Wheel Axial Force (2)

Appendix B

Derivation of Empirical Model Autocorrelation

Begin with the empirical model in the time domain:

$$m(t) = \sum_{i=1}^n C_i f_{rwa}^2 \sin(2\pi h_i f_{rwa} t + \alpha_i) \quad (\text{B.1})$$

The definition of the autocorrelation of $m(t)$ is [21]: Substituting Equation B.1 into Equation gives:

$$R_m(\tau) = E \left[\sum_{i=1}^n \sum_{j=1}^n C_i C_j f_{rwa}^4 \sin(2\pi h_i f_{rwa} t + \alpha_i) \sin(2\pi h_j f_{rwa} (t + \tau) + \alpha_j) \right] \quad (\text{B.2})$$

Equation B.2 can be simplified with the following trigonometric identity:

$$\sin a \sin b = \frac{1}{2} [\cos(a - b) - \cos(a + b)] \quad (\text{B.3})$$

The expression for the autocorrelation is now:

$$R_m(\tau) = E \left[\sum_{i=1}^n \sum_{j=1}^n \frac{C_i C_j f_{rwa}^4}{2} \left\{ \cos(2\pi f_{rwa} (h_i t - h_j (t + \tau)) + \alpha_i - \alpha_j) - \cos(2\pi f_{rwa} (h_i t + h_j (t + \tau)) + \alpha_i + \alpha_j) \right\} \right] \quad (\text{B.4})$$

Using the definition of the expected value of a random process, $X(t)$, with marginal density function $f_{X(t)}(x)$ [21]:

$$E[X(t)] = \int_{-\infty}^{\infty} x f_{X(t)}(x) dx \quad (\text{B.5})$$

the autocorrelation becomes:

$$\begin{aligned} R_m(\tau) = & \int_0^{2\pi} \int_0^{2\pi} \sum_{i=1}^n \sum_{j=1}^n \frac{C_i C_j f_{rwa}^4}{2} \left\{ \cos(2\pi f_{rwa}(h_i t - h_j(t + \tau)) + \alpha_i - \alpha_j) \right. \\ & \left. - \cos(2\pi f_{rwa}(h_i t + h_j(t + \tau)) + \alpha_i + \alpha_j) \right\} f_{\alpha_i \alpha_j}(\alpha_i, \alpha_j) d\alpha_i d\alpha_j \end{aligned} \quad (\text{B.6})$$

where $f_{\alpha_i \alpha_j}(\alpha_i, \alpha_j)$ is the joint probability density function of the random variables α_i and α_j . If it is assumed that α_i and α_j are both distributed uniformly over the interval $[0, 2\pi]$ and are stochastically independent, their probability density functions, $f_{\alpha_i}(\alpha_i)$ and $f_{\alpha_j}(\alpha_j)$, are:

$$\begin{aligned} f_{\alpha_i}(\alpha_i) &= f_{\alpha_j}(\alpha_j) = \frac{1}{2\pi} \\ f_{\alpha_i \alpha_j}(\alpha_i, \alpha_j) &= f_{\alpha_i}(\alpha_i) f_{\alpha_j}(\alpha_j) = \frac{1}{4\pi^2} \end{aligned} \quad (\text{B.7})$$

For simplicity, let:

$$\begin{aligned} A &= 2\pi f_{rwa}(h_i t - h_j(t + \tau)) \\ B &= 2\pi f_{rwa}(h_i t + h_j(t + \tau)) \end{aligned} \quad (\text{B.8})$$

Then, substituting Equations B.7 and B.8 into Equation B.4 further simplifies the autocorrelation:

$$\begin{aligned} R_m(\tau) = & \sum_{i=1}^n \sum_{j=1}^n \frac{C_i C_j f_{rwa}^4}{8\pi^2} \left[\int_0^{2\pi} \int_0^{2\pi} \cos(A + \alpha_i - \alpha_j) d\alpha_i d\alpha_j \right. \\ & \left. - \int_0^{2\pi} \int_0^{2\pi} \cos(B + \alpha_i + \alpha_j) d\alpha_i d\alpha_j \right] \end{aligned} \quad (\text{B.9})$$

Now, consider the two integrals in Equation B.9 separately for the case $i \neq j$:

$$\begin{aligned} \int_0^{2\pi} \int_0^{2\pi} \cos(A + \alpha_i - \alpha_j) d\alpha_i d\alpha_j &= 0 \\ \int_0^{2\pi} \int_0^{2\pi} \cos(B + \alpha_i + \alpha_j) d\alpha_i d\alpha_j &= 0 \end{aligned} \quad (\text{B.10})$$

and for the case $i = j$:

$$\begin{aligned} \int_0^{2\pi} \int_0^{2\pi} \cos A \, d\alpha d\alpha &= 4\pi^2 \cos A \\ \int_0^{2\pi} \int_0^{2\pi} \cos(B + 2\alpha) d\alpha d\alpha &= 0 \end{aligned} \quad (\text{B.11})$$

Since both integrals equal 0 when $i \neq j$ one of the summation signs can be eliminated. Using the results in Equation B.11 and substituting back the expression for A (Equation B.8), the final form for the autocorrelation of the empirical model is obtained:

$$R_m(\tau) = \sum_{i=1}^n \frac{C_i^2 f_{rwa}^4}{2} \cos(2\pi f_{rwa} h_i \tau) \quad (\text{B.12})$$

Appendix C

Tachometer Controller Design

The first step in the design of the controller is obtaining a model of the open loop plant. The tachometer signal is passed through a low pass filter before being compared to the input voltage to attenuate any high frequency noise. Therefore, the plant dynamics are a combination of the wheel and filter dynamics. The filter is a simple RC circuit with the transfer function:

$$H_{filt}(s) = \frac{V_{out}}{V_{\Omega}} = \frac{1/RC}{s + 1/RC} \quad (C.1)$$

where R is the resistance, C is the capacitance, V_{Ω} is the tachometer voltage and V_{out} is the output voltage of the filter. The corner frequency of the filter can be expressed as, $\omega_0 = 1/RC$ [27]. For this application, a corner frequency of 6 Hz was chosen because it is out of the bandwidth of the controller but still a decade below 60 Hz, the frequency of electrical noise. A 100 nF capacitor was used, setting the resistance, R , to 265 k Ω .

The representative reaction wheel is modeled as a flywheel with inertia, I , and damping, c , driven by a motor with resistance R_a and induced voltage, or back emf, e_b as shown in Figure C-1 [28]. The transfer function model of the mechanical system from applied torque,

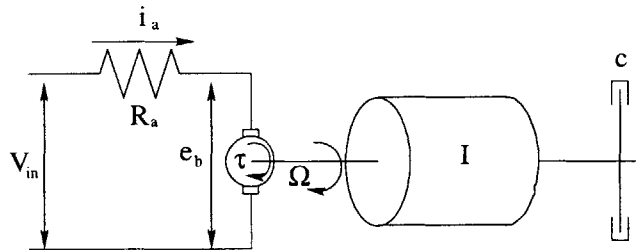


Figure C-1: Schematic Diagram of Representative Reaction Wheel Showing Flywheel and Motor

V_τ to angular velocity, V_Ω , is:

$$\frac{V_\Omega(s)}{V_\tau(s)} = \frac{1}{Is + c} \quad (\text{C.2})$$

Summing the voltages around the motor circuit results in an expression for applied voltage, V_{in} :

$$V_{in} = R_a i_a + e_b \quad (\text{C.3})$$

The relationships between the torque and the current, i_a , and the back emf, e_b , and the angular velocity are:

$$V_\tau = K i_a \quad (\text{C.4})$$

$$e_b = K_b V_\Omega \quad (\text{C.5})$$

where K is a motor-torque constant and K_b is a back emf constant. Substituting Equation C.4 into Equation C.2 and Equation C.5 into Equation C.3 and solving both equations for the current gives:

$$i_a = \frac{V_\Omega(Is + c)}{K} = \frac{V_{in} - K_b V_\Omega}{R_a} \quad (\text{C.6})$$

The transfer function of the wheel/motor is obtained through algebraic manipulation,:

$$H_{wheel}(s) = \frac{V_\Omega(s)}{V_{in}(s)} = \frac{K/R_a I}{s + \frac{R_a c + K K_b}{R_a I}} \quad (\text{C.7})$$

and can be simplified by defining the constants, $a = (R_a c + K K_b)/R_a J$ and $b = K/R_a J$:

$$H_{wheel}(s) = \frac{b}{s + a} \quad (\text{C.8})$$

The transfer function of the open loop system is obtained from Equations C.1 and C.8:

$$H_{plant} = \frac{V_{out}}{V_{in}} = H_{wheel} H_{filt} = \frac{b/RC}{(s + a)(s + 1/RC)} \quad (\text{C.9})$$

The values of a and b are determined by taking the transfer function of the open loop system and comparing it to the model as shown in Figure C-2. Setting $a = 0.22$ and $b = 3.1$ results in the close model/data fit seen in the plot. The control loop is closed by feeding the control

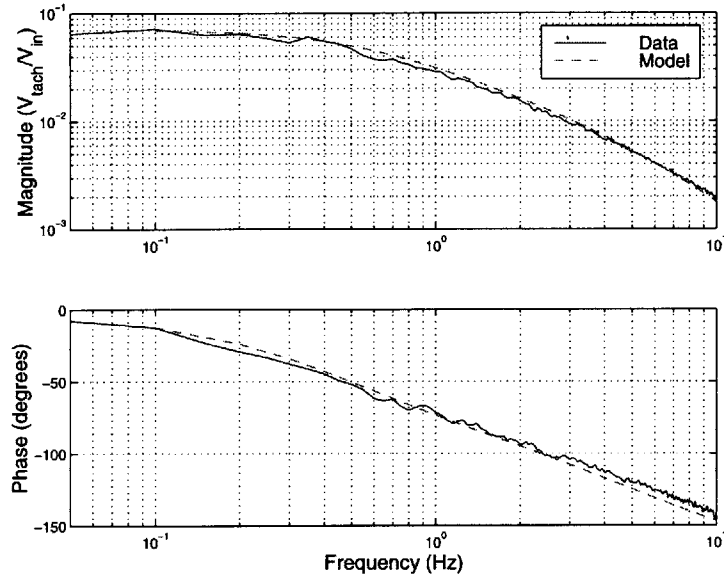


Figure C-2: Fitting Plant Transfer Function for Open Loop System

signal through an amplifier and into the wheel. The closed loop transfer function is:

$$H_{CL} = \frac{\frac{K_p b}{RC}}{s^2 + \left(a + \frac{1}{RC}\right) s + \frac{a + K_p b}{RC}} \quad (C.10)$$

where K_p is the controller gain and is set by the amplifier. A block diagram of the controller is presented in Figure C-3.

The controller was built with a series of simple circuits as shown in Figure C-4. The tachometer signal is input to a low-pass filter, and the filter output is passed through a follower. Then a summer is used to compare the filtered tachometer signal to the input from the signal generator. The output of the summer, V_{out} in the figure, is the control signal and drives the motor until V_{tach} and V_{in} are equivalent indicating that the wheel is

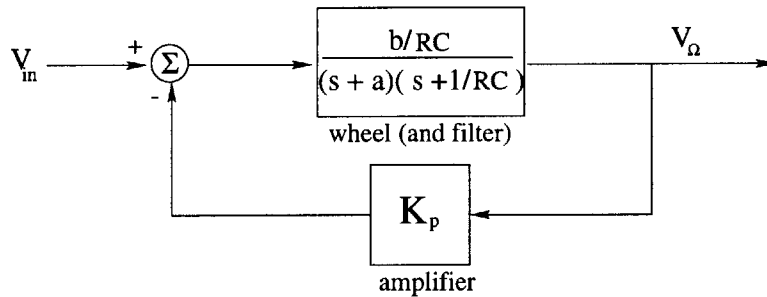


Figure C-3: Block Diagram of Tachometer Control Loop

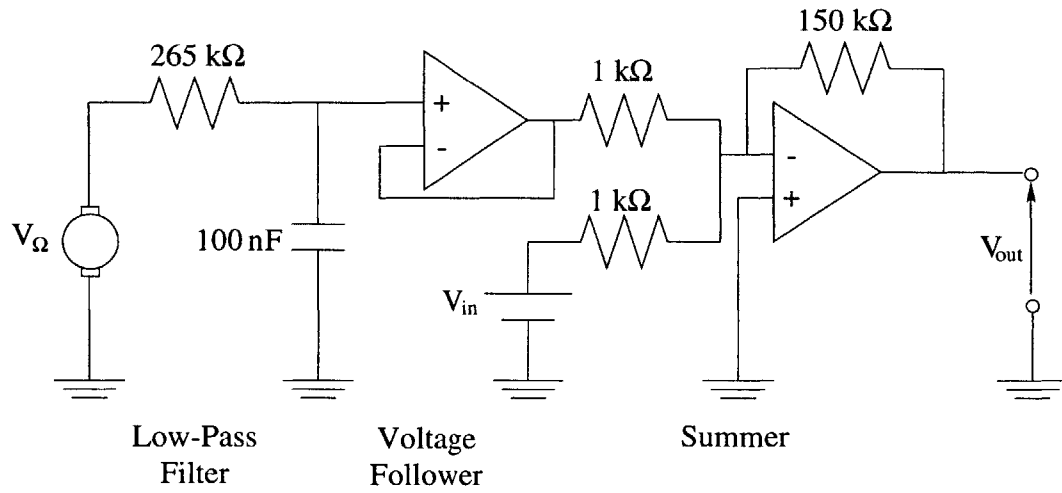


Figure C-4: Circuit Diagram of Tachometer Controller

spinning at the desired speed. The values of the resistors and capacitor used in the low-pass filter and summer are shown in Figure C-4.

Bibliography

- [1] Danner, R., S. Unwin, *et al.*, “Space Interferometry Mission: Taking the Measure of the Universe,” March 1999. Jet Propulsion Laboratory.
- [2] Laskin, R. A., “Technology for Space Optical Interferometry,” in *AIAA Aerospace Sciences Meeting and Exhibit*, January 1995. AIAA 95-0825.
- [3] Laskin, R. A. and M. S. Martin, “Control/Structure System Design of a Spaceborne Optical Interferometer,” in *Proceedings of AAS/AIAA Astrodynamics Specialist Conference*, August 1989. AAS 89-424.
- [4] de Weck, O., D. Miller, and H. Gutierrez, “Structural Dynamics and Controls for NGST - A Preliminary Study,” in *Proceedings of the 34th Liege International Astrophysics Colloquium*, June 1998, pp. 269–273.
- [5] Ingham, M., Y. Kim, E. Crawley, H. McManus, and D. Miller, “Experimental Characterization of Thermal Creak Response of Deployable Structures,” in *40th AIAA/ASME/ASCE/AHS/ASC Structures, Structural Dynamics and Materials Conference*, April 1999. AIAA 99-1269.
- [6] Bialke, B., “High Fidelity Mathematical Modeling of Reaction Wheel Performance,” in *21st Annual American Astronautical Society Guidance and Control Conference*, February 1998. AAS paper 98-063.
- [7] Marshall, T., T. Gunderman, and F. Mobley, “Reaction Wheel Control of the MSX Satellite,” in *Proceedings of the Rocky Mountain Guidance and Control Conference*, February 1991, pp. 119–138. AAS 91-038.
- [8] Davis, L. P., J. F. Wilson, R. E. Jewell, and J. J. Roden, “Hubble Space Telescope Reaction Wheel Assembly Vibration Isolation System,” March 1986.
- [9] Fukuda, T., H. Hosokai, and N. Yajima, “Flexibility Control of Solar Battery Arrays (3rd Report, Vibration and Attitude Control with Consideration of the Dynamics of a Reaction Wheel as an Actuator,” *Bulletin of the JSME*, Vol. 29, No. 255, September 1986, pp. 3121–5.
- [10] Sabnis, S., F. Schmitt, and L. Smith, “Magnetic Bearing Reaction Wheel,” Tech. Rep. N76-27336, NASA, February 1976. prepared for JPL by Sperry Flight Systems.
- [11] Bosgra, J. and J. J. M. Prins, “Testing and Investigation of Reaction Wheels,” in *Automatic Control in Space*, 1982, pp. 449–458. 9th Symposium.

- [12] Davis, P., D. Cunningham, and J. Harrell, "Advanced 1.5 Hz Passive Viscous Isolation System," in *AIAA/ASME/ASCE/AHS/ASC Structures, Structural Dynamics, and Materials Conference*, April 1994, pp. 2655–2665. AIAA 94-1651.
- [13] Sperry Flight Systems, "An Evaluation of Reaction Wheel Emitted Vibrations for Large Space Telescope," tech. rep., NASA/Marshall Space Flight Center, January 1976. NASA tech report N76-18213.
- [14] Pendergast, K. J. and C. J. Schauwecker, "Use of a Passive Reaction Wheel Jitter Isolation System to Meet the Advanced X-Ray Astrophysics Facility Imaging Performance Requirements," in *SPIE Conference on Space Telescopes and Instruments*, Vol. 3356, March 1998.
- [15] Hasha, M. D., "Reaction Wheel Mechanical Noise Variations." Space Telescope Program Engineering Memo SSS 218, June 1986.
- [16] Bialke, B., "A Compilation of Reaction Wheel Induced Spacecraft Disturbances," in *20th Annual American Aeronautical Society Guidance and Control Conference*, February 1997. AAS paper 97-038.
- [17] Li, B., G. Goddu, and M.-Y. Chow, "Detection of Common Motor Bearing Faults Using Frequency-Domain Vibration Signals and a Neural Network Based Approach," in *Proceedings of the American Control Conference*, June 1998.
- [18] Neat, G. W., J. W. Melody, and B. J. Lurie, "Vibration Attenuation Approach for Spaceborne Optical Interferometers," in *IEEE Transactions on Control Systems Technology*, Vol. 6, November 1998.
- [19] Gutierrez, H. L., *Performance Assessment and Enhancement of Precision Controlled Structures During Conceptual Design*, Ph.D. thesis, Massachusetts Institute of Technology, February 1999.
- [20] Brown, R. G., *Introduction to Random Signal Analysis and Kalman Filtering*, John Wiley & Sons, Inc., 1983.
- [21] Wirsching, P. H., T. L. Paez, and H. Ortiz, *Random Vibrations: Theory and Practice*, John Wiley & Sons, Inc., 1995.
- [22] de Weck, O., *Integrated Modeling and Dynamics Simulation for the Next Generation Space Telescope*, Master's thesis, Massachusetts Institute of Technology, June 1999.
- [23] Melody, J. W., "Discrete-Frequency and Broadband Reaction Wheel Disturbance Models." JPL Interoffice Memo #3411-95-200csi (Internal Document), June 1995.
- [24] Ehrich, F. F., ed., *Handbook of Rotordynamics*, McGraw-Hill, Inc., 1992.
- [25] C.H. Edwards, J. and D. E. Penney, *Elementary Differential Equations*, Prentice Hall Inc., 3rd ed., 1993.
- [26] Blaurock, C., *Modeling of Geometrically Nonlinear Flexible Structures for Control.*, Ph.D. thesis, Massachusetts Institute of Technology, September 1997.
- [27] Senturai, S. D. and B. D. Wedlock, *Electornic Circuits and Applications*, Krieger Publishing Company, 1993.

[28] Ogata, K., *Modern Control Engineering*, Prentice Hall Inc., 1990.